Institute of Materials Science of Seville

O. Sánchez-Sobrado

Optical Absorption and Emission of Nanomaterials Integrated in One Dimensional Photonic Crystals

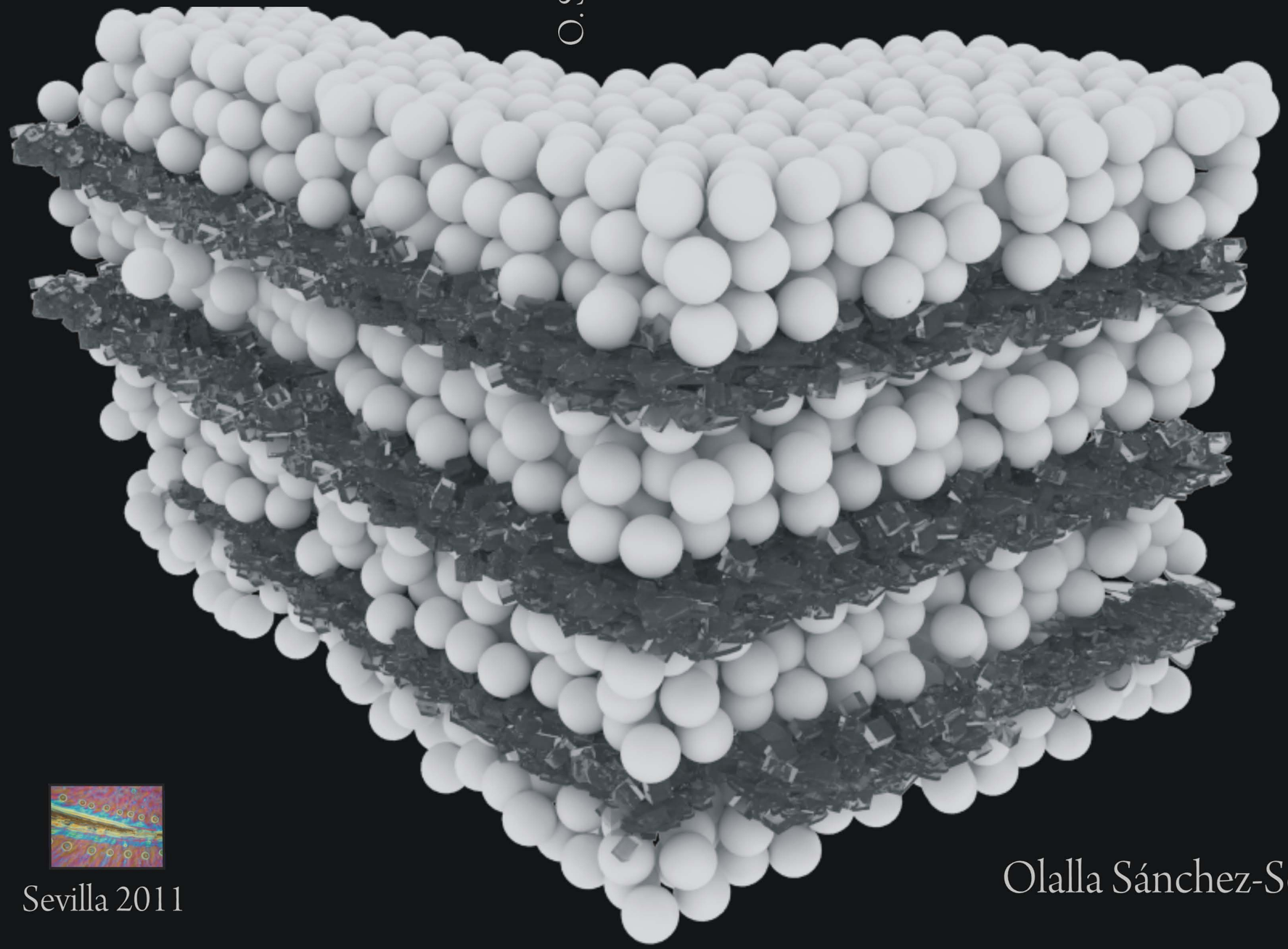

Sevilla 2011

Olalla Sánchez-Sobrado

Optical Absorption and Emission of Nanomaterials Integrated in One Dimensional Photonic Crystals

Report presented to apply for PhD degree by:

Olalla Sánchez-Sobrado

PhD Advisor:

Hernán Ruy Míguez García

Tutor of the University of Seville:

Diego Gómez García

Department of Physics of Condensed Matter
University of Seville

Institute of Materials Science of Seville
Spanish National Research Council

Seville 2011

For the ones who had a notion, a notion deep inside that ain´t no sin you be glad you´re alive.

Bruce Springsteen. "Badlands", 1978.

Agradecimientos/ Agradecementos

Quisiera agradecer, en primer lugar, a mi director de tesis. No hay mucha gente que pueda presumir de admirar a su jefe.Yo sí. Gracias por todo lo que has hecho por mí, que es mucho más que dirigirme la tesis. Tu ejemplo ha sido una gran motivación para mí a lo largo de estos cuatro años. Gracias por celebrar más que nadie mis buenos momentos y por apoyarme en los malos. Tus enseñanzas y consejos me los llevaré siempre, y vaya a dónde vaya podré decir con mucho orgullo que yo fui doctoranda del gran Hernán Míguez.

También quiero agradecer al segundo autor (a veces creo que el primero) de esta tesis: Mauricio Calvo. Todo este trabajo habría sido absolutamente imposible sin tu ayuda, y buena parte de lo que soy te lo debo a ti. Gracias por toda la paciencia que has tenido conmigo, por solucionar todas mis crisis con un "Enter" y por decir "¡Ahí voy!" … y venir, siempre.

A lo largo de estos cuatro años, mis compañeros del grupo de Materiales Ópticos Multifuncionales han estado SIEMPRE TODOS disponibles para CUALQUIER cosa que haya necesitado. Por eso, desde Agus hasta Alberto, esta tesis lleva un pedacito de cada uno de ellos. Especialmente de Silvia, que me enseñó a apilar las dichosas nanopartículas, y de Gabriel, a cuya colaboración debo algunos de mis resultados más importantes. A Mari Carmen le quiero agradecer todo su apoyo y cariño desinteresado en los momentos en los que más lo he necesitado, y también en los que menos lo he merecido. Eres muy fuerte, muy profesional y muy inteligente, y estoy segura de que tendrás una gran tesis. Y no me quiero olvidar de Curro, qué gran lección de dedicación y compañerismo nos has dado. Por último (lo bueno se hace esperar), Nuri (H, por supuesto). Juntas empezamos esto de la tesis hace cuatro años, juntas hemos quemado todas las fases y juntas estamos llegando al final. Gracias por haber sido una gran compañera y por haber estado siempre ahí. ¡Pórtate bien!

Quiero agradecer a Manuel Ocaña y Nuria Núñez por sus importantes aportaciones en esta tesis. Algunos de los resultados más destacados de mi trabajo no habrían sido posibles si no contáramos con los nanofósforos sintetizados por ellos. Sus consejos y su disponibilidad han sido una constante estos cuatro años.

A Luis Liz-Marzán y su equipo del Grupo de Química Coloidal de la Universidade de Vigo, quiero agradecer la confianza depositada en nuestro proyecto y su importante aportación mediante la síntesis de las nanopartículas de oro.

También quiero agradecer, muy especialmente, a Alejandro Giacomotti, Ariel Levenson y a toda la gente del Laboratoire de Photonique et de Nanoestructures (CNRS, Francia), por su cálido recibimiento durante mi estancia en París y todo el esfuerzo empleado en sacar adelante las medidas de las propiedades angulares de la luminiscencia de los resonadores conteniendo nanofósforos.

Gracias a Martyn Pemble y Kevin Thomas, del Tyndall Institute (UCC, Ireland), con quienes se llevó a cabo la infiltración de los espejos de Bragg con GaAs.

Quiero agradecer a Diego Gómez que haya aceptado ser mi tutor en la Universidad de Sevilla, por su ayuda desinteresada, su disponibilidad y el gran interés que ha mostrado siempre por mi trabajo.

A toda la gente del ICMSE, desde los técnicos hasta la gente de administración, porque todos contribuyen a que el trabajo de los que intentamos hacer ciencia llegue a buen puerto. Y por supuesto a todos mis compañeros

becarios, de todos los grupos, los de antes y los de ahora. Compartimos una meta. Una meta más fácil de alcanzar y un camino más fácil de recorrer porque lo hacemos juntos. Me gustaría agradecer especialmente a Lola, por enseñarme Sevilla, hacerme reír y por tantas cosas que ha hecho por mí. A Sonia, eres un ejemplo par mí por tu paciencia, compañerismo y alegría. A Anita (aunque sea técnico), que nos endulza a todos. A Víctor y Marcela que siempre me han cuidado. A David Abad que tanto me ha hecho reír. Y a los chicos guapos del instituto: los catalíticos Luisito, Óscar y muy especialmente Yesid. Algún día cumpliremos nuestra amenaza de mandar esto de la ciencia al carajo y nos retiraremos a cuidar la huerta de nuestras respectivas familias, y nos visitaremos mutuamente y tomaremos café … aunque hasta entonces, querido Yesid, los vagabundos como tú y como yo hemos nacido para correr.

Mi agradecimiento al Ministerio de Ciencia e Innovación por la concesión de una beca de formación de personal investigador.

A Rosa. Querida compañera de piso, amiga del alma y hermana para siempre. ¡Cuánto he aprendido de ti! Gracias por haberme hecho mejor, más fuerte, más segura y más feliz.

Al frente galaico popular de Sevilla, es decir, la Yols, la Mari, y la Maria Teresa Garea Pereira. Desde el día que llegué a Sevilla hace cuatro años habéis sido mi familia, me habéis cuidado y me habéis hecho reír. Gracias por haberme dejado formar parte de vuestras vidas y por haberos superapuntado a la mía.

Y a toda la muchachada con la que he compartido ratos realmente grandiosos estos cuatro años. Conchi, Ricardo, Loretta, Fran, Martina, Francesco, Chantal, Julia, Pau y Marco … (seguro que me olvido de gente, ¡lo siento!). Es gracias a vosotros que para mí Sevilla tiene y tendrá siempre un color muy espacial.

A miña curmá Sara. Nunca tiven a oportunidade de darche as grazas. Pois grazas. Por todo. Por coidarme tanto, por todo o teu apoio, polo teus miles de apuntes, pola túa infinita paciencia e pola cantidade de horas que botaches escoitando (aturando) tódalas miñas lerias diarias. Bótoche moito de menos prima. E o resto de tolos do monte da condesa e resto do universo polarizado en directa: o meu queridísimo Pacucho de Caldas, sweet Pilar , Martinsiño, o meu análogo do ICMM, Pablo, moita leria, moito chisme e moita viaxe. E tamén Silvia máis Miki, Kike, Vicente, Xullo, Xurxo, Óscar, Carlos, Sonia, Sofía, Gonzalo, David bizcochito, Carolina, Sara González, Maite (outra vez)...¿olvídome de alguén?. Seguro que sí. Ó voso carón empezou todo isto. Contei co voso apoio e axuda dende o primeiro día que entrei pola porta da facultade. A vosa amizade é moi valiosa para min e foi o voso exemplo o que me fixo, en parte, chegar ata aquí … non importa ónde estea cada un ...¡Verémonos sempre na nosa Compostela!

Ás miñas familias, polo seu apoio e polo interese mostrado en esas cousas do demo chamadas cristais fotónicos. En especial ó meu irmán Fran, que foi o meu primeiro profe de física e "arreglaproblemas" en xeral e a persoa que máis me fai encender o ordenador para explicarlle que raios fago en Sevilla.

Dende pequena aprendín que para lograr os meus obxetivos hai que facer dúas cousas. Primeiro soñalos e despois traballalos. Se son forte, é porque me fixeron forte. E se cheguei ata aquí, e se teño que chegar máis lonxe, pois será polos valores que me inculcaron, polos principios que me fan ser o que son. Por iso quero dedicar esta tese as dúas persoas que máis admiro no mundo, os meus pais Germán e Salomé.

Olalla. Sevilla, Julio 2011

Non des a esquecemento
da inxuria o rudo encono;
esperta do teu sono
fogar de Breogán.

Eduardo Pondal. "Os pinos", 1890.

Contents

Contents

Contents

Chapter I

Introduction

1. One dimensional photonic crystals.

A photonic crystal is a material that presents a periodic modulation of the refractive index in one, two or three dimensions of space.[1] These are obtained by repetition of a structural unit formed by at least two materials or compounds with different refractive index, as shown in Figure 1(a), (b) and (c). When white light impinges on the crystal it is partially reflected and transmitted at each interface between the components of different refractive index. If the wavelength of this radiation is on the order of the lattice parameter of the structure, this gives rise to interference phenomena between reflected and transmitted beams. Thus, certain frequency ranges will propagate through the photonic crystal and others will be reflected. This is illustrated in Figure 2 for the case of a one dimensional photonic crystal (1DPC). In the energy ranges for which the interference is destructive in the direction of propagation, no allowed photonic states exist inside the crystal.[2,3] This range is called photonic range of forbidden frequencies or photonic band gap (PBG). In 1987 E.Yablonovitch[2] and S.John[3] proposed, independently and simultaneously, the application of the forbidden photonic bands to study the inhibition of the

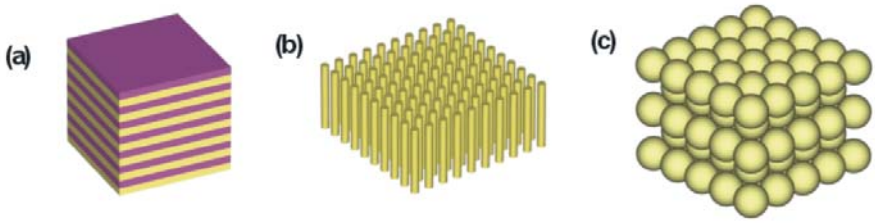

***Figure 1**. Diagrams of one (a), two (b) and three (c) dimensional photonic crystals.*

spontaneous emission and localization phenomena in these materials, respectively. Photonic bands are the result of plotting the dispersion relation between the frequency ω and the wave vector $\vec{k}$ of the allowed energy states of the crystal $\omega=\omega(\vec{k})$. This relation, in a homogeneous medium, is independent of the direction of propagation and is $\omega=(c/n)|k|$, where n is the refractive index on the medium (real and constant in the range in which the material presents no absorption) and c is the light speed in vacuum. In periodic structures, $\omega=\omega(\vec{k})$ depends on the direction of propagation.

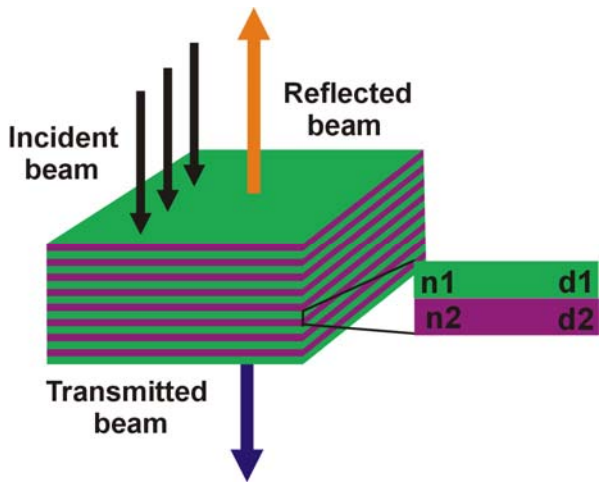

***Figure 2**. Scheme of a 1DPC formed by two types of materials. The incident white beam is diffracted.*

A one dimensional photonic crystal is a multilayer structure that presents a periodic modulation of the refractive index in only one direction of the space.[1] The band structure corresponding to a 1DPC is showed in Figure 3(a). In the figure, the frequency ω of the photons is expressed in dimensionless units, where *d* is the lattice parameter of the periodic structure. The wave vector, *k*, is given as *k d*. The case illustrated in the figure is that in which the propagation of light is perpendicular to the periodicity. The energy ranges in which the existence of optical modes in the crystal is forbidden are known as photonic band gaps. As a consequence, the electromagnetic radiation with this frequency would be reflected by a real structure with the same periodicity. This can be seen by comparing the band structure of Figure 3(a) with the reflectance spectrum plotted in Figure 3(b) corresponding to a 1DPC of ten unit cells and the same periodicity. In this spectrum, the secondary Bragg diffraction orders can be clearly distinguished. In a first approximation, the maximum of order *m* is placed at λ_0/m, where λ_0 is the spectral position of the lower energy diffraction order.

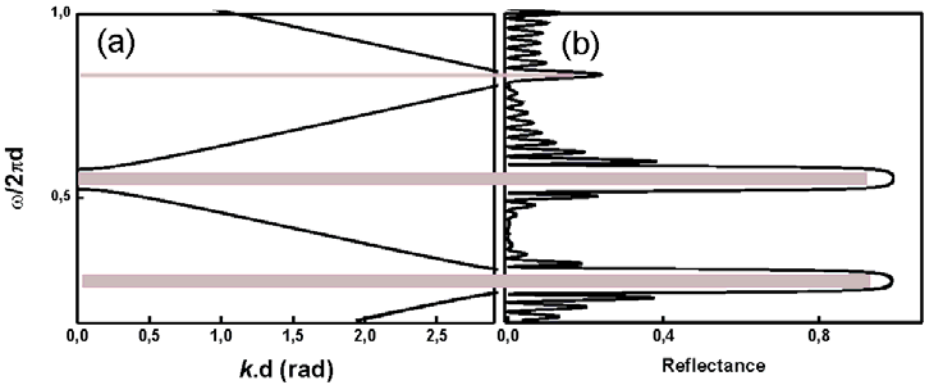

***Figure 3**. (a) Band structure corresponding to a one dimensional photonic crystal. (b) Reflectance spectrum corresponding to 1DPC of 5 unit cells with the same periodicity. The colored bands indicate the photonic band gaps of the structure.*

On the other hand, the group velocity, v_g, can be calculated from the slope of the curve ω(*k*):[4]

$$v_g = \frac{\partial \omega(k)}{\partial k} \qquad (1)$$

Thus, the optical modes propagating at frequencies in which the slope is small present low group velocity and the light will be confined at those spectral regions. These phenomena take place at the band gap edge of 1DPCs or at resonant modes corresponding to optical cavities obtained breaking their periodicity. Thus, at these resonant regions, the electromagnetic *density of modes* (DOM) present their maximum values.[4] The DOM can be calculated as the inverse of the group velocity:

$$\rho(\omega) = \frac{1}{v_g} = \frac{\partial k(\omega)}{\partial \omega} \qquad (2)$$

The orders of diffraction are usually called Bragg peaks. An example of a Bragg peak corresponding to a 1DPC is plotted in Figure 4(a). If the Bragg peak is placed at the visible range of the electromagnetic spectrum, the 1DPC displays bright colors, see Figure 4(b). Some basic features of the Bragg peak can be analyzed with approximate formulas. For instance, its spectral position λ_{Bragg} can be estimated through Bragg's law combined with Snell's law:

$$\lambda_B = \frac{2\Delta}{m}\sqrt{n_{eff}^2 - \sin^2\theta} \qquad (3)$$

where m is a diffraction order, Δ is the thickness of the basic structural unit or unit cell, θ is the angle between the direction of incidence and the direction normal to the surface of the structure and n_{eff} is the effective refractive index of the structure:

$$n_{eff} = \frac{n_1 d_1 + n_2 d_2}{d_1 + d_2} \qquad (4)$$

$$\Delta = d_1 + d_2 \qquad (5)$$

Where n_1 and n_2 are the refractive index of each one of the two types of layers and d_1 and d_2 their respective thickness. Thus, λ_{Bragg} can be modified by changing these parameters. The position of the Bragg peak λ_{Bragg} can be calculated through the Equation 3. Thus, the first order diffraction (m=1) at normal incidence occurs at:

$$\lambda_{Bragg} = 2n_{eff}\Delta \qquad (6)$$

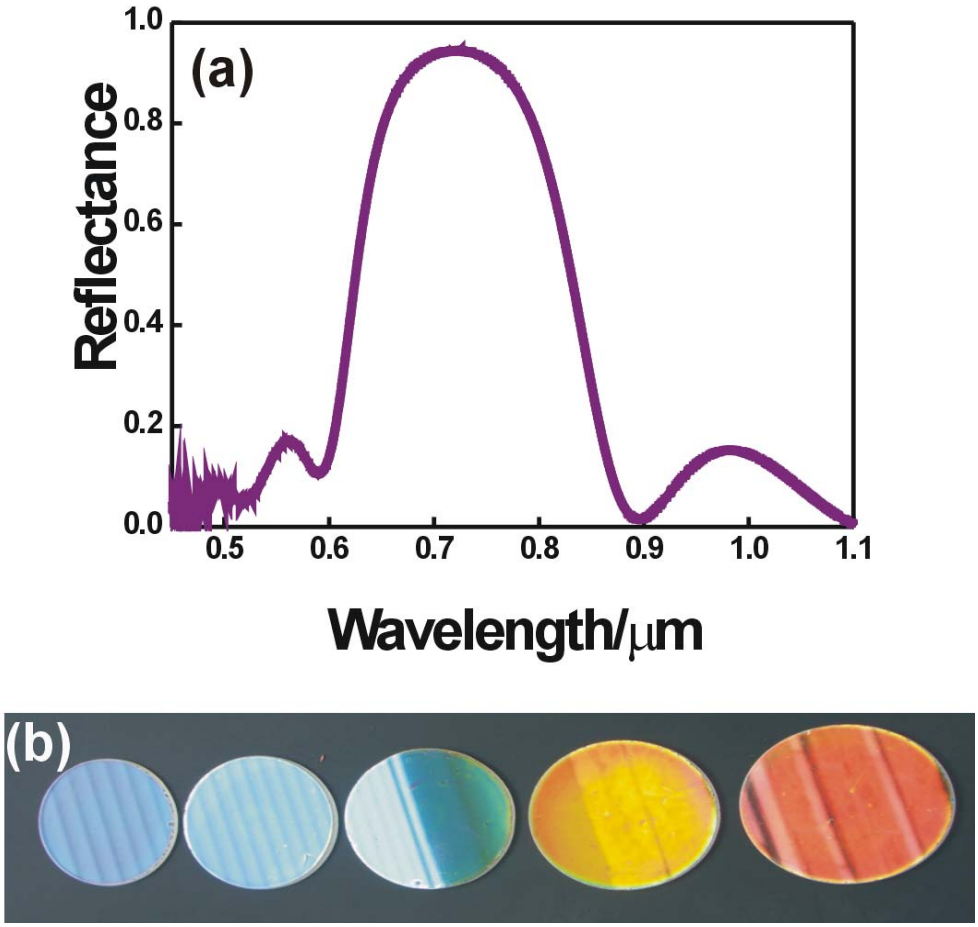

Figure 4. *(a) Specular reflectance spectrum showing a peak corresponding to the first order of the Bragg diffraction typical of a 1DPC made of 6 unit cells. (b) 1DPCs with different thickness of the unit cell displaying different colors.*

The simplest way to construct these structures is alternating layers of materials with different refractive index. To get these ensembles of high optical and structural quality, each layer must be uniform and the refractive index contrast between layers of different materials must be high, in order to attain a wide reflection peak. The optical response depends on three parameters: the refractive index of the components, the thickness of each type of layer and the number of layers. The Bragg peaks observed in the reflectance spectra are wider and more intense as the number of cells increases.[5] On the other hand, the thickness and the refractive index of the materials forming the unit cell determine the position of the reflectance maximum.

A wide variety of techniques based on physical vapour deposition methods are used to fabricate these Bragg reflectors with very good results.[6] These procedures consist in heating a material until its temperature of evaporation is reached and make it condense on a substrate forming a film. Then, the sample is kept below its temperature of fusion. Thus, resistant and durable coatings of metal oxides with good optical properties are obtained. The main inconvenient of this kind of techniques is the request of high temperatures to evaporate. A very important parameter to control along the process is the thickness of the film, which can be determined by optical methods like ellipsometry, reflectance and transmittance. Another important factor to take into account is the type of substrate. An inappropriate substrate leads to a bad adherence of the film. Thin films built by physical vapour deposition present dense microstructure, with low or null porosity. This assures the stability against environmental changes. This is an advantage for their use as passive optical elements, but renders them useless as base for sensors because their optical properties are not modified in response to environmental changes. On the other hand, methods based in the wet deposition of sol-gel precursors of inorganic compounds on flat substrates, as *dip coating*[7] and *spin coating*,[8] are also employed, very satisfactory results being attained. These are simple methods to deposit different materials like semiconductors, oxides, piezoelectric or ferroelectric materials as thin films on substrates made of polymers, ceramics, metals or semiconductors. The multilayers built using these techniques present very high reflectance. One of the most important obstacles of these structures is the deterioration of the photonic crystal as the layers are deposited. As a solution, after the deposition of each layer, the samples are subjected to short heat treatments of densification at high temperatures.[7,8] But heat treatments also present disadvantages. Each heating cycle causes densification, thus the firstly deposited layers may end up having less thickness than those formed later. This gives rise to an undesirable gradual modification of the optical thickness along the direction normal to the layers. Dense coatings deposited by using this process are also not responsive against environmental changes.

2. Porous 1DPCs.

For applications as detectors of liquids and gases, it would be desirable to build 1DPCs presenting optical response to environmental changes. Porous structures in which the control of optical properties depends on the control of the composition and the morphology and size of the pores, have been proposed with this aim.[9] Recently, a wide variety of porous Bragg stacks have been realized following methods based on electrochemical etching, physical vapor deposition at glancing angle or wet deposition. These materials have several applications in fields such as biological and chemical sensing,[10, 14] detection and recognition,[15] photovoltaics,[16] conducting[17] and photoconducting coatings,[18] radiation shielding,[19,20] or light emission.[21]

The electrochemical etching is a methodology in which tubular pore structures are constructed by selective elimination of well-defined regions of a metal wafer, normally silicon or alumina, through the combination of oxidation and latter dissolution in an acidic electrolyte. The size and shape of the pores, and therefore the optical response of the structure, are determined by the modulation of a current density applied to the substrate. Thus, the refractive index of a specific layer of the structure is determined by the thickness of the pore walls. The fabrication process is schematized in Figure 5(a). The first porous multilayer was made of silicon. A single silicon wafer was made porous by passing an anodic current in a fluorhydric acidic solution, obtaining pores with size comprised between 2 nanometers and a few microns depending on the charge density, the concentration of the ion fluoride and the doping level of the silicon wafer.[22] As an example of this kind of structures, Figure 5(b) shows a scanning electron microscopy (SEM) of the cross section of a 1DPC made by alternating porous silicon layers of different porosity.[23] Its reflectance spectrum is plotted in Figure 5(c). Alumina is another important material used to fabricate porous 1DPCs by electrochemical etching.[24] In a first electrochemical step, a mirror-polished aluminum substrate is anodized in an acidic solution to generate a surface array of regularly arranged stem pores. In a second anodic step, the current is sinusoidally modulated to generate a pore structure from the seminal pores previously obtained. The Figure 5(d) displays a SEM image of a cross section of a 1DPC made of alumina.[13] The three transmittance spectra plotted in Figure 5(e) coorespond to porous alumina mutilayers composed by 15, 30 and 45 unit cells (spectra 1, 2, and 3 respectively). The advantage of the electrochemical etching techniques is the great reproducibility and accuracy of the pore modulation achieved, whereas the main drawback is that it can only be applied to materials that can be obtained in the shape of conducting wafers.

The physical vapor deposition at glancing angle (GLAD) is another

methodology to fabricate porous 1DPCs. It combines the traditional thin film vacuum deposition with a particular geometry in which the substrate is tilted with respect to the line connecting the target and the substrate.[25] The final ensemble is provided with highly accessible and tunable interconnected porosity. This technique allows controlling the refractive index along the stacking direction. Bragg stacks can be attained by deposition of one or two different materials. In the first case, the contrast between the refractive index of layers forming the unit cell can be reached through the control of the angle of the deposition since this determines the porosity. By using only one material, bulk properties are not affected. Titanium dioxide and indium tin oxide have been used to obtain conductive[26] or photoconductive[17] porous Bragg mirrors. In Figure 6(a) a SEM image of the cross section of a TiO_2 1DPC built using this technique is shown.[10] An example of deposition of two different materials is that in which SiO_2 and TiO_2 multilayers are fabricated keeping the interconnected porous structure between layers.[27] This technique allows controll the size and the density of the interstitial sites very precisely for each layer individually.

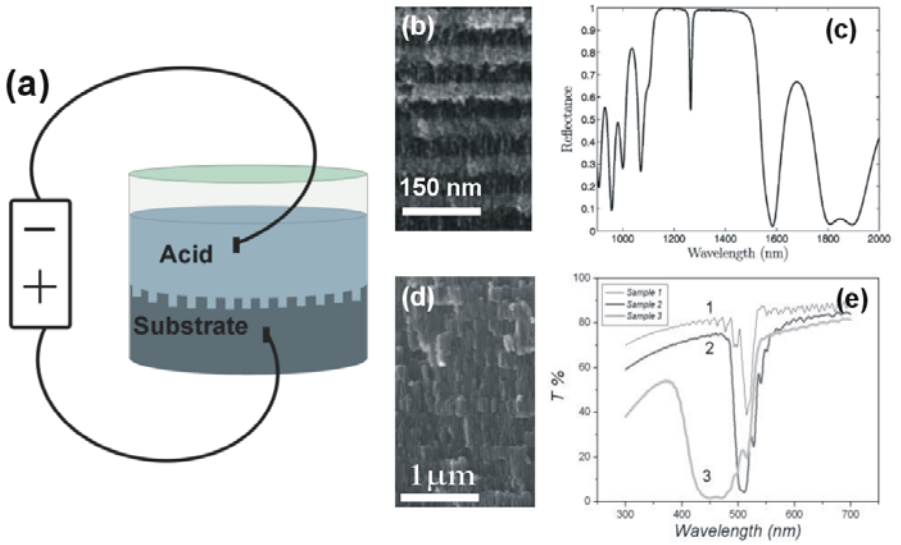

***Figure 5**. (a) Diagram of the electochemical etching process. Scanning electron microscopy images of the cross section of porous one dimensional photonic crystals made of (b) silicon and (d) alumina. (c) Reflectance spectrum corresponding to the structure displayed in (b). (e) Transmittance spectra corresponding to multilayers as that showed in (d) made of 15, 30 and 45 unit cells (1, 2 and 3 respectively). (Figures (b) and (c) are extracted from reference 23. Figures (d) and (e) are extracted from reference 13).*

The methods based on wet deposition also assure fine control over the properties of porous structures and the reproducibility of the whole pore system. These methods consist in the sequential deposition of two types of porous layers from solution-derived precursors by spin[28] or dip coating.[31] The materials that have been used for this purpose are supramoleculary templated metal oxides, clays and nanoparticles of different sort. The experimental conditions of the deposition and the composition of the liquid precursor dispersions yield control over the pore size distribution and overall porosity of the mesoporous networks.

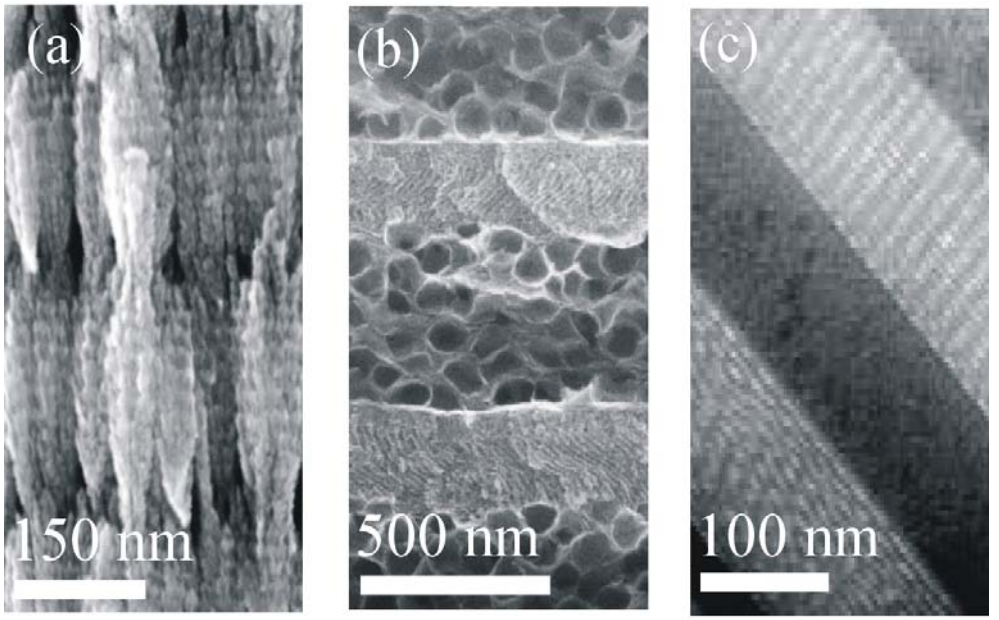

Figure 6. *Scanning electron microscopy images of the cross section of porous one dimensional photonic crystals made of (a) titanium dioxide by physical vapor deposition at glacing angle (b) laponite – TiO_2 system.(c) supramolecularly templated layers of SiO_2 and TiO_2. (Images extracted from references 10, 28, 29).*

Clay Bragg Stacks (CBS)[28] are made alternating layers of laponite (a synthetic philosilicate clay of empirical formula $Na_{0.7}[(Si_8Mg_{5.5}Li_{0.3})O_{20}(OH)_4]$) and metal oxides porous layers as TiO_2. These two materials present a high contrast between their refractive indices, which leads to a good optical response of the ensemble. The cross section of this system is pictured in the SEM image of Figure 6(b). The holes observed in the layers of laponite are, actually, spheres of polyestyren which have been removed from the layers. Clays are well known for their versatility as

adsorbents, ion exchange materials and catalysis. On the other hand metal oxides are used to stack meso-ordered porous metal oxide thin films by using an organic template. The choice of the metal oxide precursor, the solvent and the organic templating agent are crucial factors to determine the pore size and the morphology of the network. The number of materials that can be shaped as mesostructured thin films, hence used to build 1DPCs, is limited practically to SiO_2 and TiO_2.[29-31] Alcoholic solutions of titanium (IV) or silicon (IV) compounds are usually chosen as precursors and cationic surfactant like CTAB (cetyl trimethyl ammonium bromide) or block copolymers like Pluronics F127 are used as templates. After the deposition of the precursors by spin or dip coating, the polymer is removed by a heating treatment that consolidates the inorganic wall. These Bragg stacks are foreseen to be used as base materials in optical sensing due to their narrow pore size distribution. A cross section of one of these structures is shown in the SEM image of Figure 6(c).[35]

3. 1DPCs made of nanoparticles.

In this thesis, we present a complete study of the structural and optical properties of 1DPCs made of nanoparticles, as well as of their capacity to modify the optical properties of several nanomaterials of different morphologies. This ability of the nanoparticle Bragg mirrors to adapt to any arbitrary shape of the guest material is a key factor that leads to preserve the optical quality of the periodic structures studied along the research work herein presented. Methods based in deposition of sol-gel precursors are usually chosen to obtain a rich variety of metal oxide colloidal suspensions controlling the size and the shape of the resulting particles. This kind of materials presents the optimal features to attain 1DPCs with the required structural and optical properties. In order to construct the Bragg mirror, nanoparticles are sequentially deposited from their colloidal suspensions (preferably in alcoholic media). To assure a good optical response, the variation of the refractive index between the different materials forming the 1DPC must be high and a smooth interface between layers is necessary. The surface charge and the pore size distribution of the particles play an important role in the stacking and in the interpenetration of the layers respectively. Some metal oxide colloids are commercial while others particles have to be synthesized taking into account the different experimental parameters that influence the size and the shape of the obtained nanoparticles. Due to their high refractive index contrast, the most employed nanoparticles are those of SiO_2 and TiO_2.[32] Other examples include the stacking of alternated porous layers of SnO_2 and $Sb:SnO_2$ with SiO_2 nanoparticles.[33] Another reported example is that in which the alternated deposition of layers of TiO_2 particles

with different aggregation state were stacked to generate the refractive index contrast.[34]

One dimensional photonic crystals made of nanoparticles of SiO_2 and TiO_2 were firstly fabricated within the Multifunctional Optical Materials group by Silvia Colodrero et al.[32] In this work, our group presented a Bragg stack made by alternated deposition of these colloids under strict control of the aggregate state by using the spin coating technique. The resulting layers are well packed but keep a highly accessible and interconnected porosity. This structure is schematized in Figure 7(a). The study of the optical and structural properties of these photonic crystals, as well as their application to modify optical absorption and photoluminescence of different materials integrating them, are the main objectives of this thesis. Preliminary studies about the environmental response of different porous 1DPCs have proved their potential as base materials for detection of gases and liquids.[32,35,36] It has been also demonstrated that nanoparticle one dimensional photonic crystals amplified the conversion of the efficiency of solar energy into electricity in certain type of photovoltaic cells.[16]

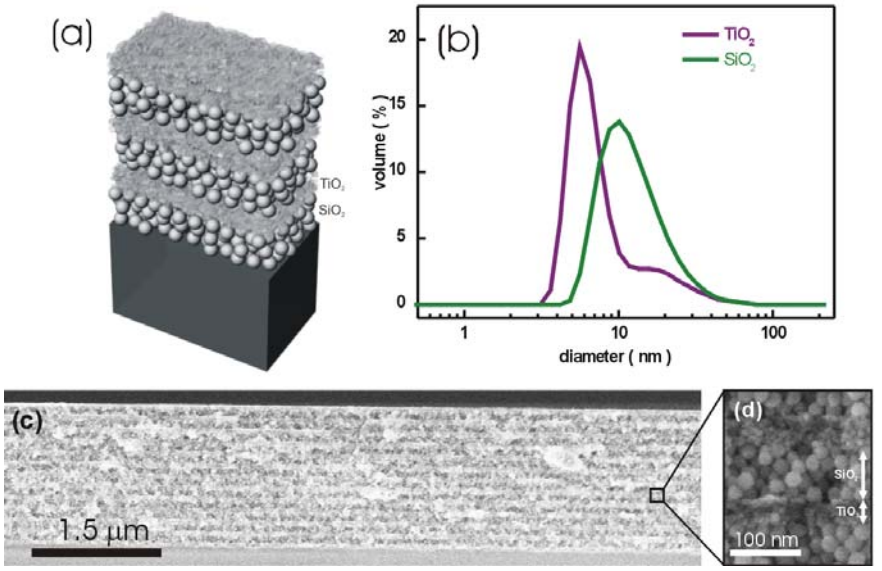

***Figure 7**. (a) Model of a nanoparticle 1DPC. Spherical beads represent SiO_2 nanocolloids, smaller ones of irregular shape are TiO_2 nanocrystals. (b) Size distribution (vol %) of the suspensions employed to build a multilayer structure formed by packed nanoparticles of silica (green line) and titania (violet lines) (extracted from reference 32). (c) Low and (d) high magnification SEM images of the cross section of a twelve unit cell nanoparticle 1DPC. The two different types of nanoparticles forming the structure, SiO_2 (spherical shape) and TiO_2 (irregular shape) can be distinguished.*

The starting materials are colloidal suspensions of both types of particles in methanol using concentrations comprised between 1 and 6 % wt. This solvent was chosen because no coagulations was observed in the suspension when it is prepared in this way[37] and at the same time the liquid is volatile enough to completely leave the structure during the formation process. SiO_2 colloids were purchased from Dupont (Ludox TMA, Aldrich), and TiO_2 crystallites were synthesized using a procedure described in the Appendix. The most important parameter that influences on the uniformity of layers is the size of the particles. The control over the size distribution and the amount of aggregates is crucial to obtain smooth interfaces between the two types of layers in order to attain a good optical response. The monodispersity of nanoparticles was checked using photocorrelation spectroscopy.[35] Monomodal distributions of TiO_2 nanocrystals and SiO_2 colloids were attained as shown in Figure 7(b). One of the advantages that these materials present is the sequentiality of depositions. When a layer is formed, the next can be immediately deposited, no intermediate treatment being necessary. The Figure 7(c) shows a scanning electron microscopy image of the cross section of a twelve unit cell 1DPC made of nanoparticles of oxides of titanium and silicon. Uniformity in the long range can be clearly appreciated, while the different morphology of the spherical SiO_2 and the more irregular TiO_2 particles is evident in Figure 7(d), which is a magnification of 7(c). The two types of interfaces can be also distinguished. The surface between neighboring layers is flat when SiO_2 nanoparticles are deposited onto the more compact TiO_2 crystallites and is more diffuse when the opposite occurs, since TiO_2 crystallites are then able to penetrate a few nanometers into the larger pores of the layers of SiO_2 colloids. This does not significantly affect the fact that a high dielectric contrast between neighboring layers can be attained.

As it was described before, the intensity of the Bragg peak of a 1DPC depends on the number of cells forming the structure. The evolution of the optical response of a SiO_2-TiO_2 nanoparticles multilayer with the number of deposited cells is shown in Figure 8(a). The observed Bragg maxima, associated to the presence of a photonic band gap in the direction normal to the layers, are more intense and narrower as the number of unit cells increases.[4] In the figure, red, blue and green lines corresponds to 5, 4 and 3 unit cell stacks respectively. Intense (up to 90%) and wide Bragg reflection peaks are observed, which is a direct consequence of the large refractive index contrast between the SiO_2 nanoparticle layers and the TiO_2 nanocrystal ones. The way to modify the spectral position of the Bragg peak of these structures is by changing the thickness of the forming layers. The reflectance spectra measured for multilayers with different lattice parameter are plotted in Figure 8(b). Red, blue and green lines spectra correspond to stacks made from silica suspensions with concentrations of 3,

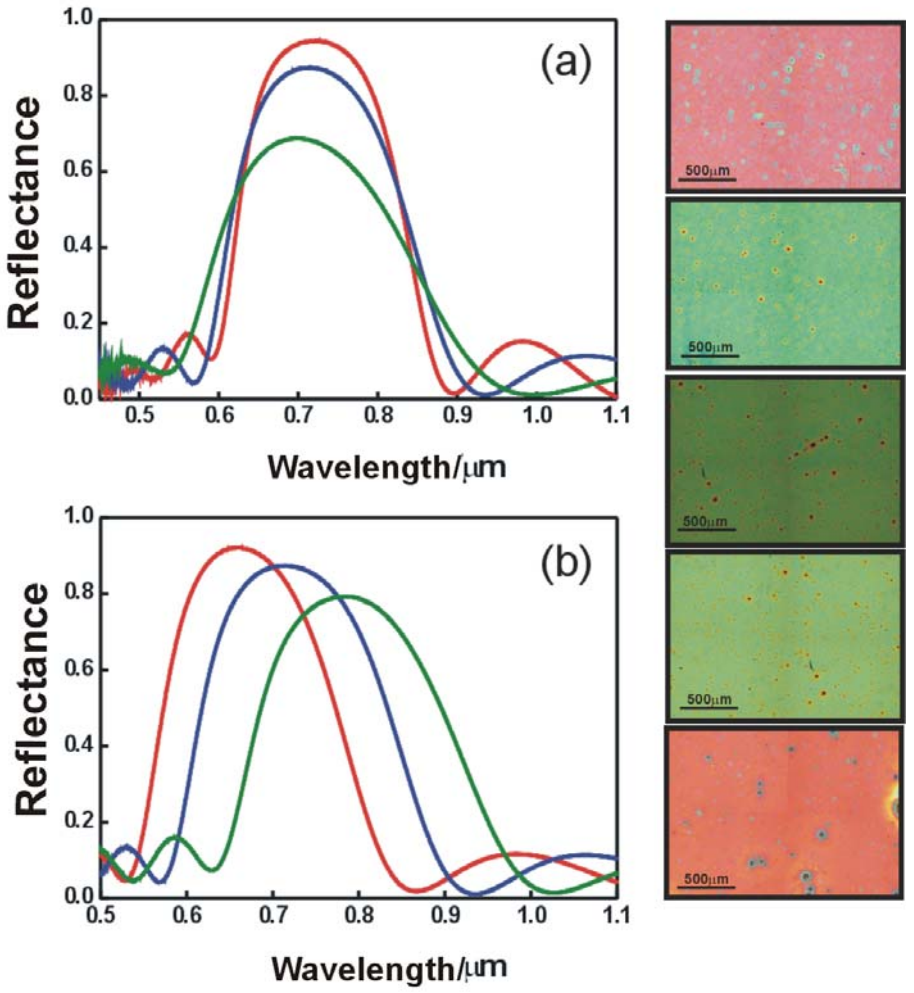

Figure 8. *Evolution of the reflectance spectrum of a SiO_2-TiO_2 nanoparticle multilayer with the number of cells. Red, blue and green lines correspond to 5, 4, and 3 unit cell multilayers respectively (a) and with the lattice parameter (b); red, blue and green lines corresponds to silica concentrations of 3, 3.5, and 4 % wt respectively. (c) Optical microscope pictures of multilayers with different lattice parameters.*

3.5, and 4 % wt., respectively, the concentration of the suspension of titania as well as the rest of the experimental parameters remaining fixed. This is the proof that nanoparticles 1DPCs with high reflectivities can be attained over the whole UV-Vis-IR electromagnetic spectrum. Optical microscope images are displayed in left panel of Figure 8 to show the different colors reflected by nanoparticle 1DPCs with different lattice parameters. The refractive index of TiO_2 and SiO_2 nanoparticle layers are actually an average of the refractive index of bulk materials (2.4 and 1.45

respectively) and the air of the pores. It can be estimated by fitting the optical reflectance spectra using a scalar wave approximation.[38,39] The calculated values are 1.74 for titania and 1.24 for silica layers. This implies that the pore volume fraction in the films is around 45% in both cases,[40] as calculated using the Bruggeman equation:

$$\frac{n_d^2 - n^2}{n_d^2 + 2n^2} ff_d + \frac{n_a^2 - n^2}{n_a^2 + 2n^2} ff_a = 0 \qquad [7]$$

Where n is the average refractive index of a layer, n_d is the refractive index corresponding to the bulk material, n_a is the refractive index of the air filling the pores and ff_d and ff_a the corresponding filling factors. These equation will be used for most calculations of porosity from average refractive index values presented in this thesis.

4. Motivation and objectives of this thesis.

One of the most developed areas in nanotechnology in the last years is that of nanoparticles that present resonant absorption or optical activity. On one hand, several examples have been reported about the properties of metallic nanoparticles with a well defined resonant absorption peak placed at the visible range due to the excitation of the localized surface plasmon. This kind of particles has been applied in fields such as catalysis[41], sensing[42] or optics.[43] The optical absorption is normally controlled through the surrounding material[44] or by controlling the size and shape of the particles.[45] On the other hand, there are lots of examples of luminescent nanoparticles with applications in fields as light emitting diodes (LEDs),[46] sensing[47] and bio-labelling.[48] Again, the optical properties of these nanoparticles are usually controlled by controlling their size and shape.[49] The available emission patterns of nanoparticles range from white light emission of certain semiconductor quantum dots,[50] to the narrow, atom-like ones of rare earth based nanophosphors.[51]

Taking into account their implantation in optoelectronic devices, it is important to modify the optical properties of nanoparticles by changing exclusively their photonic environment, that is, by integrating them in periodic structures like those studied in this thesis. In the case of metallic particles, in most reported studies, modifications of the optical absorption of particles are observed by infiltration in three dimensional photonic crystals, due to the interaction between both photonic and plasmonic resonances.[52,53] Nevertheless, no enhancement of the absorption has been

observed, probably because this kind of structures presents weak field localization at their resonance frequencies. Also, sharp and intense optical absorption fluctuations have been predicted for Bragg mirrors containing arrays of noble metal particles.[54] But most multilayers studied so far show several difficulties to host nanoparticles with different shape and size.

In the case of luminescent particles, there are various reported works about the infiltration of quantum dots in different photonic structures and the modification of their luminescence.[55,56] However, only two examples has been reported about the integration of rare earth doped nanophosphors in three dimensional photonic crystals.[57,58] In these experiments, significant modification of the luminescence lifetime was observed at photonic band gap frequencies. However, no selective and controlled suppression or enhancement of luminescence bands has been observed by integration of the nanophosphors in optical resonant cavities. Again, this is probably due to the difficulty to embed particles with arbitrary shape and size in periodic structures with the capacity to localize light.

Therefore, the motivation of this thesis was to build photonic structures provided with high optical quality, and hence, with the ability to confine light strongly in the frequencies of their resonances and with the capacity to host either absorbing or optically active nanoparticles with different shape and size, to significantly modify their optical properties. By infiltration in nanoparticle one dimensional photonic crystals, the controlled and selective amplification of the absorption of gold nanoparticles and of the photoluminescence of nanophosphors has been observed for the first time. The objectives of the thesis herein presented, entitled *"Optical Absorption and Emission of Nanomaterials Integrated in One Dimensional Photonic Crystals",* were:

– To sstudy of techniques of fabrication of nanoparticle 1DPCs and to analyze the dependence of both optical and structural properties on the experimental parameters. The results of this analysis are presented in Chapter II.

– To fabricate porous multilayers by using the studied procedures. Optimize the optical properties of porous multilayers over the range NIR-Vis-UV. These results are explained in Chapter III.

– To infiltrate nanoparticle 1DPCs with materials of high refractive index. The obtained results are explained in Chapter IV.

– To analyze the modification of optical absorption and photoluminescence properties of different kinds of nanomaterials integrated in nanoparticle multilayers. This study is presented in Chapters V and VI.

5. References.

[1] J.D. Joannopoulos, R.D. Meade, J.N. Winn. "Photonic Crystals: Molding the Flow of Light", *Princeton University Press*, Princeton, **1995**.

[2] E.Yablonovitch. "Inhibited spontaneous emission in solid-state physics and electronics", *Physical Review Letters, 58,* **1987**, 2059.

[3] S.John. "Strong localization of photons in certain disordered dielectric superlattices", *Physical Review Letters, 38,* **1987**, 2486.

[4] J.M. Bendickson, J.P. Dowling, M. Scalora. "Analytic expressions for the electromagnetic mode density in finite, one dimensional, photonic band gap structures", *Phys.Rev.E, 53*, **1996**, 4107.

[5] A. Yariv, P. Yeh. "Optical Waves in Crystals", John Wiley and Sons Inc., ISBN 0-471-43081-1. **2003**

[6] Macleod, H. A., "Thin Film Optical Filters", 4rd Edition, Published by Institute of Physics Publishing, London, **2001**.

[7] S. Rabaste, J. Bellessa, A. Brioude, C. Bovier, J.C. Plenet, R. Brenier, O. Marty, J. Mugnier, J. Dumas. "Sol-Gel fabrication of thick multilayer applied to Bragg reflectors and microcavities", *Thin Solid Films, 416,* **2002**, 242.

[8] R.M. Almeida, A. S. Rodrigues. "Photonic bandgap and structures by sol-gel processing", *Journal of Non-Crystalline Solids, 326*, **2003**, 405.

[9] N. Hidalgo, M. E. Calvo, H. Míguez. "Mesostructured Thin Films as Responsive Optical Coatings of Photonic Crystals", *Small*, 5, **2009**, 2309.

[10] J.J. Steele, A.C. van Popta, M.M. Hawkeye, J.C. Sit, M.J. Brett. "Nanostructured gradient index optical filter for high-speed humidity sensing" *Sensors & Actuators , 120,* **2006**, 213.

[11] K. A. Killian, T. Böcking, J.J. Gooding, *Chem. Commun.* **2009**, 630.

[12] S.Colodrero, M.Ocaña, A.R.González-Elipe, H.Míguez."Response of nanoparticle one dimensional photonic crystals to ambient vapour pressure" *Langmuir, 24*, **2008**, 9135.

[13] D.L. Guo, L.X. Fan, F.H. Wang, S.Y. Huang, X.W. Zou, "Porous Anodic Aluminum Oxide Bragg Stacks as Chemical Sensors", *J. Phys. Chem. C, 112,* **2008**, 17952.

[14] B.V. Lotsch, G.A. Ozin. "Clay Bragg Stack Optical Sensors", *Adv. Mater, 20*, **2008**, 4079.

[15] L. D. Bonifacio, D. P. Puzzo, S. Breslav, B. M. Willey, A. McGeer, G. A. Ozin. "Towards the Photonic Nose: A Novel Platform for Molecule and Bacteria Identification" *Adv. Mater, 22,* **2010**, 1351.

[16] S. Colodrero. A. Mihi. L. Haggman, M. Ocaña, G. Booscholoo, A. Hagfeldt, H. Míguez, "Porous One-Dimensional Photonic Crystals Improve the Power-Conversion Efficiency of Dye-Sensitized Solar Cells", *Advanced Materials, 21*, **2009**, 764.

[17] M.F. Schubert, J.Q. Xi, J.K. Kim, E.F. Schubert. "Distributed Bragg reflector consisting of high- and low-refractive-index thin film layers made of the same material" *Appl. Phys. Lett, 90,* **2007**, 141115.

[18] M.E. Calvo, S. Colodrero, T.C. Rojas, M. Ocaña, J.A. Anta, H. Míguez. "Photoconducting Bragg Mirrors based on TiO_2 Nanoparticle Multilayers" *Adv. Func. Mater. 18*, **2008**, 2708.

[19] P. Kurt, D. Banerjee, R.E. Cohen, M.F. Rubner, "Structural color via layer-by-layer deposition: layered nanoparticle arrays with near-UV and visible reflectivity bands" *J. Mater. Chem.,19,* **2009**, 8920.

[20] M.E. Calvo, O. Sánchez-Sobrado, G. Lozano, H. Míguez, "Molding with nanoparticle based One Dimensional Photonic Crystals: A Route to Flexible and Transferable Bragg Mirrors of High Dielectric Contrast.". *J. Mater. Chem. 19*, **2009**, 3144.

[21] F. Scotognella, D.P. Puzzo, A. Monguzzi, D.S. Wiersma, D. Maschke, R. Tubino, G.A. Ozin. "Nanoparticle One-Dimensional Photonic-Crystal Dye Laser" *Small, 5,* **2009**, 2048.

[22] R. Herino, G. Bomchil, K. Barla, C. Bertrand, JL. Ginoux. "Porosity and Pore-Size Distributions of Porous Silicon" *J. Electrochem. Soc., 134,* **1987**, 1994.

[23] J. J. Saarinen, S. M. Weiss, P. M. Fauchet and J. E. Sipe. "Reflectance analysis of a multilayer one-dimensional porous silicon structure: Theory and experiment" *J. Appl. Phys, 104*, **2008**, 013103.

[24] W. J. Zheng, G. T. Fei, B. Wang, Z. Jin, L. D. Zhang. "Distributed Bragg reflector made of anodic alumina membrane", *Materials Letters, 63*, **2009**, 706.

[25] M. J. Brett, M. M. Hawkeye. "Materials science - New materials at a glance" *Science, 319,* **2008**, 1192.

[26] J.J. Steele, A.C. van Popta, M.M. Hawkeye, J.C. Sit, M.J. Brett. "Nanostructured gradient index optical filter for high-speed humidity sensing", *Sensors & Actuators, 120,* **2006**, 213.

[27] L. González-García, G. Lozano, A. Barranco, H. Míguez, A. R. González-Elipe. "TiO_2-SiO_2 one-dimensional photonic crystals of controlled porosity by glancing angle physical vapour deposition" *J. Mater. Chem, 20,* **2010**, 6408.

[28] B.V. Lotsch, G.A. Ozin. "Photonic Clays: A New Family of Functional 1D Photonic Crystals" *ACS nano, 2*, **2008,** 2065,

[29] M.C. Fuertes, G. J. A. A. Soler-Illia, H. Míguez, "Process for Preparing Multilayers with an Ordered Mesoporous Structure, Material Obtained in this Manner, and Use", EP2073045

(WO2008034932), Priority date 18/09/2007

[30] S.Y. Choi, M. Mamak, G. Freymann von, N. Chopra, G.A. Ozin. "Mesoporous Bragg stack color tunable sensors", *Nano Lett*, *6*, **2006**, 2456.

[31] M.C. Fuertes, F.J. López-Alcaraz, M.C. Marchi, H.E. Troiani, G.J.A.A. Soler Illia, H. Míguez. "Photonic Crystals from Ordered Mesoporous Thin-Film Functional Building Blocks" *Adv. Funct. Mater. 17*, **2007**, 1247.

[32] S. Colodrero, M. Ocaña, H. Miguez. "Nanoparticle base done dimensional photonic crystals". *Langmuir, 24*, **2008**, 4430.

[33] D. P. Puzzo, L. D. Bonifacio, J. Oreopoulos, C. M. Yip, I. Manners, G. A. Ozin. "Color from colorless nanomaterials: Bragg reflectors made of nanoparticles" *J.Mater.Chem,19,* **2009**, 3500.

[34] M.E. Calvo, S. Colodrero, T.C. Rojas, M. Ocaña, J.A. Anta, H. Míguez, "Photoconducting Bragg Mirrors based on TiO_2 Nanoparticle Multilayers"*Adv. Func. Mater, 18,* **2008**, 2708.

[35] M. C. Fuertes, S. Colodrero, G. Lozano, A.R. González-Elipe, D. Grosso, C. Boissière, C. Sánchez, G. J. de A. A. Soler-Illia,H. Míguez, "Sorption properties of mesoporous multilayer thin films" *J. Phys. Chem. C, 112,* **2008**, 3157.

[36] S. Colodrero, M. Ocaña, A.R. González-Elipe, H. Míguez, "Response of nanoparticle-based one-dimensional photonic crystals to ambient vapor pressure" *Langmuir, 24,* **2008**, 9135.

[37] I. M. Thomas. "Single-Layer TiO_2 and Multilayer TiO_2-SiO_2 Optical Coatings Prepared from Colloidal Suspensions"*Appl. Opt* **1987**, *26*, 4688.

[38] K. W. K. Shung, Y. C. Tsai. "Surface Effects and Band Measurements in Photonic Crystals" *Phys. Re*V. *B, 48,* **1993**, 11265.

[39] A. Mihi, H. Míguez. "Origin of light-harvesting enhancement in colloidal-photonic-crystal-based dye-sensitized solar cells" *Phys. Chem. B, 109,* **2005**, 15968.

[40] H. C. van de Hulst. "Light Scattering by Small Particles" *Dover Publications*: New York, **1981**.

[41] R.M. Crooks, M. Zhao, L. Sun, V. Chechik, L.K. Yeung, "Dendrimer-encapsulated metal nanoparticles: Synthesis, characterization, and applications to catalysis", *Acc. Chem. Res, 34,* **2001**, 181.

[42] D.J. Maxwell, J.R. Taylor, S. Nie. "Self-assembled nanoparticle probes for recognition and detection of biomolecules", *J. Am. Chem. Soc, 124,* **2002**, 9606.

[43] E. Hutter, J.H. Fendler. "Exploitation of localized surface plasmon resonance", *Adv. Mater, 16,* **2004**, 1685.

[44] K. L. Kelly, E. Coronado, L. L. Zhao, G. C. Schatz, "The optical properties of metal nanoparticles: The influence of size, shape, and dielectric environment " *J. Phys. Chem. B* **2003**, *107*, 668.

[45] K. A. Willets, R. P. Van Duyne. "Localized surface plasmon resonance spectroscopy and sensing "*Ann. Rev. Phys. Chem.* **2007**, *58*, 267.

[46] V. L. Colvin, M. C. Schlamp, A.P. Alivisatos. "Ligth Emitting-Diodes made from Cadmium Selenide Nanocrystals and a Semiconductor Polymer" *Nature, 370*, **1994**, 354.

[47] I. L. Medintz, H. T. Uyeda, E. R. Goldman, H. Mattoussi, "Quantum dot bioconjugates for imaging, labelling and sensing*", Nature Mat, 4*, **2005**, 435.

[48] J. K. Jaiswal, H. Mattoussi, J. M. Mauro, S. M. Simon "Long-term multiple color imaging of live cells using quantum dot bioconjugates", Nature Biotech. 21, 2003, 47.

[49] X. Peng, L. Manna, W. Yang, J. Wickham, E. Scher, A. Kadavanich, A. P. Alivisatos, "Shape control of CdSe nanocrystals", *Nature,404*, **2000**, 59.

[50] M. J. Bowers, J. R. McBride, S. J. Rosenthal, "White-light emission from magic-sized cadmium selenide nanocrystals"*J. Amer. Chem. Soc. 127*, **2005**, 15378.

[51] J. C. Boyer, L. A Cuccia, J. A. Capobianco, "Synthesis of colloidal upconverting $NaYF_4$: Er^{3+}/Yb^{3+} and Tm^{3+}/Yb^{3+} monodisperse nanocrystals". *Nano Lett. 7*, **2007**, 847.

[52] F. García-Santamaría, V. Salgueirino-Maceira, C. López, L.M. Liz-Marzán, "Synthetic opals based on silica-coated gold nanoparticles" *Langmuir, 18*, **2002**, 4519.

[53] D.Y. Wang, V. Salgueiriño-Maceira, L.M. Liz-Marzán, F. Caruso. "Gold-silica inverse opals by colloidal crystal templating "*Adv. Mater.* **2002**, *14*, 908.

[57] E. Lidorikis, S. Egusa, and J.D. Joannopoulos. "Effective medium properties and photonic crystal superstructures of metallic nanoparticle arrays" *J. Appl. Phys, 101,* **2007**, 054304.

[58] P. Reithmaier, G. Sek1, A. Löffler, C. Hofmann, S. Kuhn, S. Reitzenstein, L.V. Keldysh, V.D. Kulakovskii, T.L. Reinecke, A. Forchel, "Strong coupling in a single quantum dot-semiconductor microcavity system". *Nature 432*, **2004**, 197.

[59] P. Lodahl, A. F. van Driel, I. S. Nikolaev, A.Irman, K. Overgaag, D. Vanmaekelbergh, W. L. Vos. "Controlling the dynamics of spontaneous emission from quantum dots by photonic crystals" *Nature, 430,* **2004**, 654.

[57] M. Aloshyna, S. Sivakumar, M. Venkataramanan, A. G. Brolo, F. C. J. M van Veggel,. "Significant suppression of spontaneous emission in SiO_2 photonic crystals made with Tb^{3+}-doped LaF_3 nanoparticles", *J. Phys. Chem. C, 111*, **2007**, 4047.

[58] Z. X. Li, L. L. Li, H. P. Zhou, Q. Yuan, C. Chen, L. D. Sun, C. H. Yan. "Colour modification action of an upconversion photonic crystal", *Chem. Commun*., *43*, **2009**, 6616.

Chapter II

Techniques of fabrication of nanoparticle one dimensional photonic crystals

1. Introduction.

All the samples prepared and analyzed to obtain the results presented in this thesis are based in multilayers formed by nanoparticles of SiO_2 and TiO_2. To design the optical response of these Bragg stacks is necessary to control both the refractive index and the thickness of the layers. These materials were first constructed by Silvia Colodrero et al. by using a spin coating process.[1] In this work different photonic crystals with different optical response were attained by changing the concentration of the precursor suspensions and keeping fixed the angular spinning speed. However, the range of suitable concentrations to obtain photonic crystals with good quality is narrow. For high values, aggregates of nanoparticles are formed leading to a bad adherence of the films. For low concentrations, the substrate is not totally covered. Also, it is very difficult to precisely control the optical response of the structures only by changing the concentration of the precursor suspensions.

In this chapter, two studies are presented on the application of both the spin and the dip coating techniques to the fabrication of Bragg mirrors made of nanoparticles

of SiO_2 and TiO_2 on flat glass substrates. The optimal parameters to build multilayers with a minimum number of defects and with the desired optical response are found for both studies. The control over the parameters of the fabrication process, acceleration ramp and final rotation speed in the case of the spin coating, as well as the concentration of precursor suspensions and the extraction speed in the case of the dip coating, is crucial to control the quality and the optical response of 1DPCs.

2. Spin coating.

2.a Nanoparticle 1DPCs built by spin coating.

Spin coating is a procedure used to apply uniform thin films on flat substrates. Briefly, an excess amount of precursor solution or suspension is placed on the substrate, which is then rotated at high speed in order to spread the fluid by centrifugal force. Rotation is continued while the fluid spins off the edges of the substrate, until the desired thickness of the film is achieved. The solvent employed is usually volatile, and simultaneously evaporates. For higher angular speed, a thinner film is attained. The thickness of the film also depends on the concentration of the precursor solution or suspension, as well as on its viscosity.

The spin coating process is completed in four phases schematized in Figure 1. The first phase is the *deposition*, see Figure 1(a). An amount in excess of the starting precursor suspension is deposited on the substrate. It can be rotated and tilted to obtain a good degree of coverage. Adding too much of the initial suspension has no impact on the final thickness of the film, since the excess is eliminated in the later stages of the process. However, if the amount deposited is not enough, the final coating of the film is not uniform. The second stage is the a*cceleration* γ, schematized in Figure 1(b). It is a phase in which the sample reaches the established final speed of rotation ω. In this part of the process the majority of excess material is removed due to centrifugal forces. A layer with a fairly uniform thickness begins to form on the substrate. During the third part of the process, the r*otation*, showed in Figure 1(c), the sample rotates at the final constant angular speed ω. The liquid film is thinned due to the centrifugal forces. As the viscosity increases, the evaporation of the volatile solvent begins to take more importance in the slimming of the film. The last phase is the *evaporation,* see Figure 1(d). It takes place during the whole process but becomes more important at the final stages of film thinning. During the evaporation, the solvent passes to the atmosphere, increasing the concentration of the solid and causing an increase in viscosity, which will eventually results in the formation of the film.

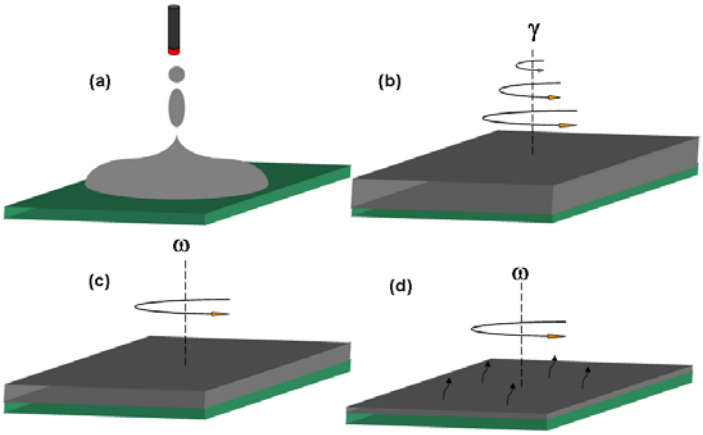

Figure 1. *Description of the spin coating process. (a) Deposition of the precursor suspension on the still substrate. (b) Acceleration. In this phase the excess amount of suspension is removed and the film begins to slim. (c) Rotation. The slimming continues when the final rotation speed is reached. (d) The evaporation of the solvent is the main factor in the formation of the film during the last part of the process.*

Being the spin coating the main method employed to prepared most structures analyzed in this research work, a thorough study of the spin coating protocol was performed. A detailed analysis of the effect of the spin coating parameters, *acceleration ramp* γ and *final rotation speed* ω, over the structural and optical properties of nanoparticle 1DPCs was carried out. Based on these results, a reliable synthetic route to attain high optical quality porous multilayers is provided. In these structures the effect of imperfections is minimized and the Bragg peak can be precisely tuned over the entire visible spectrum. This study establishes a relation between the structural variations observed with the relative importance of fluid flow and solvent evaporation on the thinning of each layer in the stack for the different deposition conditions employed. As far as we know, this is the first study of the influence of the deposition protocol on the properties of nanoparticle Bragg reflectors made by spin-coating. All the results presented in this section were reported in reference 2.

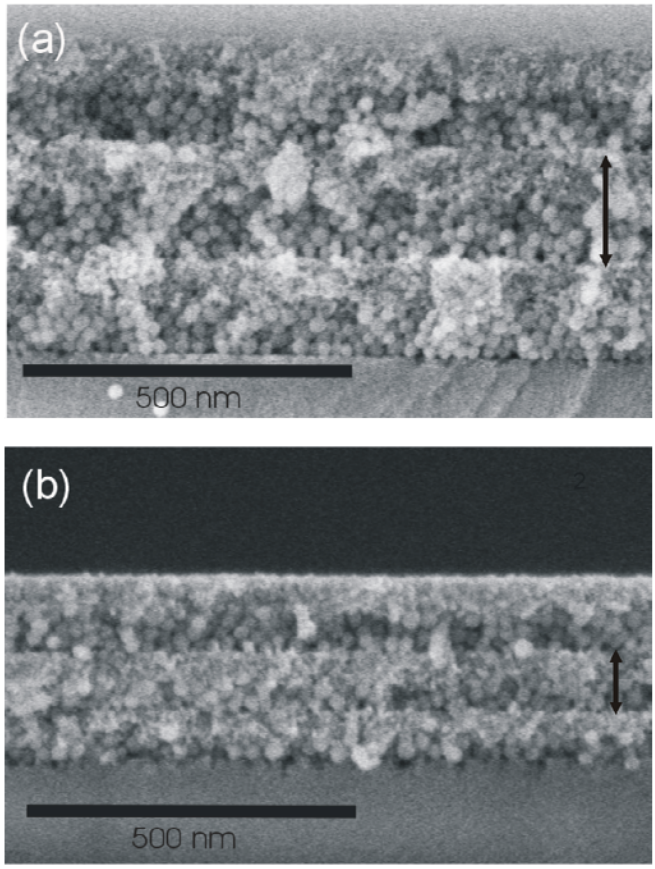

***Figure 2**. FESEM images showing the cross section of periodic nanoparticle multilayers obtained at final speeds of (a) 2500 rpm and (b) 6000 rpm.*

A total of 42 samples, of six layers each one of them, were prepared by an alternated deposition of TiO_2 and SiO_2 nanoparticle suspensions. The synthesis of nanoparticles is described in the Appendix. These sols were deposited over glass substrates using a spin coater (Laurell WS-400E-6NPP) in which both the acceleration ramp and the final rotation speed could be precisely determined. The first layer was deposited using 250 ml of SiO_2 sol and the substrate was tilted and rotated to let the suspension cover the total glass surface. Then, the sample was accelerated up to different final speed using also several ramps in each case, in order to test the effect of these parameters. The total spin coating process (ramping-up and

final speed) is completed in 60 seconds. Sequentially, another layer of a different type of nanoparticle is deposited following the procedure described above. The process is repeated until a total of six layers have been deposited. Final speed was chosen between nominal values of 2000 and 8000 revolutions per minute (rpm) and accelerations were selected between nominal values of 1950 and 13650 rpm s^{-1}. The precursor suspensions were diluted in methanol to 4 and 2 % wt. for TiO_2 and SiO_2 particles respectively. These concentrations remain constant along the experiments. The structure of the different sintered 1DPCs was studied by observing the cross sections of multilayers deposited under different conditions. Field emission scanning electron microscopy (FESEM) images of two cleaved films made of three SiO_2-TiO_2 bilayers are displayed in Figure 2. As expected, increasing the final rotation speed diminishes the final thickness of the layers, as Figures 2(a) and 2(b) illustrates. In each case, the black arrows indicate the thickness of the unit cell. In these examples, the same SiO_2 and TiO_2 solutions were deposited and spun at 2500 rpm and 6000 rpm, unit cells of 180 nm and 120 nm being obtained respectively. The acceleration used was 8450 rpm s^{-1} in both cases.

2.b Optical and structural quality.

In order to check the dependence of the quality of the multilayer with the experimental deposition conditions, namely acceleration ramp and final rotation speed, an optical study was performed by measuring and analyzing rreflectance spectra that were performed using a Fourier Transform infrared spectrophotometer (Bruker IFS-66 FTIR) attached to a microscope and operating in reflection mode with a 4X objective with 0.1 of numerical aperture (light cone angle ±5.7º). Because the main sign of the interference effects that occur as a consequence of the built up periodicity is a reflectance peak whose position and width depend on the refractive index and thickness of the layers, different spectra were attained from different spots of the same 1DPC in order to test its structural uniformity, since lack of layer thickness homogeneity along the substrate would result in variations of the optical response. Taking advantage of the radial symmetry of the spin coating process, reflectance spectra were collected from 1 mm^2 area spots every 2 mm from the geometrical centre of the substrate to one of its sides in all samples. In Figures 3(a) and 3(b), the results obtained for multilayers built at a fixed acceleration ramp of 3250 rpm s^{-1} and two final speeds, namely 2000 rpm 3(a) and 8000 rpm 3(b), are plotted. In addition, in Figures 3(c) and 3(d) the spectra obtained for samples made using a fixed acceleration of 8450 rpm s^{-1} and final rotation speeds of 2000 rpm 3(c) and 8000 rpm 3(d) are shown. It can be straightforwardly concluded from the analysis of these results that a better structural uniformity of the 1DPCs is achieved when multilayer deposition is carried out using high final rotation speeds, and that it

further improves if steep accelerations ramps are employed. Variations of the reflectance maximum intensity can be directly related to the presence of imperfections in the sample, since they give rise to diffusely scattered light that is actually removed from the reflected and transmitted beams. In this case, regardless of the uniformity of the response, the height of the peaks is never below 60% for 6 layer (3 unit cell) films.

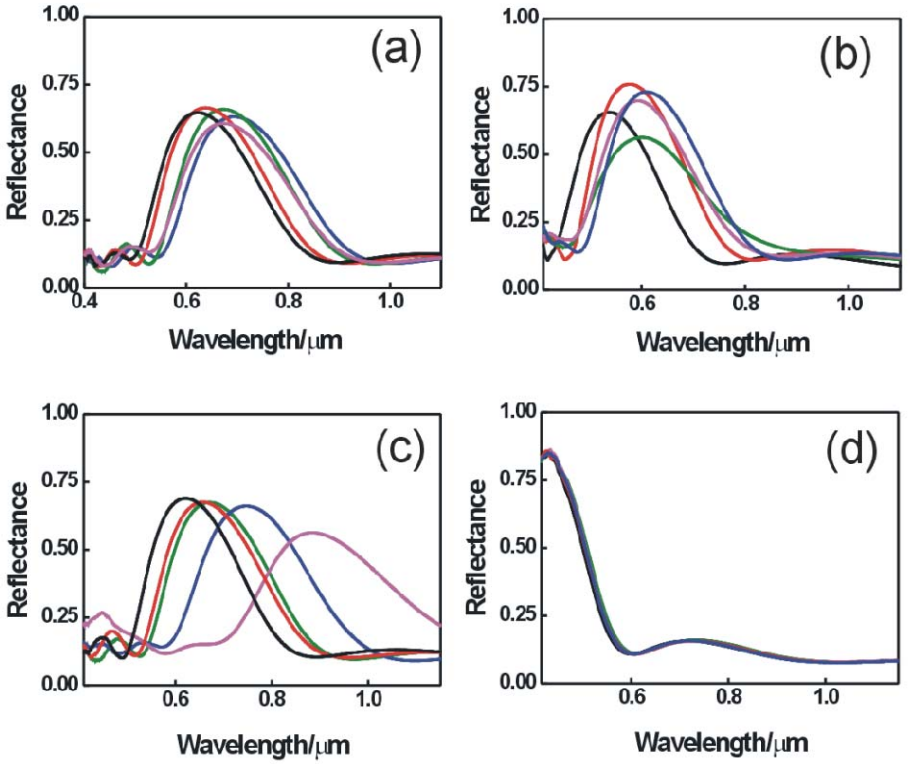

Figure 3. *Specular reflectance spectra taken from 1DPCs deposited using different spin coating conditions: (a) ω= 2000 rpm, γ= 3250 rpm s^{-1}; (b) ω= 8000 rpm, γ= 3250 rpm s^{-1}; (c) ω= 2000 rpm, γ= 8450 rpm s^{-1}; (d) ω= 8000 rpm, γ= 8450 rpm s^{-1}. In each case, spectra taken at different distances from the centre of the sample are plotted using a different line colour:* ▬ *0 mm,* ▬ *2 mm,* ▬ *4 mm,* ▬ *6 mm,* ▬ *8 mm.*

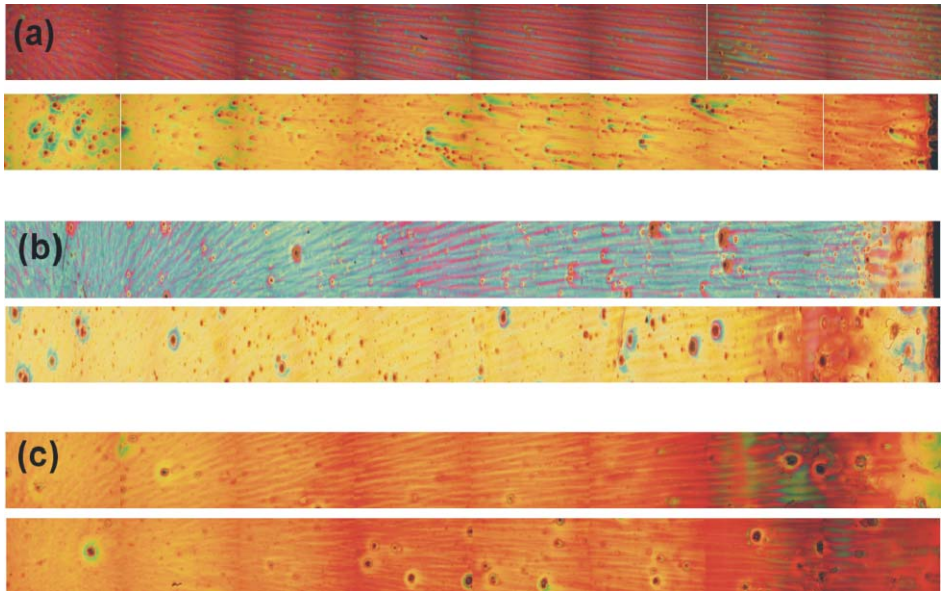

Figure 4. *Optical microscopy images of different multilayer built at different final and ramp accelerations. Each pair of images were obtained from multilayers deposited at the same final rotation speed and accelerations of* γ*=11050 rpm* s^{-1} *and* γ*=1950 rpm* s^{-1} *(top and bottom images in each case, respectively). (a)* ω*=8000 rpm, (b)* ω*=6000 rpm and (c)* ω*=2000 rpm.*

Among the defects typically observed in films deposited from particle suspensions by spin coating, the most relevant ones are those known as striations and comets. *Striations* are radially oriented undulations of the film, and are the result of the rotation of a surface cell pattern.[3,4] Such pattern may be present in any liquid film with one of its surfaces exposed to air as a result of the Marangoni effect.[5] In such films, surface tension gradients, which in this case could be originated by local fluctuations of the suspended particle concentration or the temperature, induce fluid flows that set up a cell surface pattern. Rotation of such pattern gives rise to the elongation of the cells, an effect that is more intense as the distance from the centre increases, which yields the striation pattern typically observed in spin coated films.[6] *Comets* are abrupt disruptions of the film uniformity caused by the presence of large particle aggregates that may be already present in the precursor suspension or formed during the spreading of the suspension on the substrate. These two types of imperfections can be readily seen when the multilayers are observed under the optical microscope. A series of pictures taken from 1DPCs deposited using different spin coating protocols are displayed in Figures 4(a) and 4(b) that show, respectively, pairs

of images of 1DPCs prepared using ω=8000 rpm and ω=6000 rpm and accelerations of γ=11050 rpm s^{-1} (top images) and γ=1950 rpm s^{-1} (bottom images). In all cases, the density of comets increases dramatically when slow ramps are used. In this case, the amount of comets observed in films deposited simultaneously onto similar substrates and from the same precursor suspension, changes with the conditions used in the spin coating protocol, as it can seen by comparing each pair of images shown in Figures 4(a), 4(b), and 4(c). This indicates that such comets originate during fluid flow and solvent evaporation from the rotating film. In the case of an impulsive acceleration (higher γ values) solvents abandon the suspension rapidly, which causes an abrupt increase of viscosity and a decrease of fluid flow. Under these conditions, aggregation of the nanoparticles may be hindered and, consequently, the formation of comets.

2.c Control of the optical response.

Optical microscopy images of Figure 4 also show the large difference in colour resulting from using different acceleration ramps to reach higher final rotation speeds (ω>3000 rpm). Colour remains invariable when the 1DPCs are deposited at low ω, as it can be seen by comparing the bottom images, while the colour displayed corresponding to the three samples deposited at high acceleration ramp but with different rotation speed (top images) is considerably different. In Figure 5 it is shown a set of reflectance spectra obtained using different final rotation speeds but fixed accelerations of γ=1950 rpm s^{-1}, see Figure 5(a), and γ=11050 rpm.s^{-1}, see Figure 5(b). For the sake of comparison, all spectra were taken from spots located at 2 mm from the geometrical centre of the substrate on which the 1DPC is deposited. These graphs illustrate a clear trend observed in the course of the experiments: the higher γ is, the stronger the dependence of the Bragg peak position on the final rotation speed used. At the lower acceleration rate, the Bragg peak maximum oscillates around 600 nm for all final speeds, whereas for the fastest ramps the reflectance peak shifts from 620 nm to 380 nm as final speed increases. These results serve as examples to highlight the extraordinary importance of the spin coating protocol in order to determine the structural, and thus optical, properties of the 1DPCs.

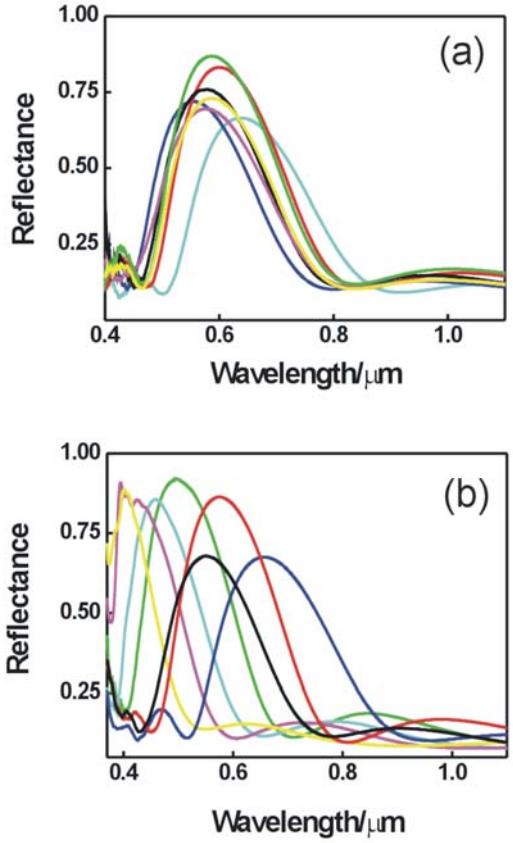

Figure 5. *Reflectance spectra obtained at acceleration ramps (a) γ=1950 rpm s^{-1} and (b) γ=11050 rpm s^{-1}. Final speeds, ω (rpm) = 2000 (blue), 2500 (red), 3000 (black), 3500 (green), 4000 (cyan), 6000 (pink), 8000 (yellow).*

2.d Analysis of the spin parameter.

To facilitate the analysis of the results attained for all the conditions employed, the reflectance peak positions obtained for the 1DPCs are plotted as a function of the ramp stage acceleration for all final rotation speeds used in Figure 6. The length of the error bars are extracted from a statistical analysis of the position of the Bragg peak in various points of each sample. Thus, these bars can be interpreted as an estimation of the uniformity of the optical response of the crystal. The set of graphs

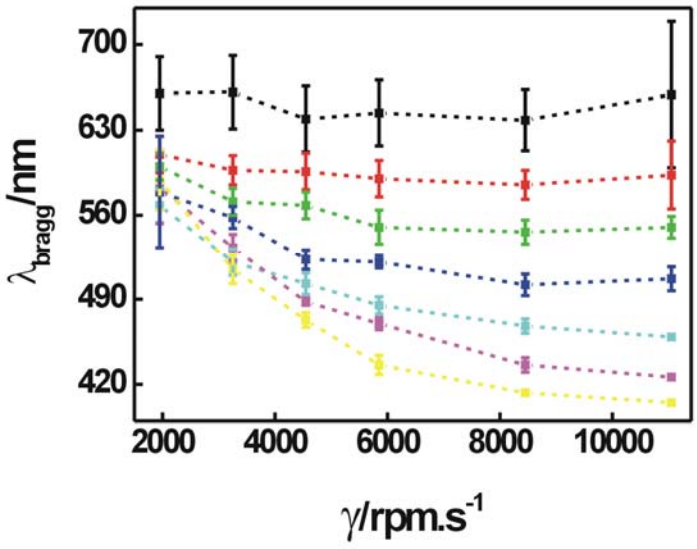

Figure 6. *Bragg peak spectral position (nm) versus ramp stage acceleration γ. The different lines correspond to different final rotation speeds ω (rpm): 2000 (black), 2500 (red), 3000 (green), 3500 (blue), 4000 (cyan), 6000 (pink), 8000 (yellow).*

plotted in Figure 6 can be used as a guide to attain 1DPCs of high structural quality whose Bragg peak precisely matches the desired wavelength range. Hence, it can be seen that worse optical quality is attained when the slowest ramps (γ=1950 rpm s^{-1} and γ=3250 rpm s^{-1}) are used, independently of the nominal final rotation speed. As the slope of the ramp increases, so too does the optical quality of the multilayer. In general, the optical quality attained is good when ω and γ take values above 2500 rpm and 4550 rpm s^{-1} respectively. Regarding the control of the optical response, the results summarized in Figure 6 clearly show that when the final rotation speed is reached fast, be it due to the large γ (γ>5850 rpm s^{-1}) or the low nominal ω (ω<3000 rpm) employed, then the position of the specular reflectance Bragg peak maximum, λ_{Bragg}, depends almost entirely on ω. Contrarily, for slower ramps, which implies that it takes a longer time to reach ω, then ω does not influence λ_{Bragg}. This can be understood in terms of the relative effect on the process of film thinning of viscous fluid flow, on one side, and, on the other hand, solvent evaporation, as explained in what follows. In a work reported by Meyerhofer,[7] it is defined that the thickness T of a film deposited by spin coating depends on ω thorough the expression $T \sim \omega^{-b}$, where

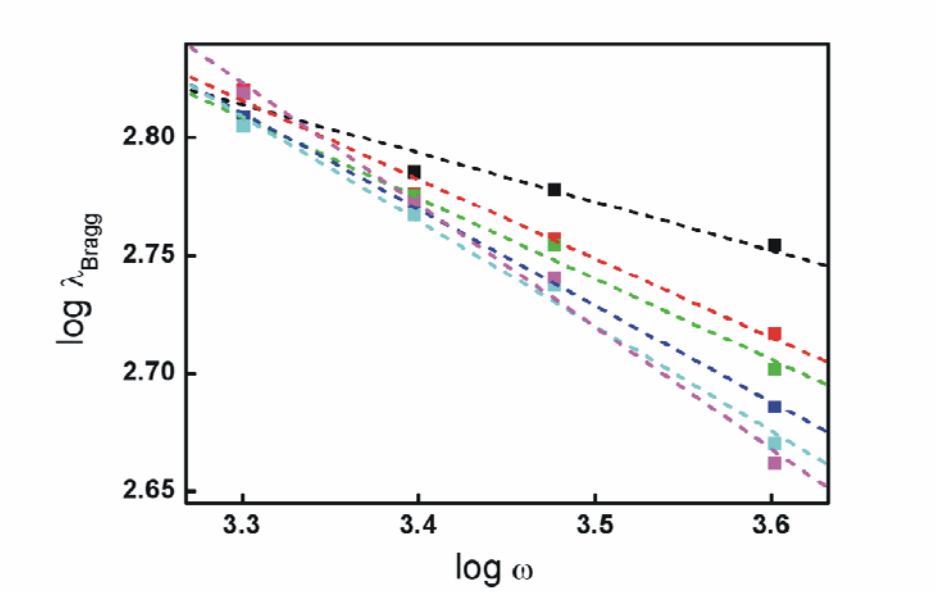

***Figure** 7. Log-Log graph representation of the Bragg peak position against final rotation speed. Best fitting obtained in ramp, γ (rpm.s^{-1}): 1950 (black), 3250 (red), 4550 (green), 5850 (blue), 8450 (cyan), 11050 (magenta).*

b is a constant known as *the spin parameter*, with a typical value of 0.5 for newtonian fluids. The solutions of nanoparticles used to construct the structures of this study are considered as newtonian fluids, which are defined as fluids whose stress versus strain rate curve is linear, being the viscosity the constant of proportionality. In his work, Meyerhofer also introduced the concept of *cross-over point*, which is the time at which the contribution of fluid flow becomes, due to the increasing viscosity of the forming film, so small that equals that of evaporation. The relation $T \sim \omega^{-0.5}$ is obtained considering that thinning is first and foremost caused by viscous fluid flow due to spinning and, to a minor extent, by solvent evaporation. Recently, Birnie et al. have theoretically demonstrated that this expression is only valid if the cross-over point is reached when the fluid is already rotating at the final nominal speed ω.[8] After their study, if most film thinning takes place during the ramp stage, i.e., the cross-over point occurs before the nominal ω is reached, then the spin parameters should be $b<0.5$. This prediction is used to provide some insight into this study of the spin coating method. In our case, in a first approximation λ_{Bragg} depends linearly on the

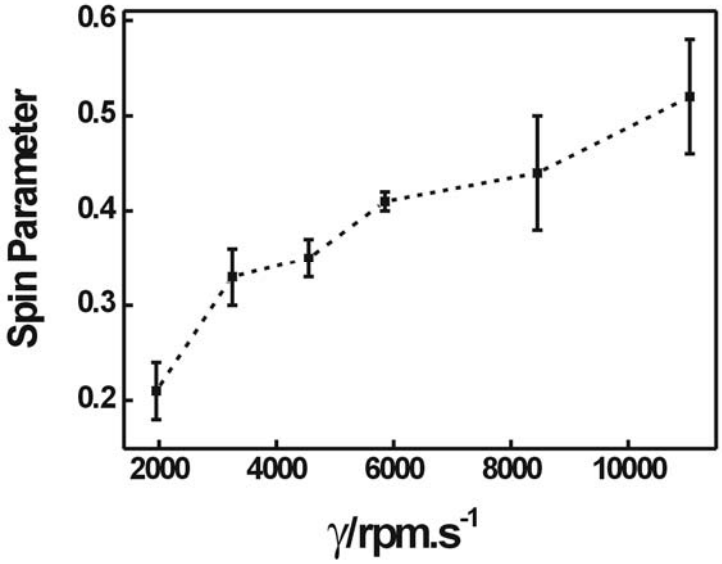

Figure 8. *Spin parameter, b, versus ramp acceleration, γ.*

average refractive index and the lattice constant of the ordered multilayer. The former is determined by the porosity and refractive index of the layers, which in turn depend on the composition, shape and packing of the nanoparticles that form them, hence being independent of ω and γ. The latter, however, is determined by the thickness of the two types of nanoparticle layers (SiO_2 and TiO_2), which should depend on ω thorough the expression $T=\omega^{-b}$. Assuming that both kinds of layers depend on ω on a similar way, then the Bragg peak maximum is expected to follow the expression $\lambda_{Bragg}\sim\omega^{-b}$. So, it can be estimated the spin parameter of these multilayers by plotting λ_{Bragg} versus ω^{-b} in a logarithmic graph for each acceleration ramp used in these experiments and extracting their slope. Curves are shown in Figure 7 only for ω<6000 rpm, since the asymptotic trend of T vs. ω towards a finite final thickness is not accounted for in Meyerhofer's model,[7] thus failing when that plateau has been reached. The linearity of such curves confirms the predicted exponential dependence of λ_{Bragg} with b, and from their slope it can be estimated the value of the spin parameter b. In Figure 8, b is plotted versus γ. Interestingly, as γ increases, the spin parameter tends to b=0.5. After Birnie's model, this curve shows that for the larger γ employed, the cross-over point is reached when the substrate is already rotating at the

final speed. In those cases, it is observed a clear correlation between λ_{Bragg} and ω. Thus, it can be established that precise control of the lattice parameter is attained by varying exclusively ω if the thinning of each layer in the 1DPC due to fluid flow caused by substrate rotation is still larger than the thinning due to solvent evaporation when the final rotation speed is reached. On the contrary, low values of *b* are attained when small γ are used. For those cases it is observed that λ_{Bragg} does not depend strongly on ω (see Figure 6). In such cases, the final thickness of each layer in the 1DPC is achieved before the substrate reaches the final rotation speed, i.e., the cross-over occurs during the ramp stage.

3. Dip coating.

3.a Nanoparticle 1DPCs built by dip coating.

The spin coating technique allows building multilayers under strict control over Bragg peak position and over the optical and structural quality, as seen in the previous section. As a consequence, most structures analyzed in this research work have been satisfactorily designed and constructed using this method. Another procedure susceptible of allowing the formation of thin nanoparticle films onto flat substrates is dip coating. Several multilayers have been prepared with this method in order to analyze their optical and structural quality. The results obtained are presented in this section.

The dip coating technique is a method employed to create uniform thin films[9,10] that can be deposited onto flat or cylindrical substrates. The dip coating procedure is completed in five steps.[11] The first is the *immersion*. The substrate is immersed in the solution or suspension of the coating material at a constant speed. Then, the *start-up,* in which, the substrate remains inside the solution for a while and then starts to be pulled up at a constant speed. The third phase is the *deposition*. A thin layer is deposited on the substrate while it is being lifted. The speed determines the thickness of the coverage (faster extraction speeds leads to thicker films). During *drainage,* excess liquid will drain from the surface. Finally, during the phase of e*vaporation,* the solvent evaporates from the liquid, forming the thin layer. For volatile solvents, such as alcohols, evaporation starts already during the deposition and drainage steps.

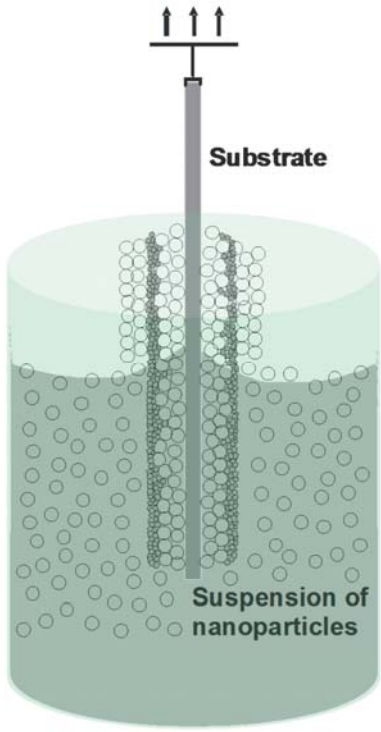

***Figure 9**. Scheme of the formation of a nanoparticle 1DPC by dip coating.*

The dip coating technique, applied to the construction of nanoparticle 1DPCs, is schematized in Figure 9 for the colloidal suspensions used in the experiments of this study. The concentrations of the precursor suspensions were 3.5 % wt. for TiO_2 nanocrystals, while concentration of SiO_2 particles were 2, 2.5, 3, 3.5, 4, 4.5 % wt. The following values for the extraction speed were used: 1.25, 1.5, 1.75 and 2 mm/s. The procedure, explained before, was repeated alternating the solutions of SiO_2 and TiO_2 nanocrystals to build the whole multilayer.

3.b Optical and structural quality.

All the samples studied in this section were composed by three unit cells, easily distinguished in the FESEM image of Figure 10. In the image, all the features of nanoparticle 1DPCs observed in the structures constructed following the spin coating procedure are clearly shown. The SiO_2 spheres are perfectly distinguished of the smaller TiO_2 nanocrystals with irregular shape. The two types of boundaries typical of these Bragg stacks can be observed. The border is much smoother when the SiO_2 nanoparticles are deposited onto the TiO_2 layer. This is because the pores of the latter are small comparing to the size of the SiO_2 spheres, which prevents them to penetrate the TiO_2 layer.

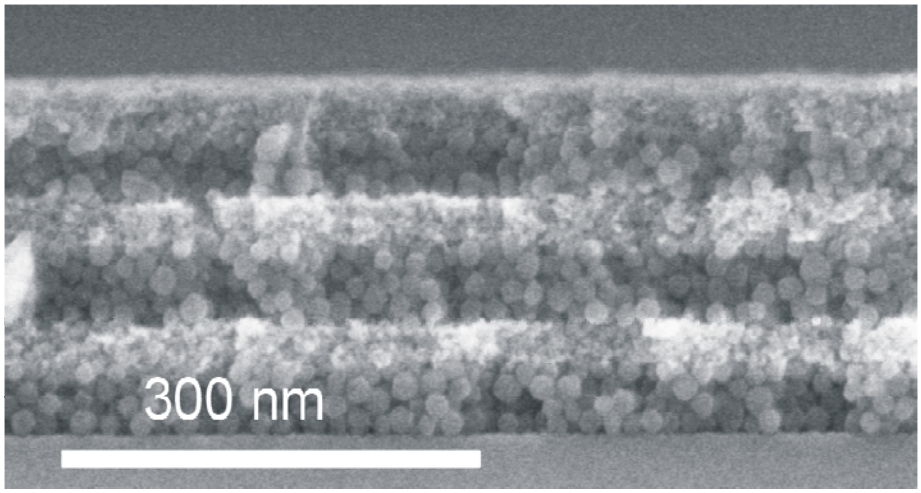

***Figure 10**. FESEM image of a three unit cell nanoparticle one dimensional photonic crystal. The SiO_2 nanospheres are clearly distinguished of the smaller TiO_2 nanocrystals*

The dip coating technique allows to build 1DPCs with areas up to 10 cm^2 using a glass substrate immersed in 60 ml of suspension. The most important factor that limits the total surface obtained is the border effect. Defective borders in the lower and upper sides of the glass are systematically observed and they become larger as the number of deposited layers and concentration of silica suspensions increase. Under these experimental conditions and for the materials here considered, the border effect becomes relevant using silica concentrations of more than 4 % wt.

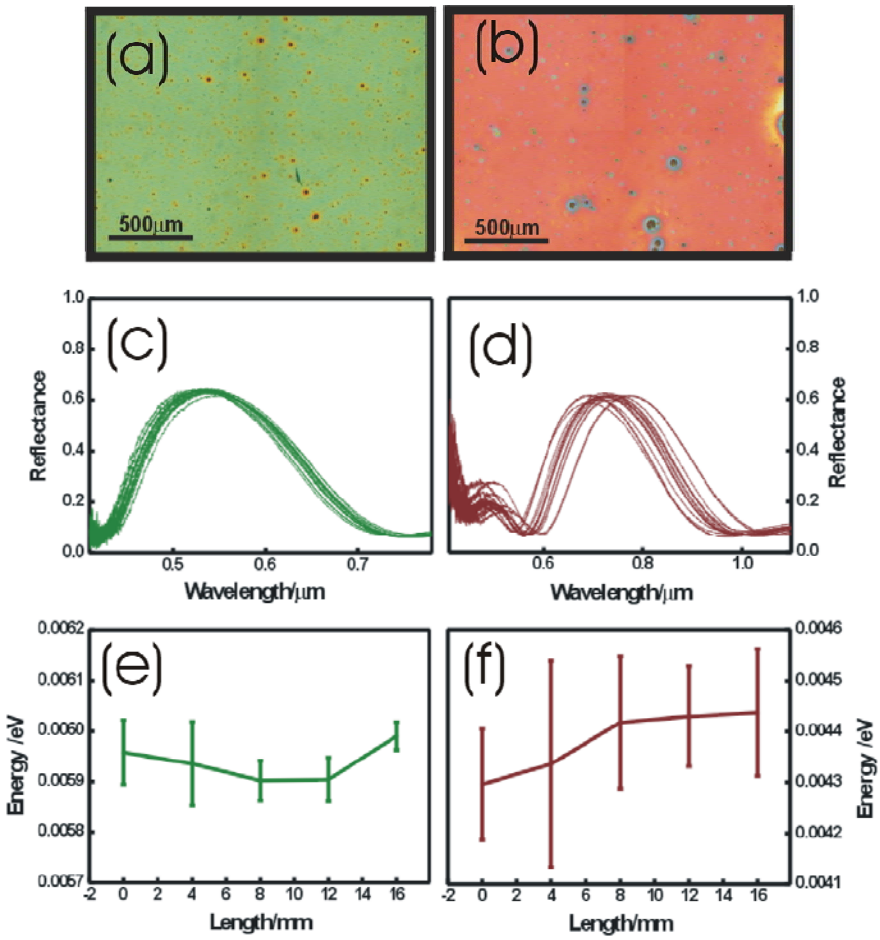

Figure 11. *Optical microscopy images 11(a) and 11(b) show surfaces of two multilayers that differ only in the concentration of silica, which are 3.5% wt. and 4.5% wt. respectively. Their corresponding sets of reflectance spectra, 11(c) and 11(d), were obtained from 15 different measurements of the reflectance in 15 different point of each sample. For those samples, in figures 11(e) and 11(f) the position of the maximum of reflectance spectra (units of energy) versus the point, in mm, where these measurements were taken, are plotted. Error bars are the standard deviation of the average value of five measurements taken in a perpendicular line to the direction of growth and separated by 4 mm.*

The number and size of defects influence the structural and optical quality of 1DPCs. One of the main types of defects typical of these kinds of constructions, made of nanoparticles, are the large particle aggregates that are present in precursor suspensions. The pictures displayed in Figures 11(a) and 11(b) correspond to two multilayers built using silica suspensions with concentrations of 3.5 and 4.5 % wt.

respectively, keeping fixed the rest of experimental parameters. The homogeneous coloured background is a proof of the good uniformity that layers present. This uniformity is only broken by particle aggregates. Most defects are very small and their effect in the uniformity of layers is almost not appreciable. However, larger defects can be easily differentiated. These are minor in number, but their big size influences the uniformity of layers and can lead to dispersion in the measurement of the position of the Bragg peak, deteriorating the optical quality of the materials. By studying carefully both pictures, it can be appreciated that aggregates are slightly bigger when the concentration of the silica suspension is higher and, consequently, the dispersion observed in the Bragg peak position is also going to be higher. To check this, 15 reflectance spectra from 1 mm^2 area spots placed at the nodes of a virtual rectangle net and separated from each other by 4 mm were collected. In every case the total area studied was 3 cm^2. These spectra are plotted in Figures 11(c) and 11(d). The multilayers were made from suspensions of silica with concentrations of 3.5 and 4.5% wt respectively. The spectral position of the Bragg peak practically does not change in the multilayer with smaller defects, while certain dispersion was measured for some spots in the sample in which the size of aggregates is higher. But, even this dispersion is low since the total area analyzed is very large. The multilayer obtained is endowed with high uniformity. The homogeneity depends on the size of defects and therefore the concentration of silica in the precursor suspension. This dependence is confirmed after carefully studying the Figures 11(c) and 11(d). In Figures 11(e) and 11(f), five Bragg peak position values are plotted, in units of energy for the sake of clarity, since the observed change is then independent of the spectral range in which it takes place, versus the position at which the measurement was taken, separated by 4 mm along the direction of growth. Each data is in turn the average value of five measurements taken in a perpendicular line to the direction of growth and also separated by 4 mm. Error bars are the standard deviation of these values, so their lengths should be interpreted as a measurement of the deviation of each Bragg peak position from its average value and, hence, as an estimation of the uniformity of the optical response of the crystal.

3.c Control of the optical response.

If the refractive index of the layers forming the structure is kept fixed, the only way to control the optical response of 1DPCs is by changing the thickness of the layers that they are made of. This is the main strategy followed along this research work. In the previous section it was explained how to get it by

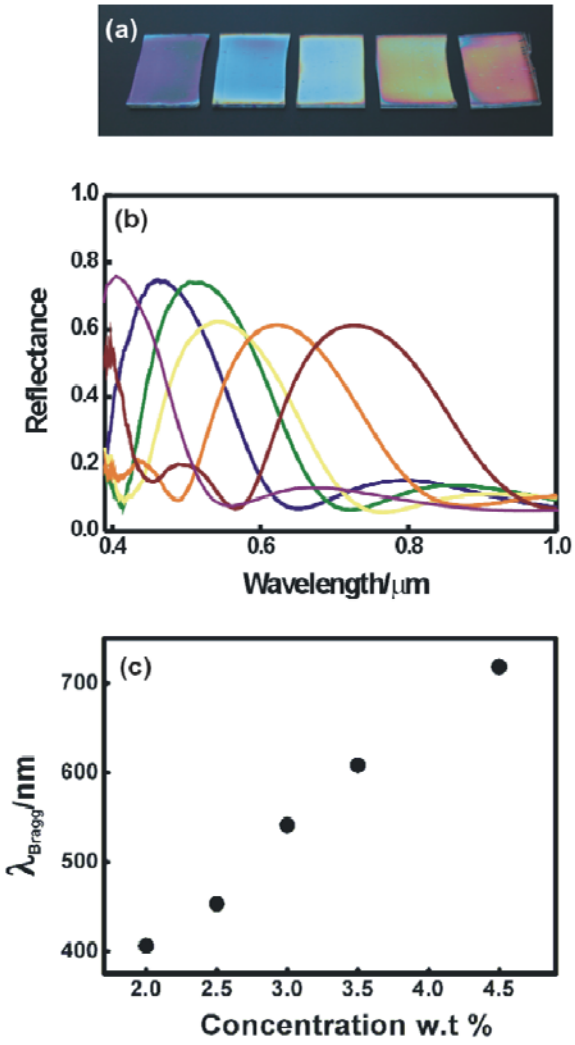

Figure 12. *Pictures of five different nanoparticle 1DPCs prepared by dip coating are shown in 12(a) The reflectance spectra corresponding to multilayers prepared using different concentrations of silica nanoparticle and keeping the rest of parameters constant are plotted in 12(b) (from left to right: 2, 2.5, 3, 4 and 4.5 % wt.). Graph of (c) shows the increment of the position of the Bragg peak with the concentration of silica suspension for a fixed withdrawal speed of 1.5 mm/s.*

controlling the spin coating parameters i.e., final rotation speed and acceleration ramp. On the other hand, the thickness of films built by using dip coating depends on several parameters as the extraction speed, the concentration and the viscosity of the fluid precursors, the surface tension, the boiling point of the precursor solvent or the kind of substrate employed. In this section, a study about how to control the optical response of nanoparticle Bragg stacks constructed by dip coating is presented. Only two parameters are modified: the extraction speed and the concentration of the SiO_2 precursor suspension.

As it was explained before, a change in the thickness of the unit cell leads to a change of the position of the Bragg peak, that is, different colours are reflected by the structure. The figure 12(a) displays a photograph of five samples with an area of 3 cm^2 prepared by dip coating. The reflectance spectra of this kind of structures are shown in figure 12(b). These multilayers differ only in the concentration of the precursor suspension of SiO_2 nanocolloids in methanol, while extraction speed remains constant. From left to right, the concentrations used were 2, 2.5, 3, 4, and 4.5 % wt. By increasing this concentration, the thickness of silica layers becomes larger and the position of Bragg peak red-shifts. By using this method, multilayers with optical response over the whole range of visible spectrum were constructed, as the set of spectra of Figure 12(b) confirms. This dependence is also shown in the graph plotted in Figure 12(c). The position of Bragg peak linearly increases with the concentration of the silica solution for a fixed withdrawal speed of 1.5 mm/s.

To study the dependence of the optical response with the deposition parameters, different multilayers were constructed modifying the concentration of the SiO_2 precursor suspensions and the available withdrawal speed. Results are summarized in Figure 13, which may serve as a guide to obtain 1DPCs with high optical quality, homogeneity over a large surface, and with reflectance spectra that can be placed at the desired spectral position. It shows the position of the Bragg peak measured for 20 samples versus the extraction speed employed to raise the substrate. Each line corresponds to multilayers built from silica suspensions with the same values of concentration: 4.5 (black), 4 (red), 3.5 (green), 2.5 (blue) and 2 % wt. (violet). The chosen values for the withdrawal speed were 1.25, 1.5, 1.75 and 2 mm/s. Regarding the control of the Bragg peak position, it can be extracted from the analysis of these curves that by changing only the concentration of precursor silica suspension is possible to obtain nanoparticle based 1DPCs with their Bragg peak located at any position of the visible spectrum keeping fixed the withdrawal speed. As it happened in Figure 11, each point represented in Figure 13 is, actually, the average of 25 values of the reflectance maximum taken from 25 spots located at the nodes of a virtual square net placed on the surface of each sample and separated each

other by 4 mm. As well as before, error bars are obtained from the standard deviation and should be again interpreted as a measure of the homogeneity of layers. It can be seen that the error bars are shorter if multilayers are built from precursor silica suspension with lower concentration. It should be noted that the violet line is drawn without error bars. This is because the system used to measure reflectance spectra, consisting in a microscope attached to a spectrophotometer, introduces noise in measurements of spectra under 400 nm and it is not possible to distinguish accurately positions of Bragg peaks in different points of the sample. However, due to the small size of defects of this set of multilayers made from the lowest concentration silica suspension, it can be predicted that the length of bars must be very short. Clearly, it can be concluded that the position of the Bragg peak is not dependent on the withdrawal speeds in the available range.

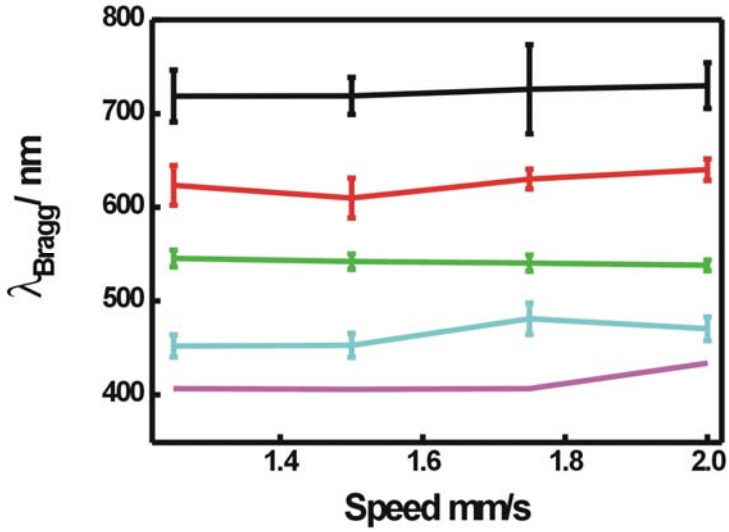

***Figure 13**. Bragg peak spectral position versus extraction speed. The different lines correspond to different concentrations of SiO_2 suspensions: 4.5 (black), 4 red), 3.5 (green), 2.5 (blue) and 2 wt % (violet). Error bars are the standard deviation of the average value of 25 measurements taken in different points of each sample.*

By using dip coating, high quality nanoparticle 1DPCs can be constructed. Nevertheless, the spin coating methodology allows controlling the optical response of the structures with a much higher precision. This is the reason why the latter has been chosen to build the samples studied to obtain most of the results presented in this

thesis. By application of this procedure, the properties and the functions of nanoparticle 1DPCs described in next chapter, as well as the samples analyzed of Chapters V and VI, have been developed. Only the multilayers studied in Chapter IV (in which the position of the Bragg peak is not a critical factor) were fabricated following the dip coated process.

4. Conclusions.

In this chapter, two different methodologies, spin and dip coating, used to construct all the samples studied in this work, have been explained. For each technique, the conditions to construct nanoparticle 1DPCs of controlled optical response have been found.

For the case of spin coating it has been determined that only for high values of acceleration ramp the thickness of the layers can be controlled and, therefore, the optical response of the structures, by modifying the final rotation speed. The number of comets is significantly lower and leads to better optical and structural quality.

Based on an analysis of the spin parameter, the structural variations observed have been related to the relative importance of fluid flow and solvent evaporation on the thinning of each layer in the stack for the different deposition conditions employed.

Bragg mirrors with very uniform layers have also been obtained by using the dip coating as nanoparticle film deposition method. Two magnitudes have been studied: the extraction speed and the concentration of the SiO_2 suspensions. It has been concluded that, within the extraction speed ranges available, the position of the Bragg peak is controlled only by the concentration of the precursors.

5. References.

[1] S. Colodrero, M. Ocaña, H. Miguez. "Nanoparticle base done dimensional photonic crystals". *Langmuir, 24*, **2008**, 4430.

[2] M. Calvo, O. Sánchez-Sobrado, S. Colodrero, H. Míguez. "Control over the Structural and Optical Features of Nanoparticle based One-Dimensional Photonic Crystals" *Langmuir, 25*, **2008**, 2443.

[3] D.E. Haas, D.P. Birnie III, M.J. Zecchino, J.T. Figueroa, "The effect of radial position and spin speed on striation spacing in spin on glass coatings". *J. Mater. Sci. Lett. 20*, **2001**, 1763.

[4] K.E. Strawhecker, S.K. Kumar, J.F. Douglas, A. Karim. "The critical role of solvent evaporation on the roughness of spin-cast polymer films" *Macromolecules, 34*, **2001**, 4669.

[5] L.E. Scriven, C.V. Sternling. "Marangoni effects". *Nature, 187*, **1960**, 186.

[6] T.J. Rehg, B.G. Higgins. "Spin Coating of colloidal suspensions" *Aiche Journal,. 38*, **1992**, 489.

[7] D. Meyerhofer. "Characteristics of resist films produced by spinning". *J. Appl. Phys. 49*, **1978**, 3993.

[8] D.P. Birnie, S.K. Hau, D.S. Kamber, D.M. Kaz. "Effect of ramping-up rate on film thickness for spin-on processing". *J.Mater. Sci.-Mater. Electronics. 16*, **2005**, 715.

[9] C.F. Brinker, C.G. Frye, A.J. Hurd. "Fundamentals of Sol-Gel dip coating". *Thin Solid Films*. **1991**, *201*, 97.

[10] Y.F. Lu, R. Ganguli, C.A. Drewien. " Continuous formation of supported cubic and hexagonal mesoporous film by sol-gel dip coating" *Nature, 389*, **1997**, 364.

[11] M.N. Rahaman. "Ceramic Processing". *CRC Press*. **2007**, 242.

Chapter III

Control and optimization of the optical properties of nanoparticle one dimensional photonic crystals

1. Introduction.

In this chapter the optical properties of nanoparticle based one dimensional photonic crystals (1DPCs) are evaluated. These properties are controlled from the fabrication process of the structures, following the spin coating protocol studied in the previous chapter. The prospective applications of these versatile materials as passive optical elements are analyzed. Results herein presented prove that nanoparticle 1DPCs constitute an excellent platform to develop novel multifunctional optical materials to be used in numerous application fields, such as radiation shielding,[1] photovoltaics,[2] or sensing.[3]

First, a pathway to attain nanoparticle multilayers showing flat spectral response in transmittance at photonic band gap frequencies is described. As long as we know, the samples analyzed in this section are the first nanoparticle multilayers presenting flat spectral response at frequencies whose propagation is forbidden, indicative of having achieved enough number of unit cells as to develop a full one

dimensional photonic band gap. Vapour adsorption-desorption isotherms are obtained in order to test the environmental response of multilayers. Resonators with flat optical response are also achieved. These are structures in which the periodicity is broken at the centre of the stack by a thicker layer of SiO_2. As a result, a resonant mode appears whose fingerprint is a transmittance window in the photonic band gap. The fabrication of these flat optical response resonators is one of the most important results presented in this chapter, since these are the structures that will mainly be used to control the absorption and the emission of nanomaterials, as it will be shown in following chapters. Strict control over the structural parameters yields multilayers in which the opening or closing of higher order photonic band gaps can be devised. This allows tailoring to measure the optical response of the ensemble to create, for instance, films capable of blocking simultaneously near infrared (NIR) and ultraviolet (UV) ranges while leaving the visible transparency unaltered. Also, optimized preparation routes to attain flexible nanoparticle multilayers with important optical activity in a well-defined frequency range are described. These structures are achieved by infilling the porous of the stacks with two different polymers: Polycarbonate (Bis phenol A carbonate) and PDMS (poly dimethyl siloxane). All the results developed in this chapter are reported in references 4 and 5.

2. High reflectance multilayers in the UV-Vis-NIR.

2.a Flat Optical Response.

As mentioned before, no nanoparticle multilayers presenting a flat spectral reflectance or transmittance at frequencies whose propagation is forbidden had been reported up to this work. Experimentally, two main factors limit the maximum specular reflectance that can be achieved from a Bragg stack. First, mechanical stability is lost when films are too thick due to the tensile stress occurring between the substrate and the film. This determines that there are a maximum number of unit cells that can be deposited before cracks arise. Second, the presence of defects in the individual layers, which may cause undesired diffuse scattering and loss of transparency in spectral pass-band regions. The first limiting factor difficults more the realization of highly reflecting mirrors operating in the red or near infrared, since thicker unit cells are required, while the second one has a larger impact on UV or blue reflecting stacks, since they are made of thinner films hence more sensitive to imperfections. Taking these considerations into account, in the work of Colodrero et al.,[3] 1DPCs were fabricated by stacking a total of three bilayers of nanoparticles of SiO_2 and TiO_2 by spin coating. These multilayers operate as efficient photonic crystals over the whole visible range which is achieved by using a different

concentration of SiO_2 (comprised in the range 2 to 6 % wt.) in each sample while keeping the concentration of TiO_2 (5 % wt.) as well as the acceleration ramp and the final rotation speed. Their corresponding reflectance spectra are plotted in Figure 1 reaching reflectivities up to 80%.

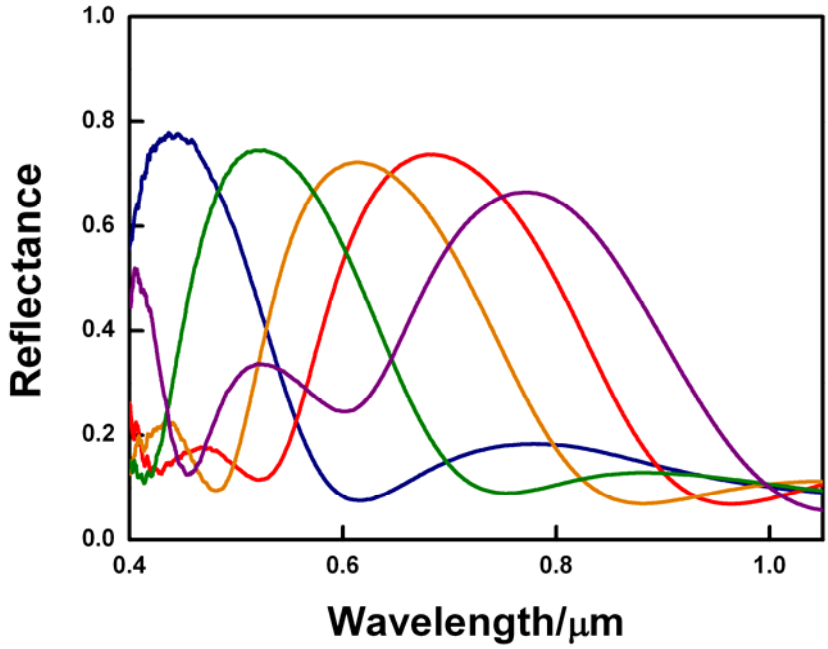

Figure 1. *Reflectance spectra of three unit cell Bragg stacks. Each line corresponds to a different concentration of the SiO_2 precursor suspension. Figure extracted from reference 5.*

In the work presented in this section, we demonstrate that the obstacles found before have been overcome and nanoparticle Bragg stacks showing close to a hundred percent reflectance at the desired spectral position within the ultraviolet, visible and near infrared (UV-Vis-NIR) region can be realized. Strict control over the presence of aggregates in the original suspensions was a key factor leading to this improvement. Both precursor suspensions were diluted in methanol with concentrations between 2 and 4 % wt. and filtered later using a syringe driven filter unit from Millipore of 450 nm and 220 nm for SiO_2 and TiO_2 nanoparticles respectively. Also, from a certain thickness of layers, which leads to locate the Bragg

peak at λ>500nm, an intermediate thermal stabilization to mechanically stabilize the ensemble and allow further deposition of layers was necessary. The synthesis of nanoparticles is detailed in the Appendix.

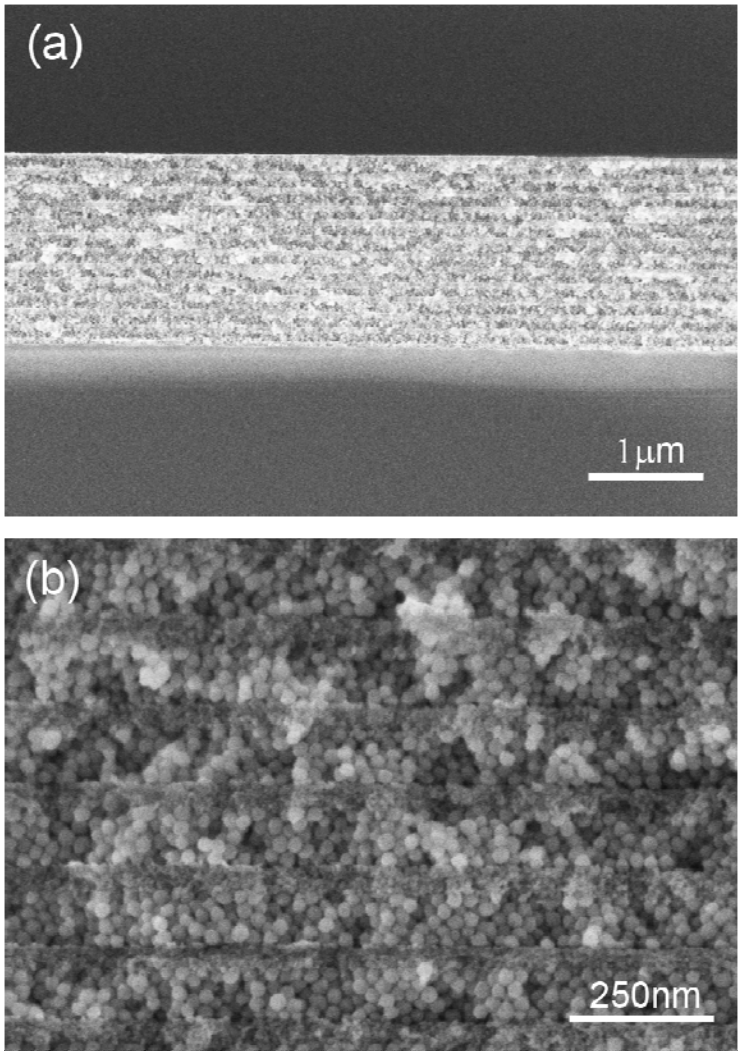

Figure 2. *(a) Low and (b) high magnification SEM images of the cross section of a twelve unit cell nanoparticle 1DPC. The two different types of nanoparticles forming the structure, SiO_2 (spherical shape) and TiO_2 (irregular shape) can be seen.*

Figures 2(a) and 2(b) display two pictures, taken at low and high magnification respectively, of the cross section of one of the multilayers prepared in this way, in which twelve unit cells have been deposited. Uniformity in the long range can be appreciated in Figure 2(a), while the different morphology of the two kinds of nanoparticles is evident in Figure 2(b). Also, in both, the lack of defects at the optical length scale can be clearly seen.

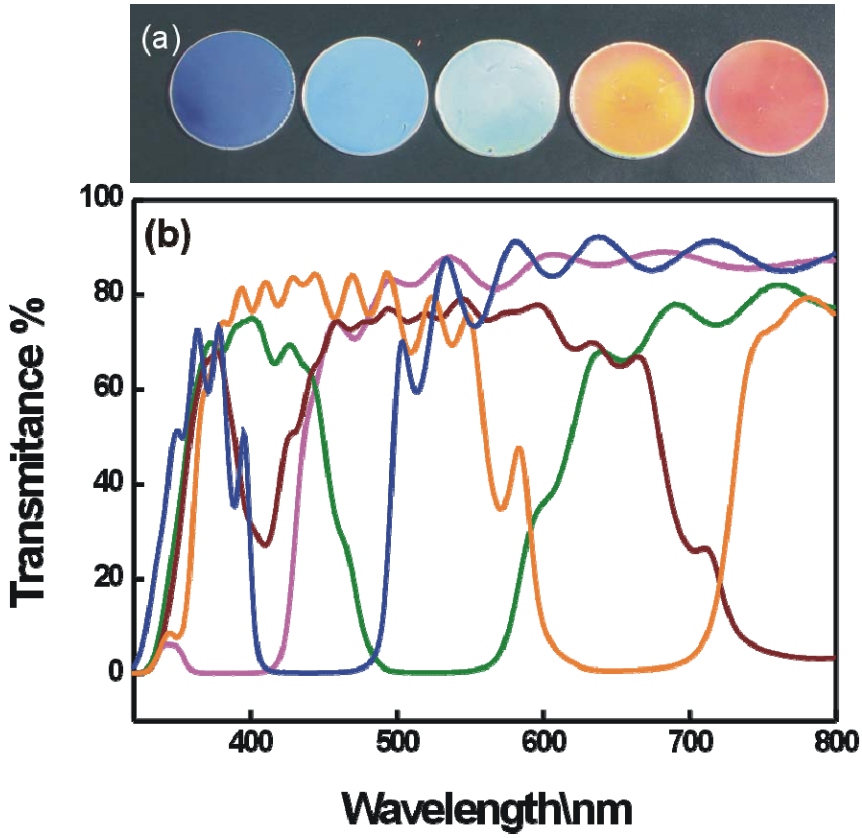

Figure 3. *(a) Pictures, taken from a digital camera, of five different multilayers of 5 cm diameter. (b) Flat transmittance spectra of this kind of structures that reflect different spectral regions in the visible range. Each picture displayed in (a) and each spectrum showed in (b) corresponding to a 1DPC deposited using a different rotation speed.*

Large areas can be covered with an acceptable degree of uniformity with the method herein proposed. In Figure 3(a) a serie of photographs taken with a digital camera of nanoparticle based Bragg stacks devised to efficiently block different spectral ranges within the UV-Vis-NIR region is shown. All of them were deposited onto circular glass wafers of 5 cm diameter. All transmitance spectra attained from nanoparticle 1DPCs, using an ultraviolet-visible scanning spectrophotometer (SHIMADZU UV-2101PC) and plotted in Figure 3(b), present similar features: a spectrally wide and deep drop of transmission at the forbidden propagation region. Since TiO_2 and SiO_2 are transparent in the visible range, specular reflectance R and ballistic transmittance T are complementary and related through the expression 1=R+T, taking into account that diffuse scattering losses are low enough. The flat optical response could be attained due to the newly acquired ability to pile up a high number of layers. The secondary lobes observed are caused by the interference of beams partially reflected and transmitted at the top and bottom surfaces. It can be seen that incoming radiation is completely blocked at the desired spectral range. A practical advantage of spin coating nanoparticles to create the multilayer is that mirrors can be prepared in a few minutes, since each layer is formed in seconds. As soon as the solvent evaporates, the structure is ready to be coated by a new layer.

2.b Optical response to environmental changes.

In principle, as multilayers get thicker, their response to environmental changes could be hindered by the non-uniform filling or closing of the pores at a certain depth, which might render part of the pore network unaccessible. In this section a study of the physico-chemical properties of porous Bragg mirrors is presented to prove that the highly reflecting multilayers herein analyzed show similar mass transport properties than those made of a much lower number of porous layers,[3] as it can be seen in Figure 4(a). This study consists in performing vapor adsorption-desorption experiments. In order to achieve this, the multilayer structure was introduced in a closed chamber in which the partial pressure of a volatile liquid is varied from P/P_0 =0 to 1 (being P_0 the saturation vapour pressure of the liquid at room temperature). The chamber possesses a flat quartz window through which the reflectance spectra at normal incidence could be measured *in situ,* using a Fourier Transform infrared spectrophotometer (Bruker IFS-66 FTIR) attached to a microscope and operating in reflection mode with a 4X objective with 0.1 of numerical aperture (light cone angle ±5.7º). The flat spectral response at photonic band gap frequencies, achieved by stacking a large number of nanoparticle films, gradually red-shifts as the partial pressure of the selected solvent, in this case isopropanol, increases in the chamber as shown in Figure 4(b) (black dots). Consequently, as the pressure is lowered, the reflectance peak blue-shifts with almost

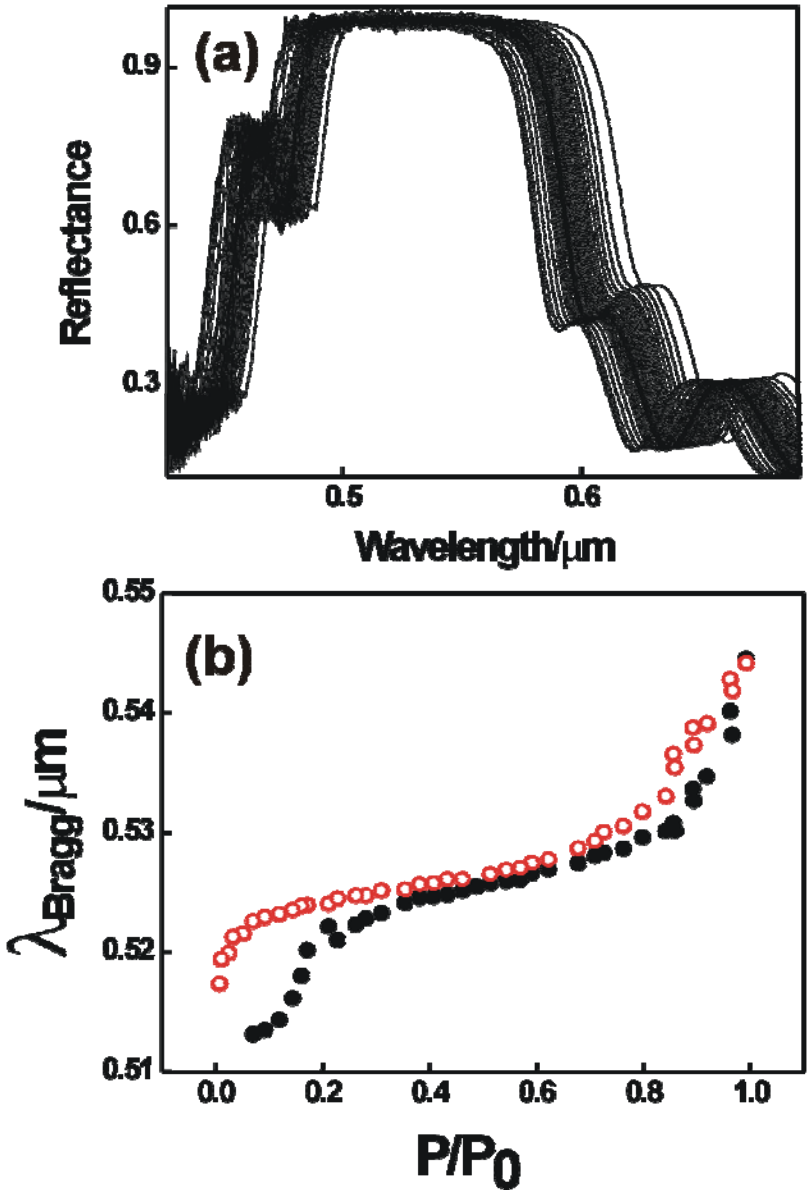

Figure 4. *(a) Series of reflectance spectra from a porous 1DPC attained at different partial pressures of isopropanol. (b) Evolution of the position of the reflectance maximum for different partial pressures of isopropanol.*

no hysteresis, as displayed in Figure 4(b) (red dots). The adsorption-desorption isotherm attained indicates the presence of mesopores of quite regular size, since the particles forming the ensemble are monodisperse.[7,8] For high values of P/P_0, the abrupt red shift observed indicates rapid condensation within these mesopores. This is a result of the increase of the average refractive index of the multilayer caused by adsorption and later condensation of isopropanol onto the pore walls.

2.c Resonant modes.

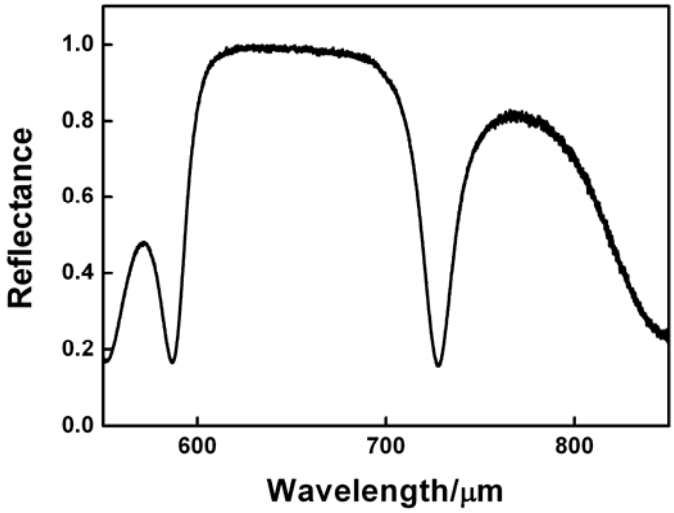

Figure 5. *Reflectance spectra corresponding to 10 unit cell multilayer containing a thicker layer of SiO_2 in the middle.*

The optical response of nanoparticle 1DPCs can be also tuned through the disruption of the periodicity of the layers forming the structure by the inclusion of an optical defect. This disruption breaks the translational symmetry of the lattice and gives rise to a resonant mode, characteristic of an optical cavity. Such mode is an allowed state in the forbidden photonic band gap, and it can be readily identified as a dip in the reflectance spectrum of the structure. The defect consists in a thicker layer of one of the two materials composing the stack, introduced in the middle of the ensemble. The flat reflectance spectrum plotted in Figure 5 corresponds to a 1DPC formed by twenty layers alterning nanoparticles of SiO_2 and TiO_2 and whose periodicity is broken by a thicker layer of SiO_2 placed at the centre of the structure. The number and the position of the dips depend on the thickness of the defect layer

and it can be controlled through the parameters of the fabrication process.[10] Thus, resonators are made to modify the optical properties of nanoparticles integrating them, as described in next chapters.

3. Engineering higher order diffraction.

By careful design of the relative thickness of the layers that form the unit cell it is possible to modify the intensity of the different diffraction orders typical of the Bragg diffraction, and even suppress completely one of them while keeping the rest almost unaltered. In order to show the versatility of nanoparticle 1DPCs in this respect, a series of samples that display a similar fundamental band gap, but in which higher orders are selectively suppressed or allowed to arise, was prepared. In a first approximation, the central wavelength of the Bragg reflection of order m is $m\lambda_B=2\cdot(n_1d_1+n_2d_2)$, where n_i and d_i denote the refractive index and thickness of layer i. Hence the only condition to keep the different peaks at the same spectral position is that the sum of the optical thickness of the individual layers forming the unit cell remains constant. Then, relative peak intensity can be tailored through the ratio between the optical thickness of the layers, $Z=n_1d_1 / n_2d_2$. Four mirrors presenting the same value for $n_1d_1+n_2d_2$ but different Z were studied. The reflectance of the different designs proposed was previously simulated using a code written in MATLAB. This program had been successfully employed several times to fit the optical response of multilayers.[3,4] In this case, the values of refractive index previously attained for the SiO_2 and TiO_2 nanoparticle layers,[5] namely $n_1=1.27$ and $n_2=1.74$, respectively, have been employed. Details of the cross sections, as seen in the SEM, of the periodic nanoparticle multilayers prepared following this design are shown in Figure 6, where the different relative thickness between the SiO_2 and TiO_2 layers can be readily appreciated. All samples used for this study present three unit cells and the parameter Z takes the values 1, 2, 3, and 4. Their corresponding normal incidence specular reflectance spectra are plotted in Figure 7 (black lines), where it can be clearly seen that, as expected, the intensity of higher order peaks strongly depends on the value of Z. Thus, for Z=1, the second order peak (m=2) is absent, while the third diffraction order peak (m=3) can be clearly observed. For Z=2, the peak labelled as m=2 is present and that corresponding to m=3 has disappeared. The third diffraction order starts rising again for Z=3, and, finally, all orders are clearly detectable when the optical thickness of the SiO_2 layer is 4 times that of the TiO_2 one. In all cases, the simulated spectra used as a guide to extract the structural parameters are included (red lines). The simulated spectra were obtained using a code written in Matlab and based on a transfer matrix formalism.[9] Agreement between theory and experiment is

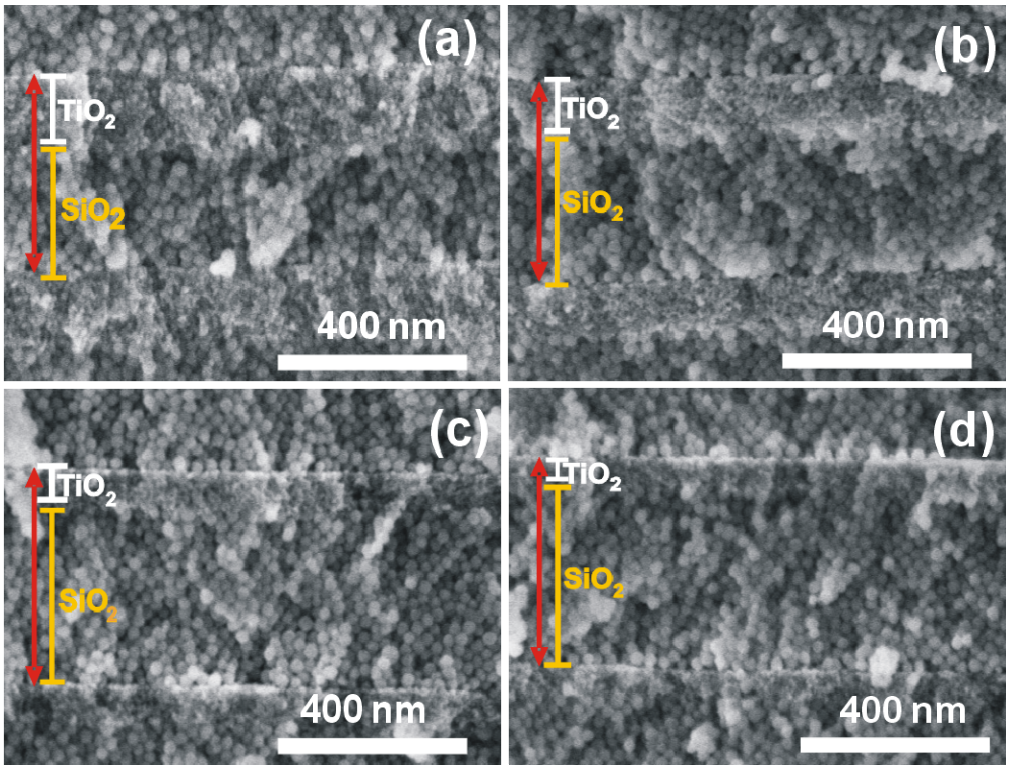

***Figure 6**. SEM images showing the unit cell of different 1DPCs whose ratios between the optical thickness of the constituent layers are (a) Z=1, (b) Z=2, (c) Z=3, (d) Z=4 (d). Layer thickness is indicated using white (TiO_2 layer) and yellow (SiO_2 layer) lines. The thickness of a complete unit cell is drawn using a red arrow.*

fairly good. The possibility to eliminate the second diffraction order opens the route to the fabrication of films transparent to the eye and that can simultaneously protect against near infrared and UV radiation. This is experimentally demonstrated in next section, where the higher order diffraction peaks are engineered to create a flexible transparent film with such properties.

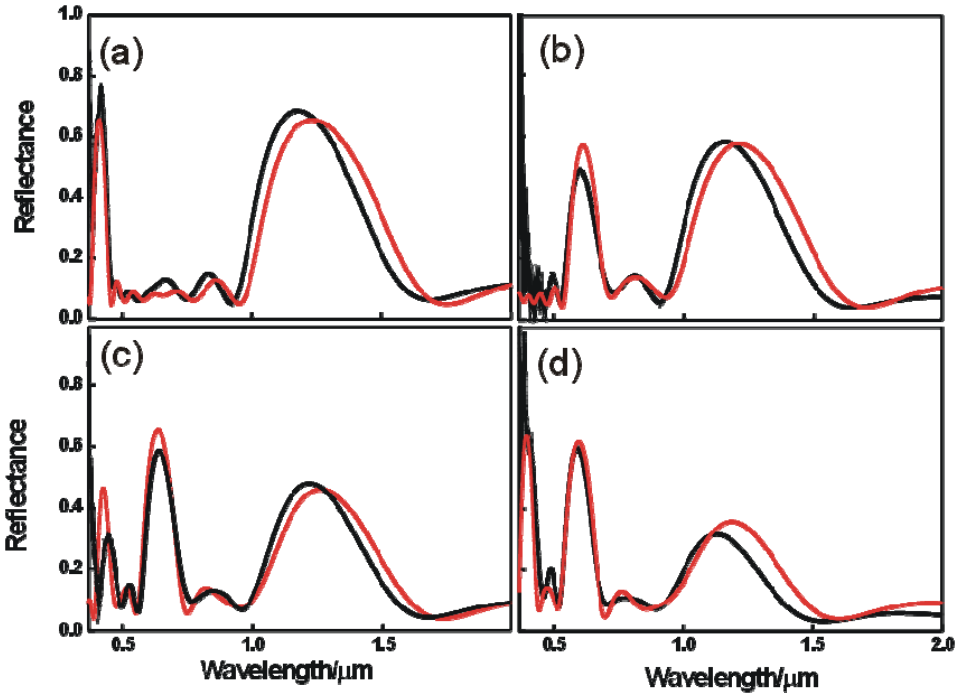

Figure 7. *Reflectance spectra corresponding to 3 unit cell multilayers built with a ratio between the optical thickness of SiO_2 and TiO_2 of (a) Z=1, (b) Z=2, (c) Z=3, and (d) Z=4. Red lines correspond to the spectra simulated and used as a guide for the design of the multilayers. Black lines are the experimental reflectance of the 1DPC actually realized.*

4. Flexible nanoparticle 1DPCs with tailored response.

Materials that combine flexibility and high reflectivity at certain wavelength ranges can be used to protect substrates of arbitrary shape from a specific radiation, or to provide them with the desired color. When this effect has a structural origin, i.e., it is due to the periodic variation of the refractive index,[8] then heating due to absorption is also prevented. In spite of their interest, there exist few examples of such materials operating in the visible and near infrared. This is due to the difficulty of devising and realizing materials possessing simultaneously a periodic modulation of the refractive index at the submicron length scale and a mechanically stable flexible structure. In recent years, some important advances in this direction have been made by using different materials chemistry approaches. Flexible lamellar structures with 1DPC properties were developed by self assembly of a mixture of copolymers and homopolymers.[9] Alternating regions of polyisoprene (refractive

index n=1.51) and polystyrene (n=1.59) gave rise to the periodic dielectric structure. Polymer layers were also used combined with inorganic materials to make flexible mirrors in the infrared region.[10,11] In another case, the porous lattice of polystyrene artificial opals is infiltrated with an elastomer (PDMS, n=1.43) to build the so called "photonic paper", a highly reflecting sheet whose color may vary selectively when put in contact with the adequate ink.[12] Based on this achievement, flexible polymer colloidal crystal lasers with light emitting planar defects have been developed.[13] Also, three dimensional self organization of polystyrene microspheres within a hydrogel matrix ($1.33<n<1.6$) has been used to attain flexible colored mirrors with glucose sensing properties.[14,15] Also, melt compression of all latex core shell particles gives rise to three dimensionally ordered arrays of the polystyrene cores in a matrix made of flexible polyethylacrylate (n=1.41).[16] In all these examples, color arises as a result of the built-up periodicity of two different organic materials whose refractive index contrast is low. This implies a limitation in the range of frequencies that can be reflected by the mirror, since the photonic stop band width in terms of frequency is directly proportional to the refractive index contrast between the two layers.[9] Besides, low contrast also implies that the intensity of the Bragg reflectance peak also is small for a reduced number of layers.

Herein, a route to attain flexible Bragg mirrors of high dielectric contrast through molding with nanoparticle 1DPCs is presented. In order to achieve this, the porous nanostructures are infiltrated with two different polymer compounds, the polycarbonate (Bis phenol A carbonate, n=1.58) and the PDMS (poly dimethyl siloxane, n=1.43), providing them with enough mechanical stability as to be lifted off and as a flexible nanoparticle 1DPCs.

4.a Infiltration with Polycarbonate.

For the purpose pursued in this section, the nanoparticle multilayers are infiltrated with a solution of polycarbonate. In order to do so, drops of such solution are deposited and uniformly spread onto the 1DPC film. Once the solution has embedded the interstices of the multilayer, the substrate is rotated using a spin coater. By doing so, the excess liquid is removed from the film surface and the solution is evenly distributed within the porous multilayer. In the final stages of the spin coating process, the organic solvent is evaporated from the interstitial sites, which are then partially filled with polycarbonate.

As-grown multilayers were infiltrated with a 5% solution of Poly(bisphenol-A-carbonate), in methlyene chloride warmed at 30ºC. Strict control over temperature within this range is crucial to ensure that the whole nanometre size void interstices of the multilayer are embedded, since at lower temperatures the increase of viscosity

prevents total infiltration, and at higher ones evaporation of the solvent is too fast as to allow proper diffusion of the precursor. Infiltration was made by depositing the Poly(bisphenol-A-carbonate) solution onto the nanoparticle packing, allowing for the structure to be embedded, and then spin coating at 6000 r.p.m. for 40 seconds. The hybrid films so obtained were heated at 60ºC during 2 hours to remove solvent traces. In order to attain self-standing membranes, the polycarbonate filled multilayer films were peeled off using mechanical traction from one vertex of the substrate. Then, these films could be transferred to different types of substrates and put into conformal contact by applying some mild pressure. This polymer forms also a layer few micron thick onto the film. The infiltrated and coated 1DPC is then mechanically stable and can be lifted off the substrate without loosing its optical properties. In Figure 8(a), a scheme of the nanoparticle multilayer (orange polygons are TiO_2 and pink spheres are SiO_2) is drawn. The structure is infiltrated with the polymer (blue material). In Figure 8(b), a high magnification scanning electron microscope image of the cross section of a 1DPC infiltrated with polycarbonate and separated from the substrate is shown. It can be clearly seen that polycarbonate accumulates in the form of thin layers at the interfaces between the SiO_2 and TiO_2 nanoparticle layers, when the SiO_2 layer was deposited on top of a TiO_2 one. This indicates that the vertical downwards convection of the precursor solution induced by the rotation of the substrate is hindered in the compact upper surface of the TiO_2 layers. Concurrent evaporation of the organic solvent leaves behind thin layers of polycarbonate deposited in the vicinity of that interface. Contrarily, the solution already embedding the TiO_2 layers can easily flow towards the SiO_2 layers, of much larger pores. The infiltrated multilayers present enough mechanical stability to be lifted off the substrates where they were deposited on.

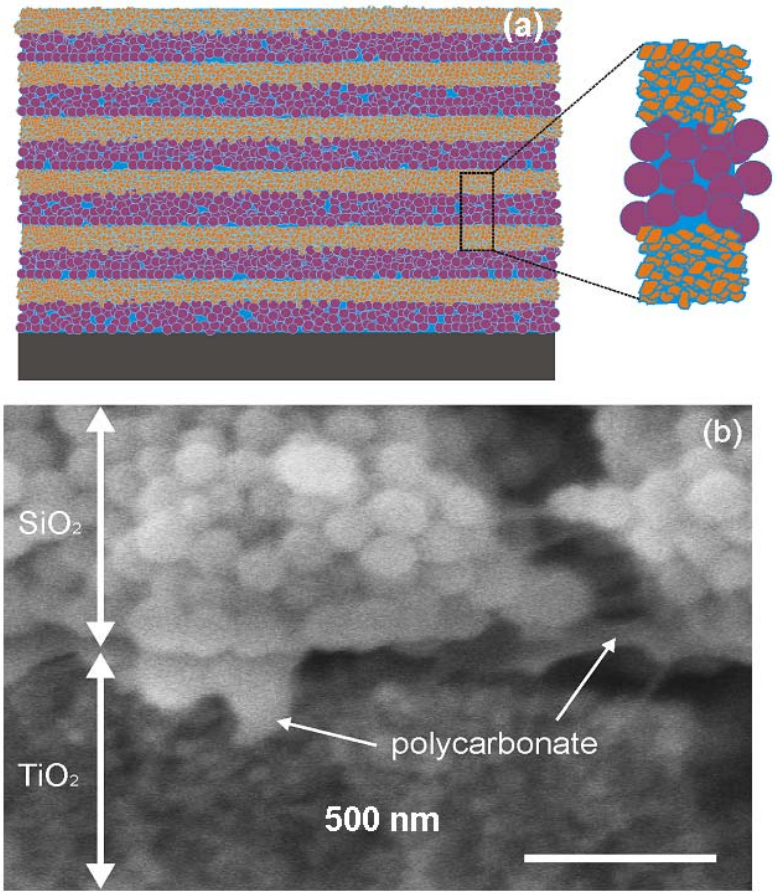

Figure 8. *(a) Scheme of the cross-section of a porous 1DPC film, formed by six alternating layers of SiO_2 nanoparticles (violet circles) and TiO_2 nanocrystals (orange polygons) deposited onto a flat substrate. The detail shows the interpenetration of the TiO_2 layer into the SiO_2 layer and their porous structure. (b)) FESEM image showing a local structural fracture in the SiO_2 layer that allows observing the polycarbonate threads connecting the nanoparticles as well as a detail of the accumulation layer between upper silica and lower titania layers.*

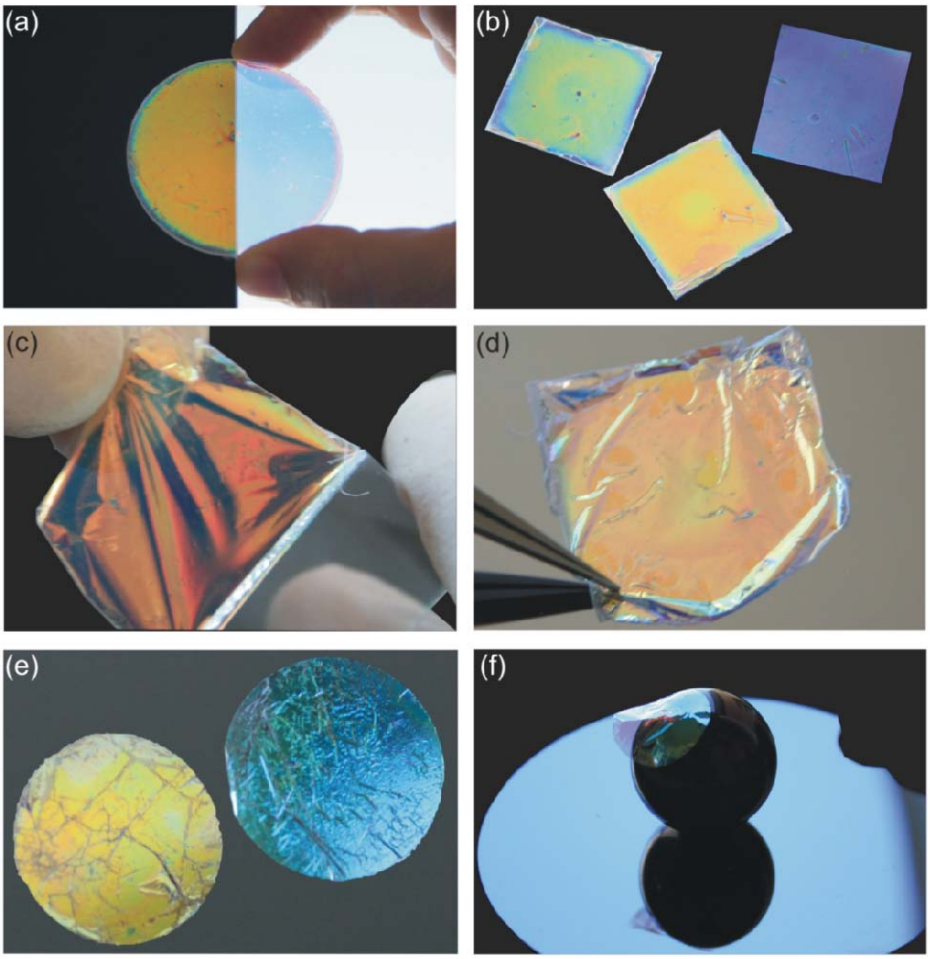

Figure 9. *Photographs of some Bragg mirrors. (a) A twelve layer nanoparticle based 1DPC deposited on a circular glass and infiltrated with polycarbonate. One half of the photonic crystal coated glass is exposed to daylight from the back and the other is placed onto a black background to observe the different transmission and reflection optical response. (b) 1DPC of different lattice parameters deposited on different square Si and glass substrates and infiltrated with polycarbonate. (c) A picture taken while peeling off a polycarbonate infiltrated 1DPC previously deposited on glass. The flexibility of the resulting film can be readily appreciated. (d) The flexible Bragg mirror shown in Figure 3(c) while being put in conformal contact with the flat surface of a Si wafer. (e) Different round cuts of flexible Bragg mirrors of different lattice parameter deposited on a Si wafer. (f) A circularly cut 1DPC film while being put in conformal contact with a black painted steel sphere.*

This process yields flexible Bragg mirrors that can be transferred to coat another surface. In Figure 9, a series of pictures corresponding to the process of lifting off and transferring of such flexible photonic crystals are shown. Figures 9(a) and 9(b) show different polycarbonate filled nanoparticle based 1DPCs of different lattice parameters deposited onto different types of substrates, namely glass (a) and silicon wafers (b). In Figure 9(c), an infiltrated nanoparticle based 1DPC is lifted off the glass substrate it was deposited on. The flexibility and highly colored reflection of the film can be readily seen in this photograph. Once separated, it can be transferred to a silicon wafer, as shown in Figure 9(d), keeping its high reflectance intact. These films can be shaped in different forms and stick to surfaces of arbitrary curvature. This is illustrated in Figures 9(e) and 9(f), in which a couple of circular cut flexible 1DPCs films are shown, one of them in conformal contact with the surface of a steel sphere. It can be appreciated how the blue Bragg mirror adapts to the curved surface maintaining its high reflectance.

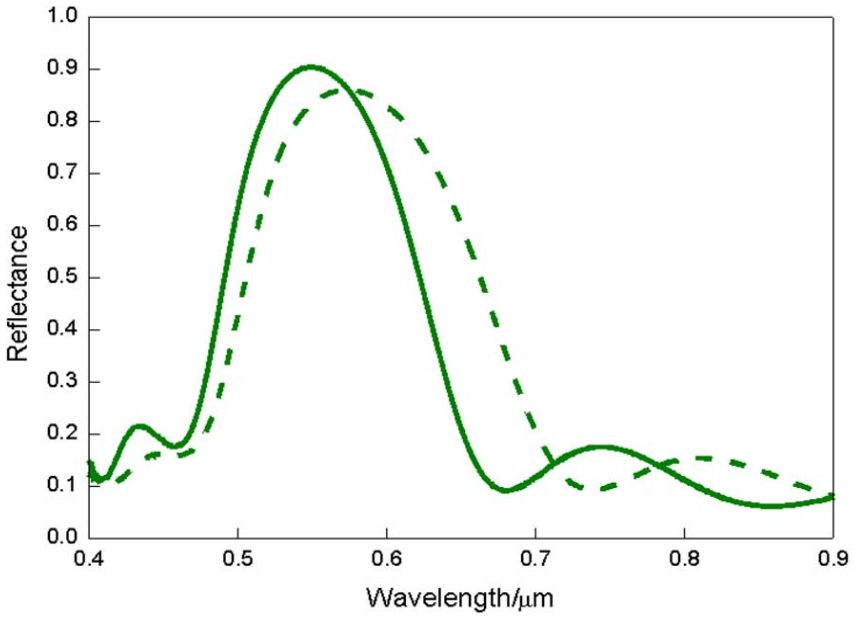

Figure 10. *Specular reflectance spectra obtained from a ten layer nanoparticle based 1DPC before (solid line) and after (dashed line) infiltration with polycarbonate.*

The high dielectric contrast existing between the SiO_2 and TiO_2 layers within the photonic crystal template is preserved after infiltration of the void volume with polycarbonate. Thus, the resulting flexible film presents wide Bragg reflectance peaks ($\Delta\lambda/\lambda\approx40\%$) of high intensity ($I_{max}\approx70\%$). In Figure 10, the specular reflectance spectra of a nanoparticle based 1DPC film before and after being infiltrated with polycarbonate is plotted. An intense (90% reflectance for stacks made of 12 alternate layers) and wide Bragg reflection peak is observed for the original template, which is a direct consequence of the large refractive index contrast between the SiO_2 and TiO_2 nanoparticle layers. After infiltration, the Bragg peak intensity slightly decreases (80% reflectance) and its position shifts towards longer wavelengths, which indicates that the void interstices of the template are being filled with polycarbonate and also that it causes the refractive index contrast to diminish a little.

4.b Infiltration with PDMS.

Nanoparticle 1DPCs with the optical properties developed in sections 2 and 3 of this chapter can be also turned into flexible Bragg stacks by infiltration of another polymer, PDMS. This is achieved by infiltrating the polymer and then cooling down the hybrid structure below the glass transition temperature T_g=120K. This is represented as route (i) in the scheme shown in Figure 11. Also, if the polymer overlayer is peeled off at room temperature, it is possible to fill up the multilayer right to the top layer of nanoparticles, leaving part of their surface exposed to air. The steps to make this type of structure are summarized in route (ii) in Figure 11. Such multilayer is not porous any longer, thus becoming stable versus environmental changes.

These films were made by infiltrating the multilayer with an elastomer (Sylgard 184®, Dow Corning). A curing mix (an oligomer and curing agent) was deposited onto the multilayers by spin coating (40 seconds, 700 rpm). After that, samples were cured at 120ºC in a stove during 30 minutes. Next, straight incisions are made in the PDMS layer with a blade, and the infiltrated multilayer supported onto the glass was immersed in liquid nitrogen (77K). Then the samples reach room temperature and at the same time, the films are lifted mechanically from the substrate.

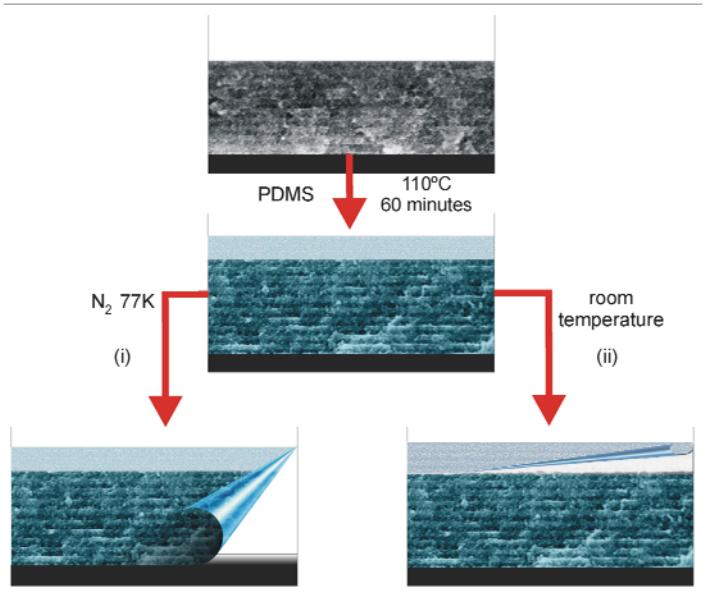

Figure 11. *Scheme of the polymer infiltration process and the subsequent possible thermal post-treatments to obtain either (i) a self-standing 1DPC or (ii) a self-cleaning 1DPC.*

In Figure 12, pictures of two flexible 1DPCs are shown. The multilayer displayed in 12(a) has been tailored to provide total blocking of visible radiation in the desired spectral range. The film of 12(b) presents almost total transparency in the visible while protecting against near infrared and ultraviolet radiation. The latter effect was devised by tuning the relative thickness of the SiO_2 and TiO_2 layers, as described in the section 3 of this chapter, to totally suppress the second diffraction order. The corresponding transmittance spectra (red lines) are also plotted in figures 12(c) and 12(d) along with the spectra of the multilayers prior to infiltration (black lines).

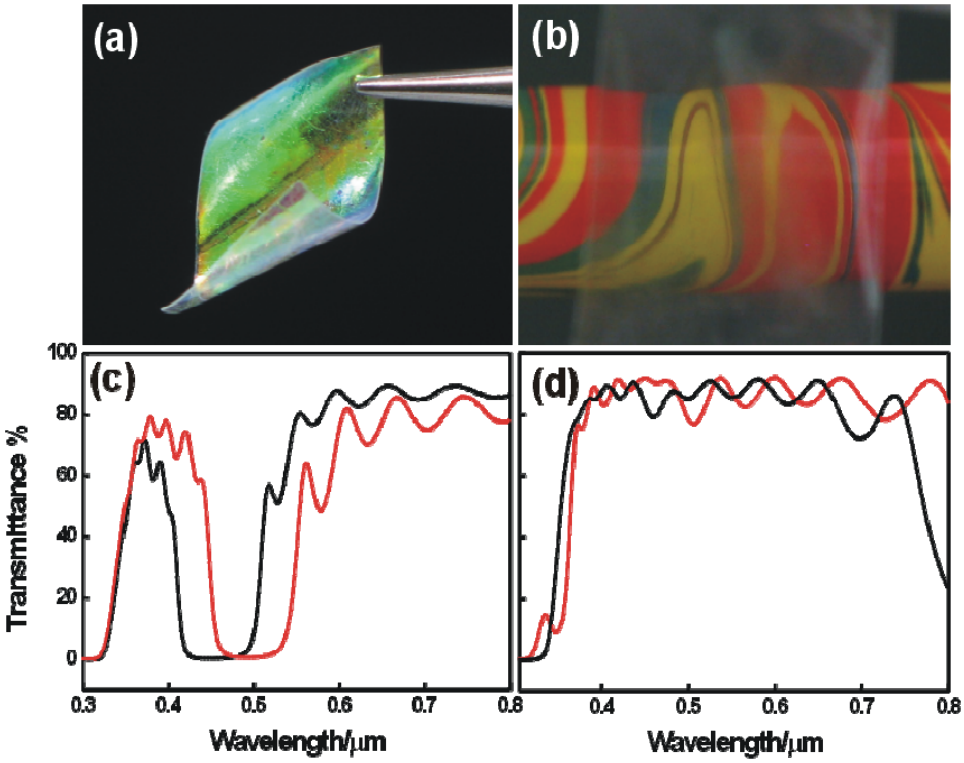

***Figure 12**. Pictures of two flexible 1DPCs, with flat optical response in the visible range (a) and with no reflection maximum in the visible region (b). 8(c) and 8(d): Transmittance spectra of samples shown in Figures 8(a) and 8(b). (Red lines). Spectra in black belong to the non-infiltrated samples used as matrices for the polymer.*

As another example of the ability of these structures to host a wide variety of materials, GaAs has been infilled in porous stacks. This is a semiconductor highly valued in electronics and optically characterized by its high refractive index. The structure obtained from this infiltration has been considered very innovative, due its excellent optical properties and its semiconductor nature. In the next chapter a study of the infiltration of this material in nanoparticle 1DPCs is presented.

5. Conclusions.

In this chapter we have demonstrated that it is possible to achieve multifunctional Bragg mirrors made of nanoparticles with spatially uniform response and spectrally flat reflectance/transmittance.

Adsorption-desorption isoterms have been performed to show that the optical response of nanoporous 1DPCs is affected by environmental changes.

The opening or closing of higher order photonic band gaps can be devised and have been demonstrated.

Flexible films capable of blocking selective spectral ranges over the whole UV-Vis-NIR have been constructed by infiltration with two different polymers: Polycarbonate and PDMS.

6. References.

[1] T. Druffel, N.Mandazy, M. Sunkara, E. Grulke, "Polymer nanocomposite thin film mirror for the infrared region"*Small, 4*, **2008**, 459.

[2] S. Colodrero. A. Mihi. L. Haggman, M. Ocaña, G. Booscholoo, A. Hagfeldt, H. Míguez, "Porous One-Dimensional Photonic Crystals Improve the Power-Conversion Efficiency of Dye-Sensitized Solar Cells",*Advanced Materials, 21*, **2009**, 764.

[3] S.Colodrero, M.Ocaña, A.R.González-Elipe, H.Míguez."Response of nanoparticle one dimensional photonic crystals to ambient vapour pressure" *Langmuir, 24*, **2008**, 9135.

[4] O.Sánchez-Sobrado, M.Calvo, H. Míguez. "Versatility and multifunctionatility of high reflecting Bragg mirrors based on nanoparticlemultilayers", *J.Mater.Chem, 38*, **2010**, 8240.240.

[5] M. Calvo, O. Sánchez-Sobrado, G. Lozano, H. Míguez. "Molding with nanoparticle based One Dimensional Photonic Crystals: A Route to Flexible and Transferable Bragg Mirrors of High Dielectric Contrast." *J. Mater. Chem,19*, **2009**, 3144.

[6] S.Colodrero, M.Ocaña, H.Míguez. "Nanoparticle based one dimensional photonic crystals" *Langmuir.24*, **2008**, 4430.

[7] S. Brunauer, L.S.Deming, W.S. Deming and E. Teller "On a theory of the Van de Waals adsorption of gases", *J. Am. Chem. Soc., 62*,**1940**, 1723.

[8] S.J. Gregg and K. S. W. Sing, "Adsorption, Surface Area and Porosity",Academic Press, London, ISBN 0-12-300956-1, **1982**.

[9] A. Yariv, P. Yeh, "Optical Waves in Crystals", **2003** John Wiley and Sons Inc., ISBN 0-471-43081-1

[10] H. A. Macleod, Thin Film Optical Filters, 3rd Edition, Published by Institute of Physics Publishing, London, **2001**.

[11] A. Urbas, R. Sharp, Y. Fink, E.L. Thomas, M. Xenidou, L.J. Fetters." Tunable block copolymer/homopolymer photonic crystals" *Advanced Materials.12*, **2000**, 812.

[12] T.Druffel, N. Mandzy, M. Sunkara, E. Grulke." Polymer nanocomposite thin film mirror for the infrared region" *Small. 4*, **2008**, 459.

[13] R. G. DeCorby, N. Ponnampalam, H. T. Nguyen, T. J. Clement. " Robust and flexible free-standing all-dielectric omnidirectional reflectors" *Advanced Materials,19,***2007**, 19.

[14] H. Fudouzi, Y. Xia. "Colloidal crystals with tunable colors and their use as photonic papers" *Advanced Materials, 15*, **2003**, 892.

[15] S. Furumi, H. Fudouzi, H.T. Miyazaki, Y. Sakka. "Flexible polymer colloidal-crystal lasers with a light-emitting planar defect"*Advanced Materials, 19*, **2007**, 2067.

[16] J.H. Holtz, S.A. Asher. "Polymerized colloidal crystal hydrogel films as intelligent chemical sensing materials" *Nature, 389*, **1997**, 829.

[17] V.L. Alexeev, S. Das, D.N. Finegold, S.A. Asher. "Photonic crystal glucose-sensing material for noninvasive monitoring of glucose in tear fluid" *Clinical Chemistry, 50*, **2004**, 2353.

[18] T. Ruhl. P. Spahn, G.P. Hellmann. "Artificial opals prepared by melt compression" *Polymer, 44*, **2003**, 7625.

Chapter IV

Infiltration of high refractive index materials in nanoparticle one dimensional photonic crystals

1. Introduction.

Infiltration of high dielectric constant materials into porous photonic crystals has become a standard way of enhancing the optical performance of these optical lattices.[1] In the vast majority of cases, periodic three-dimensional structures have been employed as matrices to host all type of materials of high refractive index, such as TiO_2,[2,3] Si,[4,5] Ge,[6] InP,[7] GaAs,[8] or InSb.[9] The driving force of this research has been the possibility to attain highly symmetric crystals with a strong modulation of the refractive index, since that would lead to the opening of a full photonic band gap, i.e., spectral ranges for which propagation is forbidden irrespective of the crystalline direction.[10,11] In practical terms, the consequent increase of the dielectric contrast implies larger widths and intensities of the reflectance (transmittance) maxima (minima) associated to photonic stop bands.

The recent advent of high optical quality porous one dimensional photonic crystals[12-15] has boosted their use as matrices for different types of materials and compounds that endow the stack with novel functionalities or enhanced optical properties. Environmentally responsive colored mirrors,[16,17] photoconducting[18] or

lasing Bragg stacks,[19] or electrolyte filled back mirrors to boost the efficiency of dye solar cells,[20] have been developed. In the previous chapter, the porous multilayers were infiltrated with polymers to attain flexible and adhesive frequency selective filters.[21] As far as we know, no high refractive index material had been infiltrated in such lattices to enhance and/or tune their optical response until the work herein presented. All the results explained in this chapter have been reported in reference 22.

Here, a viable synthetic route designed to infiltrate a high refractive index semiconductor, gallium arsenide (GaAs), is developed. GaAs has some electronic properties which are superior to those of another important semiconductor: silicon. It presents higher electron mobility, allowing transistors made from it to function at frequencies in excess of 250 GHz. Unlike silicon junctions, GaAs devices are relatively insensitive to heat due to their higher band gap. Also, GaAs devices tend to have less noise than silicon devices especially at high frequencies which is a result of higher carrier mobility. These properties recommend GaAs circuitry in mobile phones, satellite communications, and higher frequency radar systems or solar cells.[23] Also, in the context of this research work, the most important advantage that GaAs presents respect to Si is its direct band gap, which means that it emits light very efficiently whereas silicon has an indirect band gap and so is very poor at emitting light. However, as it will be discussed later, no luminescence has been measured for the samples analyzed in this chapter.

2. The metalorganic chemical vapor deposition.

Metalorganic chemical vapor deposition (MOCVD) is a chemical vapor deposition method of epitaxial growth of materials, specially compound semiconductors, from the surface reaction of organic or metalorganic compounds and metal hydrides containing the required chemical elements.

Epitaxy refers to the method of depositing a monocrystalline film on a monocrystalline substrate. The deposited film is denoted as epitaxial film or epitaxial layer and may be grown from gaseous or liquid precursors. Because the substrate acts as a seed crystal, the deposited film must take on a lattice structure and orientation identical to those of the substrate. This method has been widely used in nanotechnology and in semiconductor fabrication. Indeed, is the only affordable method of high quality crystal growth for many semiconductor materials, including technologically important materials as silicon, germanium, gallium nitride, gallium arsenide, indium phosphide and graphene. It is used in silicon-based manufacturing

processes for Bipolar Junction Transistors (BJTs) and modern Complementary Metal Oxide Semiconductor (CMOS), but it is particularly important for compound semiconductors such as gallium arsenide. Manufacturing issues include control of the amount and uniformity of the deposition, resistivity and thickness, the cleanliness and purity of the surface and the chamber atmosphere, diffusion of dopant to the new layers, imperfections of the growth process and protecting the surfaces during the manufacture and handling.

The epitaxial growth of the GaAs crystal from the precursors is schematized in Figure 1. Gallium arsenide is usually formed in a reactor on a substrate by introducing trimethylgallium $(CH_3)_3Ga$ and gas arsine AsH_3. Formation of the epitaxial layer occurs by final pyrolysis of the constituent chemicals at the substrate surface. The growth of crystals is by chemical reaction and not physical deposition. This does not take place in vacuum, but from the gas phase at moderate pressures (up to 100 kPa). As such, this technique is preferred for the formation of devices incorporating thermodynamically metastable alloys, and it has become a major process in the manufacture of optoelectronics.

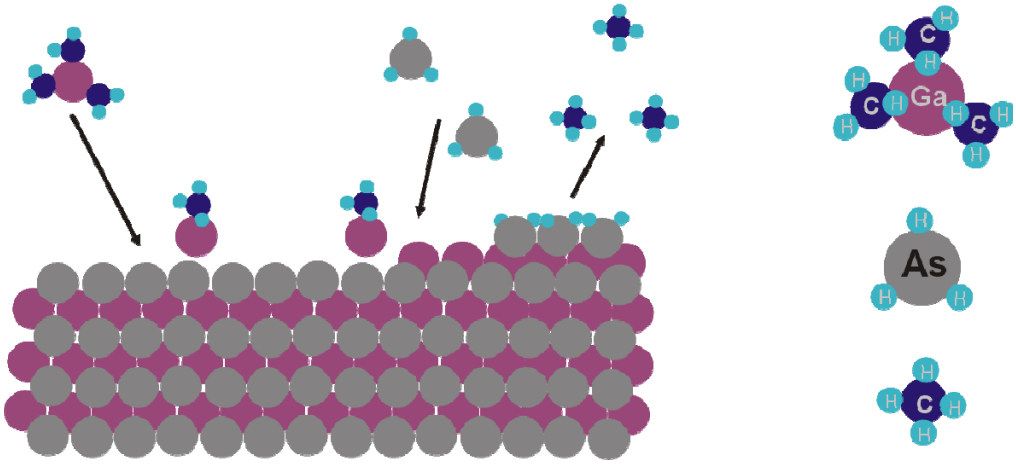

Figure 1. *Scheme of the epitaxial growth of a GaAs crystal following the MOCVD method. Formation of the epitaxial layer occurs by final pyrolysis of the constituent chemicals at the substrate surface. As a result of the reaction crystalline AsGa is formed on a substrate while methane is generated as a waste material.*

The process takes place in a horizontal reactor consisting in a chamber made of a material that does not react with the chemicals being used. It must also withstand

high temperatures. This chamber is composed by reactor walls, susceptor, gas injection units, and temperature and pressure control units. Usually, the reactor walls are made from stainless steel or quartz. To prevent overheating, cooling water must be flowing through the channels within the reactor walls. A substrate sits on a susceptor which is at a controlled temperature. The susceptor is made from a material resistant to the metalorganic compounds used as graphite.

In Figure 2, the MOCVD process to grow GaAs is described. The gas is introduced in the system via devices known as bubblers. In a bubbler, a carrier gas (usually nitrogen or hydrogen) is bubbled through the metalorganic liquid, which picks up some metalorganic vapor and transports it into the reactor. The amount of metalorganic vapor transported depends on the rate of carrier gas flow and the bubbler temperature, and is usually controlled automatically. At the end of this process, the system is purged by a current of the carrier gas and then the hydride gas is introduced into the reaction chamber. Then the system is purged again. These stages are repeated cyclically until completing the whole process and the GaAs crystal is formed. Toxic waste products, in this case methane, must be converted to liquid or solid wastes for recycling or disposal. Ideally processes will be designed to minimize the production of waste products.

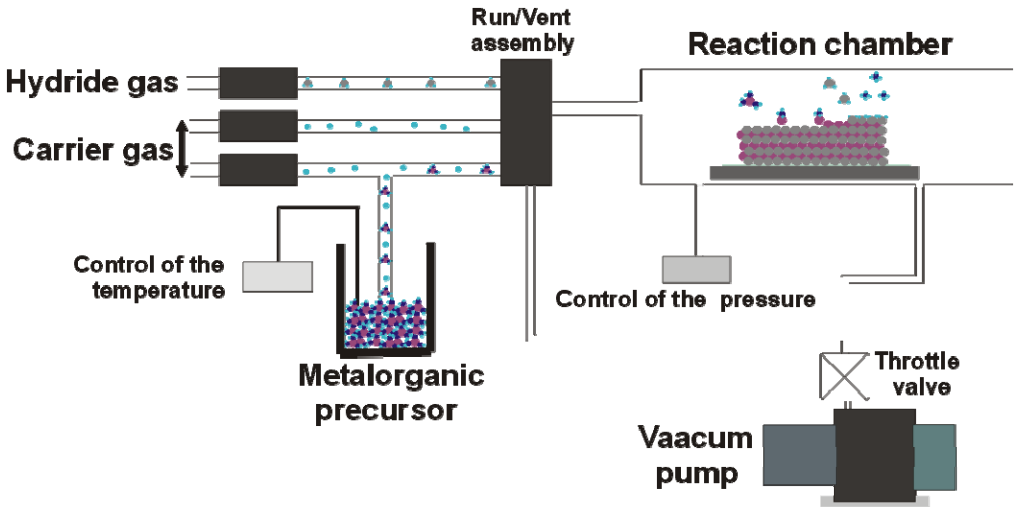

***Figure 2**. Scheme describing the set up usually used to grow GaAs by MOCVD method. The material is formed in the horizontal reaction chamber.*

The process described above corresponds to the formation of a perfect layer of GaAs crystal, whose thickness is determined by the number of cycles. To attain this perfection, several conditions are assumed. The most important is that the semiconductor is growing on a substrate that has its same lattice structure and orientation. In this case, the substrate must be made of GaAs. In this work, gallium arsenide is formed in the pores of a nanoparticle 1DPC. Therefore, this environment is not the most suitable for the growth of the semiconductor, due to the impurities contributed by the surrounding particles of SiO_2 and TiO_2. In next section, results that demonstrate that it is possible to grow crystalline GaAs in the porous net of these types of multilayers are presented.

3. Gallium arsenide infiltration of nanoporous multilayers.

3.a Structural properties.

Samples studied in this chapter were composed by six alternate layers (thus three unit cells) in total. Both suspensions, SiO_2 and TiO_2, were diluted in methanol in concentrations comprised between 2 and 4.5 wt %. The synthesis and the preparation of these nanoparticle precursor suspensions are explained in the Appendix. The samples whose results are presented in this chapter are the only multilayers prepared for this research work that were built by using dip coating following the procedure described in Chapter II. Glass substrates were alternately immersed in the precursor solutions vertically and lifted at a controlled speed, which was comprised between 1 mm/s and 1.75 mm/s, depending on the final thickness desired. Since the precision in the control of the position of the Bragg peak was not that important to perform the study, the dip coating was chosen as a good method to attain multilayers with high optical quality.

GaAs grows inside pores by atomic layer deposition in a horizontal reactor system (Thomas Swam Scientific Equipment single 2-n. wafer horizontal MOVPE reactor) maintained at 400ºC and 200 torr (~27 kPa) using trimethilgallium (TMGa) and arsine (AsH_3) as precursors. Alternating gas pulses of TMGa (3 s) and AsH_3 (8 s) at flow rates of $5.3.10^{-5}$ and $2.2.10^{-5}$ mol min^{-1}, respectively, were separated by a hydrogen purge (2 s) to prevent the reactant gases from mixing in the gas phase. This treatment constitutes one GaAs deposition cycle. Abrupt switching of precursors was achieved using a pressure-balanced-run-and-vent gas manifold. The flow rate of hydrogen through the reactor was 16 dm^3 min^{-1} throughout precursor pulsing and purging. Figures 3(a) and 3(b) show two electron scanning microscopy of both cross sections and upper surfaces of the nanoporous multilayers used as hosts. Figures 3(c)

and 3(d) display the same structures after being treated in the MOCVD chamber employing 800 cycles. The shape of the spherical SiO_2 and polyhedral TiO_2 nanoparticles forming the original matrix can no longer be distinguished after the infiltration, which indicates that the deposition of GaAs takes place onto the particles surface rather than within the interstitial space as individual crystallites. SEM pictures also reveals that the gas phase infiltration apparently causes the uniform loading of the whole width of the photonic crystal with the semiconductor, as well as preserving the long range order of the matrix, as it can be seen in Figure 3(e).

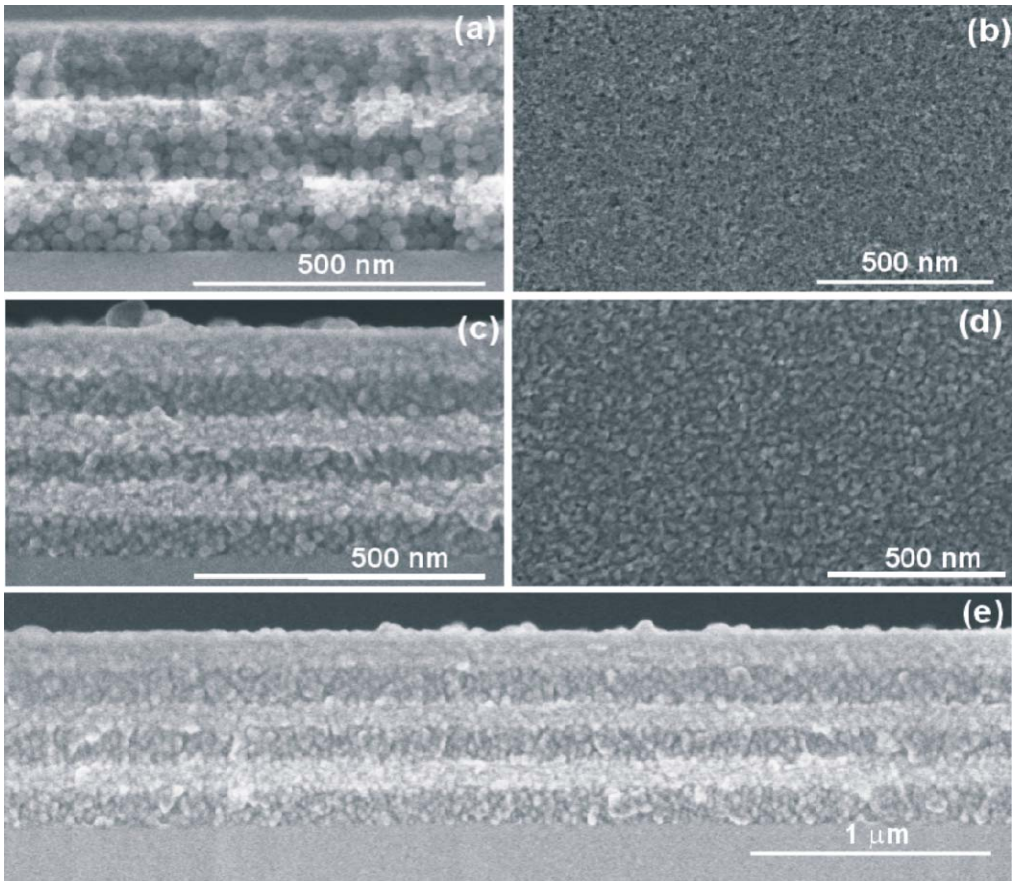

Figure 3. *SEM images of the cross sections and upper surfaces of nanoparticle multilayers before, (a) and (b), and after, (c) and (d), being infiltrated with GaAs using 800 CVD loops. (e) Lower magnification image of the cross section of the infiltrated sample.*

The crystalline nature of the as-grown GaAs was confirmed by X-ray diffraction analysis of the resulting films, the three peak pattern characteristic of the zinc-blende structure of the semiconductor being clearly observed independently of the number of cycles performed. In Figures 4(a), 4(b) and 4(c), diffractograms corresponding to 200, 366 and 800 cycles are plotted. The Scherrer formula was used to estimate the crystallite size, which was found to be around 6 nm in all cases. Elemental analysis realized using energy-dispersive X-ray spectroscopy reveals the increasing presence of Ga and As in the multilayer as the number of deposition cycles is gradually raised. Figures 4(d), 4(e), and 4(f) explicitly show this effect.

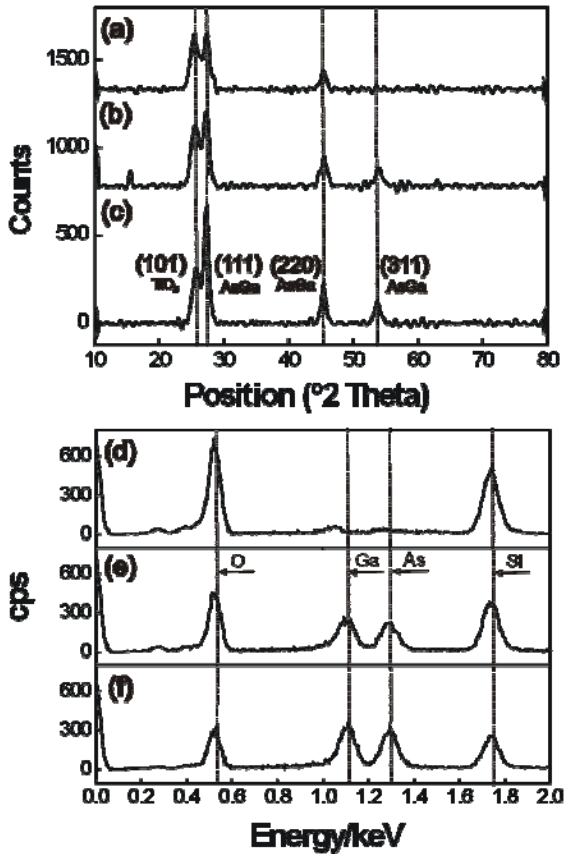

Figure 4. *X-ray diffractograms performed for the same nanoparticle multilayer after being infiltrated with GaAs using (a) 200, (b) 366, and (c) 800 CVD loops. Elemental analysis performed by energy dispersive X-ray spectroscopy for (d) the original nanoparticle multilayer, and the same multilayer after being infiltrated with GaAs using (e) 200 and (f) 800 CVD loops*

3.b Optical properties.

The modifications of the optical properties of the ensemble as a consequence of the presence of GaAs in the voids were studied using a Fourier Transform infrared spectrophotometer (Bruker IFS-66 FTIR) attached to a microscope and operating in reflection mode with a 4X objective with 0.1 of numerical aperture (light cone angle ±5.7º). The spectra attained for a series of photonic crystals infilled using different number of GaAs deposition cycles, namely 200, 366 and 800, are displayed in the graph of Figure 5. Photographs of the surface of the different samples whose spectra are plotted in such graph, attained using a digital camera, are also shown. It can be readily seen that the effect of the filling with the semiconductor on the photonic response is dramatic.

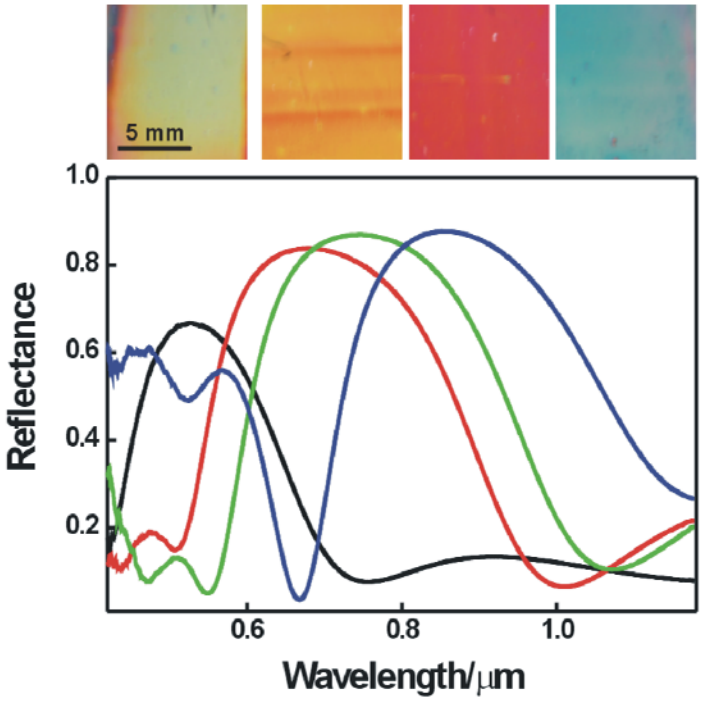

***Figure 5**. Upper panel: digital camera pictures of the same nanoparticle multilayer before and after being infiltrated with GaAs using 200, 366 and 800 loops, from left to right. Lower panel: Typical reflectance spectra attained from each one of these photonic crystals plotted, correspondingly, using black, red, green and blue lines.*

A summary of the changes observed experimentally in the primary maximum or Bragg peak that occur at the different degrees of infiltration of the structure achieved is presented in Figure 6. As it is known, this peak results from the constructive interference of the multiple reflections that occur at each interface present in the multilayer and its features are very sensitive to modifications of the refractive index of the layers. The evolution of the Bragg peak position, herein estimated as the wavelength of maximum reflectance λ_0, is plotted in Figure 6(a); the maximum reflectance intensity is displayed in Figure 6(b); finally, the gap to midgap ratio, estimated as the ratio between the spectral full width at half maximum and the spectral position of such maximum in terms of frequency, $\Delta\omega/\omega_0$, is shown in Figure 6(c). First of all, λ_0 gradually red-shifts as the number of infiltration loops increases, see Figure 6(a). This causes the color of the films to strongly vary, as it can be seen in the accompanying pictures. Such effects can be understood in terms of the approximate expression to estimate the spectral position of the Bragg peak, $\lambda_{Bragg} = 2n_{eff}\Lambda$, where Λ is the thickness of the unit cell and n_{eff} is the average refractive index of the ensemble. The refractive index of a non magnetic material n is related to its dielectric constant ε through $n = \sqrt{\varepsilon}$. The value of ε rapidly increases as the high dielectric constant semiconductor ($\varepsilon \approx 12.25$ at $\lambda \approx 1000$ nm) fills the void space between the nanoparticles in each layer, which gives rise to the spectral shift of the Bragg peak. Simultaneously, the maximum reflectance intensity increases from 65% for the non-treated three-unit cell lattice used as matrix, to almost 90% after 800 cycles of GaAs deposition, as seen in Figure 6(b). This rise of the reflectance intensity is, for the sample containing the lower loads of semiconductor, accompanied by a large increase of the gap to midgap ratio, which rises from 40% to 50%, Figure 6(c). However, the experimentally determined $\Delta\omega/\omega_0$ decreases for higher degrees of infiltration, even reaching the values attained for the original host. It is worth noticing that the intensity remains approximately constant for all infiltration treatments performed. The two different trends observed for the reflectance intensity and the gap to midgap ratio can be explained on the following basis: although both parameters are directly proportional to the difference between the refractive indexes of the two types of layers present in the multilayer (Δn), $\Delta\omega/\omega_0$ is also inversely proportional to the non-weighted refractive index average $n=(n_1+n_2)/2$, where n_1 and n_2 are the generic refractive index of the layers present in the multilayer, as given by the expression $\Delta\omega/\omega_0 \approx 2/\pi \cdot \Delta n/n$.[24] Hence the expected increase of $\Delta\omega/\omega_0$ caused by the rise of Δn could be compensated by the decrease caused by higher values of n. This seems to be the case for the multilayers treated with 366 and 800 GaAs deposition cycles. Simultaneously, reflectance intensity is mainly determined by the dielectric contrast and less sensitive to the increase of the

average refractive index. These hypotheses are in good agreement with the values of the optical parameters extracted from the fitting of the reflectance spectra, as it is shown in the following section.

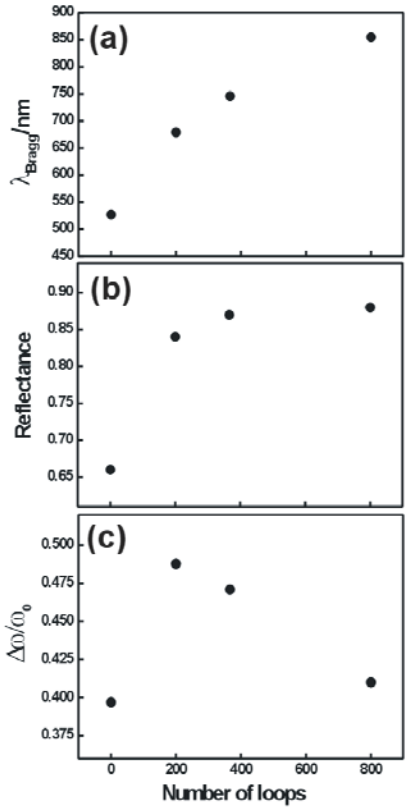

Figure 6. *Experimentally observed evolution of (a) the spectral position of the primary reflectance maximum, (b) the reflectance intensity, and (c) the full width at half maximum to midgap ratio as the number of infiltration cycles increases for the photonic crystal whose optical response is shown in figure 5.*

3.c Analysis of the results.

Theoretical reflectance spectra were obtained using a code written in Matlab and based on a transfer matrix formalism.[24] Using as input values the thickness of the alternated slabs observed in the SEM, the fill fraction of each material present is estimated from their relative contribution to the effective refractive index of each type of layer. Frequency dependent curves for the real and the imaginary parts of the

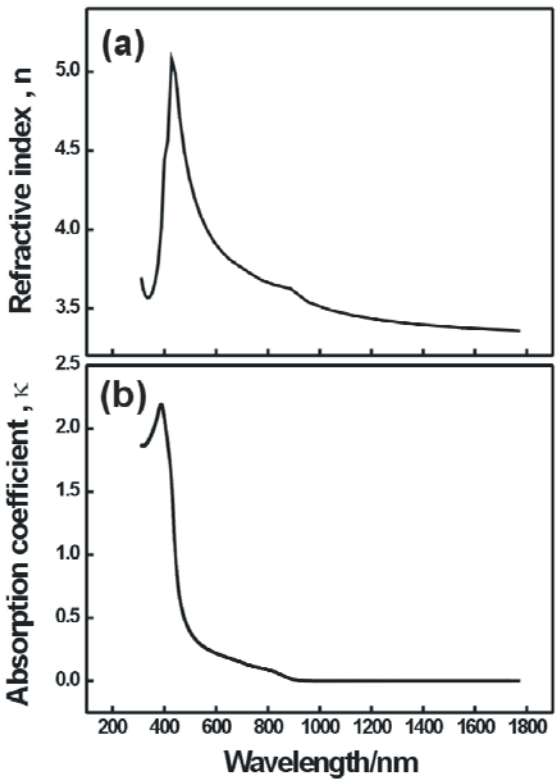

Figure 7. *Spectral dependence of the (a) real and the (b) imaginary part of refractive index, n and κ of Gallium Arsenide. Curves are extracted from reference 25.*

GaAs, $n(\lambda)$ and $\kappa(\lambda)$, extracted from the literature,[25] are plotted in Figure 7 and used for the calculations. In Figure 8, the experimental reflectance spectra (red lines) and the corresponding theoretical fittings (black lines) are plotted for a multilayer before, Figure 8(a), and after, Figure 8(b), being subjected to 200 cycles of GaAs CVD process. In Figure 8(c), the evolution of the filling fraction of the pore volume is plotted respect to the number of GaAs deposition loops for both titania (black circles) and silica (red circles) layers, as extracted from the simulations. It is clear that the filling of the much smaller pores present in titania layers, due to the finer size of the crystallites that form it, is significantly more effective than that occurring in the pores of the silica layers. This is in good agreement with a deposition mechanism in which the void space is filled by the growth of the III-V semiconductor onto the surface of

the individual nanoparticles, as suggested by the SEM characterization results. Thus, even when the starting empty volume of each type of layer is similar (the filling fraction of air in the original matrix is ff_{air}≈46% for titania and ff_{air}≈35% for silica layers), smaller pores are filled more rapidly. These results indicate that neither the interstitial space of the titania nor that of the silica layers is completely filled by GaAs, as expected for a layer by layer deposition process. Solvent adsorption experiments at controlled partial pressure, as previously performed for similar porous multilayers,[17] confirmed that the remaining porosity is not accessible. On a different note, it should be noticed that the estimated trend for the GaAs loading indicates that the dielectric contrast Δn is kept approximately constant while the average dielectric constant increases with the number of CVD cycles. This result supports the hypothesis proposed above to explain the different trends observed for the reflectance maximum intensity and spectral width versus the number of CVD cycles. Finally, it should also be remarked that the fitting of the fine features observed in the spectra is only possible by considering the modulations introduced by a thin layer of GaAs deposited onto the upper surface of the photonic crystal. The theoretically estimated thickness of this overlayer of GaAs *versus* the number of loops is also plotted in Figure 8 (empty circles, right axis).

As it was explained before, within a photonic crystal, the photonic density of states is changed dramatically near the edges of the bandgap and at the spectral position of the resonances, caused by a break in the periodicity of the refractive index or the thickness of the layers, showing a maximum at these frequencies. Thus, the optical properties of a material integrated in the multilayer will be affected, enhanced or attenuated, by the structure. The photoluminescence of GaAs, that is its most remarkable optical property, could be modified by integrating it in the porous net of a photonic structure. However, luminescence was not observed from the semiconductor. To justify this, it is necessary to remind that the emission of luminescence from a direct gap semiconductor like the GaAs demands an extremely high crystallinity, which is typically reached with an epitaxial growth process of GaAs over a GaAs substrate, while in this case a glass substrate was employed.

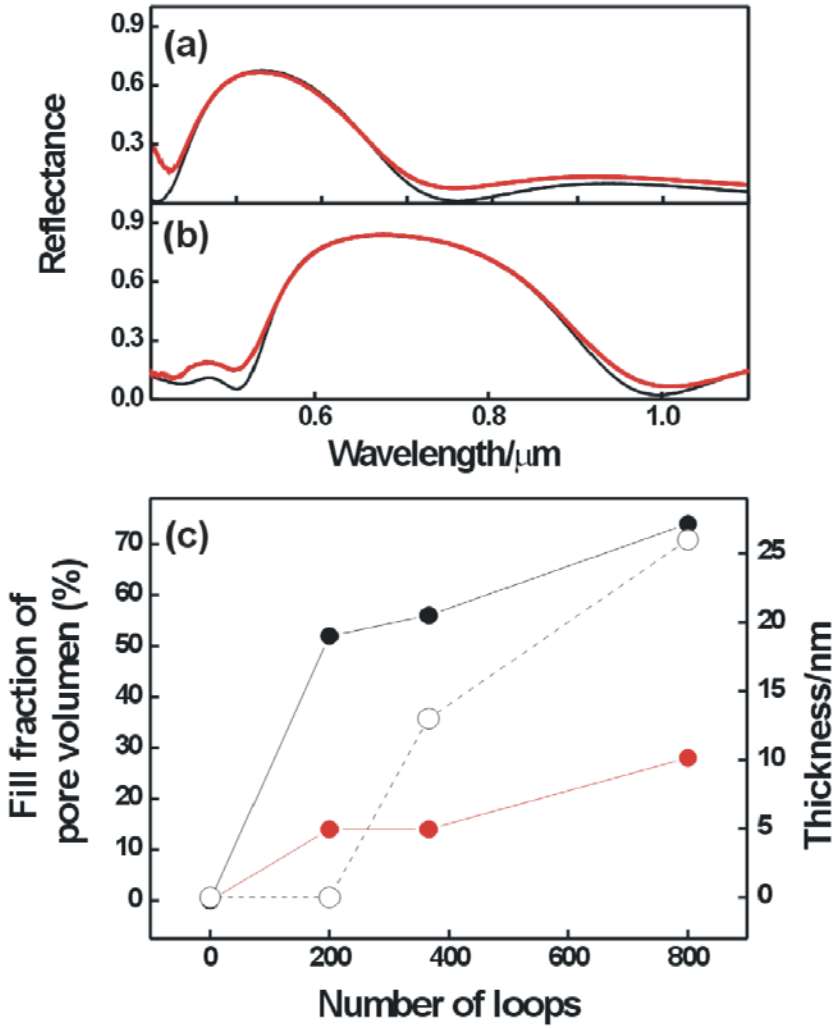

Figure 8. *Experimental reflectance spectra (red lines) and their corresponding theoretical fittings (black lines) of a multilayer (a) before and (b) after being infiltrated with GaAs (200 cycle deposition). (c) Evolution of the filling fraction of the pore volume with the number of GaAs deposition loops for both the titania (black circles) and the silica (red circles) layers, as extracted from the simulations. The theoretically estimated thickness of the layer of GaAs deposited on the top of multilayers versus the number of loops is also plotted (empty circles, right axis).*

4.Conclusions.

A viable synthetic route to infiltrate gallium arsenide within nanoparticle based periodic multilayers has been studied to yield a photonic material displaying wider and more intense reflectance peaks in the visible and near infrared regions.

An MOCVD process is shown to provide an efficient load of the structure even when the pore size is on the order of the few nanometers. Optical properties show that reflectance intensities close to 90% are reached for stacks only six layers wide, as well as gap to midgap ratios of 50%.

All changes observed in the optical properties have been understood in terms of the variation of relevant parameters such as the average dielectric constant and the dielectric contrast between the layers.

The optical response of the hybrid ensemble can be accurately tuned through the number of infiltration cycles performed. The method proposed is generic and can be extended to any other III-V or IV type semiconductor that can be synthesized from the gas phase.

5. References.

[1] C. López. "Materials Aspects of Photonic Crystals"*Adv. Mater. 15*, **2003**, 1679.

[2] T. Holland, C. F. Blanford, A. Stein "Synthesis of Macroporous Minerals with Highly Ordered Three-Dimensional Arrays of Spheroidal Voids" *Science, 281*, **1998**, 538.

[3] J. E. G. J. Wijnhoven, W. L. Vos. "Preparation of Photonic Crystals Made of Air Spheres in Titania" *Science, 281*, **1998**, 802.

[4] A. Blanco, E. Chomski, S. Grabtchak, M. Ibisate, S. John, S.W. Leonard, C. López, F. Meseguer, H. Míguez, J.P. Mondia, G.A. Ozin,O. Toader, H.M. van Driel. "Large-scale synthesis of a silicon photonic crystal with a complete three-dimensional bandgap near 1.5micrometres" *Nature, 405*, **2000**, 437.

[5] N. Tetreault, G. von Freymann, M. Deubel, M. Hermatschweiler, F. Pérez-Willard, S. John, M. Wegener, G.A. ."New Route to Three-Dimensional Photonic Bandgap Materials: Silicon Double Inversion of Polymer Templates" *Adv. Mater, 18*, **2006**, 457.

[6] H. Míguez, E. Chomski, F. García-Santamaría, M. Ibisate, S. John, C. Lopez, F. Meseguer, J. P.Mondia, G. A. Ozin, O. Toader, and H.M. van Driel. "Photonic Bandgap Engineering in Germanium Inverse Opals by Chemical Vapor Deposition" *Adv. Mater. 13*, **2001**, 1624.

[7] H.M. Yates, M. Pemble, H. Míguez, E. Chomski, F. García-Santamaría, M. Ibisate, S. John, C.le, E. Palacios-Lidón, I. Rodríguez, F. Meseguer, C. "Modification of the Natural Photonic Bandgap of Synthetic Opals via infilling with crystalline InP" *Adv. Func. Mater. 15*, **2005**, 411.

[8] I.M. Povey, D. Whitehead, K. Thomas, M.E. Pemble, M. Bardosova, J. Renard. "Photonic crystal thin films of GaAs prepared by atomic layer deposition"*.Appl. Phys. Lett. 89,* **2006**, 104103.

[9] B.H. Juárez, S. Rubio, J. Sánchez-Dehesa, C. López. "Antimony trisulfide inverted opals: Growth, characterization, and photonic properties", *Adv. Mater. 14*, **2002**, 1486.

[10] E. Yablonovitch. "Inhibited Spontaneous Emission in Solid-State Physics and Electronics" *Phys. Rev. Lett. 58*,**1987**, 2059.

[11] S. John. "Strong Localization of Photons in Certain Disorderer Dielectric Superlattices". *Phys. Rev. Lett. 58*, **1987**, 2486.

[12] S. Colodrero, M. Ocaña, H. Miguez, *Langmuir, 24*, **2008**, 4430.

[13] M.C. Fuertes, F.J. López-Alcaraz, M.C. Marchi, H.E. Troiani, G.J.A.A. Soler Illia, H. Míguez. "Photonic Crystals from Ordered Mesoporous Thin-Film Functional Building Blocks" *Adv. Funct. Mater. 17*, **2007**, 1247.

[14] S.Y. Choi, M. Mamak, G. von Freymann, N. Chopra, G.A. Ozin. "Mesoporous Bragg Stack Color Tunable Sensors", *Nano Lett,. 6*, **2006**, 2456.

[15] B.V. Lotsch, G.A. Ozin,. "Photonic Clays: A New Family of Functional 1D Photonic Crystals" *ACS Nano, 2*, **2008**, 2065.

[16] B.V. Lotsch, G.A. Ozin. "Clay Bragg Stack Optical Sensors", *Adv. Mater, 20*, **2008**, 4079.

[17] S. Colodrero, M. Ocaña, A.R. González-Elipe, H. Míguez. "Response of nanoparticle-based one-dimensional photonic crystals to ambient vapor pressure" *Langmuir, 24*, **2008**, 9135.

[18] M.E. Calvo, S. Colodrero, T.C. Rojas, M. Ocaña, J.A. Anta, H. Míguez. "Photoconducting Bragg Mirrors based on TiO2 Nanoparticle Multilayers" *Adv. Func. Mater. 18*, **2008**, 2708.

[19] F. Scotognella, D.P. Puzzo, A. Monguzzi, D.S. Wiersma, D. Maschke, R. Tubino, G.A. Ozin. "Nanoparticle One-Dimensional Photonic-Crystal Dye Laser" *Small, 5,***2009**, 2048.

[20] S. Colodrero, A. Mihi, L. Häggman, M. Ocaña, G. Boschloo, A. Hagfeldt, H. Míguez. "Porous One-Dimensional Photonic Crystals Improve the Power-Conversion Efficiency of Dye-Sensitized Solar Cells" *Adv. Mater. 21*, **2009**, 764.

[21] M.E. Calvo, O. Sánchez-Sobrado, G. Lozano, H. Míguez, "Molding with nanoparticle based One Dimensional Photonic Crystals: A Route to Flexible and Transferable Bragg Mirrors of High Dielectric Contrast.". *J. Mater. Chem***.** *19*, **2009**, 3144.

[22] O. Sánchez-Sobrado, K. Thomas, I. Povey, M. Pemble, H. Míguez, "Gallium arsenide infiltration of nanoporous multilayers: A route to high dielectric contrast one-dimensional photonic crystals", *Small, 6*, **2010**, 1283.

[23] Z. I. Alferov, V. M. Andreev, M. B. Kagan, I. I. Protasov, V. G. Trofim, ''Solar-energy converters based on p-n AlxGa1-xAs-GaAs heterojunctions,'' *Sov. Phys. Semicond. 4*,**1971**, 2047.

[24] A. Yariv, P. Yeh, "Optical Waves in Crystals", **2003** John Wiley and Sons Inc., ISBN 0-471-43081-1.

[25] S. Zollner. "Optical constants and critical-point parameters of GaAs from 0.73 to 6.60 eV" *J. Apply. Phys. 90*, **2001**,515.

Chapter V

Modification of the optical absorption of metallic nanoparticles integrated in one dimensional photonic crystals

1. Introduction.

Enhancement and confinement of the electromagnetic field at length scales on the order of nanometers constitutes the subject of plasmonics.[1] The plasmon is a quasiparticle resulting from the quantization of oscillations of the free electron gas typical of metals, for example, at optical frequencies, just as photons and phonons are quantizations of light and mechanical vibrations, respectively. The plasmon frequency of oscillation is characteristic of each type of material and it depends on the density of electrons. Plasmons play a large role in the optical properties of metals. Light of frequency below the plasma frequency is reflected because the electrons in the metal screen this electric field. Light of frequency above the plasma frequency is transmitted, because the electrons cannot respond fast enough to screen it. In most metals, the plasma frequency is in the ultraviolet, making them reflective in the visible range. In some metals, such as copper or gold, specific visible light energies are absorbed, yielding their distinct color. On the other hand, surface

plasmons are those that occur at the interface between vacuum or a material with a positive dielectric constant and a negative dielectric constant material, as metals.

Metal nanoparticles are a very good platform to study plasmonic phenomena[2] and their potential applications in fields like catalysis,[3] energy,[4] sensing[5] or optics,[6] being one of the more characteristic features of metal particles the well-defined resonant optical absorption peak at visible wavelengths caused by the excitation of localized surface plasmons.[7] Such enhanced electromagnetic modes are confined in the boundary between a metallic bead and its dielectric environment, thus being also extremely sensitive to the refractive index of the surrounding medium.[8] Also, they are particle size and shape-dependent. Through this dependence, the interaction of light with the surface can be controlled and therefore the colour of materials. This latter property actually makes them suitable as base materials to be use in detection of chemical or biological compounds.[9] At the same time, it implies that, when required, some type of coating is needed to stabilize their optical response versus environmental changes, which has boosted active research in methods to obtain core-shell structures, in which the outer layer is typically a dielectric material.[10] Once plasmonic interactions between neighboring particles are screened by a dielectric shell, the color of the metallic particle will depend exclusively on its size and shape, and these are actually the means commonly employed to control their absorption.

In this chapter, the optical absorption caused by gold nanoparticles has been modified exclusively by controlling their photonic environment. Particles were synthesized in the Colloid Chemistry Group of Universidade de Vigo, with a determined shape and size and they were silica coated to keep their optical properties isolated of material environment. Nanoparticle one dimensional photonic crystals (1DPCs) containing such silica coated gold nanoparticles have been constructed to demonstrate that the interplay between localized surface plasmons in metal nanoparticles and the field confinement effects occurring in optical structures containing them leads to selective spectral enhancement and fine tuning of the optical absorption of the ensemble. The porous 1DPCs were fabricated following the procedures described Chapter II.

The interplay between plasmonic and photonic resonances has gathered considerable attention in the last years. A significant number of methods have been developed to incorporate metallic particles, mainly made of gold, into periodic structures.[11-17] In the vast majority of cases, their integration has been achieved by infiltration into three-dimensional self-assembled photonic crystals, the effect of the metal guest being the tuning or enhancing of the reflection peaks (or transmission dips) caused by the presence of a photonic stop band in such structures. Also, sharp

and intense optical absorption fluctuations have been predicted for Bragg mirrors containing arrays of noble metal particles.[18] In spite of all these efforts and technologically promising properties, no experimental studies report on the controlled tuning and enhancement of the absorption properties of hybrid plasmonic-photonic materials as a result of the enhanced field localization in the vicinity of metal particles. The reason for this is probably due to the weak localization effects observed in three dimensional self-assembled photonic crystals, in which both dielectric contrast and the degree of ordering are low, or the difficulty to embed the metallic particles in actual optical resonators in which the localization effects are stronger. This difficulty arises from the incompatibility existing between the highly sophisticated processing techniques of photonic crystals and the handling of nanoparticle based suspensions.

These obstacles are overcome, as it is shown in this chapter, by integrating the gold nanoparticles in the SiO_2-TiO_2 multilayers developed as part of this research work. The particulate nature of these materials allows a perfect integration of metallic nanospheres without disrupting the optical quality of the ensemble. The optical response characteristic of these constructions (high selective reflectance/transmittance) leads to a strong modification of the optical absorption. The results herein presented have been reported in reference 19.

2. Optical absorption of silica coated gold nanoparticles.

Stabilized silica coated gold nanoparticles, Au@SiO_2, used in this study were prepared following a well-established and generic procedure that had been reported before by Liz-Marzan et al.[20] The synthesis is described in the Appendix. The final particles present a gold core of 6.5 nm radius and a silica corona of 16 nm thickness, as can be seen in the transmission electron micrograph displayed in Figure 1(a). The SiO_2 coating thickness was chosen taking into account that it has been shown that a 15 nm thick silica layer is enough to both screen the plasmonic interactions between neighboring gold cores and remove the dependence of the absorption spectra on the dielectric constant of the surrounding medium.[10] In order to confirm so, a layer of Au@SiO_2 nanoparticles was deposited onto a TiO_2 nanoparticle layer by spin coating, whose cross section as observed by field emission scanning electron microscopy (FESEM) is shown in Figure 1(b).

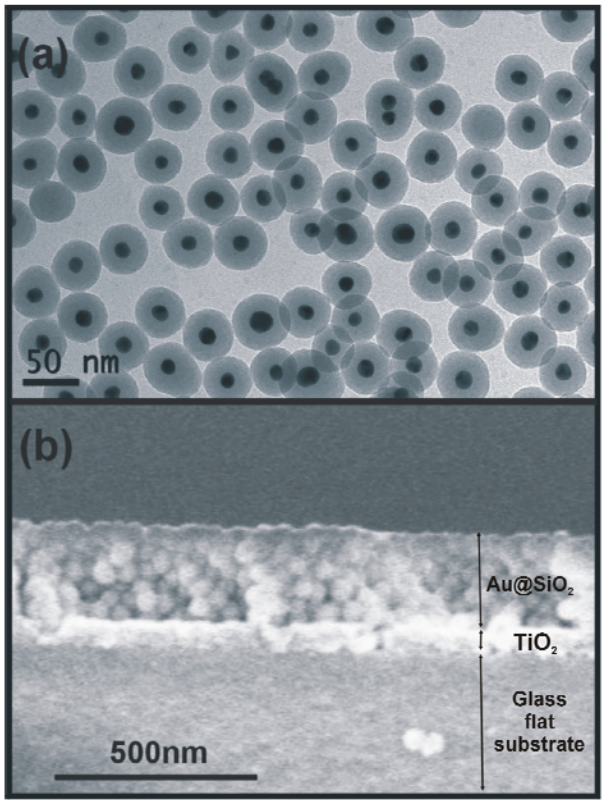

Figure 1. *(a) Transmission electron microscopy image of the Au@SiO_2 core-shell particles employed in this work. (b) Field emission scanning electron microscopy image of a cross section of a layer of the same particles made by spin coating the precursor suspension on a thin TiO_2 nanoparticle film, which was in turn deposited on glass. Similar layers were used as reference samples for the optical characterization experiments.*

The visible absorption spectra of the precursor colloidal suspension containing the Au@SiO_2 particles in a concentration of 2 vol. % in methanol was compared with that of a 300 nm thick layer deposited from it and that of the same layer with its void network infiltrated with isopropanol (refractive index n=1.38), as can be seen in Figure 2 (black, blue and red curves respectively). The spectra are plotted normalized for a better comparison. It was found that the absorptance peaks occur at the same spectral position in three cases, and they present the same shape at the range of interest, demonstrating the efficient screening effect of the silica coating. Similar layers were prepared to be used as references for all the optical studies conducted.

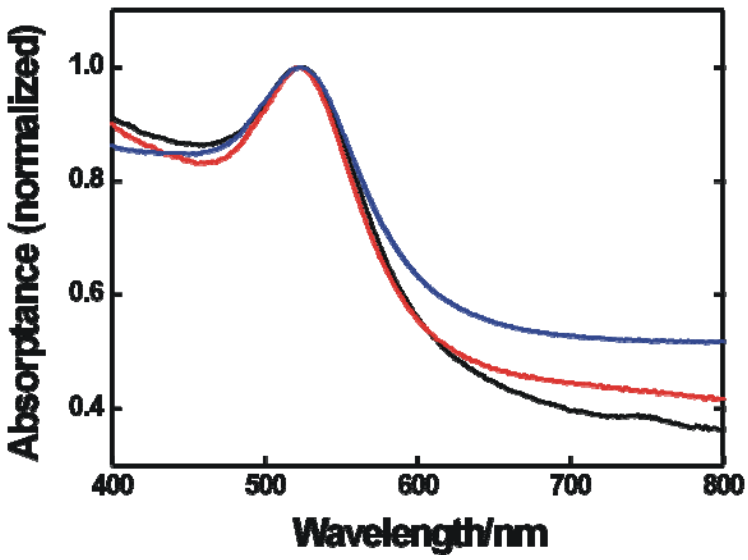

***Figure 2**. Absorptance of the Au@SiO_2 nanoparticle suspension (black curve) and of a 300 nm thick layer of the same particles deposited on glass before (blue) and after (red) being infiltrated with isopropanol.*

3. Structural characterization of 1DPCs integrating gold nanoparticles.

Most results presented in this chapter were obtained from optical resonators integrating metallic particles, which were built by introducing a middle layer of gold nanoparticles within four unit-cell one dimensional photonic crystals comprising alternate layers of controlled thickness of silica and titania nanoparticles. These were deposited on flat glass substrates by spin coating following the procedure explained in Chapter II. A cross section of one of these ensembles is shown in the FESEM image of Figure 3(a). It can be seen that the larger size of the spherical core-shell particles sandwiched within the two periodic multilayers does not alter the long range order of the structure. This adaptability is a characteristic feature of Bragg stacks made of nanoparticles. Smaller TiO_2 nanocrystals create a layer of uniform thickness when deposited onto a rougher surface. This property has been also demonstrated in optical resonators integrating large rare earth particles of rhombohedral shape, in

which enhancement or suppression of selected luminescence emission lines can be achieved, as it will be shown in the next chapter of this thesis. Another photonic structure has been constructed to study the optical absorption of gold particles. It consists in a four unit-cell TiO_2-SiO_2 nanoparticle multilayer in which one layer of SiO_2 was replaced by a $Au@SiO_2$ layer with a thickness designed to attain an optical response without resonance. This structure is shown in the FESEM image of Figure 3(b). In the picture white arrows indicate the different thickness of the $Au@SiO_2$ layer in both cases.

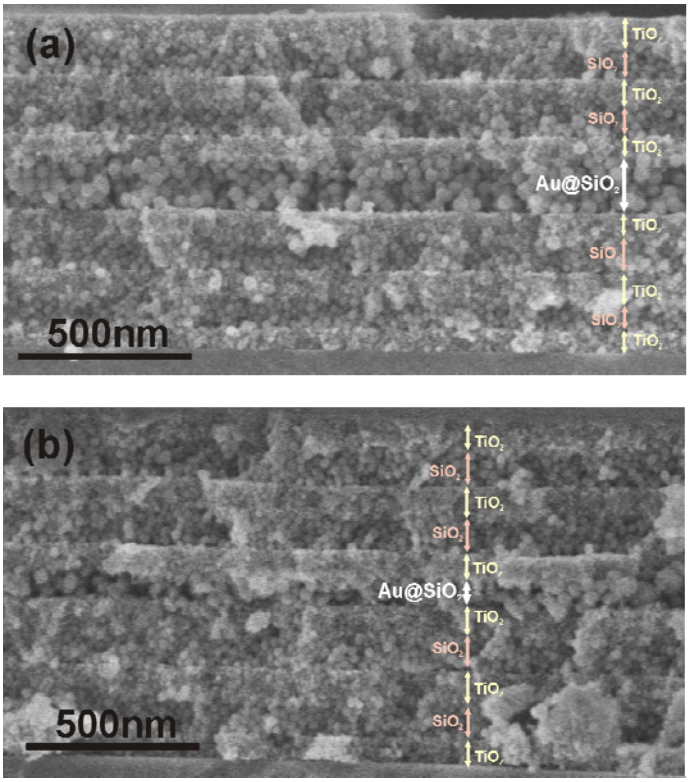

Figure 3. *FESEM image of a cross section of two one dimensional SiO_2-TiO_2 nanoparticle photonic crystal in which a $Au@SiO_2$ nanoparticles middle layer was embedded. In one of them, (a), the gold layer acts as a photonic defect. In the multilayer showed in (b), the gold layer does not give rise to a resonant mode at photonic band gap frequencies.*

The synthesis of de TiO_2 and the SiO_2 nanoparticles as well as the preparations of their suspensions are described in detail in the Appendix. Both suspensions were

diluted in methanol with concentrations between 2 and 4 wt. %. The layers of $Au@SiO_2$ nanoparticles were introduced in the middle of the stacks also by spin coating 200 µL drops of a 1.45 wt. % suspension in methanol. The three kinds of layers were attained using final speeds in the range 3000-7000 rpm, with a fixed acceleration ramp of 11340 rpm s^{-1}. The samples used as reference were deposited following similar conditions.

4. Optical characterization of 1DPCs integrating gold nanoparticles.

4.a Measurements.

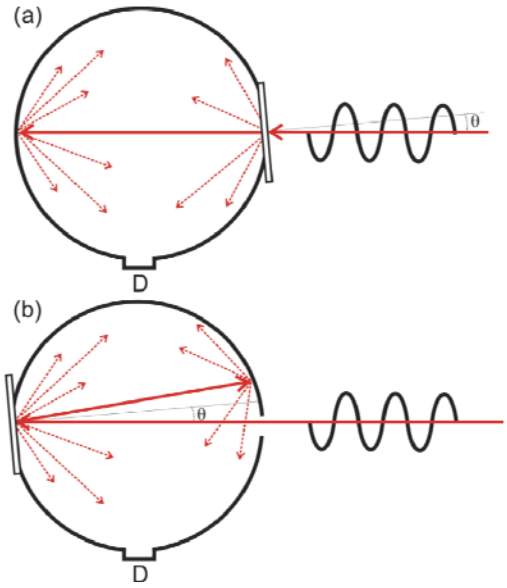

Figure 4*. Scheme of the integrating sphere employed to detect (a) total transmitted and (b) total reflected light. The incident angle θ (5º) is enlarged in the drawing for the sake of clarity. The sample is represented by a thin rectangle and D stands for detector.*

Optical characterization was carried out using a UV-visible scanning spectrophotometer (SHIMADZU UV-2101PC) attached to an integrating sphere operating in both total reflection and total transmission modes. Such configurations are illustrated Figure 4. Extreme care was taken to collect all reflected and transmitted light (that is, the specularly reflected and ballistically transmitted beams,

as well as the forward and backward diffuse light) from precisely the same area of the crystal, as well as to minimize losses caused by geometrical constraints of the device employed. The optical absorptance of gold nanoparticles inside the multilayer is attained through the expression $A= 1- T_T - R_T$, in which T_T and R_T are the total transmittance and the total reflectance respectively. In order to check this, another type of structure was fabricated. It consists in a four unit-cell nanoparticle resonator, as the one analyzed before, but without gold nanoparticles integrated in it. Measurements of both reflectance and transmission are plotted in Figure 5(a). It can be clearly seen how the spectra are complementary. The absorptance of the structure is calculated by adding these two spectra and subtracting it from one, Figure 5(b). By analyzing this spectrum it can be concluded that the error committed when estimating the absorptance accounts for less than 3%. It must be noted that there are no compounds forming the multilayer that present absorption in the visible range.

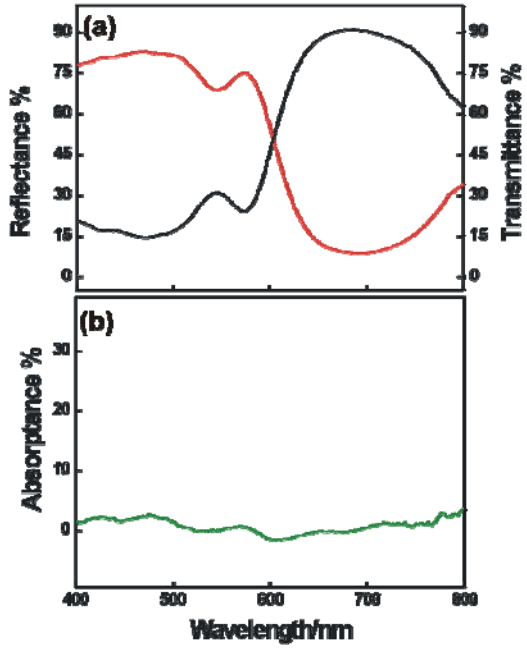

***Figure 5**. (a) Reflectance (black curve) and transmittance (red curve) spectra of the resonator used as a blank, i.e. not containing any Au@SiO_2 particles. No reinforcement effect is detected at blue-edge or at red-edge frequencies, as expected. The absorptance spectrum plotted in green color shown in (b) results from adding these two spectra and subtracting it from one.*

4.b Modification of the optical absorption.

Representative results for the optical resonator are shown in Figure 6. It can be clearly seen in Figure 6(a) that total reflectance (R_T, black curve) and total transmittance (T_T, red curve) display the typical spectral features of an optical resonator which have been explained in the section 2 of the chapter III. In this case, the intensity reflected by the multilayers is maximum for 450 nm <λ<750 nm, and the transmission window caused by the resonant cavity mode opens up at around 535 nm (see vertical dashed line). A clear dip in reflectance, coincident with a peak in transmittance, centered at this wavelength is detected. It should be noted that the improvement of the quality of nanoparticle 1DPCs attained during this research work allows constructing multilayers with the number of layers necessary to obtain flat optical response. Nevertheless, most cases require a heat treatment of 450ºC at the middle and at the end of the fabrication process. This treatment cannot be applied to the gold nanoparticles because the effects of the temperature over their structural and optical properties are deleterious.

Optical absorptance, A, was calculated from the total reflectance and transmittance measurements. The result is plotted in Figure 6(b) for the resonator containing Au@SiO_2 particles (orange curve), and for a reference layer of Au@SiO_2 particles of the same thickness deposited on a thin film of TiO_2 nanoparticles (black curve). For the optical resonator containing Au@SiO_2 particles, the maximum absorptance is now centered at a wavelength that coincides with the resonant mode of the optical cavity (as indicated by the vertical dashed line), with an absorptance intensity that is almost double than that in the reference. This implies that the absorptance peak is slightly red-shifted with respect to that measured from the reference layer. It should also be noted that the absorption of light with wavelength within the photonic band gap but off-resonance is lower than in the reference layer, which is due to the screening effect of the photonic crystal mirror. To illustrate these effects, the enhancement factor calculated through the expression $A_{resonator}/ A_{reference}$ is plotted in Figure 7 (blue line). The reflectance spectrum (black line) is included for the sake of comparison. It can clearly be seen that this magnitude presents a relative maximum at the frequencies of the band gap edge, an absolute maximum at frequencies of the resonance, and values below one at the spectral positions in which the reflectance spectra presents its maximum values.

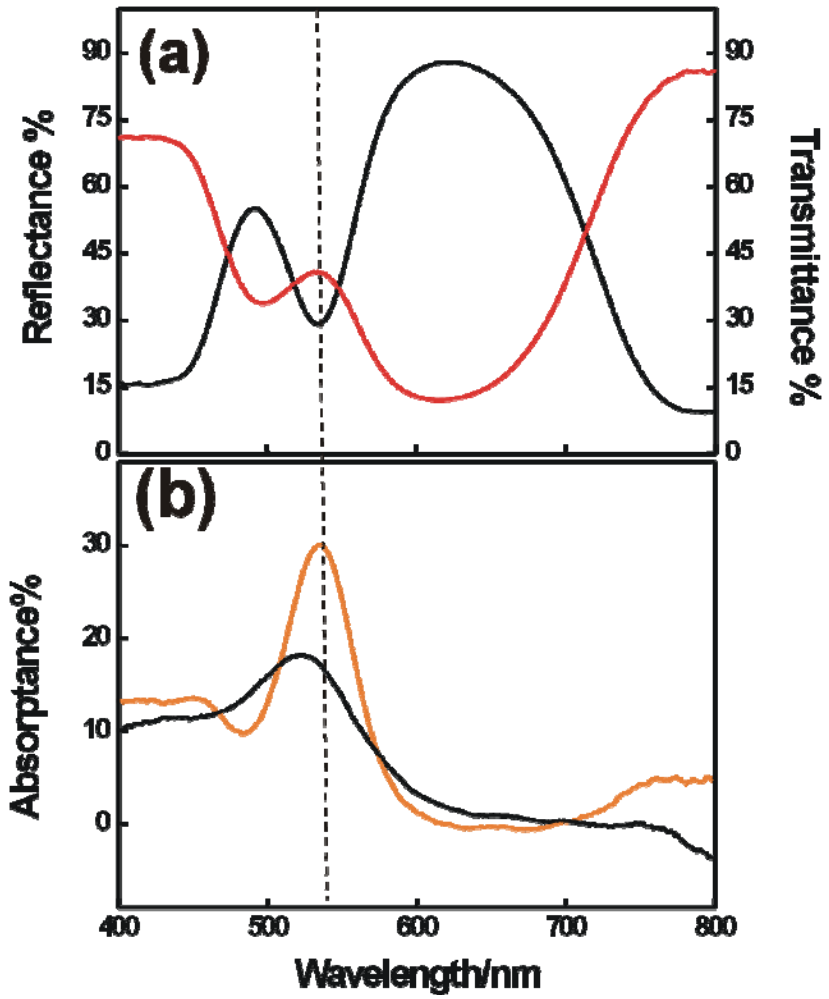

***Figure 6**. (a) Total reflectance (black curve) and total transmittance (red curve) spectra of an optical cavity made of Au@SiO_2 nanoparticles sandwiched between two one dimensional photonic crystals. (b) Optical absorptance spectrum of the resonator (orange curve), compared to that of a layer of Au@SiO_2 nanoparticles with the same thickness (black curve). The vertical dashed line indicates the spectral position of the cavity resonance.*

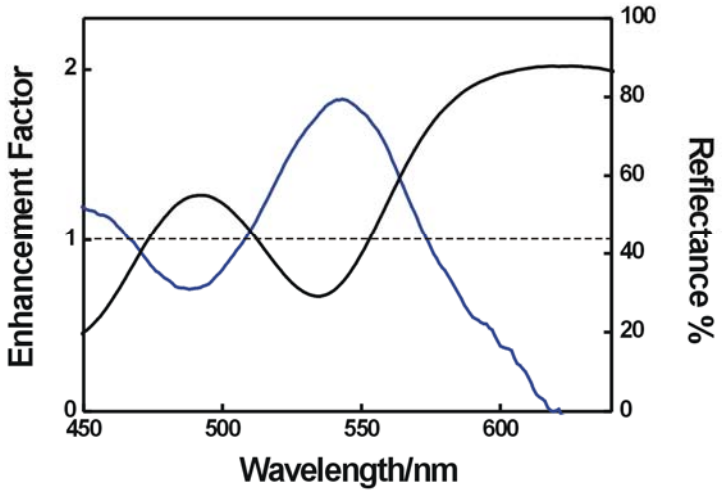

Figure 7*. (a) Total reflectance (black curve) of an optical cavity made of Au@SiO_2 nanoparticles sandwiched between two 1DPCs and the enhancement factor (blue line) extracted from the ratio of the absorptance of the resonator containing gold nanoparticles and that of the reference.*

4.c Confinement of the electric field.

This example illustrates well the effects arising from the interplay between the optical cavity and the intrinsic localized surface plasmon resonance of the Au@SiO_2 particles, i.e. spectral shift and selective enhancement of the absorption by the metallic particles. All these selective absorption reinforcement or decrease phenomena are due to preferential confinement of the resonant electromagnetic modes within the layers containing Au@SiO_2 nanoparticles. In few words, the increase of the photon density of states caused by confinement in specific slabs of the multilayer implies a lower group propagation velocity for those modes,[21] which in turn yields longer light-matter interactions and thus a higher probability of absorption.[22] On the contrary, reduction of the field intensity in selected regions gives rise to weaker interactions, hence to lower probability of absorption. To better illustrate this, in Figure 8 the calculated spatial distribution of the squared electric field is shown along a cross section of the photonic crystal embedding and

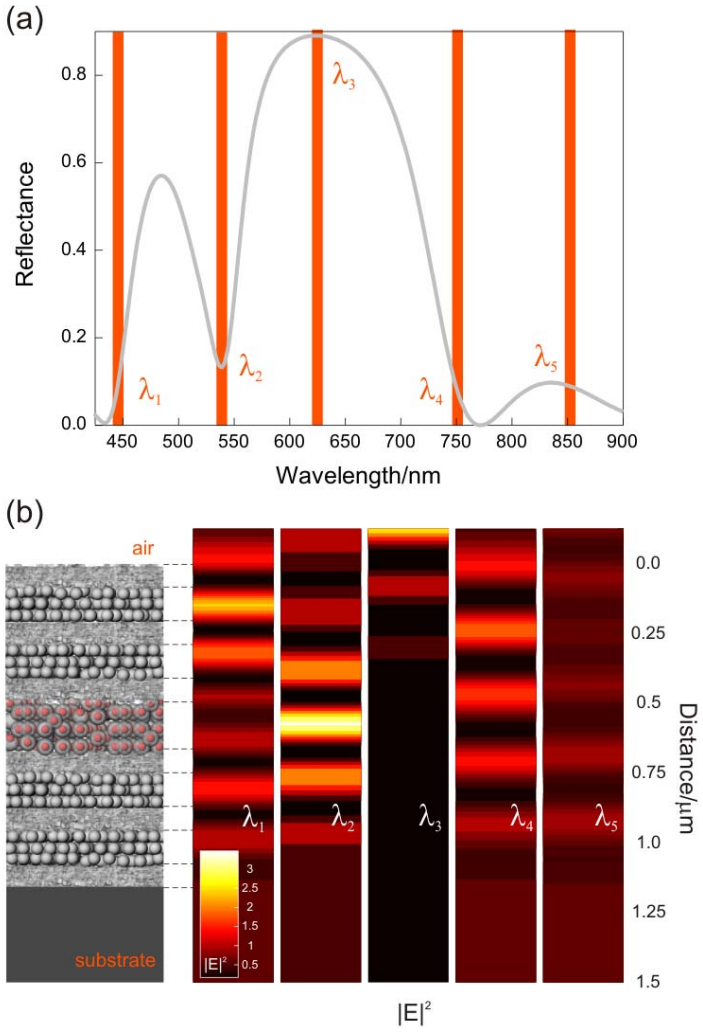

***Figure 8**. (a) Calculated specular reflectance of a multilayer with similar structural parameters to those obtained experimentally. Vertical bars indicate the spectral position of photon modes located at the blue-edge of the photonic band gap (λ_1), the center of the resonance (λ_2), the center of the photonic band gap (λ_3), the red-edge of the photonic band gap (λ_4), and the passband of the photonic crystal (λ_5). (b) Left panel shows a model of the simulated structure, where Au@SiO_2 particles are represented by grey spheres with a red core. Panels on the right show the calculated spatial distribution of the squared magnitude of the electric field along a cross section of the multilayer for all wavelengths highlighted in the reflectance spectrum shown in Figure 8(a). A color intensity scale is provided.*

optical cavity made of Au@SiO_2 nanoparticles, represented as red spheres within the center of the structure. Theoretical calculations were performed using a transfer matrix approach, as described earlier,[23] and using reported optical data for Au@SiO_2 nanoparticles.[24] Results were drawn for wavelengths: λ_1, located at the blue-edge of the photonic band gap; λ_2, at the optical resonance, for which the dip is observed in the reflectance spectrum; λ_3, within the photonic band gap and for which reflectance is maximum; λ_4, at the red-edge of the photonic band gap; and λ_5, at the pass-band of the photonic crystal. All these wavelengths are highlighted in the reflectance spectrum plotted in Figure 8(a). It can be clearly seen in the field distribution patterns plotted in Figure 8(b) that light localizes preferentially within the lower refractive index layers (i.e., silica layers) for λ_1, as expected for a mode in the higher energy band of a photonic crystal. The electric field is even more intensely reinforced within the middle Au@SiO_2 layer for λ_2, as expected for a resonant mode of the cavity. These modes show actually the highest absorptance in the experimental results presented. On the contrary, light transmission is blocked for λ_3, thus showing a very short penetration depth, or localized within the higher refractive index non-absorbing titania layers for λ_4 and λ_5, thus a decrease of absorptance is observed.

4.d Environmental response.

Further evidence of the effect of this interplay was achieved by infiltrating the porous network of the photonic crystal with liquids of different refractive index *n*. As it has been proved before,[25] this causes an effective red-shift of the optical cavity resonance. Isopropanol (n=1.377), toluene (n=1.497) and chlorobenzene (n=1.525) were employed as infiltrating liquids. For the sake of clarity, only the total reflectance spectra recorded after each infiltration are displayed in Figure 9(a). The full reflectance and transmittance spectra used to estimate the absorptance spectra plotted in Figure 9(b) are displayed in Figure 10. It can be clearly observed that upon infiltration of the pores, the absorptance spectra display a double peak structure, as a consequence of two different enhancement effects that occur simultaneously. On one hand, photon modes with wavelength matching that of the cavity resonance are localized at the Au@SiO_2 layer, thus increasing their absorption. As the refractive index of the pores increases when liquid is infiltrated, this phenomenon takes place at longer wavelengths. Such gradual shift can be clearly seen in Figure 9(b). At the same time, since the whole photonic crystal is porous, the Bragg peak is red-shifted and at some point its higher energy edge will also match the absorptance band of the Au@SiO_2 particles. Those photon modes will be preferentially localized within the lower dielectric constant layers of the

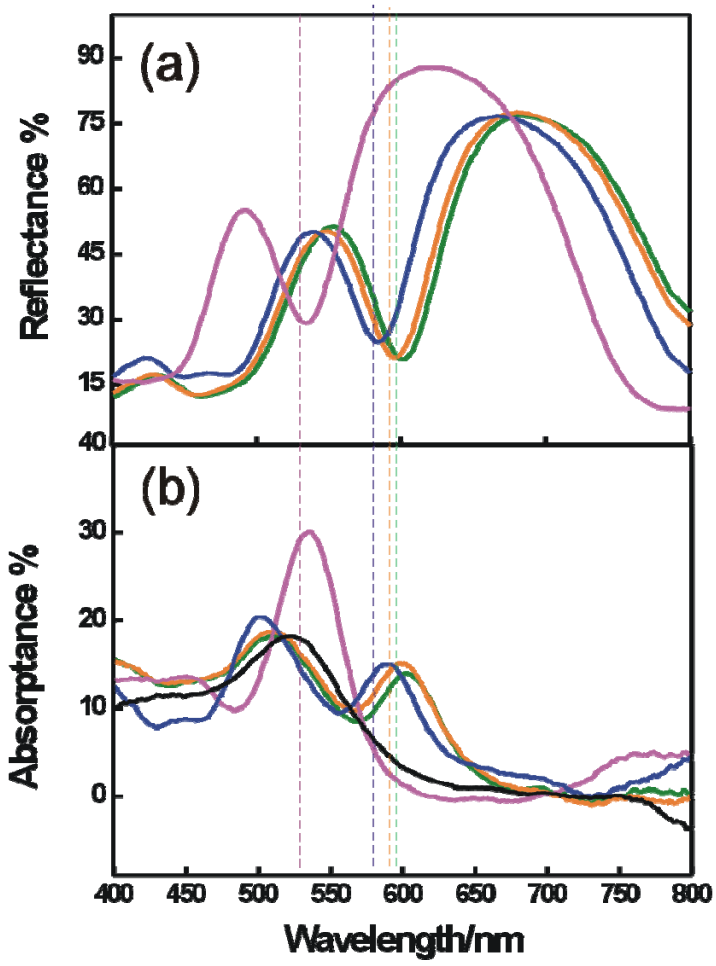

***Figure 9**. (a) Total reflectance spectra of an optical cavity made of Au@SiO_2 nanoparticles sandwiched between two 1DPCs before (magenta curve) and after being infiltrated with isopropanol (n=1.377, blue curve), toluene (n=1.497, orange curve) and chlorobenzene (n=1.525, green curve). (b) The corresponding optical absorptance spectra (same color code). Vertical dashed lines indicate the spectral position of the cavity resonance in each case. The optical absorptance spectrum of a layer of Au@SiO_2 nanoparticles of similar thickness is also shown as a reference (black curve).*

stack, including the $Au@SiO_2$ mid-layer, hence providing a second source of absorptance enhancement. The spectral position at which this effect occurs is also dependent on the refractive index of the guest compound, as can be seen in Figure 9(b). In Figure 11, the fitting of two of the absorptance spectra measured from the multilayers under analysis are plotted. Figure 11(a) corresponds to the as-prepared optical cavity for which the resonance matches the maximum of the localized surface plasmon absorption peak and Figure 11(b) corresponds to the same multilayer infiltrated with chlorobenzene, n=1.525, (see magenta and green curves in Figure 9 respectively). The fitting was made by the same model used to calculate the confinement of the electromagnetic field.

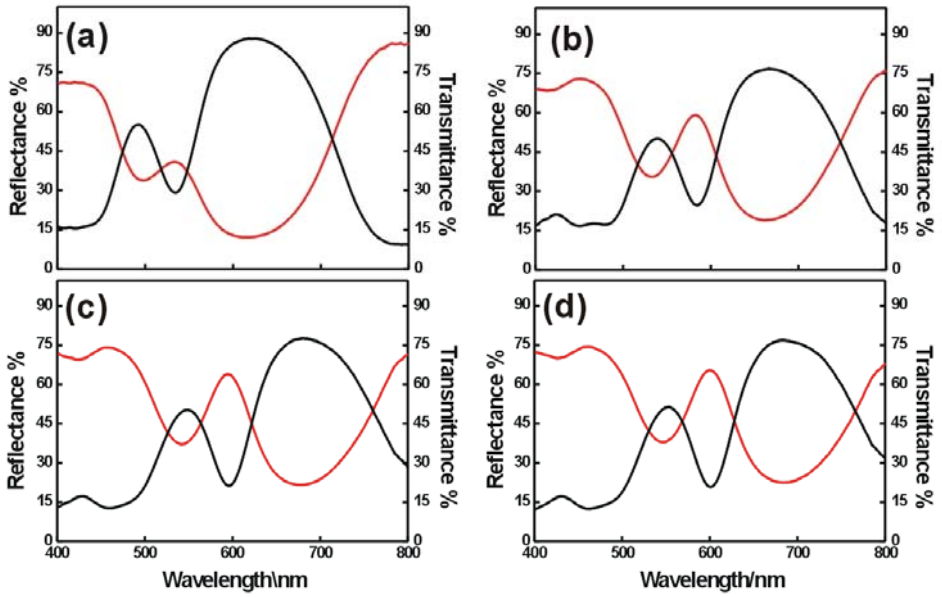

Figure 10. *Reflectance (black curves) and transmittance (red curves) spectra of an optical resonator containing a mid-layer $Au@SiO_2$ particles (a) before and after being infiltrated with (b) isopropanol (n=1.377), (c) toluene (n=1.497) and (d) benzene (n=1.525). These spectra were used to obtain the absorptance spectra shown in Figure 9(b).*

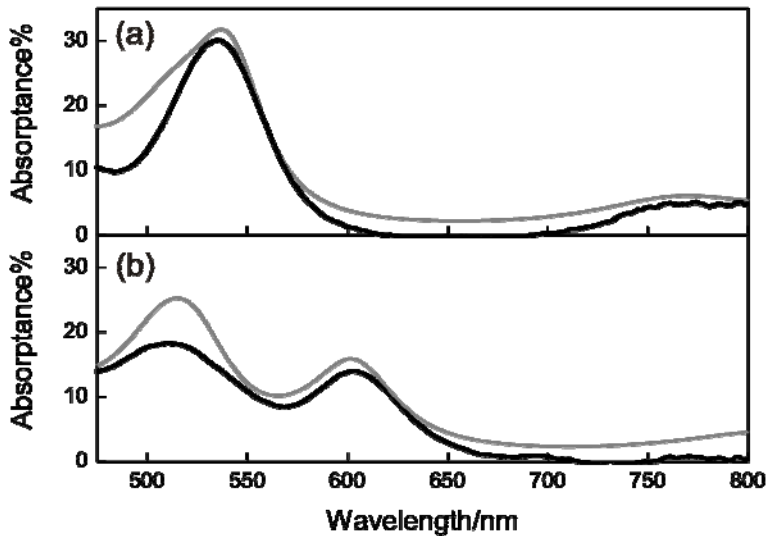

Figure 11. *Experimental (black curves) and calculated (grey curves) absorptance spectra of (a) a multilayer containing a mid-layer of Au@SiO_2 nanoparticles acting as an optical cavity and of (b) the same structure after being infiltrated with chlorobenzene (n=1.525).*

4.e Effect of the band gap edge.

Further analysis of the higher energy band edge enhancement effect was attained from samples in which one of the silica layers was substituted by a layer of Au@SiO_2 nanoparticles but designed so that no optical cavity mode was created. This was achieved by controlling the optical thickness, resulting from multiplying its thickness by its average refractive index, of the middle layer of Au@SiO_2 nanoparticles so that it was similar to the remaining silica layers in the multilayer. In this case, the only source of absorption increase is the coincidence between the optical absorption of the gold particles and the blue-edge of the photonic band gap. Total optical reflectance and absorptance spectra are displayed in Figure 12(a) and 12(b) respectively for the as-prepared multilayer before (magenta curves) and after being infiltrated with isopropanol (blue curves), toluene (orange curves) and benzene (green curves). The blue band edge shift and enhancement effect on the absorptance spectra can be readily seen. A much minor reinforcement effect is detected at the red-edge frequencies, for which the electric field is concentrated within the higher refractive index TiO_2 layers. Again a better understanding of the results can be

achieved by analyzing the enhancement factor of the structure that is plotted in Figure 13 (blue line). The black line is the reflectance spectrum. As expected, the higher enhancement of the optical absorption is spectrally reached at frequencies in which the blue band edge matches the optical absorption. The enhancement corresponding to the red band edge is much lower, while at the spectral range corresponding to the band gap, the enhancement factor takes values below one.

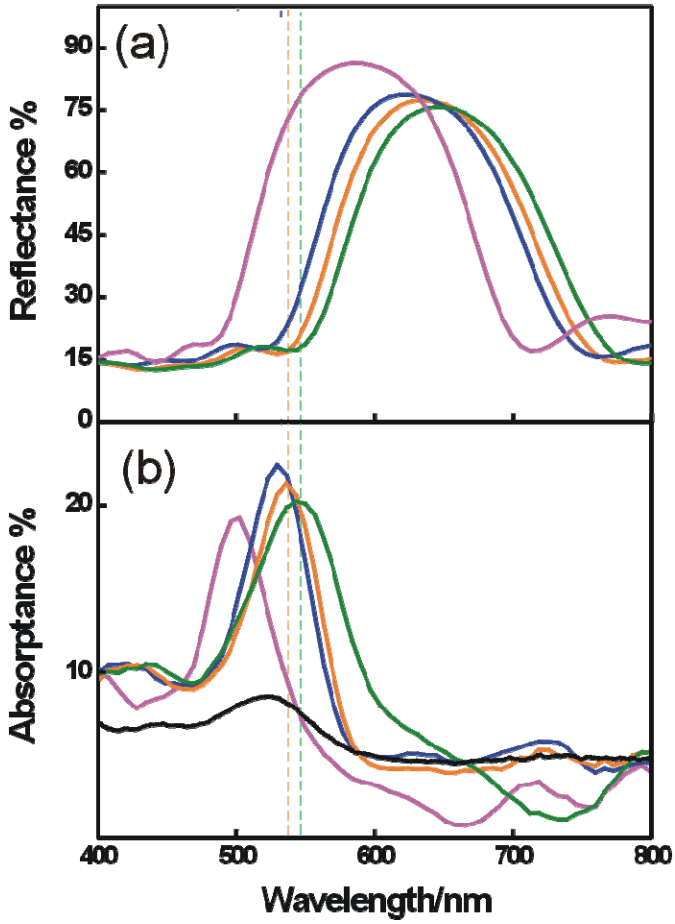

Figure 12. *(a) Reflectance spectra of a 1DPC in which one of the constituent silica layers has been substituted by a 100 nm thick layer of Au@SiO_2 nanoparticles before (magenta curve) and after being infiltrated with isopropanol (n=1.377, blue curve), toluene (n=1.497, orange curve) and benzene (n=1.525, green curve). The "blue-edge" enhancement effect on the absorptance spectra can be readily seen.*

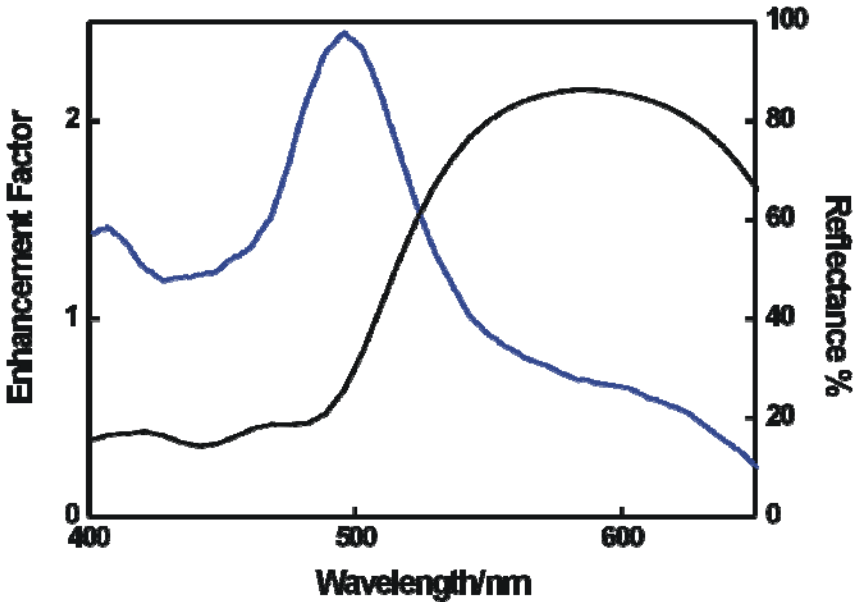

***Figure 13**. (a) Total reflectance (black curve) of 1DPC in which one silica layer has been substituted by a Au@SiO_2 nanoparticle layer and the enhancement factor (blue line) extracted from the absorptances of the multilayer containing gold nanoparticles and the reference.*

In this chapter one of the main objectives of this research work has been reached: the modification of the wide optical absorption typical of metallic nanoparticles by their integration in porous 1DPCs. In the next chapter the same structure hosts another kind of nanoparticle: nanophosphors doped with rare earths. These particles are optically characterized by presenting narrow emission bands in the visible ranges. These bands can be tuned exclusively due to their photonic environment.

4. Conclusions.

The interplay between localized surface plasmons in gold nanoparticles and the field confinement effects occurring in 1DPCs containing them can be used to achieve spectrally selective enhancement of the optical absorption of the ensemble by matching the absorption band with both the higher energy band edge and with the resonance of an optical cavity embedded in the structure.

The porous nature of the final hybrid material provides a means to precisely control the absorption spectrum of the multilayer as a function of the refractive index of guest compounds, providing the structure with potentially relevant sensing properties.

5. References.

[1] E. Ozbay, "Plasmonics: Merging photonics and electronics at nanoscale dimensions", *Science, 311,* **2006**, 189.

[2] P.V. Kamat, "Photophysical, photochemical and photocatalytic aspects of metal nanoparticles" *J. Phys. Chem. B, 106,* **2002,** 7729.

[3] R.M. Crooks, M. Zhao, L. Sun, V. Chechik, L.K. Yeung, "Dendrimer-encapsulated metal nanoparticles: Synthesis, characterization, and applications to catalysis", *Acc. Chem. Res, 34,* **2001**, 181.

[4] H.A. Atwater, A. Polman. "Plasmonics for improved photovoltaic devices" *Nat. Mater,9,* **2010**, 124.

[5] D.J. Maxwell, J.R. Taylor, S. Nie. "Self-assembled nanoparticle probes for recognition and detection of biomolecules", *J. Am. Chem. Soc, 124,* **2002**, 9606.

[6] E. Hutter, J.H. Fendler. "Exploitation of localized surface plasmon resonance", *Adv. Mater, 16,* **2004**, 1685.

[7] S. Link, M.A. El-Sayed. "Spectral properties and relaxation dynamics of surface plasmon electronic oscillations in gold and silver nanodots and nanorods" *J. Phys. Chem. B* **1999,** *103,* 8410

[8] K.L. Kelly, E. Coronado, L.L. Zhao, G.C. Schatz, "The optical properties of metal nanoparticles: The influence of size, shape, and dielectric environment " *J. Phys. Chem. B* **2003**, *107,* 668.

[9] K.A. Willets, R.P. Van Duyne. "Localized surface plasmon resonance spectroscopy and sensing "*Ann. Rev. Phys. Chem.* **2007**, *58,* 267.

[10] L.M. Liz-Marzán, P. Mulvaney. "The assembly of coated nanocrystal" *J. Phys. Chem. B* **2003,** *107,* 7312.

[11] F. García-Santamaría, V. Salgueirino-Maceira, C. López, L.M. Liz-Marzán, "Synthetic opals based on silica-coated gold nanoparticles" *Langmuir* **2002**, *18,* 4519.

[12] D.Y. Wang, V. Salgueiriño-Maceira, L.M. Liz-Marzán, F. Caruso. "Gold-silica inverse opals by colloidal crystal templating "*Adv. Mater.* **2002**, *14,* 908.

[13] D.Y. Wang, J. Li, C.T. Chan, V. Salgueiriño-Maceira, L.M. Liz-Marzán, S. Romanov, F. Caruso. "Optical properties of nanoparticle-based metallodielectric inverse opals" *Small* **2005**, *1,* 122.

[14] J. Wang, S. Ahl, Q. Li, M. Kreiter, T. Neumann, K. Burkert, W. Knoll, U. Jonas. "Structural and optical characterization of 3D binary colloidal crystal and inverse opal films prepared by direct co-deposition". *J. Mater. Chem, 18,* **2008**, 981.

[15] D. Yu, M.C. George, P.V. Braun. "Holographically Defined Nanoparticle Placement in 3D Colloidal Crystals" *J. Amer. Chem. Soc, 132,* **2010**, 9958.

[16] S. Shukla, A. Baev, H. Jee, R. Hu, R. Burzynski, Y.K. Yoon, P.N. Prasad. "Large-Area, Near-Infrared (IR) Photonic Crystals with Colloidal Gold Nanoparticles Embedding", *ACS Appl. Mater. Inter, 4,* **2010**, 1242.

[17] M. Barth, S. Schietinger, S. Fischer, J. Becker, N. Nuesse, T. Aichele, B. Loechel, C. Soennichsen, O. Benson. "Nanoassembled Plasmonic-Photonic Hybrid Cavity for Tailored Light-Matter Coupling" *Nano Lett, 10,* **2010**, 891.

[18] E. Lidorikis, S. Egusa, and J.D. Joannopoulos. "Effective medium properties and photonic crystal superstructures of metallic nanoparticle arrays" *J. Appl. Phys, 101,* **2007**, 054304.

[19] O. Sánchez-Sobrado, G.Lozano, M.E.Calvo, A.Sánchez-Iglesias, L.M.Liz-Marzán, H.Míguez. "Interplay of resonant cavity modes with localized surface plasmons: optical absorption properties of Bragg stacks integrating gold nanoparticles" *Adv. Mater, 23,* **2011**, 2108.

[20] L.M. Liz-Marzán, M. Giersig, P. Mulvaney. "Synthesis of nanosized gold-silica core-shell particles"*Langmuir, 12,* **1996**, 4329.

[21] J.M. Bendickson, J. P. Dowling, M. Scalora. "Analytic expressions for the electromagnetic mode density in finite, one-dimensional, photonic band-gap structures"*Phys. Rev. E, 53,* **1996,** 4107.

[22] N. A. R. Bhat, J. E. Sipe. "Optical pulse propagation in nonlinear photonic crystals"*Phys. Rev. E, 64,* **2001**, 056604.

[23] G. Lozano, S. Colodrero, O. Caulier, M. E. Calvo, H. Míguez. "Theoretical Analysis of the Performance of One-Dimensional Photonic Crystal-Based Dye-Sensitized Solar Cells"*J. Phys. Chem. C, 114,* **2010**, 3681.

[24] T. Ung, L. M. Liz-Marzán, P. Mulvaney. "Optical properties of thin films of Au@SiO2 particles" *J. Phys. Chem. B, 105,* **2001**, 3441.

[25] S. Colodrero, M. Ocaña, H. Miguez. "Nanoparticle base one dimensional photonic crystals". *Langmuir,24*, **2008**, 4430.

Chapter VI

Control of the photoluminescence of nanophosphors integrated in one dimensional photonic crystals

1. Introduction.

Luminescent nanoparticles[1,2] present a wide range of applications in several fields such as light emitting diodes,[3] sensing,[4] or bio labelling.[5,6,7] The spectral position and the width of emission bands can be tailored to match any visible or near infrared ranges by varying the composition and the size of nanoparticles.[8] Actually, from the spectral point of view, the available emission patterns of nanoparticles range from the narrow, atom-like ones of rare earth based nanophosphors[9,10] to the white light emission of certain semiconductor quantum dots.[11]

As in the case of the optical absorption of metallic nanoparticles, one way to control the emission of luminescent nanomaterials is to integrate them in optical resonators whose modes coincide with a range of frequencies emitted by the material.[12] By doing so, it is possible in principle to mould the emission spectrum, enhancing or suppressing luminescence in the desired spectral ranges.[13] However, resonators operating in the visible and near infrared regions present structural features of sizes on the order of the few hundreds of nanometers. This has in turn

restricted the size of particles to be included in such cavities and, consequently, the range of luminescent particles whose emission can be tuned. While there exist several reports on the modification of luminescence from semiconductor quantum dots (with sizes typically below 10 nm) incorporated in different type of photonic nanostructures,[14,15] hardly any example can be found on the integration of other optically active nanoparticles of arbitrary shape and composition in such matrices. In particular, as far as we know, there are only two precedents of infiltration of rare earth based nanophosphors in a three dimensional photonic crystals.[16,17]

In the work presented in this chapter, rare earths based nanophosphors of complex shape and of size on the order of a 100 nm are embedded in nanoparticle optical resonant cavities built up in one dimensional photonic crystals as those studied in section 1.c of Chapter III. Optical quality is preserved due to the ability of the embedding nanoparticles to adapt to any arbitrary shape of the guest nanomaterial. The photon modes of these cavities, the corresponding to the blue band gap edge and the defect resonance, can be precisely controlled from the fabrication process, allowing for precise tailoring of the photoemission of the nanophosphors. It is demonstrated that their luminescence can be selectively enhanced or suppressed in tuneable wavelength ranges. Again, the porous character of the nanoparticle based building blocks of these optical cavities can be functionalized as sensors hosting different liquid and gas compounds. Totally different emission spectra from the same nanophosphors are obtained by the environmentally induced changes of the photonic modes of the cavity. Also, an experimental study of the dependence of the intensity of photoluminescence bands on the angle of collection is performed. Most results presented in this chapter are reported in references 18 and19.

2. Preparation and structure of nanoparticle based optical cavities.

Figure 1 pictures a model of the proposed hierarchical nanostructure. Two optical resonators of ten and six unit cells were constructed by sandwiching a layer of rhombic $EuYF_3$ nanoparticles between two multilayers made of alternate coatings of spherical SiO_2 particles and smaller TiO_2 nanocrystals of arbitrary shape. The structure of the optical cavity is shown in detailed in the amplified scheme drawn on the right, in which its different parts can be readily identified. The multilayers were built by spin coating as described in Chapter II. The synthesis of SiO_2, TiO_2, and $EuYF_3$ nanoparticles are described in the Appendix and diluted in methanol to 2 and 4% and in ethylenglycol to 1.5% wt respectively. The final speed of the spin coating process was chosen between nominal values of 2000 and 8000 revolutions per minute (rpm) and accelerations were selected between 1950 and 13650 rpm s^{-1}. In order to

quantify the magnitude of the modifications of the photoemission properties caused by the photonic structure, a reference sample was prepared consisting of just a layer of nanophosphors sandwiched between two SiO_2 nanoparticle layers, i.e., the exact same replica of the intermediate layer that behaves as an optical cavity when surrounded by the Bragg mirrors. In all cases, an intermediate annealing treatment of 450ºC was necessary to keep the stability of the structures.

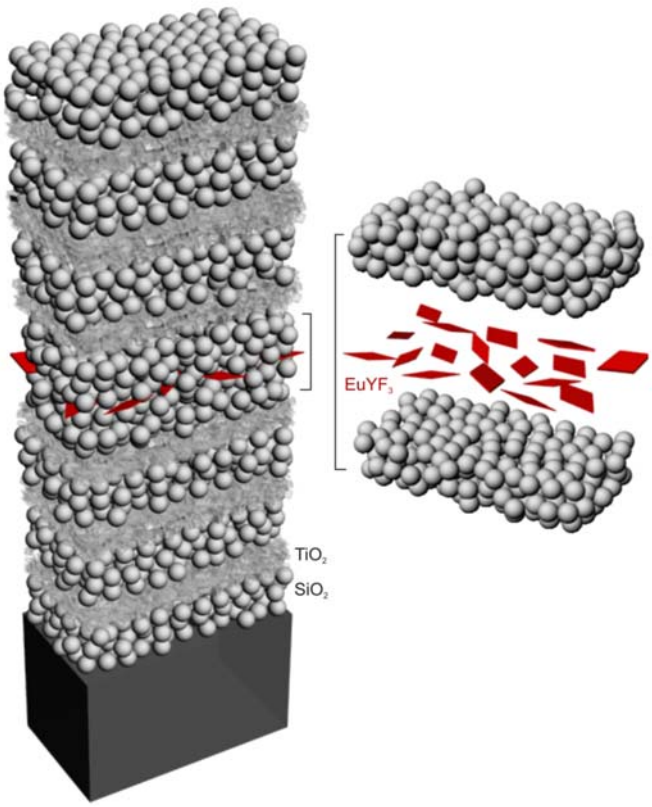

Figure 1. *Model of the proposed nanoparticle based optical resonator. Spherical beads represent SiO_2 nanocolloids, smaller ones of irregular shape are TiO_2 nanocrystals and red rhombic particles are the embedded nanophosphors. On the left, the different components of the optical cavity are amplified and separated for the sake of clarity.*

Images of the actual intermediate and final structures are shown in Figure 2, in which pictures attained by FESEM (Hitachi 5200 operating at 5kV and without using any conducting coating) are displayed. Figure 2(a) and 2(b) show low and high

magnification top views, respectively, of the surface of the silica nanoparticle layer deposited on top of the first photonic crystal, after the deposition of the rhombic lanthanide nanoparticles. Their number density on such surface is uniform at the few microns length scale that is herein optically tested. Figures 2(c) and 2(d) show cross sections of the final structure, i.e., after the second half of the optical cavity and the second photonic crystal have been built up and thermally annealed. It is clear from this images that total thickness of the optical cavity is primarily determined by the thickness of the SiO_2 nanoparticles surrounding the thin layer of $EuYF_3$ nanoparticles. Also, they demonstrate that, due to the ability of the silica nanoparticles to form a uniform layer even on rough surfaces, the presence of the nanophosphors do not alter the structural and hence optical quality of the ensemble.

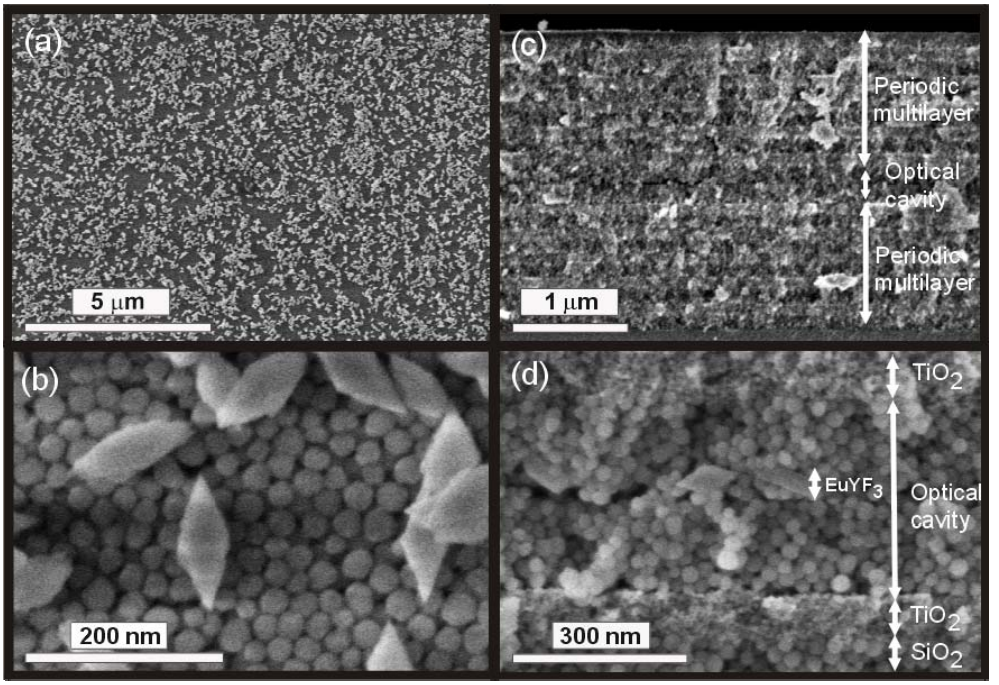

Figure 2. *FESEM images showing a (a) low and (b) high magnification top views of a layer of rhombic shape $EuYF_3$ nanoparticles deposited onto a SiO_2 and TiO_2 nanoparticle multilayer. Spherical particles are SiO_2 nanocolloids. Picture displayed in (c) shows the cross section of a periodic multilayer made of 20 alternated layers (10 unit cells) made of SiO_2 and TiO_2 nanoparticles containing an optical cavity in the middle. The structure of the optical cavity, made of two silica layers sandwiching the nanophosphors, is shown in detail in (d).*

3. Tailoring the emission bands.

3.a Enhancement and suppression of photoluminescence bands.

Photoluminescence and reflectance spectra were obtained using a LabRam spectrophotometer attached to a microscope operating in reflection mode with a 10X objective with 0.1 of numerical aperture (light cone angle ±5.7º). Emission was measured using a λ=532 nm line of a diode pumped doubled-frequency Nd-YAG solid state laser as excitation source. The laser beam impinged on the sample along the direction perpendicular to the layers and luminescence was collected with the same objective employed to illuminate the sample.

The photoemission spectrum of the layer of nanophosphors employed as reference is shown in Figure 3(a). The emission bands arising from the $^5D_0 \rightarrow {}^7F_J$ transitions characteristic of Eu^{3+} can be clearly identified and are indicated in the figure.[20] Aiming at creating a photonic environment capable of controllably modifying this emission, each one of the multilayers surrounding the optical cavity is designed to behave as a dielectric mirror in a wide wavelength range that includes the spectral positions at which the nanophosphor emission takes place. Inclusion of a middle SiO_2 layer, into which the nanophosphors have been integrated as shown in Figures 1 and 2, breaks the translational symmetry of the lattice and gives rise to a resonant mode, characteristic of an optical cavity. Such mode is an allowed state in the forbidden photonic band gap, and can then be readily identified as a dip in the reflectance spectrum of the structure. These can be seen in the reflectance spectra shown in Figures 3(b) and 3(c) (thin black solid lines), taken from samples in which the nanoparticle Bragg mirrors used to surround the optical cavity are three and five unit cell thick, respectively. In both examples, the thickness of the middle SiO_2 layer was chosen so that the resonance matches the nanophosphor emission line observed at λ=708 nm. The corresponding photoemission spectra measured from the layer of sandwiched nanophosphors is plotted in Figures 3(b) and 3(c) as red thick solid lines. Emission peaks at λ=610 nm and λ=628 nm are first partially, see Figure 3(b), and then totally, see Figure 3(c), suppressed, while the originally secondary luminescence maxima at λ=708 nm is gradually enhanced as the thickness of the Bragg mirrors increases until it reaches six times its original value.

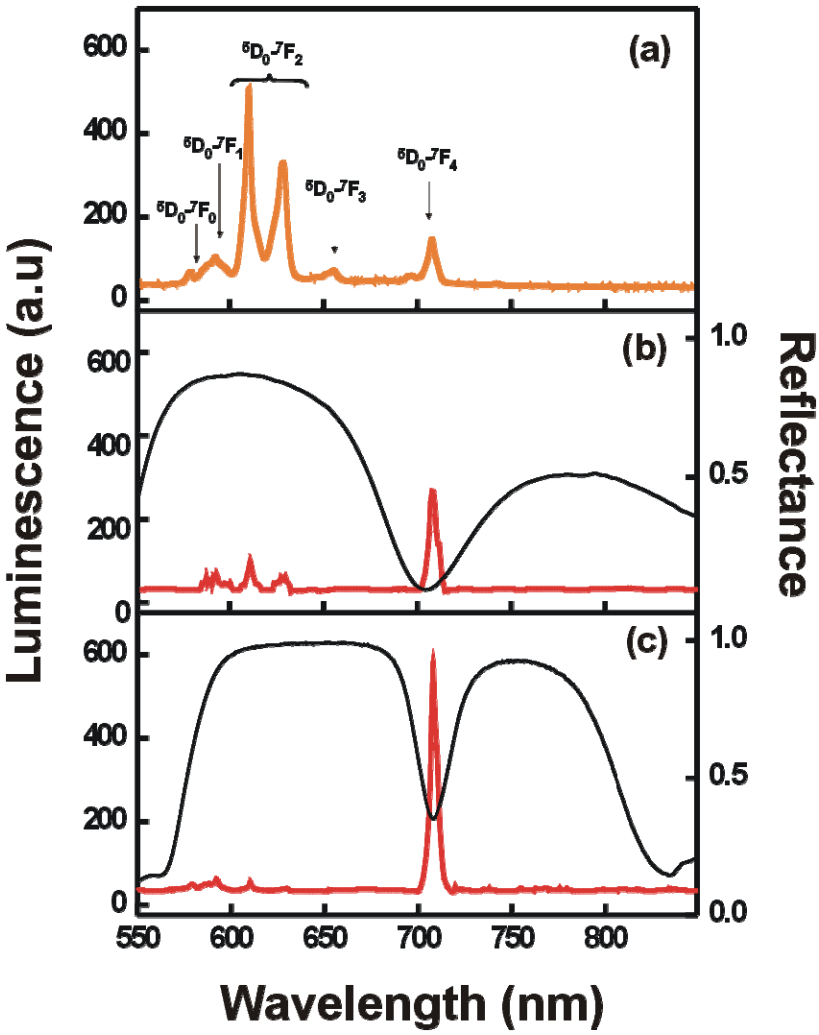

Figure 3. *(a) Luminescence spectrum obtained from the reference sample, consisting of a nanophosphor layer sandwiched between two SiO_2 layers deposited on zero-fluorescence glass. Luminescence (thick red line) and reflectance (thin black line) spectra obtained from nanophosphor containing optical resonators built using Bragg mirrors made of (b) 6 and (c) 10 unit cells.*

The amplification effect of the cavity can be related to its quality factor Q, defined as the quotient between the spectral position and the width of the resonant mode, $\omega_R/\Delta\omega_R$. Its value is determined by the photonic strength of the periodic structure surrounding the cavity, which depends, in a first approximation, on the refractive index contrast existing between the layers (n_{TiO2}/n_{SiO2}=1.74/1.35=1.29), the filling fraction (ff_{SiO2}=55%, ff_{TiO2}=45%), and on the number of unit cells present in the mirrors. Experimental Q factors can be estimated from the position and full width at half maximum of the dip associated to the resonance detected in the reflectance spectra of Figure 3(b) and 3(c). From these data, a value of Q≈8 is estimated for optical resonators built using three unit cells Bragg mirrors, while for those that incorporate five unit cell mirrors Q≈30, much larger than what has been reported so far for optical cavities built within colloidal particle base materials.[21] Although these Q factors are low when compared to optical cavities created within semiconductor Bragg stacks, the effect of these nanoparticle based mirrors is strong enough as to suppress or significantly amplify the luminescence of embedded particles at selected spectral ranges. Although not easily appreciable in the spectra, the shape of the luminescence peaks exiting the photonic nanostructure is also affected by the Q factor of the cavity. An analysis of the ratio between the position and full width at half maximum of the line emitted at λ=708 nm ($\omega_L/\Delta\omega_L$) reveals that this quotient rises from $\omega_L/\Delta\omega_L$=125 in the reference, to $\omega_L/\Delta\omega_L$=140 for the Q≈8 cavity and to $\omega_L/\Delta\omega_L$=170 for the Q≈30 one. So, as expected, not only the emission peak intensity increases, but its width narrows as the Q factor increases.

3.b Modification of the relative intensities between photoluminescence bands.

The spectral position of a resonant mode corresponding to a photonic structure, in which the translational symmetry of the lattice is broken by a planar defect, can be controlled through the thickness of this defect.[21] Three reflectance spectra are plotted (black lines) in Figure 4(a), 4(b) and 4(c), corresponding to resonators built using two Bragg mirrors made of three unit cells, in which the thickness of the SiO_2 middle layer is gradually increased. Thus, as the dip red-shifts, the photoemission bands matched by the resonance can be finely tailored. The luminescence spectra of these multilayers are presented as blue lines in Figure 4. For each position of the resonant mode the shape of the photoemission changes, that is, the relative intensities between the peaks of the doublet corresponding to the transition $^5D_0 \rightarrow {}^7F_J$. For a better understanding of this effect, in Figure 5 the ratio of the intensities of bands placed at λ_M=610 nm, I_M, and λ_m=628 nm, I_m, is plotted versus the position of the defect resonance λ_d relative to the position of the band placed at λ_m=628 nm. As expected, the quotient is maximum when λ_d is further from λ_m. This is due to two effects: the band at 610 nm matches the resonance and the band

at 628 nm is spectrally placed at the forbidden band gap frequencies. Then, as λ_d red-shifts, I_M/I_m decreases until a minimum value is reached when the resonance matches the band at 628 nm. From the spectrum plotted in Figure 3(a), a value I_M/I_m=1.5 is extracted for the photoluminescence of a reference layer, whereas this ratio can take a value of 10 by integrating the nanophosphors layer in a nanoparticle 1DPC.

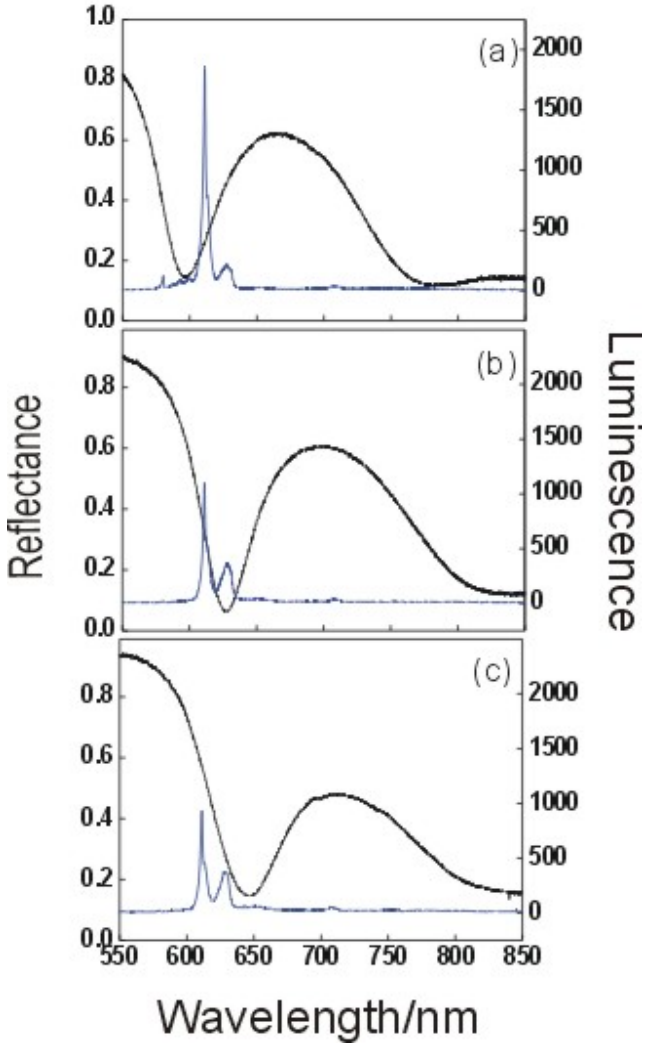

Figure 4. *Reflectance (black lines) and luminescence (blue lines) corresponding to resonators built using two Bragg mirrors made of three unit cells and with different thickness of the middle SiO_2 layer.*

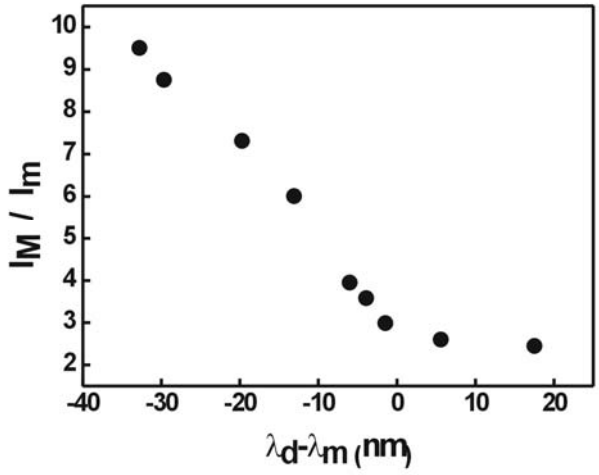

Figure 5. *The ratio of the intensities of bands at* λ_M=610 nm *and* λ_m=628 nm *vs the position of the resonance* λ_d *relative to the position of the band at 628 nm.*

4. Response to environmental changes.

4.a Sensing liquids.

As studied Chapter III, the porous nature of the multilayer renders the photonic structure responsive to variations in the environment. The gradual increase of the ambient vapor pressure gives rise to condensation within the mesopores, thus changing the refractive index of the layers and consequently the reflectance of the Bragg stacks.[22] These structures present a different color depending on the refractive index of the liquid they are soaked in, as seen in the previous chapter. It should be noted that, as opposed to other standard luminescent species such as organic dyes or quantum dots, the rare earth based nanophosphors used in this work do not change their emission properties as a result of their interaction with fluid or gases, since the active ions are embedded in a protective yttrium fluoride matrix. This feature is particularly important to prevent unwanted variations of the luminescence that are not related to structural changes, which are the subject of our study. Another advantage of these nanophosphors is found in their ease of processing. As it is herein proven, these nanocrystals do not lose their luminescent properties when heated up to 450ºC, which is needed to mechanically stabilize the optical resonators that embed them. Nor organic dyes neither quantum dots can be heated up to such temperatures without

being removed or degraded. These are actually the two main reasons supporting the use of nanophosphors to build optically active, environmentally responsive, optical resonators.

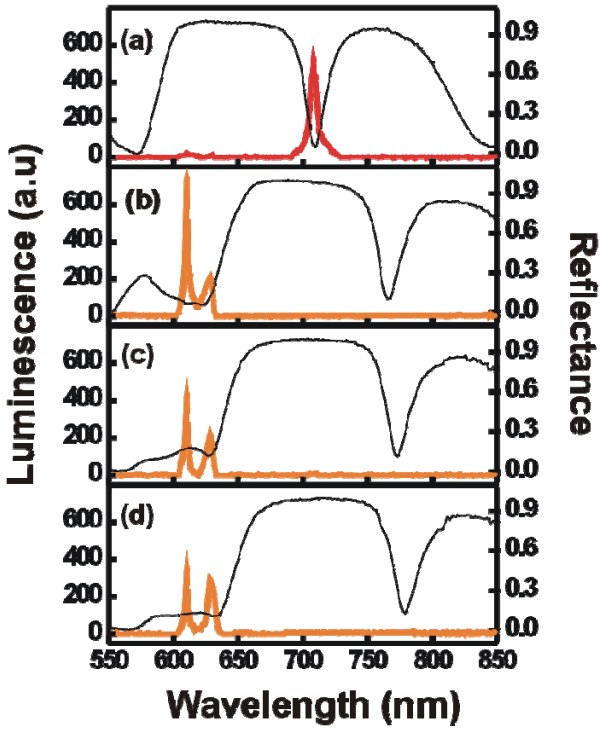

***Figure 6**. Luminescence (color lines) and reflectance (black lines) spectra obtained from a nanophosphor containing optical resonator built using two Bragg mirrors made of 5 unit cells (a) before and after being infiltrated with (b) methanol, (c) isopropanol, and (d) tetrahydrofurane.*

In the case of the optical cavities herein analyzed, the luminescence spectrum of the nanophosphors is finely modulated by the optical response of the photonic structure. Hence, infiltration of its void volume with a liquid should cause an abrupt and strong modification of the photoluminescence. This concept was proven by measuring the luminescence before and after infiltrating the lattice with a series of liquids of different refractive index, namely, methanol (n=1.33), isopropanol (n=1.38) and tetrahydrofurane (n=1.41). Results are shown in Figure 6. The red-shift

of the cavity mode to λ=762 nm, as seen in the reflectance spectrum of the soaked sample, causes the emission peak at λ=708 nm to be off-resonance. At the same time, the shift of the photonic band gap edges allows now the propagation and detection of the fine bands at λ=610 nm and λ=628 nm. Again, the ratio of intensities of such bands is rather different to that measured from the reference sample, see Figure 6(a). Such ratio is also dependent on the refractive index of the guest liquid, see Figures 6(b), (c), and (d). These effects, although much less significant than for the resonant frequencies of the cavity, are a consequence of the enhancement and suppression of the photoluminescence that occurs at wavelengths close to the photonic band gap edge. In Figure 7 the variation of the position of the resonant mode (λ_R, black solid circles) and the higher energy edge of the Bragg peak ($\lambda_{\Delta E}$, red open circles) are plotted as the refractive index of the embedded liquid is increased. In both cases a linear behavior is observed, which is in good agreement with theoretical predictions.[22] The spectral position of the emission lines of the embedded nanophosphors are also drawn as dashed horizontal lines.

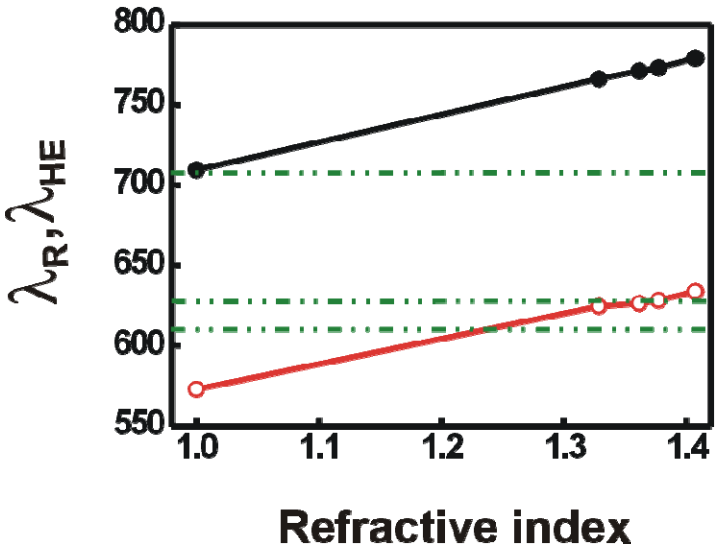

***Figure 7**. Variation of the spectral position of the resonant mode, λ_R, (black solid circles) and the higher energy edge of the Bragg peak, λ_{HE}, (red open circles) with the refractive index of the infiltrated liquid. Data were attained from the curves shown in Figure 4 plus similar ones attained for ethanol (n=1.37). Horizontal dashed lines indicate the spectral position of the three main emission lines of the nanophosphors. Lines connecting data points are just a guide for the eye.*

4.b Sensing gases.

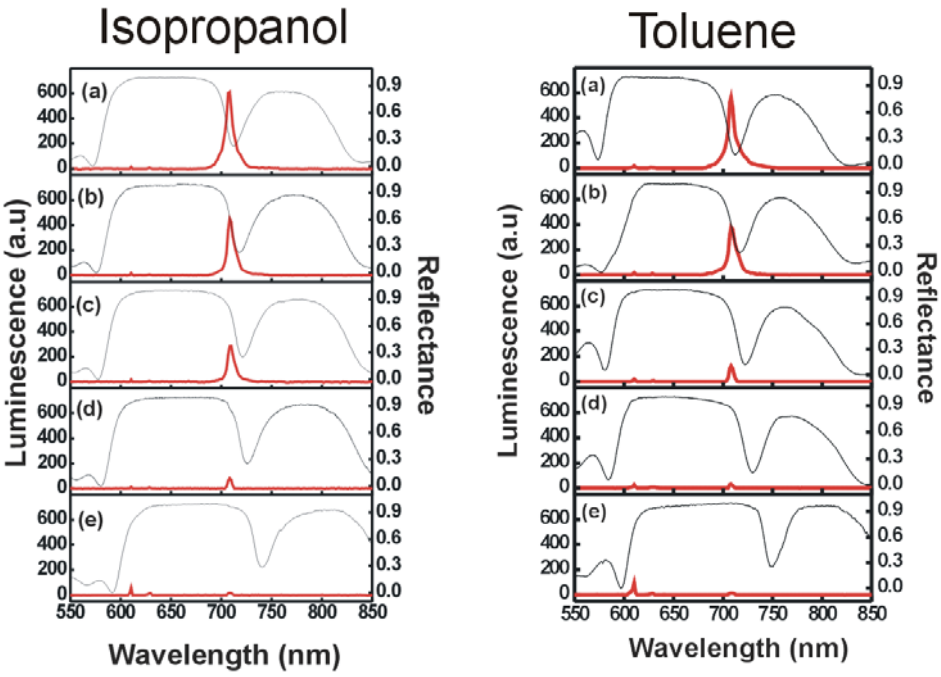

***Figure 8**. Luminescence (red lines) and reflectance (black lines) spectra obtained from a nanophosphor containing optical resonator built using two Bragg mirrors made of 5 unit cells after being exposed to a gradually increasing partial pressure of isopropanol and toluene (left and right sets respectively) vapor, namely (a) P/P_0=0 (b) P/P_0=0.07, (c) P/P_0=0.19, (d) P/P_0=0.66, and (e) P/P_0=1.*

In order to further prove the sensitivity and selectivity of the optical response to variations in the surrounding ambient, the changes induced in both the position of the resonant mode and the luminescence of the embedded nanophosphors by gradual variations of the partial vapor pressure of different compounds is analyzed. In order to do so, the multilayer structures were introduced in a closed chamber in which the partial pressure of a volatile liquid could be varied from P/P_0 =0 to 1 (P_0 being the saturation vapour pressure of the liquid at room temperature). The chamber possesses a flat quartz window through which the reflectance spectra at normal incidence and the luminescence spectra could be measured *in situ*. In Figure 8, a series of reflectance (thin black solid lines) and luminescence (thick red solid lines) spectra attained at different values of P/P_0 of isopropanol and toluene vapor in the chamber are plotted. It can be clearly seen that the intensity of the emission peak at λ=708 nm

slowly diminishes as the matching with the resonant mode decreases due to its gradual red shift. This is a result of the increase of the average refractive index of the multilayer originated in the adsorption and later condensation of gases onto the pore walls. By plotting the evolution of the luminescence peak intensity versus P/P_0 one can obtain an adsorption isotherm whose particular features depend mainly on the refractive index of the adsorbed species. Two of such curves attained vaporizing isopropanol (n=1.38, black solid circles) and toluene (n=1.50, red open circles) in the chamber are plotted in Figure 9. It can be seen that, as expected, for a fixed P/P_0, the adsorption of a higher refractive index liquid gives rise to larger shifts of the position of the resonant mode and thus to more abrupt drops of the emission peak intensity.

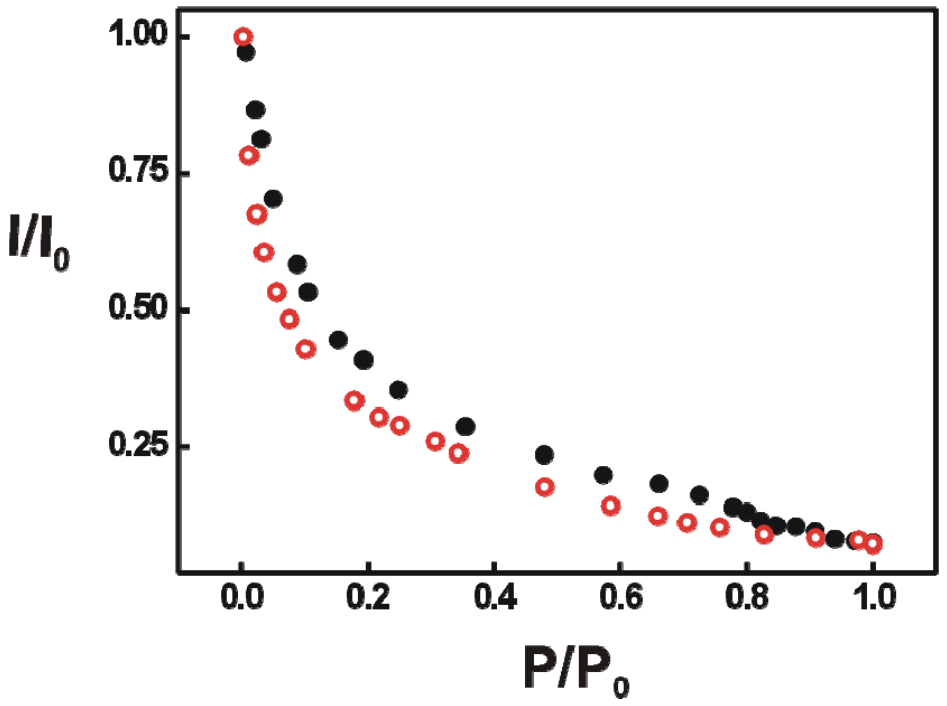

***Figure 9**. Variation of the photoluminescence intensity of the emission line located at λ=708 nm as the partial pressure of isopropanol (black solid circles) and toluene (red open circles) increases in the chamber.*

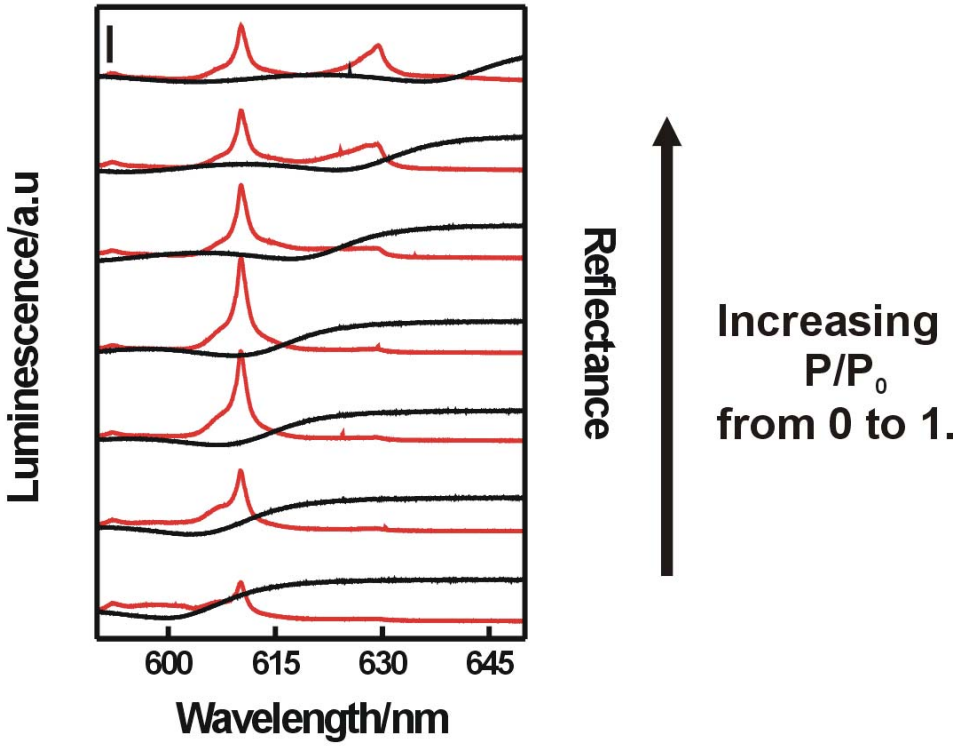

***Figure 10**. Luminescence (red lines) and reflectance (black lines) spectra obtained from a nanophosphors embedded in a nanoparticle 1DPC of 10 unit while being exposed to a gradually increasing partial pressure of isopropanol. The black scale bar represents a reflectance of 1.*

Taking advantage of the red-shift of reflectance spectrum due to the gradual increment of the partial vapor pressure of a gas in the pores of the structure, the photoluminescence bands that match the band gap blue edge (λ=610 nm and λ=628 nm), can be also modulated. In Figure 10, reflectance spectra of the structure, corresponding to different values of partial pressure of isopropanol infiltrated, are plotted as black lines. The partial pressure increases following the direction of the arrow. For the sake of clarity, only the spectral range of the blue band gap border is plotted. The band at 610 nm is enhanced as the reflectance spectrum red-shifts and the blue band gap edge matches this band. For higher values of the partial pressures, the band at 628 nm, initially attenuated by the structure, is enhanced by the matching with the border band. Again, further analysis can be carried out by plotting the relative intensities of bands at 610 and 628 nm versus the partial vapor pressure, as it

can be seen in Figure 11. I_M/I_m increases until the maximum value reached when the blue edge is placed at the same spectral position than the band at 610 nm and then decreases due to two effects, the matching of the band at 610 nm ends and the band gap edge begins to match the band at 628 nm. From the analysis of this graph it can be concluded that the ratio of intensities of the doublet $^5D_0 \rightarrow {}^7F_J$ can be enhanced in a factor of 12 with respect to that corresponding to the reference.

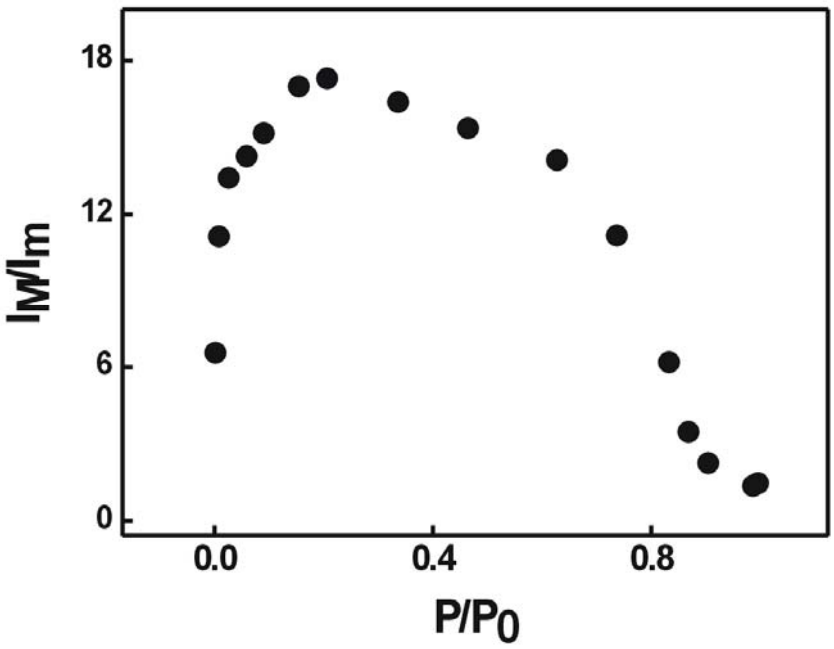

Figure 11. *The ratio of the intensities of bands at 610 nm and 628 nm vs the partial pressure of isopropanol.*

These results prove the sensitivity of the luminescence spectra of the embedded nanophosphors to the degree of matching between the resonant or forbidden modes and the emission lines. Furthermore, the variations observed depend, in a first approximation, on the refractive index of the guest compound, which implies a certain selectivity of the response. This analysis shows the potential of these structures may offer in the field of sensing and detection.

5. Angular emission properties.

In this section, an experimental study is presented about the variation of the intensity of photoluminescence bands of optical resonators containing nanophosphors as the angle of collection is changed. A strong angular dependence of the spectrally selective enhancement achieved with respect to reference samples is observed, which is in turn largely affected by the values of the optical parameters of the resonator. Experimental data are analyzed on the basis of a simple theoretical model proposed by H.Benisty et al.,[24] an excellent qualitative agreement being found for the directional properties of both the extracted intensity and the enhancement of selected emission lines.

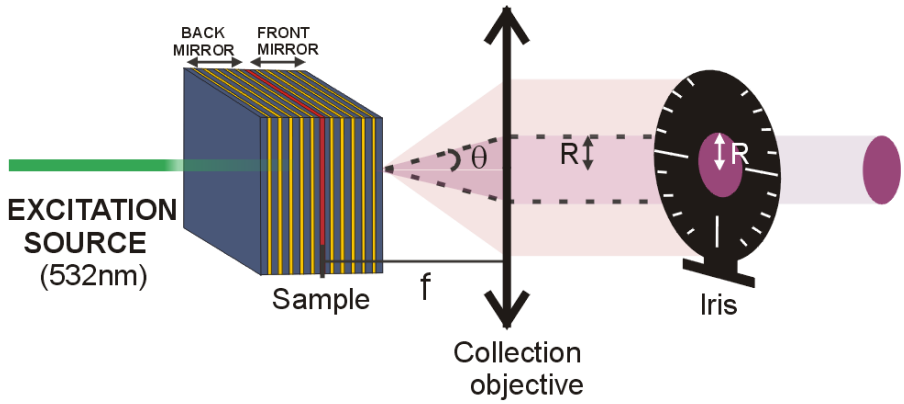

Figure 12. *Experimental set-up employed for the angular characterization of the emission. The source represented is the 532 nm laser and the sample is the resonator made of nanoparticles of SiO_2 (yellow layers) and TiO_2 (blue layers). The red layer represents the nanophosphor layer.*

In order to realize the required measurements, the set up presented in Figure 12 was disposed. A green solid-state laser emitting at λ=532 nm is used as an excitation source. A 30 mW beam is normally incident to the sample surface, focused down by means of a 10 cm-focal length lens. The light coming out of the multilayer structure in transmission mode is collected by an objective with a numerical aperture N.A.=0.6, coupled into a multimode fiber, and spectrally dispersed by a monochromator attached to a charge-coupled device (CCD) detector camera. An iris is placed between the objective and the detector to study the relation between the intensity of the emission bands and the light cones of angular widths comprised between 5.7º and 36.8º. The extraction angle θ is determined through the radio R of

the iris according to tgθ = R/f, where f is the focal of the objective (f=5 mm). The maximum detectable angle is smaller than the critical angle of extraction θ_c~52°, above which cavity modes remain guided, i.e. they do not radiate to air. The transmittance spectra were obtained by the same set up but using a white supercontinuum laser that allows us to measure optical spectra between 400 nm and 800 nm.

Transmittance and photo-emission spectra corresponding to resonators with different cavity modes, namely λ_c = 708 nm and λ_c = 742 nm, are plotted in Figure 13 (left and right panels respectively). The transmittance spectra (red lines) as well as the luminescent emission spectrum of the reference (black lines), are shown in figures 13(a) and 13(e). The peaks observed in the transmittance spectra correspond to the transmitting window opened due to the presence of a resonant mode. In one case, the resonance coincides with the emission band at λ_c= 708 nm (on-resonance), while in the other it does not match any luminescence line (off-resonance). The two sets of Figures 13(b-d) and 13(f-h) display the photoluminescence emitted by the nanophosphors embedded in each type of resonator respectively. For small angles of collection, the luminescent band at λ_B = 708 nm is strongly enhanced when it is on-resonance, see Figure 13(b), and it is almost totally attenuated when it is off-resonance, see Figure 13(f). For the first case, it is observed that the intensity of the band at λ_B = 708 nm increases as the iris is gradually opened, until it reaches a constant value. The angular dispersion of the extracted power stabilizes at a larger angle in the case of the second resonator. The angular response observed is the result of the spectral blue-shift of the cavity resonance as the angle of emission of light increases with respect to the normal to the multilayer surface. Since the spectral position of the resonance moves towards shorter wavelengths as the angle of emission increases, above a certain collection angle θ, it will eventually match the position of an emission band, whose intensity is then amplified. Thus, the cavity favors the extraction of different wavelengths at different solid angles of collection.

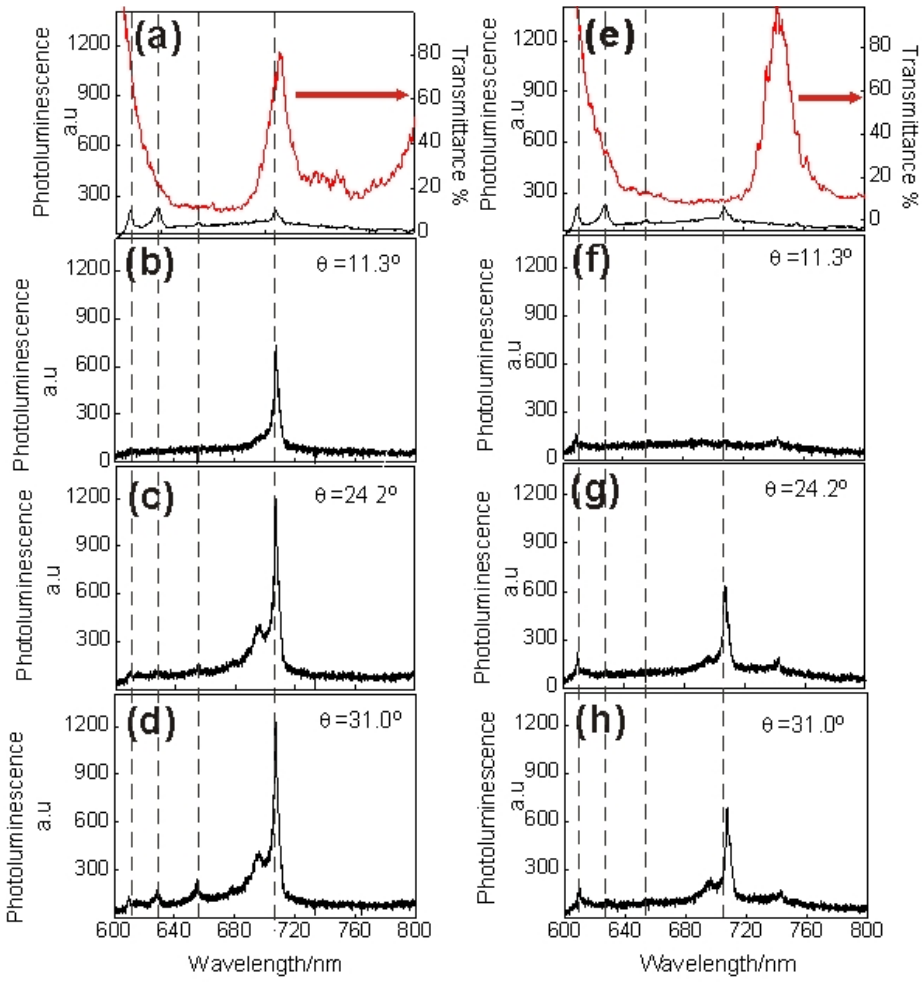

Figure 13. *Transmittance (red lines) and photoluminescence (black lines) spectra of optical resonators whose cavity modes are centered at λ_c = 708 nm, 13(a), and at λ_c = 742 nm, 13(e). Their photoluminescence spectra collected at different angles are plotted in sets of graphs 13(b)-(d) and 13(f)-(h) respectively. Vertical dashed lines indicate the position of the emission bands of the nanophosphors*.

In Figure 14, the experimentally observed evolution of the normalized intensity of the emission bands affected by the cavity resonances is plotted versus collection angle for the two resonators considered, with λ_c = 708 nm (14.a) and λ_c = 742 nm (14.b). In the first case the normalized intensities of bands placed at λ_B = 655 nm (red circles) and λ_B = 708 nm (black circles) are plotted, while in the second case only the results for the band at λ_B = 708 nm are drawn, since only this band matches the

resonant mode at a certain angle among those considered. The angular variation of the intensity of the peaks emitted by the layer of nanophosphors used as reference is plotted for the sake of comparison (black and red crosses for λ_B = 708 nm and λ_B = 655 nm, respectively). The information for the rest of the bands is omitted for clarity.

An analysis of these angular trends was performed by comparing them to the behavior expected for a perfectly uniform resonator made of an emitting dipole placed in the center of a cavity sandwiched between two mirrors. This system was analyzed theoretically by H. Benisty et al.[24] In that study, an expression that relates the power extracted out of the resonator, P_{out}, in a specific direction θ is derived:

$$\mathbf{P_{out}}(\theta) \propto \frac{2\mathbf{T}_1}{\left|1-\mathbf{r}_1\mathbf{r}_2\mathbf{e}^{2i\phi}\right|^2}\frac{1+\mathbf{r}_2^2-2\mathbf{r}_2\cos(2\phi')}{2} \qquad (1)$$

where L is the thickness of the cavity, k the wavenumber of the emitted light inside the cavity at a wavelength λ_B ($k=2\pi n_c/\lambda_B$), r_1 and r_2 are the reflection coefficients of the fields reflected by the front and back mirror respectively, $T_1=1-r_1^2$ is the transmittance of the front mirror, $\phi'=kz\cos\alpha$, z being the distance from the emitter to the back mirror (considered z=L/2), $\phi=kL\cos\alpha$, and α is the internal radiance angle related to the outer angle θ and the refractive indexes of the inner (n_C) and outer (n_{air}) media by Snell's law:

$$n_c \sin\alpha = n_{air}\sin\theta \qquad (2)$$

Thus, the total power escaping from the resonator and collected within a cone of angular width θ is given by:

$$P_{TOT}(\theta) \propto 2\pi\int_0^{\theta} P_{out}(\theta)\cdot\sin\theta\cdot d\theta \qquad (3)$$

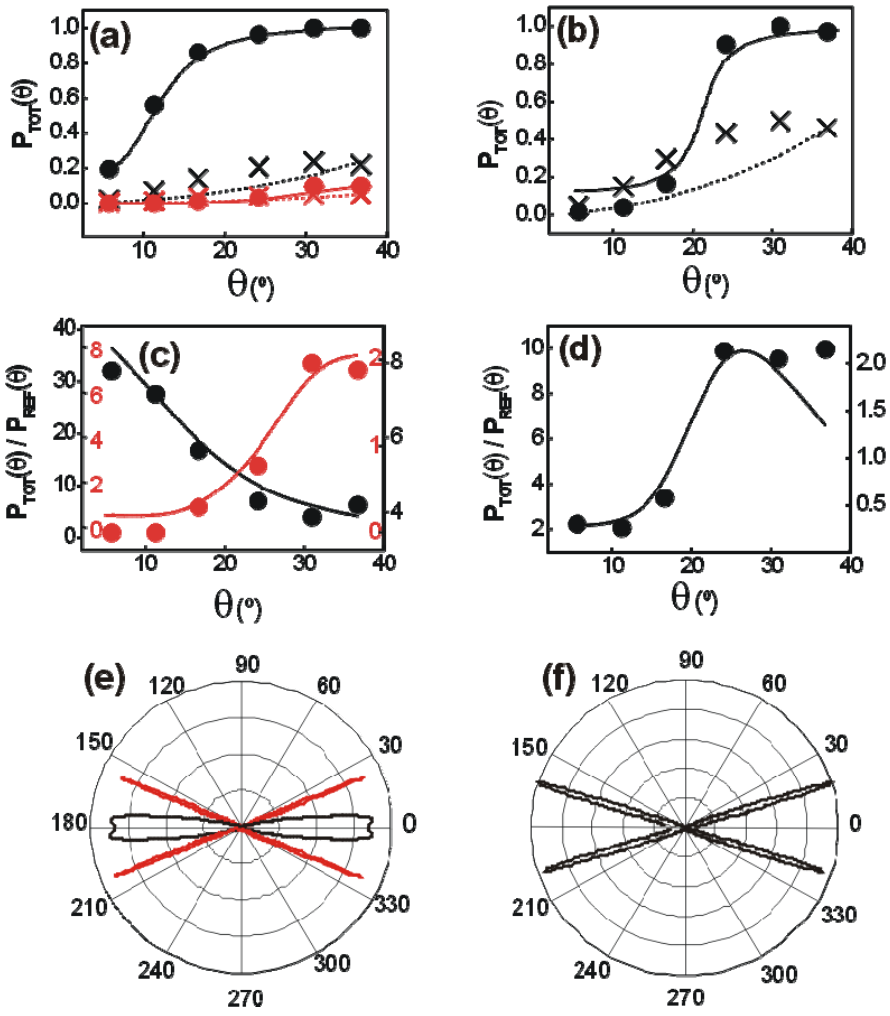

Figure 14. *(a) Extraction intensity in an escape cone of angle θ of emission bands centered at λ_B=708 nm and λ_B=655 nm measured from the resonator whose cavity mode is located at λ_C = 708 nm (black and red dots, respectively) and for reference layers (black and red crosses, respectively). (b) Similar plot of $P_{TOT}(\theta)$ vs. θ from a resonator characterized by λ_C = 742 nm. (c) and (d) show the experimental enhancement factors for these two resonators, respectively, using the same symbol and color code to identify bands. Theoretical curves obtained from equation (3) are plotted as solid lines for both resonators and as dotted lines for references. Finally, (e) and (f) show the corresponding calculated polar emission patterns of bands λ_B=708 nm (black lobes) and λ_B= 655 nm (red lobes).*

The input parameters are the spectral position of the luminescent band, λ_B, and the finesse of the resonance, F, extracted from the measured spectra. The coefficients r_1 and r_2 are estimated from F through the expression:

$$F = \frac{\pi\sqrt{r_1 r_2}}{1 - r_1 r_2} \tag{4}$$

Also in Figures 14(a) and 14(b), the calculated trends for $P_{TOT}(\theta)$ versus θ, obtained from equation (3), are plotted as solid lines for the chosen bands, and as dashed lines for homogeneous media, the latter accounting for measurements on the reference layers. It can be seen that these are in good qualitative agreement with the experimental ones in all cases. Please notice that, since the model does not take into account the intensities of the different emission bands of the nanophosphors of the reference, only qualitative information can be extracted from the evolution of the curve. All calculated curves shown in Figures 14(a) and 14(b) are drawn so that the relation between the intensities of the different bands observed experimentally is preserved.

The monotonic growth of the intensity emitted at λ_B = 708 nm presents a very different angular dependence as a function of the relative position of λ_c and λ_B. In Figures 14(c) and 14(d) the experimental and theoretical angular dependence of the emission enhancement are shown, estimated as the ratio between the photoluminescence power extracted at a certain collection angle θ from the resonator and that collected from the reference samples, $P_{TOT}(\theta)/P_{ref}(\theta)$. It can be seen that the theoretical trends (black and red solid lines in Figures 14(c) and 14(d)) are, again, in excellent qualitative agreement with the measurements (black and red circles in Figures 14(c) and 14(d)). Quantitatively, however, experimental and theoretical data differ by a factor comprised between 4 and 5. The differences observed are very likely due to the deviations of the experimental structure from the simulated theoretical one. The main differences arise from the fluctuations of the thickness of the optical cavity as a result of being made of silica nanoparticles, whose average size is around 30 nm. Also, the emitters are not exactly placed in the middle of the cavity as assumed in the theoretical model, since the thickness of the layer of rare-earth based particles sandwhiched between silica layers represents approximately 10% of the total thickness of the cavity. In addition, both polarization effects and the real multilayer structure of the cavity mirrors have been neglected in the model.

Remarkably, in spite of all these simplifications, the model solutions nicely reproduce the main observed features. Finally, theoretical polar emission patterns are shown in Figures 14(e) and 14(f) to further illustrate the effects herein discussed. Very different angular distribution of energy for the bands emitted at 708 nm and 655 nm are attained as a function of the resonator in which the nanophosphors are integrated.

6. Conclusions

A versatile method to build all-nanoparticle based optical resonators that are able to integrate nanophosphors of arbitrary shape and sizes on the order of a hundred nanometers with has been proved.

These photonic structures allow for a precise tailoring of the light emission of nanomaterials embedded.

They constitute environmentally responsive matrices whose optical parameters can be controllably varied by condensation or infiltration of an external agent, which in turn causes strong changes in the photoemission.

Abrupt angular variations of the enhancement caused by the photonic structure and the extraction power are observed, which are in excellent qualitative agreement with the solutions of a simple theoretical model for light emitted by a dipole inside a perfect microcavity.

7. References

[1] C.B. Murray, D.J. Norris, M.G. Bawendi. " Synthesis and Characterization of Nearly Monodisperse cdE (E=S, SE, TE) Semiconductor Nanocrystallites", *J. Amer. Chem. Soc. 115*, **1993**,8706.

[2] A.P. Alivisatos. "Semiconductor Clusters, Nanocrystals, and Quantum Dots", *Science*, *271*, **1996**, 933.

[3] V.L. Colvin, M.C. Schlamp, A.P. Alivisatos. "Ligth Emitting-Diodes made from Cadmium Selenide Nanocrystals and a Semiconductor Polymer" *Nature, 370*, **1994**, 354.

[4] I.L. Medintz, H.T. Uyeda, E.R. Goldman, H. Mattoussi, *"*Quantum dot bioconjugates for imaging, labelling and sensing*", Nature Mat, 4*, **2005**, 435.

[5] J.K. Jaiswal, H. Mattoussi, J.M. Mauro, S.M. Simon "Long-term multiple color imaging of live cells using quantum dot bioconjugates", *Nature Biotech. 21*, **2003**, 47.

[6] X.H. Gao, W.C.W. Chan, S.M. *J.* Nie, "Quantum-dot nanocrystals for ultrasensitive biological labeling and multicolor optical encoding"*Biomed. Opt. 7*, **2002**, 532.

[7] X.F. Yu, L.D. Chen, M. Li, M.Y Xie, L. Zhou, Y. Li, Q.Q. Wang. "Highly Efficient Fluorescence of NdF_3/SiO_2 Core/Shell Nanoparticles and the Applications for in vivo NIR Detection" *Adv. Mater. 20*, **2008**, 4118.

[8] X. Peng, L. Manna, W. Yang, J. Wickham, E. Scher, A. Kadavanich, A. P. Alivisatos, "Shape control of CdSe nanocrystals", *Nature,404*, **2000**, 59.

[9] J.C. Boyer, L.A Cuccia,, J.A. Capobianco, "Synthesis of colloidal upconverting $NaYF_4$: Er^{3+}/Yb^{3+} and Tm^{3+}/Yb^{3+} monodisperse nanocrystals". *Nano Lett. 7*, **2007**, 847.

[10] J.W. Stouwdam, F.C.J.M. van Veggel. "Near-infrared emission of redispersible Er^{3+}, Nd^{3+}, and Ho^{3+} doped LaF_3 nanoparticles"*Nano Lett. 2*, **2002**, 733.

[11] M.J. Bowers, J.R. McBride, S.J. Rosenthal, "White-light emission from magic-sized cadmium selenide nanocrystals"*J. Amer. Chem. Soc. 127*, **2005**, 15378.

[12] K.J. Vahala, "Optical microcavities". *Nature, 424*, **2003**, 839.

[13] M. Bayer, T.L. Reinecke, F. Weidner, A. Larionov, A. McDonald, A. Forchel, "Inhibition and enhancement of the spontaneous emission of quantum dots in structured microresonators"*Phys. Rev. Lett. 86*, **2001**, 3168.

[14] J. P. Reithmaier, G. Sek1, A. Löffler, C. Hofmann, S. Kuhn, S. Reitzenstein, L.V. Keldysh, V.D. Kulakovskii, T.L. Reinecke, A. Forchel, "Strong coupling in a single quantum dot-semiconductor microcavity system". *Nature 432*, **2004**, 197.

[15] P.Lodahl, A.F. van Driel, I.S. Nikolaev, A.Irman, K. Overgaag, D. Vanmaekelbergh, W.L. Vos. "Controlling the dynamics of spontaneous emission from quantum dots by photonic crystals" *Nature, 430*, **2004**, 654.

[16] M. Aloshyna, S. Sivakumar, M. Venkataramanan, A.G. Brolo, F.C.J.M van Veggel,. "Significant suppression of spontaneous emission in SiO_2 photonic crystals made with Tb^{3+}-doped LaF_3 nanoparticles"*J. Phys. Chem. C 111*, **2007**, 4047.

[17] Z. X. Li, L. L. Li, H. P. Zhou, Q. Yuan, C. Chen, L. D. Sun, C. H. Yan. "Colour modification action of an upconversion photonic crystal", *Chem. Commun*., *43*, **2009**, 6616.

[18] O. Sánchez-Sobrado, M.E Calvo, N. Núñez, M. Ocaña, G. Lozano, H. Míguez, "Environmentally Responsive Nanoparticle based Luminescent Optical Resonators" *Nanoscale, 2*, **2010**, 936.

[19] O. Sánchez-Sobrado, A. M. Yacomotti, M.E. Calvo, O. E. Martínez, M. Ocaña, N.Núñez, J. A. Levenson, H. Míguez. "Angular emission properties of a layer of rare-earth based nanophosphors embedded in one-dimensional photonic crystal coatings". *Appl.Phys.Lett*, **2011**, acepted.

[20] E.W. J. L. Oomen, A. M. A. van Dongen, "Europium (III) in Oxide Glasses-Dependence of the Emission-Spectrum upon Glass composition" *J. Non-Crys. Solids, 111*, **1989**, 205.

[21] R. Pozas, A. Mihi, M. Ocaña, H. Míguez. "Building nanocrystalline planar defects within self-assembled photonic crystals by spin-coating" *Adv. Mate, 18*, **2006**, 1183.

[22] S. Colodrero, M. Ocaña, A. R. González-Elipe, H. Míguez, *Langmuir* **2008***, 24*, 9135.

[24] H.Benisty, H. De Neve, C.Weisbuch. "Impact of planar microcavity effects on light extraction - Part I: Basic concepts and analytical trends", *IEEE Journal of Quantum Electronics. 34*, **1998**, 9.

Appendix

Synthesis of nanoparticles

SiO_2 nanoparticles.

SiO_2 nanocolloids were purchased from Dupont (LUDOX TMA, *Aldrich*). All the suspensions of silica particles used to obtain the different results presented in this thesis have concentrations comprised between 2 and 4.5 % wt. in methanol.

Synthesis of TiO_2 nanoparticles.

TiO_2 nanoparticulated sols were synthesized using a procedure based on the hydrolysis of titanium tetraisopropoxide ($Ti(OCH_2CH_2CH_3)_4$, 97% *Aldrich*, abbrev. TTIP) as it has been described before.[1] TTIP was added to Milli-Q water. The white precipitate was filtered and washed several times with distilled water. The resultant solid was peptized in an oven at 120º C for 3 hours with tetramethylammonium hydroxide (*Fluka*). Finally, the suspension obtained was centrifuged at 14.000 rpm for 10 minutes. All the suspensions of titania particles used to obtain the different results presented in this thesis have concentrations comprised between 3.5 and 5 % wt. in methanol.

Synthesis of silica covered nanoparticles Au@SiO_2.

Au@SiO_2 nanoparticles were provided by the group of Luis Liz-Marzán at the Chemistry Physics Department, University of Vigo.[2] In brief, a silane coupling agent (3-aminopropylmethoxysilane) was used to make the surface of the gold particles vitreophilic. When put into contact with silicate anions at pH close to 8, the silane modified particles were coated by a homogeneous silica shell that allowed transfer to ethanol. The final thickness of the silica shell was controlled by subsequent growth by basic hydrolysis and condensation of tetraethoxysilane in an ethanol/ammonia mixture. The Au@SiO_2 nanoparticles used in the work presented in Chapter V have a core diameter of 13 nm and a 16 nm shell thickness and a concentration between 1.5 and 2 % wt. in methanol, adjusted by centrifugation and redispersion.

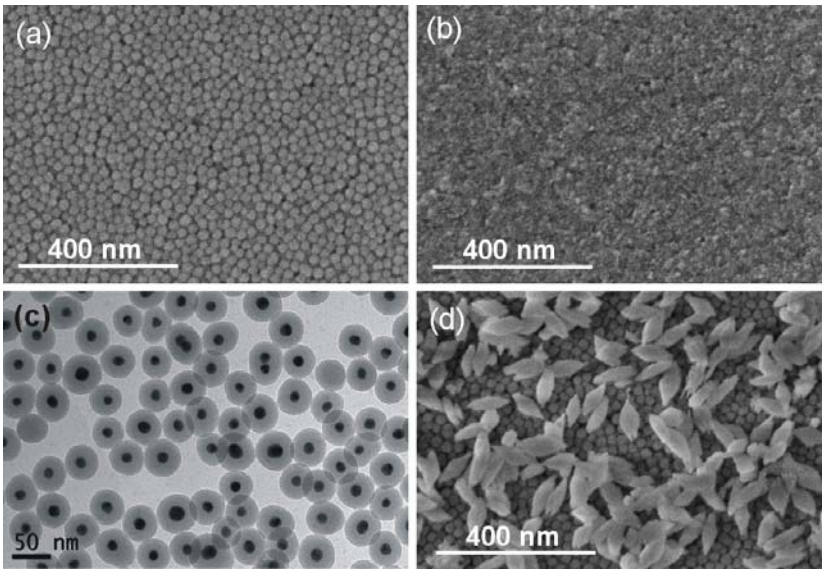

Figure 1. *Scanning electron microscopy images of top views of layers of (a) SiO_2 nanocolloids and (b) TiO_2 nanocrystals. (c) Transmission electron microscopy image of the Au@SiO_2 core-shell particles. (d) SEM image of a top view of a layer of rhombic shape $EuYF_3$ nanoparticles deposited onto a layer of SiO_2 nanoparticles.*

Synthesis of the Eu-doped nanoparticles $EuYF_3$.

Highly uniform aqueous suspensions of red emitting Eu-doped yttrium fluoride (YF_3) nanophophors were synthesised following a ionic liquid base recipe reported by the group of Manuel Ocaña at the Materials Science Institute of Seville and thoroughly described elsewhere.[3] Chemicals used were yttrium (III) acetate ($Y(CH_3COO)_3$ XH_2O, Aldrich, 99.9%) and europium (III) nitrate ($Eu(NO_3)_3 \cdot 5H_2O$, Aldrich, 99.9%), which were selected as lanthanide precursors. 1-Butyl, 2-methylimidazolium tetrafluoroborate, ($C_8H_{15}BF_4N_2$, [BMIM]BF_4, Fluka, > 97%) was used as fluoride source and ethylene glycol (Fluka, <99.5%) as solvent.

The standard procedure for the synthesis of the rare-earth fluoride nanoparticles was as follows. Weighted amounts of the rare-earth precursors were dissolved in ethylene glycol under magnetic stirring, heating the vial at ~100ºC to facilitate the dissolution process, to get a solution 0.02M of YAc_3 and 0.002M of $Eu(NO_3)_3$. The ethylene glycol solutions were cooled down to room temperature after which the required volume of [BMIM]BF_4 to achieve a concentration 6.7M of the

ionic liquid was admixed keeping the magnetic stirring. The final solutions (total volume = 5 cm^3) were then aged for 15 h in tightly closed test tubes using an oven preheated at the selected temperature. After aging, the resulting dispersions were cooled down to room temperature, centrifuged to remove the supernatants and washed, twice with ethanol and once with double distilled water. The suspension used to obtain the results presented in Chapter VI has a concentration of 1.5 % wt. in ethylene glycol.

[1] S.D. Burnside, V. Shklover, C. Barbé, P. Comte, F. Arendse, K.Brooks, M. Grätzel, "Self-organization of TiO_2 nanoparticles in thin films" *Chem. Mater. 10*, **1998**, 2419.

[2] L.M. Liz-Marzán, M. Giersig, P. Mulvaney, "Synthesis of nanosized gold-silica core-shell particles"*Langmuir, 12*, **1996**, 329.

[3] N.O.Nuñez, M. Ocaña. "An ionic liquid based synthesis method for uniform luminescent lanthanide fluoride nanoparticles" *Nanotechnology, 18*, **2007**, 455606.

General conclusions

Studies about two different methodologies, spin and dip coating, used to construct all the samples analyzed in this research work, have been presented. For each technique, optimal experimental conditions to build nanoparticle 1DPCs under strict control of their optical response, as well as structural and optical quality, have been found.

Multifunctional rigid and flexible porous Bragg mirrors have been built presenting spectrally flat reflectance/transmittance over the NIR-Vis-UV spectral range.

The controlled opening or closing of higher order photonic band gaps has been experimentally demonstrated.

A viable synthetic route to infiltrate gallium arsenide within nanoparticle based periodic multilayers has been found to yield a photonic material displaying wider and more intense reflectance peaks in the visible and near infrared regions.

The optical absorption of metallic colloids and the photoluminescence of rare earths doped nanoparticles have been modified by integrating them in porous multilayers. Also, in the latter case, the angular variation of luminescent properties has been analyzed.

The environmental response of the porous structures reported in this thesis have been studied.

Resumen en Español

Emisión y Absorción Óptica de Nanomateriales Integrados en Cristales Fotónicos Unidimensionales

Emisión y Absorción Óptica de Nanomateriales Integrados en Cristales Fotónicos Unidimensionales

1. Introducción.

Un cristal fotónico unidimensional es una estructura que presenta modulación periódica del índice de refracción en una sola de las direcciones del espacio.[1] Cuando incide luz sobre el cristal, ésta se reflejará y transmitirá parcialmente en cada superficie que separa dos medios de distinto índice. Cuando la longitud de onda de esta radiación es del orden del parámetro de red de la estructura, pueden tener lugar fenómenos de interferencia entre los haces reflejados o transmitidos. Estos fenómenos determinarán la propagación o no de determinados rangos de frecuencias a través de la estructura, reflejándose unos y transmitiéndose otros (Figura 1(a)). La interferencia debida a esta periodicidad da lugar a la aparición de una banda fotónica prohibida en el diagrama de bandas de la estructura, que en un material real se traduce en la aparición de un máximo en el espectro de reflectancia especular o pico de Bragg (Figura 1(b)). La presencia de este máximo evidencia precisamente que la propagación de fotones en este rango energético está prohibida. A este tipo de materiales se les llama también reflectores de Bragg o filtros interferenciales. Si este pico está situado en la región visible del espectro electromagnético, el cristal fotónico unidimensional presenta colores brillantes (Figura 1(c)).

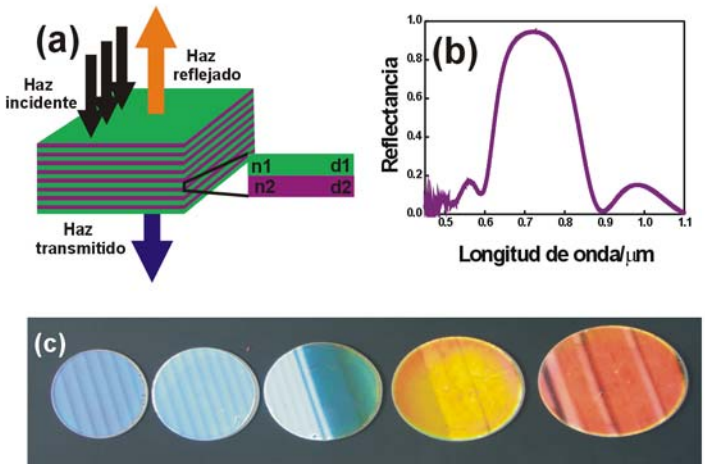

Figura 1. *(a) Esquema de un cristal fotónico unidimensional formado por dos materiales diferentes. El haz de luz incidente es parcialmente reflejado y transmitido por la estructura. (b) Primer orden de difracción típico de un cristal fotónico unidimensional. (c) Fotografía de cristales fotónicos unidimensionales con distinto tamaño de la celda unidad que reflejan diferentes colores.*

La manera más fácil de crear estas estructuras es alternar capas de materiales de distinto índice de refracción. Para conseguir apilados de alta calidad óptica, cada una de las capas debe ser uniforme y de baja rugosidad. Debido al alto contraste entre las constantes dieléctricas del TiO_2 y el SiO_2, estos serán dos buenos materiales para construir este tipo de estructuras. Las técnicas basadas en la deposición húmeda de precursores sol-gel de TiO_2 o SiO_2 sobre sustratos planos, tales como el *dip coating* o el *spin coating,*[2,3] se han empleado con resultados satisfactorios. Son métodos sencillos que permiten depositar diversos tipos de materiales como óxidos, semiconductores, piezoeléctricos o ferroeléctricos en forma de films delgados sobre sustratos hechos a base de polímeros, de metales o de cerámicas, entre otros. Los reflectores de Bragg fabricados mediante la técnica del sol-gel presentan reflectancias muy altas. Al aumentar el contraste entre los índices de refracción de los materiales depositados, será mayor el rango de frecuencias prohibidas reflejadas por el cristal. Se pueden obtener apilamientos de hasta 60 capas de entre 80 y 100 nm de espesor, con reflectividades de hasta el 99%.[3] Los recubrimientos densos depositados mediante este procedimiento poseen una gran estabilidad frente a cambios ambientales.

Para aplicaciones en campos diferentes al de los componentes ópticos pasivos, sería muy interesante poder fabricar este tipo de estructuras multicapas de forma que estas sí presentaran una respuesta óptica clara ante cambios del entorno. La presencia de poros permite condensar diferentes compuestos dentro de la estructura, modificando la respuesta óptica, ya que esta depende de los índices de refracción de las capas y estos, a su vez, de los materiales de los que dichas capas están hechas. El control sobre esta respuesta óptica depende del control sobre la composición y sobre la forma y tamaño de los poros. Mediante el apilamiento alternado de capas de SiO_2 y TiO_2 mesoporosos, se han conseguido otro tipo de estructuras[4,5] con un control estricto de la mesofase, dirigida por un molde orgánico el cual es eliminado al terminar de formarse la estructura.

Otro tipo de reflectores de Bragg porosos han sido desarrollados recientemente con muy buenos resultados en cuanto a calidad óptica y estabilidad mecánica y térmica.[12] Consisten en estructuras multicapa formadas por nanopartículas de SiO_2 y TiO_2. La Figura 2(a) muestra la fotografía de SEM de una de estas estructuras en la cual se aprecia la periodicidad de los dos materiales y como se mantiene la estructura multicapa a lo largo de la muestra. La morfología de las nanopartículas se puede observar en detalle en la fotografía de 2(b), que es una ampliación de 2(a). Los nanocoloides de sílice son esféricos, mientras que los cristales de titania presentan menor tamaño y forma poliédrica. Las capas de nanopartículas están alternadas de modo que la estructura presenta una modulación periódica del índice de refracción de alto contraste. Este tipo de reflector posee una porosidad que permite una fácil difusión de gases y líquidos a través de su estructura, como se ha podido comprobar recientemente.[6] Es precisamente este tipo de estructuras el analizado en el trabajo de investigación realizado y cuyos resultados se exponen en esta tesis. Se parte de los estudios previos realizados por Silvia Colodrero et al.,[30] que fueron llevados a cabo en el grupo de Materiales Ópticos Multifuncionales del ICMSE y que determinaron tanto la microestructura como la dependencia de las propiedades ópticas con los parámetros más relevantes de la misma. La síntesis de los dos tipos de nanopartículas está recogida en el Apéndice.

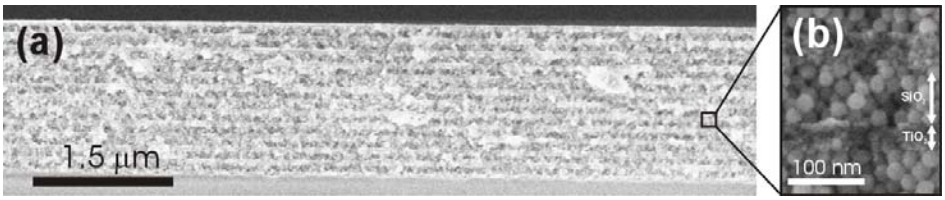

Figura 2. *Fotografías de SEM, obtenidas a menor (a) y mayor (b) aumento, de la sección transversal de un cristal fotónico unidimensional de 12 celdas formado por nanopartículas. En ellas se pueden distinguir los dos tipos distintos de partículas que forman la estructura, SiO_2 (forma esférica) y TiO_2 (forma irregular).*

En el estudio de la respuesta óptica de estos reflectores basados en nanopartículas se deben controlar dos parámetros, el grosor de las capas y su número total. La evolución de las propiedades ópticas con el número de celdas depositadas se muestra en la Figura 3(a). Los máximos de Bragg que se observan en los espectros de reflectancia, asociados a la presencia de un gap fotónico en la dirección perpendicular a las capas son más intensos y estrechos a medida que aumenta el número de celdas del cristal. Ese máximo de reflectancia es la prueba de la calidad óptica que poseen estas estructuras. Por otro lado, el tamaño de la celda unidad que resulta de sumar los correspondientes espesores de las capas de sílice y de titania que la forman determinará, junto al índice promedio de la estructura, la posición espectral del máximo de reflectancia λ_{Bragg} según la expresión 1:

$$\lambda_{Bragg} = 2n_{eff}\Delta \qquad [1]$$

En esta expresión, n_{eff} es el índice de refracción promedio de la multicapa y Δ es el tamaño de la celda unidad, que vienen a su vez dados por las expresiones (2) y (3).

$$n_{eff} = \frac{n_1 d_1 + n_2 d_2}{d_1 + d_2} \qquad [2]$$

$$\Delta = d_1 + d_2 \qquad [3]$$

En donde n_1 y n_2 son, a su vez, los índices de refracción promedio de cada uno de los dos tipos de capa y d_1 y d_2 sus respectivos espesores. El índice promedio de una capa está determinado por los índices de refracción de las partículas que la forman y el factor de llenado de las mismas, según la fórmula de Bruggeman:

$$\frac{n_d^2 - n^2}{n_d^2 + 2n^2} ff_d + \frac{n_a^2 - n^2}{n_a^2 + 2n^2} ff_a = 0 \qquad [4]$$

En dónde n es el índice de refracción promedio de una capa, n_d es el índice de refracción del correspondiente tipo de nanopartículas que la forma, n_a es el índice de refracción del aire contenido en los poros de la estructura y ff_d y ff_a los correspondientes factores de llenado.

Una manera de modificar el parámetro de red de este tipo de estructuras es variando la concentración de nanopartículas en las suspensiones precursoras de SiO_2 y TiO_2, sin modificar los parámetros que afectan al proceso fabricación, que en este caso, es el de de spin coating. Los espectros de reflectancia medidos para multicapas con distinto parámetro de red obtenidas de esta forma se muestran en la Figura 3(b). Esta es una forma de fabricar diferentes cristales fotónicos unidimensionales con reflectancias relativamente altas, en el rango del espectro electromagnético que comprende desde el ultravioleta hasta el infrarrojo cercano.

Uno de los campos más desarrollados en los últimos años en nanotecnología es de la síntesis de nanopartículas que presentan absorción o actividad óptica. Por un lado, en la literatura se pueden encontrar numerosos ejemplos de nanopartículas metálicas que presentan un pico de absorción óptica resonante bien definido en el rango visible que es consecuencia de la excitación del plasmón de superficie típico de estos materiales. Este tipo de partículas encuentran aplicaciones en catálisis[7], sensores[8] u óptica[9] entre otros campos. Normalmente, lo que se busca es controlar la absorción óptica a través del material que las rodea[10] o controlando su forma y su tamaño.[11] Por otro lado, también existen numerosos ejemplos de nanopartículas luminiscentes con aplicaciones en campos como el de los diodos emisores de luz (LEDs),[12] el de los sensores[13] y el etiquetado biológico.[14] Las propiedades luminiscentes de estos materiales también se suelen controlar a través de su forma y tamaño.[15] Las respuestas espectrales de estas nanopartículas van desde picos de

luminiscencia anchos, como en el caso de los puntos cuánticos, QD (del inglés quantum dots),[16] hasta las bandas estrechas de emisión propias de muchos nanofósforos dopados con tierras raras.[17]

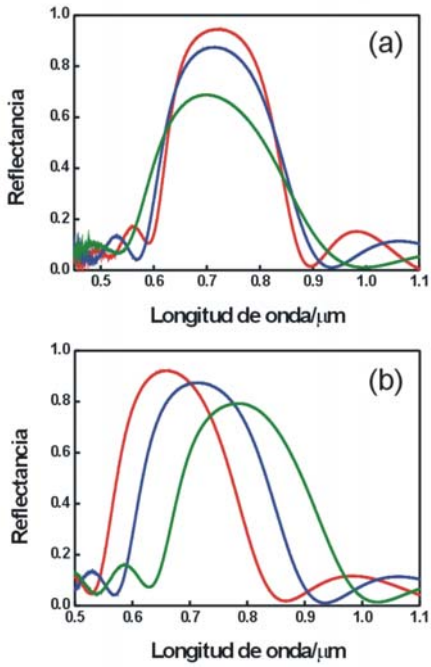

Figura 3. *Evolución del espectro reflectancia de una multicapa de nanopartículas de SiO_2 y TiO_2 con el número de celdas unidad (a) y con el grosor de la misma (b). En la figura 3(a), los espectros rojo, azul y verde se corresponden con cristales fotónicos de 5, 4 y 3 celdas respectivamente. En la figura 3(b) estos colores se corresponden con concentraciones de SiO_2: 4%, 3.5% y 3% en metanol, dejando fija la concentración de TiO_2.*

Con vistas a su implantación como parte de dispositivos optoelectrónicos, resulta importante poder modificar las propiedades ópticas de las nanopartículas controlando únicamente su entorno fotónico, esto es, implantándolas en estructuras periódicas como las estudiadas en esta tesis. En el caso de las nanopartículas metálicas, en la mayoría de los estudios publicados se observan modificaciones de la absorción óptica de las partículas al infiltrarlas en cristales fotónicos tridimensionales, debido a la interacción entre las resonancias fotónica y plasmónica.[18,19] Sin embargo, en ninguno de estos casos se ha observado un aumento de la absorción o modificaciones espectrales significativas, debido probablemente a

que los efectos de localización de la luz son muy débiles en este tipo de estructuras. También se ha estudiado teóricamente cómo se pueden obtener importantes modificaciones de la absorción óptica de arreglos periódicos de nanopartículas metálicas integradas en espejos de Bragg.[20] Sin embargo, la mayoría de la multicapas estudiadas hasta ahora presentan dificultades para albergar las diferentes nanopartículas, de forma y tamaños arbitrarios. En el caso de las partículas luminiscentes, existen varios artículos acerca de la infiltración en diferentes estructuras fotónicas y modificación de la luminiscencia de puntos cuánticos.[21,22] Sin embargo, hasta el trabajo presentado en esta tesis sólo había dos ejemplos de infiltración de nanofósforos dopados con tierras raras en cristales fotónicos tridimensionales.[23,24] En ellos se midió una modificación de las vidas medias de la luminiscencia en las frecuencias del gap fotónico. Sin embargo no se ha podido observar la supresión y aumento controlado y selectivo de las bandas de emisión de estos nanofósforos mediante su infiltración en cavidades ópticas resonantes. El motivo, nuevamente, está en la dificultad de integrar las nanopartículas en estructuras fotónicas que puedan confinar fuertemente la luz, como los espejos de Bragg.

Por lo tanto, la motivación de esta tesis fue construir estructuras fotónicas de alta calidad óptica, es decir, que presenten un fuerte confinamiento de luz en la frecuencia de sus resonancias y capaces de albergar nanopartículas ópticamente activas o que presenten absorción de diversos tamaños y formas, para modificar de manera notable sus propiedades ópticas. Mediante su integración en cristales fotónicos unidimensionales hechos de nanopartículas, se ha podido, por primera vez, amplificar, de manera selectiva y controlada, determinadas bandas de absorción de nanopartículas metálicas y de fotoluminiscencia de nanofósforos dopados con tierras raras. Los objetivos que se pretendieron lograr en el desarrollo de este trabajo de investigación titulado "*Emisión y Absorción Óptica de Nanomateriales Integrados en Cristales Fotónicos Unidimensionales"* son los siguientes:

- Estudio de métodos de fabricación de cristales fotónicos unidimensionales hechos de nanopartículas de SiO_2 y TiO_2. Análisis de la dependencia de las propiedades ópticas y estructurales de dichas multicapas con los parámetros experimentales.

- Caracterización y optimización de las propiedades ópticas de cristales fotónicos unidimensionales porosos en el rango UV-VIS-IR.

- Estudio de la modificación de la absorción óptica de nanopartículas metálicas integradas en cristales fotónicos unidimensionales porosos.

– Análisis de la modificación de la fotoluminiscencia de nanopartículas embebidas en multicapas porosas.

2. Técnicas de fabricación de cristales fotónicos unidimensionales basados en nanopartículas.

A continuación se presentan dos estudios realizados sobre los métodos de fabricación de cristales fotónicos unidimensionales basados en nanopartículas: *Spin Coating* y *Dip Coating*. Se han encontrado los parámetros de fabricación óptimos para construir multicapas con un bajo número de defectos y con la respuesta óptica deseada.

Debido a que el spin coating ha sido el principal método elegido para construir la mayoría de las estructuras estudiadas en esta tesis, se ha llevado a cabo un detallado estudio sobre la influencia ejercida por los parámetros de spin coating, *rampa de aceleración* (*γ)* y *velocidad de rotación (ω)*, sobre las propiedades estructurales y ópticas de multicapas hechas con nanopartículas. También se establece una relación entre las variaciones estructurales observadas y el efecto sobre la formación de cada capa por parte de la evaporación del solvente y la difusión de la suspensión precursora. Los resultados presentados acerca de la influencia del protocolo de spin coating sobre las propiedades de los reflectores de Bragg hechos de nanopartículas están publicados en la referencia 25.

Para estudiar la influencia de las condiciones experimentales sobre la calidad óptica y estructural de las multicapas, se prepararon 42 muestras que fueron caracterizadas ópticamente. Para esto se usó un microscopio óptico acoplado a un espectrofotómetro de transformada de Fourier (Bruker IFS-66 FTIR), operando en modo reflexión, con un objetivo 4X y una apertura numérica de 0.1, lo que supone un cono de luz de ±5.7º. Con este sistema se obtuvieron todos los espectros de reflectancia presentados en esta sección. Los espectros se obtuvieron midiendo desde el centro geométrico de la muestra hasta el borde de la misma, en una línea recta, cada 2 mm.

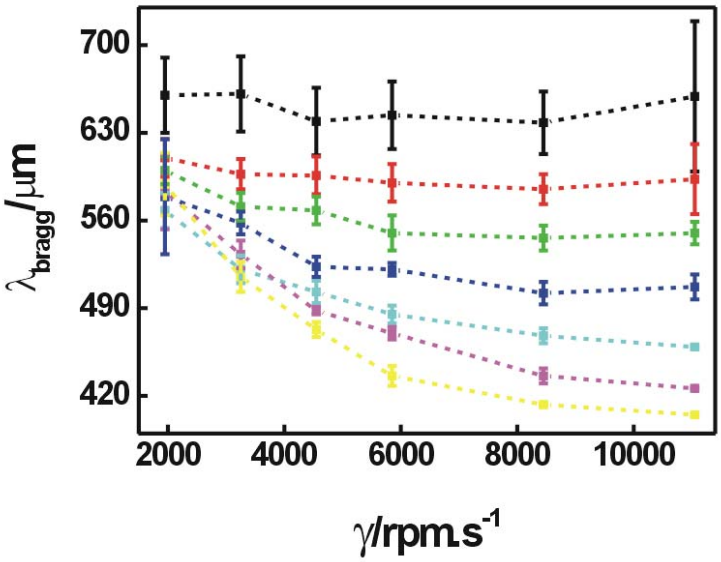

Figura 4. *Posición espectral del pico Bragg en nm frente a la rampa de aceleración γ, para diferentes velocidades finales: 2000 rpm negro, 2500 rpm rojo, 3000 rpm verde, 3500 rpm azul oscuro, 4000 rpm azul claro, 6000 rpm malva y 8000 rpm amarillo.*

En la Figura 4, se representa la posición de los máximos de reflectancia obtenidos, en función de la rampa de aceleración, para cada una de las velocidades finales utilizadas. Para las velocidades finales de rotación se usaron 7 valores comprendidos entre 2000 y 8000 revoluciones por minuto (rpm). Para las rampas de aceleración se escogieron 6 valores comprendidos entre 1950 y 13650 rpm.s^{-1}. Las longitudes de las barras de error corresponden a la desviación estándar obtenida de un análisis estadístico de la posición del pico Bragg en varias regiones de cada muestra. Estas barras se pueden interpretar como una estimación de la uniformidad de la respuesta óptica del cristal. La serie de gráficas representadas en la Figura 4 se pueden usar como una guía para construir cristales fotónicos unidimensionales de muy alta calidad estructural, y seleccionar, de forma muy precisa, la posición de sus máximos de reflectancia. Se puede observar que las multicapas de peor calidad estructural (menos uniformes) se obtienen usando las rampas de aceleración más bajas (γ=1950 rpm.s^{-1} y γ=3250 rpm.s^{-1}), independientemente de la velocidad final de rotación. A medida que aumenta la pendiente de la rampa, lo hace la calidad óptica de la multicapas. En general, para velocidades superiores a 2500 rpm y aceleraciones

mayores que 4550 rpm.s^{-1}, podemos considerar que las muestras poseen una muy buena calidad óptica y estructural.

Los resultados mostrados en la Figura 4 muestran claramente que, si la velocidad final se alcanza rápidamente, bien porque esta sea baja (ω<3000 rpm), bien porque la rampa de aceleración es lo suficientemente alta (γ>3250 rpm.s^{-1}), entonces la posición espectral del pico Bragg, λ_{Bragg} dependerá por completo de ω. Por el contrario, si las rampas de aceleración son bajas, o las velocidades finales de rotación son altas, lo que implica en ambos casos que el tiempo empleado para alcanzar dicha velocidad final será grande, es el parámetro γ el que tiene una gran influencia sobre λ_{Bragg}.

Estos efectos se pueden entender comprendiendo la importancia relativa que tienen, en la formación del film, el proceso de adelgazamiento debido al flujo de la suspensión causada por el giro del sustrato, por un lado, y el de la evaporación del solvente, por otro. Meyerhofer[26] explicó cómo el espesor T de un film, depositado por spin coating, depende de la velocidad final de rotación ω de la forma $T\sim \omega^{-b}$, donde b es una constante conocida como parámetro de spin, con un valor típico de 0.5 para fluidos newtonianos. Los fluidos newtonianos son aquellos en los que la viscosidad se mantiene constante con el tiempo, como en el caso de las suspensiones precursoras de los materiales aquí analizados. Meyehofer introdujo también el concepto de *cross-over point*, referido al momento del proceso de spin coating en el que, al aumentar la viscosidad de la suspensión que está formando el film, la contribución a dicha formación del esparcimiento de la suspensión se empieza a hacer tan pequeña que equivale a la de la evaporación del solvente. La relación $T\sim \omega^{-0.5}$ se obtiene cuando la formación del film se debe fundamentalmente al esparcimiento por flujo inducido por rotación de la suspensión y no a la evaporación del solvente. Recientemente, Birnie ha demostrado, basándose en argumentos teóricos, que esta expresión sólo es válida si el cross-over point se alcanza cuando es superada la rampa de aceleración, y la suspensión esta ya rotando a la velocidad final ω.[27] Si el cross-over point se alcanza antes de llegar a la velocidad final, el parámetro de spin deberá ser menor de 0.5. Esta predicción es muy útil para comprender mejor el proceso de spin coating que estamos analizando. En una primera aproximación, la posición del máximo de reflectancia, λ_{Bragg}, depende linealmente del índice de refracción promedio y del tamaño de las capas. El índice de refracción promedio, se determina teniendo en cuenta el índice de refracción de las nanopartículas y la porosidad de la capa que forman. No depende por tanto, ni siquiera indirectamente, ni de ω ni de γ. El espesor de las capas, sin embargo, depende de ω a través de la expresión $T\sim \omega^{-b}$. Asumiendo que ambos tipos de capas dependen de ω de forma similar, el pico máximo de Bragg dependerá de ω según la expresión $\lambda_{Bragg} \sim \omega^{-b}$. De

esta forma, se estima el valor del parámetro de spin, representando los valores obtenidos para λ_{Bragg} frente a los de ω^{-b} en escala logarítmica, para cada rampa de aceleración utilizada en los experimentos y calculando la pendiente de las rectas. A partir de la pendiente de estas rectas, podemos obtener el valor del parámetro b.

En la Figura 5, se representa *b*, calculado de la manera arriba explicada, frente a γ. Se observa que a medida que γ aumenta, el parámetro de spin tiende a b=0.5. Esta curva muestra que, para rampas de aceleración elevadas, el cross-over point se alcanza cuando el sustrato ya está girando a la velocidad final. En estos casos es muy fuerte la dependencia de λ_{Bragg} con ω, y se puede conseguir un control muy preciso sobre el tamaño de las celdas de un cristal fotónico unidimensional variando principalmente la velocidad final.

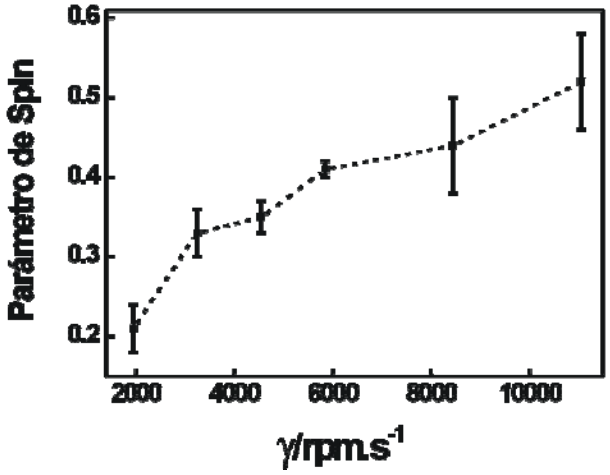

Figura 5. *Representación del parámetro de spin, b, frente a la rampa de aceleración.*

Otra técnica que permite construir láminas delgadas de nanopartículas es el dip coating, que consiste en sumergir verticalmente un substrato de vidrio en una de las suspensiones, para después retirarlo a velocidad controlada, mientras se forma una capa. El proceso se repite sucesivamente, alternando los dos tipos de suspensiones precursoras hasta completar la estructura entera. A continuación se presentan los resultados obtenidos del estudio de la calidad óptica y estructural de multicapas preparadas mediante esta técnica.

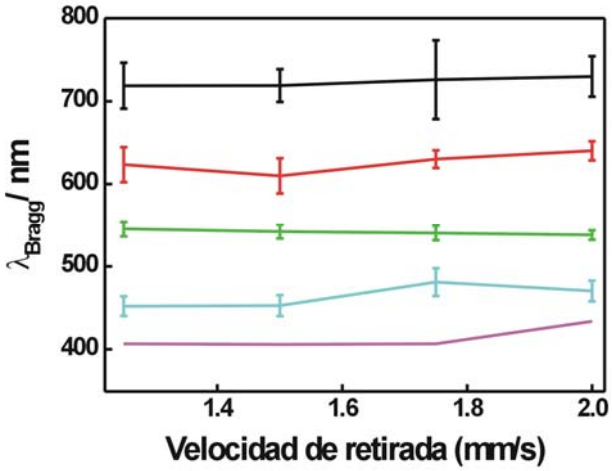

***Figure 6**. Posiciones del pico de Bragg (nm) frente a la velocidad de retirada v empleada en un proceso de dip coating. Las líneas de diferente color se corresponden a diferentes concentraciones de las suspensiones de SiO_2: 4.5 negro), 4 (rojo), 3.5 (verde), 2.5 (azul) y 2 (violeta) % en peso.*

Se construyeron diferentes multicapas modificando la concentración de la suspensión de SiO_2 y la velocidad de retirada, que es la velocidad a la que se asciende el sustrato sobre el cual se ha formado la capa de nanopartículas de la vasija que contiene la suspensión precursora. Los resultados están resumidos en la Figura 6, que sirve como guía para obtener cristales fotónicos unidimensionales de nanopartículas con alta calidad óptica en el visible y homogeneidad a lo largo de una gran superficie. La figura muestra la posición del pico de Bragg medido para 20 muestras frente a la velocidad de retirada a la que fueron hechas. Cada línea se corresponde con multicapas que fueron crecidas usando suspensiones precursoras de sílice con la misma concentración: 4.5, 4, 3.5, 2.5 y 2 % en peso (curvas negra, roja, verde, azul y violeta respectivamente). Los valores de velocidad de retirada elegidos fueron: 1.25, 1.5, 1.75 y 2 mm/s. En lo que respecta al control de la posición del pico de Bragg, del análisis de la gráfica se extrae que modificando únicamente la concentración de la suspensión precursora de sílice se pueden obtener multicapas de nanopartículas que presenten el máximo de reflectancia en cualquier posición dentro del espectro visible. Tal y como pasaba con la Figura 4, cada punto representado es, en realidad, el valor promedio de 25 valores de la posición del pico de Bragg tomados en los nodos de una cuadrícula virtual sobre la superficie de la muestra y separados 4 mm unos de los

otros. De nuevo, las barras de error son la desviación estándar y se interpretarán como una medida de la uniformidad de las capas. Se puede observar que las barras de error son más cortas si las multicapas están construidas a partir de suspensiones con menor concentración. En el caso de la línea violeta no hay barras de error representadas. Esto se debe a que el sistema usado para medir los espectros de reflectancia introduce ruido en las medidas de espectros por debajo de 400 nm y no es posible distinguir entre medidas correspondientes a diferentes puntos de la muestra. Se puede concluir claramente que la posición del pico de Bragg no depende de la velocidad de retirada en el rango disponible.

3. Control y optimización de las propiedades ópticas de cristales fotónicos unidimensionales.

En esta sección se evalúan las propiedades ópticas de cristales fotónicos unidimensionales basados en nanopartículas. Estas propiedades se controlan desde el proceso de fabricación de las estructuras que es, en este caso, el método de spin coating explicado en la sección anterior. Los resultados presentados están publicados en las referencias 28 y 29.

No se tiene constancia de ninguna estructura multicapa hecha de nanopartículas que presente reflectancia o transmitancia plana hasta el trabajo aquí expuesto. Desde el punto de vista experimental, hay dos factores que limitan el máximo de la reflectancia especular obtenida para un espejo de Bragg. Primero, la estabilidad mecánica se pierde cuando las capas son demasiado gruesas debido a tensiones entre el substrato y la capa. Esto determina un número máximo de celdas unidad que se pueden depositar antes de que la estructura comience a romperse. Segundo, la presencia de defectos en cada capa, que provoca scattering difuso y pérdida de transparencia. En el trabajo presentado en esta sección, se han superado estos obstáculos y se han construido multicapas de nanopartículas de casi el 100% de reflectancia en el rango espectral deseado, desde el ultravioleta visible hasta el infrarrojo cercano. Un estricto control sobre la presencia de agregados ha sido la clave para obtener este resultado. Las suspensiones precursoras de sílice y titania se filtraron usando filtros Millipore de 450 y 220 nm respectivamente. Además, para un determinado espesor de las capas, el que da lugar a posiciones del pico de Bragg por encima de 500 nm, ha sido necesario realizar un tratamiento intermedio de calcinación de 450ºC durante 30 min.

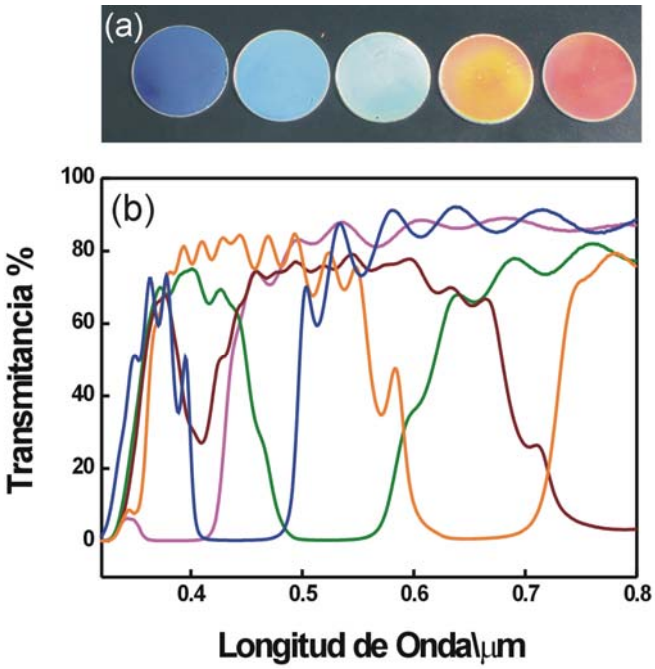

Figura 7. *(a) Fotografías, tomadas con una cámara digital, de 5 multicapas diferentes depositadas mediante spin coating. (b) Espectros de transmitancia planos correspondientes a este tipo de multicapas que reflejan diferentes regiones del espectro visible. Cada color mostrado en (a) y cada posición representada en (b) se corresponden con multicapas depositadas utilizando diferentes velocidades de rotación.*

En la Figura 7(a) se muestran una serie de fotografías de diferentes multicapas diseñadas para bloquear distintos rango del espectro visible. Todas ellas fueron depositadas sobre substratos circulares de vidrio de 5 cm de diámetro. Los espectros de transmitancia correspondientes con multicapas similares a las de la fotografía están representados en la Figura 7(b). Para obtenerlos se uso un espectrofotómetro visible-ultravioleta (SHIMADZU UV-2101PC). Estos espectros presentan las características complementarias a los de reflectancia, esto es, un mínimo de transmisión con una anchura espectral bien definida.

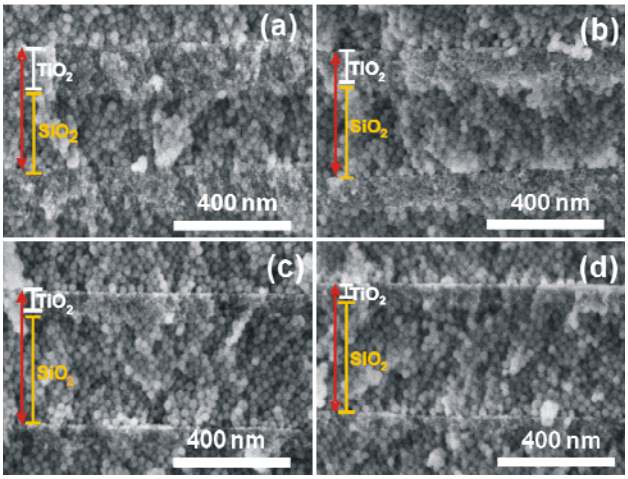

***Figura 8**. Imágenes de SEM que muestran la celda unidad de cuatro multicapas diferentes con valores de Z:(a) Z=1, (b) Z=2, (c) Z=3, (d) Z=4 (d). El espesor de las capas está indicado con flechas blancas (TiO_2) y amarillas (SiO_2). Las flechas rojas indican el espesor de las celdas unidad completas.*

A través del diseño de los espesores relativos entre las capas de diferente material que forman las estructuras, se puede modificar la intensidad de los distintos órdenes típicos de la difracción de Bragg, e incluso se puede suprimir alguno de ellos dejando el resto inalterados. Con el fin de mostrar esta propiedad, se ha construido una serie de muestras que presentan el gap fundamental en el mismo rango espectral pero en las cuales se permiten o se suprimen los órdenes superiores de manera controlada y selectiva. En una primera aproximación, la longitud de onda central de un orden *m* de la difracción de Bragg viene dada por la expresión $m\lambda_B=2\cdot(n_1d_1+n_2d_2)$, en dónde n_i y d_i denotan el índice de refracción y el espesor de una capa i. Así, la única condición para mantener los órdenes principales en la misma posición espectral es que la suma de los espesores ópticos de las capas que forman la celda tome un valor constante. Entonces, la intensidad relativa de los picos secundarios se puede modificar a través del cociente de dichos espesores ópticos $Z=n_1d_1 / n_2d_2$. Se estudiaron cuatro espejos de Bragg con el mismo valor de λ_B pero con diferente Z. La reflectancia que debían tener los cuatro diseños se simularon previamente usando un código escrito en MATLAB. Este programa, desarrollado por Gabriel Lozano en el grupo de Materiales Ópticos Multifuncionales (ICMSE-CSIC), se había utilizado previamente en diferentes trabajos para ajustar la respuesta óptica de multicapas.[30,31] Los espesores de las capas de las muestras se obtuvieron de fotografías de SEM de la Figura 8, dónde se pueden apreciar fácilmente los espesores de las capas de SiO_2 y

TiO_2. Todas las muestras estudiadas están formadas por tres celdas y el parámetro Z toma valores 1, 2, 3 y 4. Sus correspondientes reflectancias especulares se muestran en la Figura 9 (líneas negras). Se puede observar, tal y como se esperaba, la fuerte dependencia que presentan las intensidades de los órdenes secundarios con Z. En todos los casos se incluye el espectro simulado usado como guía para obtener para obtener los parámetros estructurales (líneas rojas). Se puede observar un claro acuerdo entre los espectros teóricos y experimentales.

La posibilidad de eliminar el segundo orden de difracción abre una vía a la fabricación de films transparentes en el rango visible que bloqueen de manera simultánea la radiación infrarroja y ultravioleta. A continuación se muestran los resultados obtenidos de fabricar cristales fotónicos unidimensionales flexibles con estas propiedades.

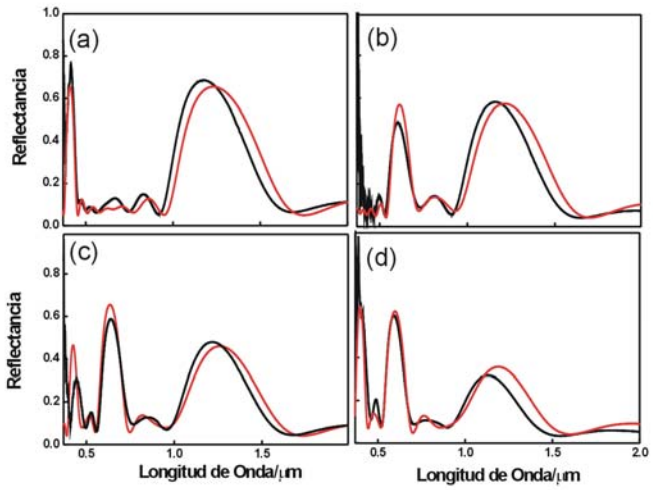

Figura 9. *Espectros de reflectancia experimentales (líneas negras) y simulados (líneas rojas) correspondientes a multicapas de tres celdas unidad con cocientes entre espesores ópticos de las capas constituyentes: (a) Z=1, (b) Z=2, (c) Z=3, y (d) Z=4.*

La red de poros presente en las multicapas de nanopartículas se ha aprovechado para convertirlas en flexibles infiltrando un polímero, PDMS (polidimetilsiloxano). Este se deposita encima del cristal y se infiltra en los poros haciendo girar todo el ensamblado por spin coating durante 40 segundos y utilizando valores para la velocidad angular ω y la rampa de aceleración γ de 700 rpm y 4550 $rpm.s^{-1}$, respectivamente. Después las muestras se calientan en una estufa a 120ºC durante 30

min. A continuación, se hacen incisiones con una cuchilla en los bordes y se sumergen en nitrógeno líquido con el fin de que el PDMS alcance su temperatura de transición vítrea. Esto es necesario para que la estructura tenga la suficiente estabilidad mecánica para ser despegada del substrato.

En la Figura 10 se pueden ver fotos de dos cristales fotónicos flexibles. La multicapa mostrada en 10(a) ha sido diseñada para bloquear totalmente la radiación deseada en el rango visible, mientras que en la Figura 10(b) se puede observar una multicapa que presenta transparencia en todo el rango visible al mismo tiempo que bloquea radiación ultravioleta y del infrarrojo cercano. Este efecto se consiguió diseñando los espesores relativos de las capas de tal forma que se ha eliminado el segundo orden de difracción, tal y como se ha explicado anteriormente. Los correspondientes espectros de transmitancia se muestran en las Figuras 10(c) y 10(d) (líneas rojas) junto con los espectros de las multicapas antes de infiltrar (líneas negras). El desplazamiento espectral observado se debe a los nuevos índices de refracción promedio adquiridos por las capas tras la infiltración.

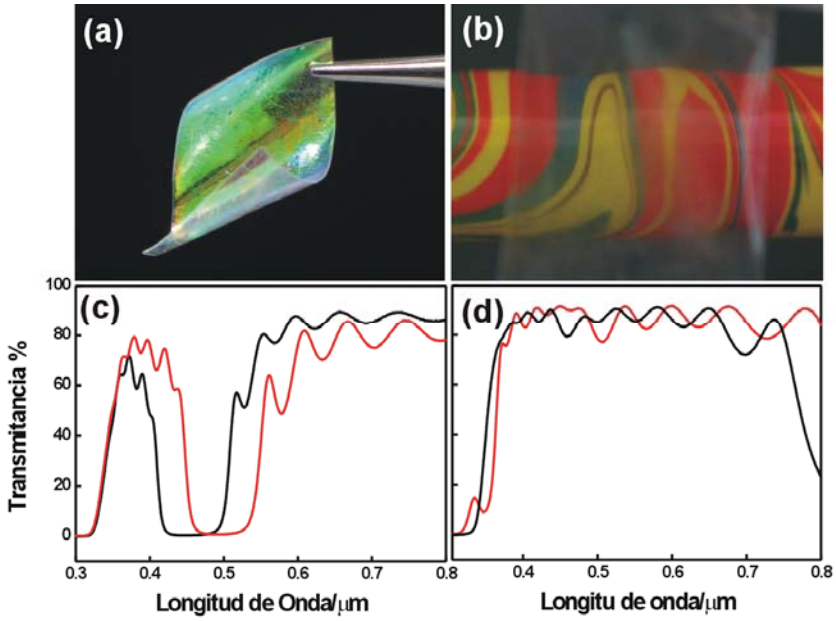

Figura 10. *Fotografías de dos multicapas flexibles con respuesta óptica plana en el rango visible (a) y sin máximo de reflexión en dicho rango (b). Sus respectivos espectros de transmisión están representados en (c) y (d) antes (líneas negras) y después (líneas rojas) de infiltrar con PDMS.*

Como un ejemplo de la capacidad que presentan este tipo de estructuras de albergar materiales de todo tipo, en la siguiente sección se estudian las propiedades de multicapas de nanopartículas infiltradas con arseniuro de galio (GaAs), uno de los materiales más interesantes tanto en óptica como en electrónica debido a su naturaleza semiconductora y actividad óptica.

4. Infiltración de materiales de alto índice de refracción en cristales fotónicos unidimensionales.

Las muestras estudiadas en esta sección están compuestas de tres celdas unidad construidas mediante el método del dip coating y usando suspensiones de TiO_2 y SiO_2 con concentraciones de 4.5% y 2% en peso respectivamente. Los resultados presentados en esta sección fueron obtenidos durante una estancia en el Tyndall Institute (Cork College University, Irlanda) bajo la supervisión del Profesor Martyn Pemble y están publicados en la referencia 32.

En este caso se aprovechó la red porosa de la multicapas para infiltrar un semiconductor de alto índice de refracción, arseniuro de galio (GaAs). El arseniuro de galio se formó dentro de los poros de las multicapas. Para ello se utilizó la técnica de MOCVD (del inglés Metalorganic Chemical Vapor Deposition), muy utilizada para crecer todo tipo de semiconductores de alta calidad. Consiste en formar el cristal mediante la deposición alternada de los distintos precursores en fase gaseosa.

En el caso de este trabajo, se ha utilizado un reactor horizontal en el que la temperatura y la presión se han mantenido constantes a 400ºC y 200 torr respectivamente. Sobre las multicapas porosas dentro del reactor, se depositan de manera alternada y pulsada los reactivos, trimetilgalio (TMGa, 3segundos) y arsina (AsH_3, 8 segundos). Ambos componentes se transportan utilizando una corriente de hidrógeno y ambos pulsos están separados por una purga de hidrógeno de 2 segundos para evitar que los reactivos se mezclen en su fase gas. Este proceso constituye un ciclo de deposición de GaAs.

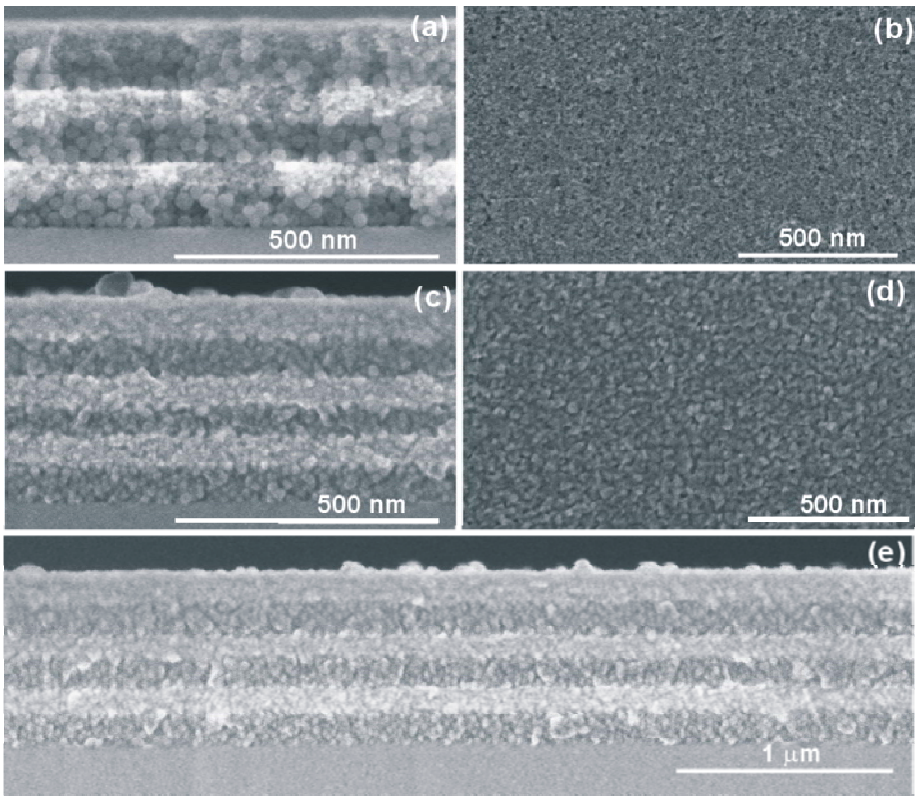

Figura 11. *Imágenes de SEM de las secciones transversales y de las superficies antes, (a) y (b), y después, (c) y (d), de ser infiltradas con GaAs usando 800 ciclos de MOCVD. (e) Imagen adquirida con baja magnificación de la sección transversal de la muestra infiltrada.*

Las Figuras 11(a) y 11(b) muestran fotografías de microscopía electrónica de barrido de la sección transversal y la superficie de una multicapa hecha con nanopartículas. Las Figuras 11(c) y 11(d) muestran las mismas estructuras tras haber sido sometidas a 800 ciclos del procedimiento de MOCVD anteriormente explicado. Como puede observarse, tras la infiltración, deja de distinguirse la forma esférica de las nanopartículas de sílice y la poliédrica de las de titania. Esto indica que la formación de GaAs tiene lugar en la superficie de las partículas que forman la estructura. Tras examinar la Figura 11(e) se puede concluir que la infiltración es homogénea a lo largo de toda la estructura y que se mantiene inalterado el ordenamiento de capas de la misma.

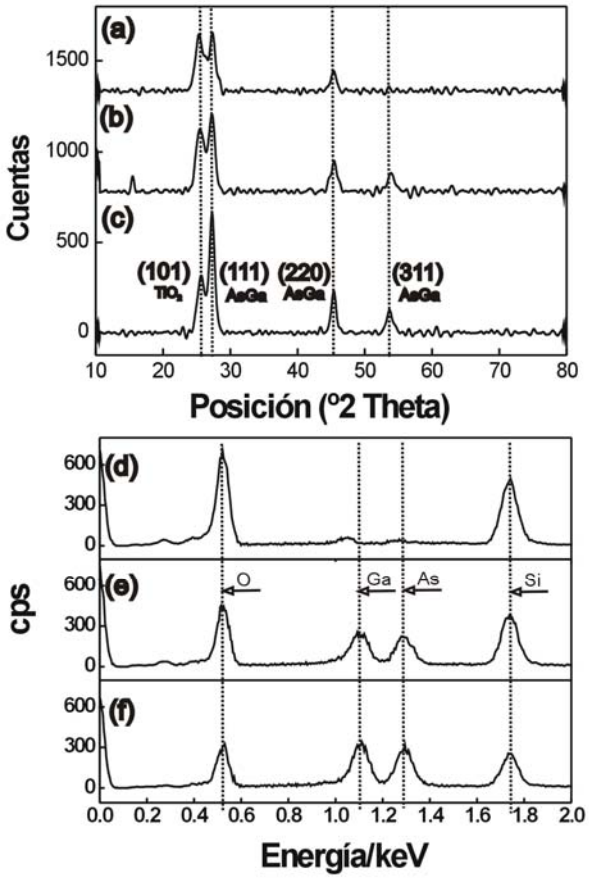

***Figura 12**. Difractogramas de rayos X obtenidos para la misma muestra tras ser infiltrada con GaAs usando (a) 200, (b) 366 y (c) 800 ciclos del proceso de MOCVD. Resultados del análisis realizado mediante espectroscopía de energía dispersiva de rayos X para la multicapa sin infiltrar (d) y tras haber sido infiltrada con (e) 200 y (f) 800 ciclos.*

La estructura cristalina del GaAs depositado se confirma con el análisis de difracción de rayos X. En la Figuras 12(a), 12(b) y 12(c) se muestran los difractogramas con los picos característicos de la fase cúbica del GaAs, correspondientes con muestras que fueron infiltradas con 200, 366 y 800 ciclos del proceso de MOCVD. El análisis de EDX (del inglés Energy Dispersive X-ray) también revela como la cantidad de As y de Ga depositado aumenta con los ciclos, como se ilustra en las Figuras 12(d), 12(e) y 12(f).

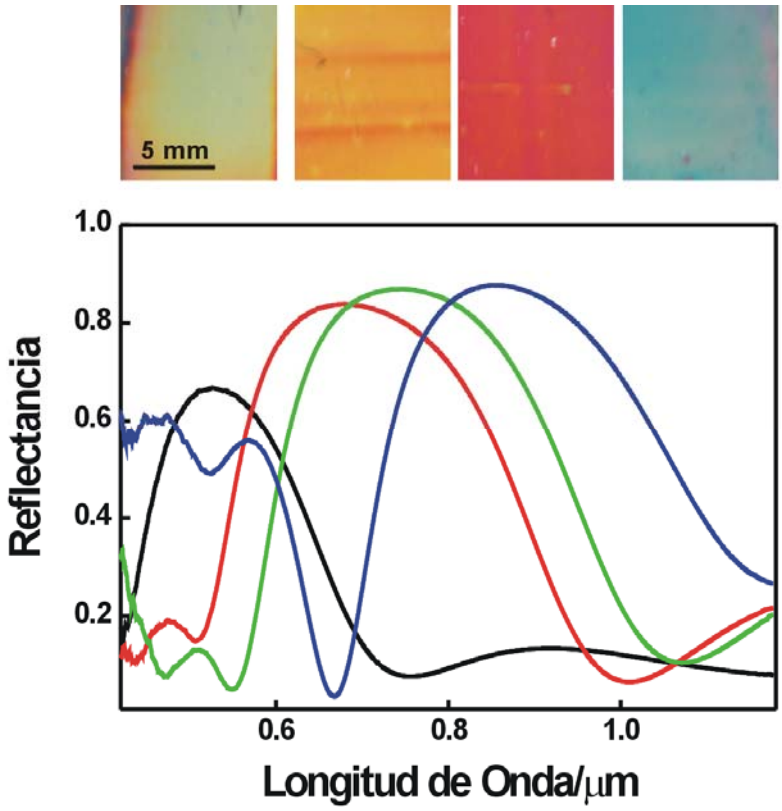

***Figura 13**. Arriba: de izquierda a derecha, fotografías de la misma multicapa de nanopartículas antes y después de haber sido infiltrada con GaAs usando 200, 366 y 800 ciclos del proceso de MOCVD. Abajo: Espectros de reflectancia correspondientes a cada una de las multicapas de la imagen, de izquierda a derecha, líneas negra, roja, verde y azul.*

Los espectros de reflectancia obtenidos para multicapas infiltradas con 200, 366 y 800 ciclos se muestran en la Figura 13. El espectro de color negro se corresponde con la estructura antes de ser infiltrada. Los espectros están acompañados de fotografías, hechas con una cámara digital, de las superficies de cada una de las muestras. Se puede apreciar de inmediato lo importante que es el efecto de infiltrar el semiconductor sobre la respuesta óptica del material.

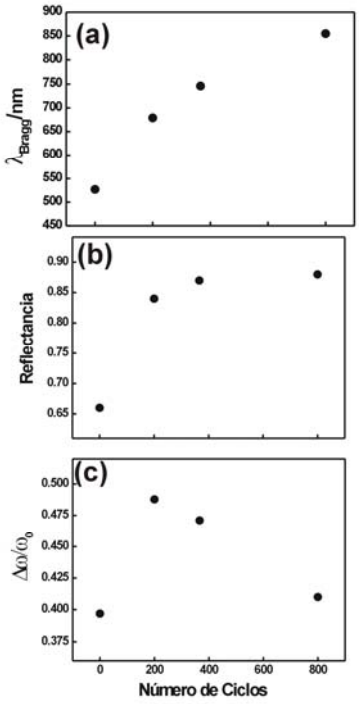

Figura 14. *Evolución experimental observada para (a) posición espectral del máximo de reflectancia, (b) intensidad de la reflectancia y (c) el cociente del ancho de banda y la posición del máximo de reflectancia, a medida que aumenta el número de ciclos de infiltración, para la estructura cuya respuesta óptica se muestra en la Figura 13.*

En la Figura 14, se presenta un resumen de los cambios experimentales observados en el pico de Bragg que ocurren con los diferentes grados de infiltración obtenidas. Este pico es muy sensible ante cambios en el índice de refracción de las capas que forman la estructura. La evolución de la posición del pico de Bragg, λ_{Bragg}, está representada en la Figura 14(a), la de la intensidad de este máximo de reflectancia, en 14(b) y, finalmente, en 14(c) se muestra el cociente entre el ancho del band gap y la posición del máximo de este en frecuencia $\Delta\omega/\omega_0$.Tal y como se esperaba, el pico de Bragg se desplaza gradualmente a longitudes de onda mayores a medida que el número de ciclos de infiltración aumenta. De manera simultánea, la intensidad del máximo de reflectancia se incrementa de un 65% para la estructura no infiltrada hasta casi un 90% tras 800 ciclos de deposición de GaAs. Este aumento de la reflectancia está acompañado, en el caso de la multicapa infiltrada con menor número de ciclos, de un importante aumento de $\Delta\omega/\omega_0$, que pasa de 0.4 a 0.5. Sin

embargo $\Delta\omega/\omega_0$ decrece para mayores grados de infiltración. Estas dos tendencias diferentes se explican teniendo en cuenta que, aunque ambas magnitudes dependen directamente de la diferencia de los índices de refracción de los dos tipos de capas, Δn, $\Delta\omega/\omega_0$ es también inversamente proporcional al índice de refracción promedio de la estructura completa $n=(n_1+n_2)/2$.[33] El incremento que se espera para $\Delta\omega/\omega_0$, debido al aumento de Δn, se verá compensado para los valores más elevados de n promedio.

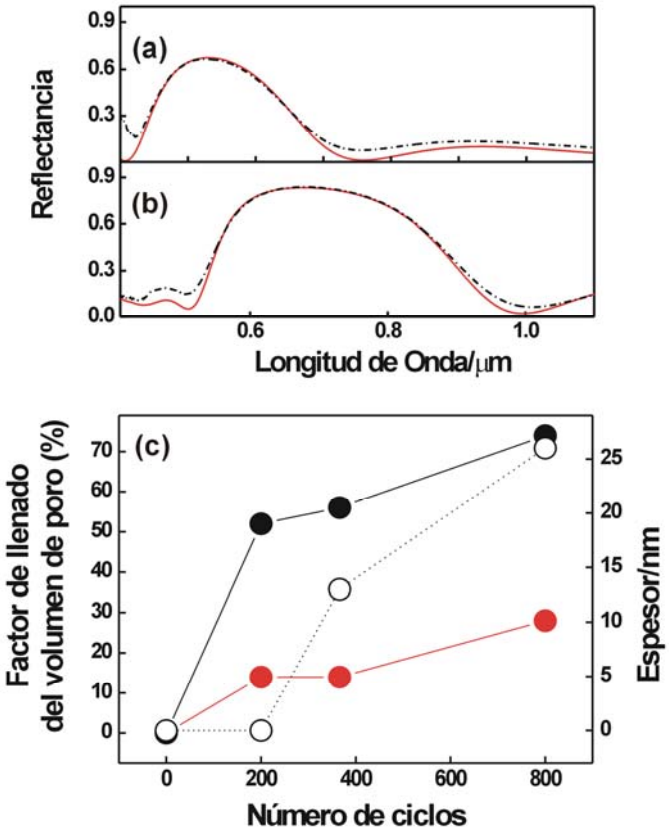

Figura 15. *Reflectancia experimental (líneas rojas) y su respectivo ajuste teórico (líneas negras) correspondientes a una multicapa antes (a) y después (b) de infiltrar con GaAs usando 200 ciclos de MOCVD. (c) Evolución de la fracción de llenado del volumen de poro, obtenido de las simulaciones, con el número de ciclos para las capas de titania (círculos negros) y sílice (círculos rojos). El espesor estimado de la capa de GaAs depositada encima de la estructura frente al número de ciclos está también representada (círculos blancos, eje de la derecha).*

Esta hipótesis concuerda con los valores de los parámetros ópticos obtenidos del ajuste de los espectros de reflectancia. Usando como parámetro de entrada el espesor de las capas obtenidas a partir de las imágenes de SEM, se puede estimar el factor de llenado teniendo en cuenta las contribuciones relativas de los índices de refracción de los distintos materiales que componen cada capa. Las partes real e imaginaria de la constante dieléctrica del GaAs se obtuvieron de la literatura.[34] En la Figura 15 se muestran los espectros de reflectancia teóricos (líneas negras) y experimentales (líneas rojas) correspondientes a una multicapa antes (Figura 15(a)) y después de ser infiltrada con 200 ciclos de deposición de GaAs (Figura 15(b)). En la Figura 15(c) el valor obtenido para la fracción de llenado de poro está representado frente al número de ciclos del proceso MOCVD, para las capas de titania (círculos negros) y para las de sílice (círculos rojos). Estos valores están extraídos de las simulaciones. Del análisis de estas gráficas se puede extraer que, el llenado de los poros de las capas de titania es mucho mayor que el de las de sílice. Esto es debido a que tienen un tamaño mucho menor y se llenan antes. Todos estos ajustes han sido posibles considerando las modulaciones introducidas por una fina capa de GaAs depositada sobre la superficie del cristal fotónico. Los valores estimados teóricamente de esta capa también están representados frente al número de ciclos en la Figura 15(c) (círculos abiertos, eje derecho).

5. Modificación de la absorción óptica de nanopartículas metálicas integradas en cristales fotónicos unidimensionales.

En esta sección se presenta un estudio acerca de la modificación de la absorción óptica de nanopartículas metálicas integradas en cristales fotónicos unidimensionales hechos de nanopartículas se SiO_2 y TiO_2. Se usaron nanopartículas de oro recubiertas de sílice Au@SiO_2, proporcionadas por el grupo de Profesor Luis Liz-Marzán de Universidad de Vigo, para crear controladamente un defecto óptico en una multicapa de formada por cuatro celdas unidad. La absorción se controla haciendo coincidir los modos de la cavidad con diferentes regiones espectrales de la resonancia del plasmón de superficie del oro. Para ello se han de modificar los parámetros estructurales del cristal, construido por spin coating tal y como se explica en la Sección 2. Los resultados presentados en está sección fueron publicados en la referencia 35.

La sección transversal de una estructura como la descrita se muestra en la fotografía de microscopía electrónica de barrido de la Figura 16. En el centro se puede distinguir la capa de nanopartículas de oro recubierto de sílice que son de mayor tamaño. Una de las propiedades más importantes de estas multicapas hechas

de nanopartículas es la capacidad de albergar diferentes materiales de diversas formas sin alterar su estructura, consecuencia de su elevada adaptabilidad, como se puede observar claramente en la fotografía.

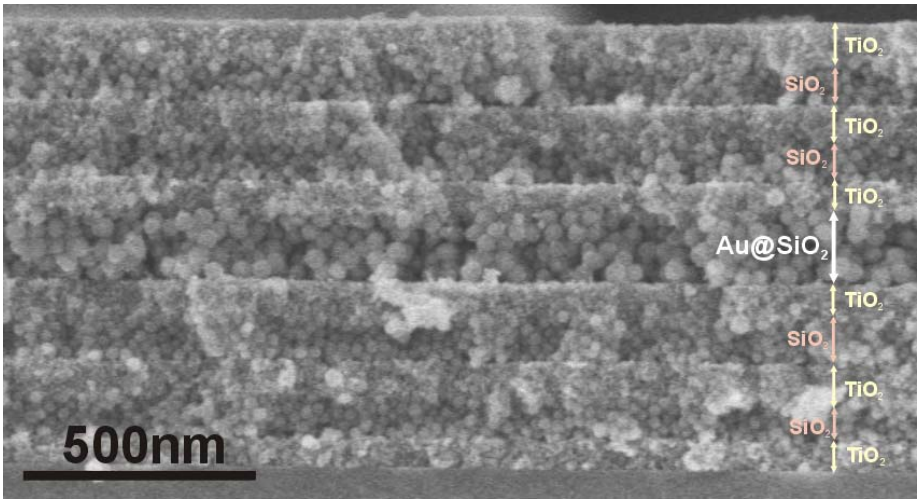

***Figura 16**. Fotografía de SEM de la sección transversal de un cristal fotónico unidimensional poroso, en el cual ha sido integrada una capa de nanopartículas de Au@SiO_2.*

Para fabricar esta estructura se utilizaron suspensiones de nanopartículas de SiO_2 y de TiO_2 en metanol con concentraciones de 2% y 4% en peso respectivamente. La capa de nanopartículas de Au@SiO_2 se introdujo en la estructura por spin coating de gotas de 200 µl de una suspensión de dichas partículas también en metanol con una concentración de 1.45 % en peso. Los tres tipos de capas se obtuvieron utilizando velocidades con valores comprendidos entre 3000-7000 rpm y una aceleración de 11340 rpm^{-s}. También se utilizaron muestras de referencia, que fueron construidas de la misma manera y poniendo especial cuidado en que el grosor de la capa de referencia fuera el mismo que el de la introducida en el resonador. La síntesis de las nanopartículas se encuentra explicada en el Apéndice.

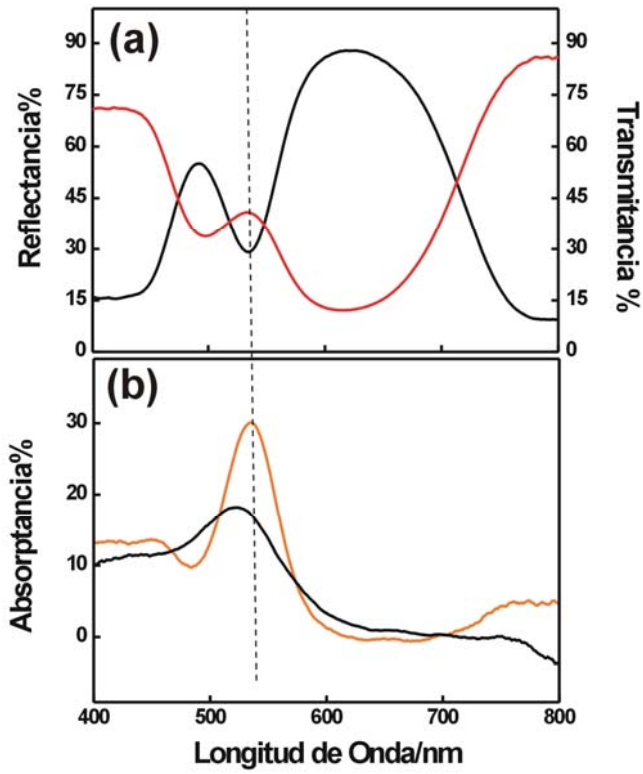

Figura 17. *(a) Espectros de reflectancia (línea negra) y transmitancia (línea roja) total correspondiente a una cavidad óptica hecha de nanopartículas de Au@SiO_2 integradas en una multicapa porosa. (b) Espectro de la absorción óptica del resonador (línea naranja) comparada con la de una capa de nanopartículas de Au@SiO_2 del mismo espesor (línea negra). La línea vertical punteada indica la posición espectral de la resonancia de la cavidad.*

Los resultados obtenidos del estudio de las propiedades ópticas de este resonador se muestran en la Figura 17. La reflectancia total (línea negra) y la transmitancia total (línea roja) típicas de este tipo de estructuras están representadas en 17(a). La intensidad reflejada por la muestra es máxima en el rango 450 nm<λ<750 nm, y una ventana de transmisión debida al modo resonante de la cavidad aparece a 535 nm, señalada en la figura por la línea vertical punteada. Coincidentes con esta longitud de onda, se aprecia un mínimo en reflectancia y un pico en transmitancia. La absorción óptica se calcula a partir de la reflexión y transmisión total a partir de la expresión $A=1-T_T-R_T$. El resultado se muestra en la Figura 17(b) para el resonador que contiene las nanopartículas de Au@SiO_2 (línea naranja) y para

una capa de las mismas nanopartículas de oro depositadas sobre una capa de titania que sirve como referencia (línea negra). Para el caso del resonador, el máximo de absortancia está ahora situado a una longitud de onda que coincide con el modo resonante de la cavidad óptica (tal y como indica la línea vertical), con una intensidad que es ahora casi el doble que en la referencia. Además, el pico de absorción está desplazado hacia longitudes de onda mayores respecto del medido para la capa de referencia y la absorción de aquellos rangos coincidentes con el band gap de la estructura es atenuada.

Estos fenómenos de aumento y atenuación selectivos de la absorción óptica se deben a que los modos electromagnéticos resonantes se confinan preferencialmente en la capa que contiene las nanopartículas de Au@SiO_2. El incremento de la densidad fotónica de estados, debida al confinamiento en capas específicas de la estructura, implica una baja velocidad de grupo para estos modos,[36] lo que propicia una mayor interacción radiación-materia y, por lo tanto, una mayor probabilidad de absorción.[37] Por el contrario, la reducción de la intensidad de campo en ciertas regiones da lugar a interacciones más débiles y a una menor probabilidad de absorción. Todo esto se ilustra en la Figura 18. En ella está representada la distribución espacial del cuadrado de la amplitud del campo eléctrico a lo largo de la sección transversal del cristal fotónico en el que está integrada la cavidad formada por nanopartículas de Au@SiO_2, representadas como esferas con un núcleo rojo en el centro de la estructura. A partir de las propiedades ópticas de estas nanopartículas,[38] se hicieron cálculos teóricos usando una aproximación de matriz de transferencia.[30] Los resultados se muestran para las siguientes longitudes de onda: λ_1, el borde de banda del band gap a alta energía; λ_2, la resonancia óptica a la que se observa el mínimo de reflectancia; λ_3, dentro del band gap, en dónde la reflectancia es máxima; λ_4, el borde de banda a baja energía; y λ_5, la banda de paso del cristal fotónico. Estas longitudes de onda están indicadas en la Figura 18(a) con barras rojas. En los patrones de distribución de campo de la Figura 18(b) se observa claramente como la luz se localiza preferencialmente en las capas de menor índice de refracción, las de sílice, para λ_1, como se espera para un modo situado en la banda de alta energía de un cristal fotónico. El campo eléctrico es incluso más intenso para λ_2, como se espera para un modo situado en la cavidad resonante. Para estas longitudes, se obtendrán los máximos de absorción. Por el contrario la transmisión de luz se bloquea para λ_3, y se confina en las capas no absorbentes de titania para λ_4 y λ_5, disminuyendo la absorción.

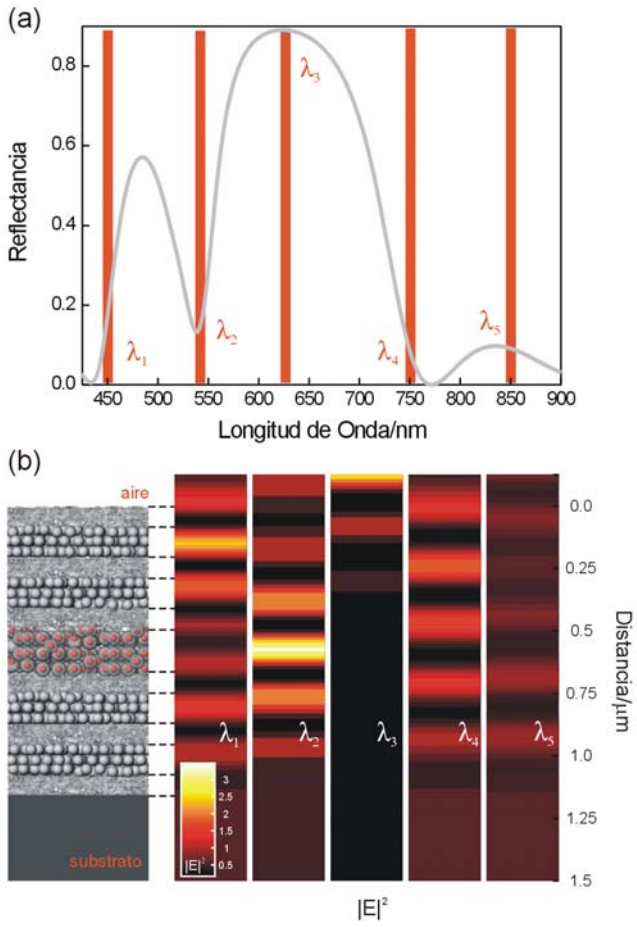

Figure 18. *(a) Reflectancia especular calculada para una multicapa con parámetros similares a los obtenidos experimentalmente. Las barras verticales indican las posiciones espectrales de los modos fotónicos localizados en el borde de banda a alta energía (λ_1), el centro de la resonancia (λ_2), el centro del band gap fotónico (λ_3), el borde de banda a baja energía (λ_4) y en la región paso de banda de la estructura (λ_5). (b) A la izquierda se muestra un modelo de la estructura simulada, en dónde las nanopartículas de $Au@SiO_2$ están representadas mediante esferas grises con un núcleo rojo. Los paneles de la derecha muestran la distribución espacial del cuadrado de la amplitud del campo eléctrico a lo largo de la estructura para todas las longitudes de onda señaladas en el espectro de reflectancia de la Figura 18(a). La representación está acompañada de una escala de intensidad de color.*

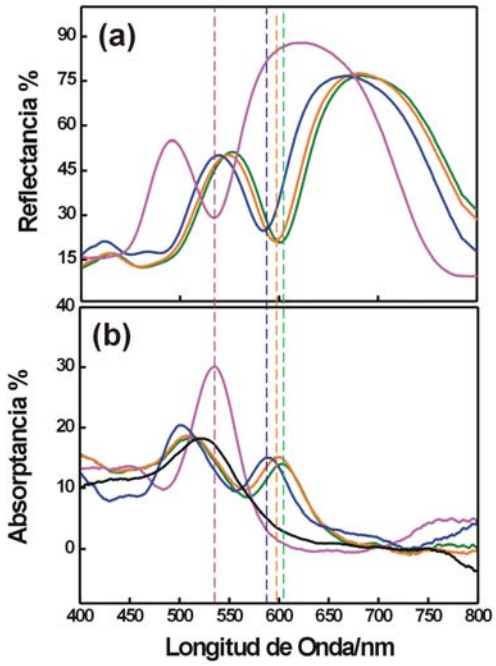

***Figura 19**. (a) Espectros de reflectancia total de una cavidad óptica hecha de nanopartículas de $Au@SiO_2$ integradas en una multicapa porosa, antes (línea magenta) y después de ser infiltrada con isopropanol (n=1.377, línea azul), tolueno (n=1.497, línea naranja) y clorobenzeno (n=1.525, línea verde). (b) Los correspondientes espectros de absorción óptica (mismo código de colores). Las líneas verticales punteadas indica la posición espectral de la resonancia de la cavidad en cada caso. Como referencia se muestra el espectro de absorción óptica (línea negra) de una capa de nanopartículas de $Au@SiO_2$ de un espesor similar.*

Otra forma de estudiar los efectos de la interacción entre los modos resonantes de la estructura y los plasmónicos de las partículas de oro es infiltrando la multicapa con líquidos de diferentes índices de refracción *n*. Esto causará un desplazamiento hacia longitudes de onda mayores del pico de Bragg.[12] Los líquidos empleados fueron isopropanol (n=1.377), tolueno (n=1.497) y clorobenzeno (n=1.525). En la Figura 19(a) se muestran los espectros de reflectancia total medidos tras cada una de las distintas infiltraciones. A partir de estas medidas y de las de transmitancia total se obtuvieron los espectros de absorción representados en 19(b). Se observa claramente como tras la infiltración de los líquidos aparece una estructura de doble pico en los espectros de absorción. Esto es consecuencia de los dos diferentes aumentos simultáneos de la absorción que se producen. Por un lado, los modos fotónicos que

coinciden espectralmente con la resonancia de la cavidad se localizan en las nanopartículas de oro y aumenta su absorción. A medida que el índice de refracción de las capas aumenta debido a la infiltración de los líquidos, este fenómeno tendrá lugar a longitudes de onda mayores. Este desplazamiento gradual se observa claramente en la Figura 19(b). Al mismo tiempo y como toda la estructura es porosa, el pico de Bragg se desplaza a longitudes de onda mayores y en algún punto el borde de alta energía del gap coincide con la absorción de las nanopartículas de Au@SiO_2. Estos modos fotónicos están situados preferencialmente en las capas de menor índice de refracción de la estructura, incluyendo la capa de oro recubierta de sílice, por lo que supone una segunda fuente de aumento de la absorción. La posición espectral a la que se observan estos efectos también es dependiente del índice de refracción de los líquidos infiltrados en la multicapa, tal como se puede ver en la Figura 19(b).

6. Control de la fotoluminiscencia de nanopartículas dopadas con tierras raras e integradas en cristales fotónicos unidimensionales.

En esta sección se mostrarán los resultados del estudio de la modificación de la fotoemisión de nanopartículas dopadas con tierras raras integradas en resonadores porosos basados en cristales fotónicos unidimensionales. Mediante el control preciso de las características de la cavidad óptica, las bandas de emisión serán suprimidas o aumentadas direccionalmente de manera controlada y selectiva. Los resultados más importantes presentados en esta sección fueron publicados en las referencias 39 y 40.

Para realizar este estudio se construyeron dos resonadores ópticos de diez y seis celdas unidad respectivamente. En ellos se han integrado nanopartículas de $EuYF_3$ de forma romboédrica, cuya síntesis está explicada en el Apéndice. Las estructuras se construyeron por el método de spin coating, según se ha explicado en la Sección 2, a partir de suspensiones de nanopartículas de SiO_2 y TiO_2 con concentraciones de 2 y 4 % en peso respectivamente. Las nanopartículas de $EuYF_3$ se encuentran dispersas en etilenglicol con una concentración de 1.5 % en peso. Las velocidades finales elegidas durante el proceso de spin coating tenían valores comprendidos entre 2000 y 8000 rpm y las aceleraciones entre 1950 y 13650 $rpm.s^{-1}$. Del mismo modo que para el oro, con el fin de cuantificar la modificación de las propiedades ópticas debido a la estructura fotónica, se preparó una muestra de referencia consistente en una capa de nanofósforos entre dos de nanopartículas de sílice.

En las Figuras 20(a) y 20(b) se muestran dos fotografías de microscopía electrónica de barrido que muestran dos imágenes a bajo y gran aumento

respectivamente de las nanopartículas de $EuYF_3$ depositadas sobre la superficie de media estructura. Se puede ver claramente que la deposición es uniforme en la escala de las micras. En la Figura 20(c) se puede ver la sección transversal de la estructura final y en la 20(d) un detalle de la cavidad cuyo espesor está determinado por el de las nanopartículas de sílice que rodean a los nanofósforos. Se puede observar que el orden de la estructura completa se preserva.

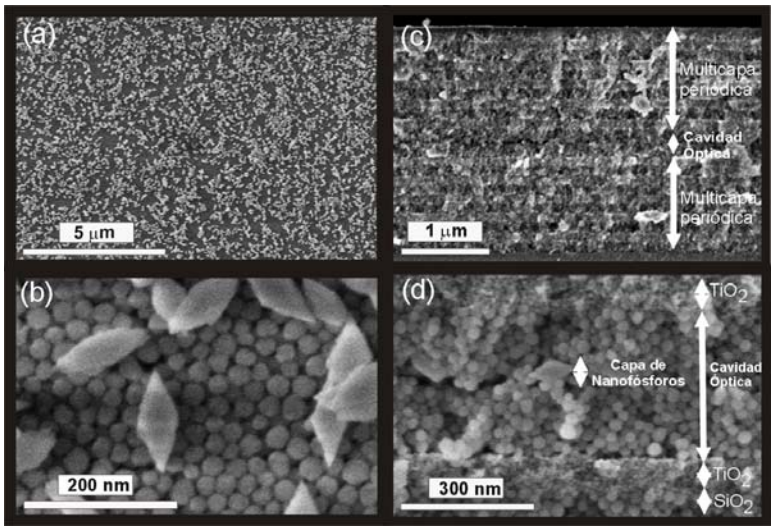

Figura 20. *Imágenes de SEM a (a) baja y (b) alta magnificación correspondientes a una capa de nanopartículas de $EuYF_3$ depositadas sobre una multicapa de nanopartículas de SiO_2 y TiO_2 . Las partículas esféricas son los nanocoloides de SiO_2 . La imagen de (c) muestra la sección transversal de una multicapa periódica hecha de 20 capas alternadas de nanopartículas de SiO_2 y TiO_2, la cual contiene una cavidad óptica en el medio. La estructura de dicha cavidad se puede observar en detalle en la sección mostrada en la imagen de la Figura (d).*

Para llevar a cabo las medidas de fotoluminiscencia y reflectancia se utilizó un espectrofotómetro LabRam acoplado a un microscopio operando en reflexión con un objetivo 10X, con una apertura numérica de 0.1 (cono de luz de ±5.7º). La luminiscencia se midió usando un láser verde (λ=532 nm), incidiendo en la muestra en la dirección perpendicular a la periodicidad de las capas, y fue colectada con el mismo objetivo empleado para iluminar la muestra.

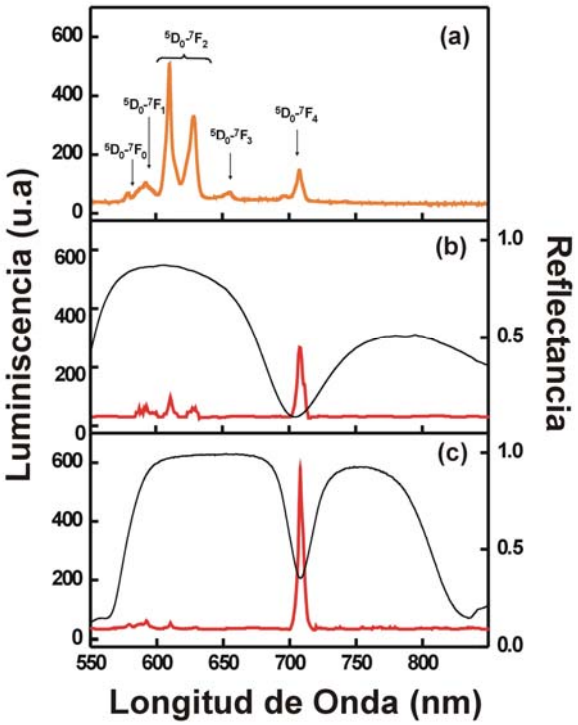

Figura 21. (a) Espectro de luminiscencia correspondiente a la muestra de referencia, consistente en una capa de nanofósforos integrados entre dos capas de sílice. Los espectros de luminiscencia (líneas rojas) y reflectancia (líneas negras) obtenidos para una capa similar de nanofósforos integrada en multicapas de 6 y 10 celdas unidad se muestran en (b) y (c) respectivamente.

El espectro de emisión de la capa de nanofósforos empleada como referencia se muestra en la Figura 21(a). Las bandas de luminiscencia correspondientes a las transiciones características del Eu^{3+} están indicadas en la figura.[41] La capa de nanopartículas de sílice incluida en el medio de la estructura rompe la periodicidad de índices de refracción dando lugar a un modo resonante, característico de una cavidad óptica. Este modo es un estado permitido dentro del band gap y se identifica como un mínimo en el espectro de reflexión de la estructura. Esto es lo que se puede observar claramente en las Figuras 21(b) y 21(c) (líneas negras), obtenidos de resonadores formados por 6 y 10 celdas unidad respectivamente. En ambos ejemplos el espesor de la capa central de sílice se eligió de forma que la resonancia coincidiese espectralmente con la banda de emisión situada a λ=708 nm. Los espectros de

emisión tomados para los nanofósforos integrados en estas dos estructuras también se muestran en las Figuras 21(b) y 21(c) (líneas rojas). En la dirección perpendicular a la multicapa, los picos de emisión situados a λ=610 nm y λ=628 nm son parcialmente, primero, y totalmente, después, suprimidos, mientras que el pico de luminiscencia situado a λ=708 nm (originalmente secundario) es gradualmente aumentado a medida que el número de las celdas unidad que forman los espejos de Bragg se hace mayor. Para la multicapa de 10 celdas unidad, esta banda alcanza un valor seis veces mayor que el original.

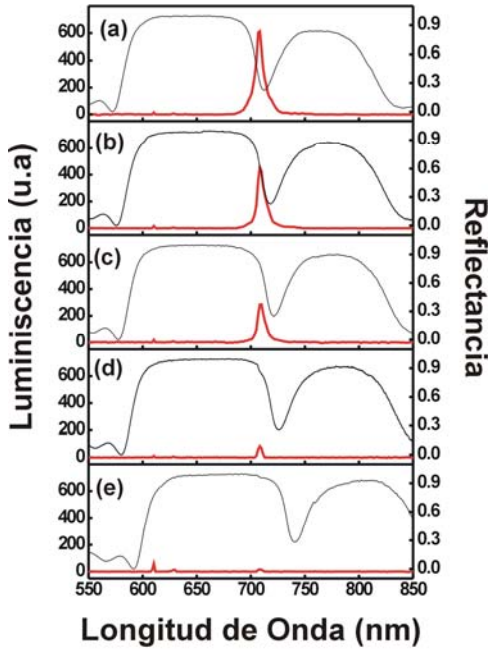

Figura 22. *Espectros de lumininiscencia (líneas rojas) y reflectancia (líneas negras) correspondientes a nanopartículas de $EuYF_3$ integradas en una cavidad óptica construida en una multicapa de 10 celdas unidad y expuesta a un incremento gradual de la presión parcial de vapor de isopropanol: (a) P/P_0=0 (b) P/P_0=0.07, (c) P/P_0=0.19, (d) P/P_0=0.66, y (e) P/P_0=1.*

Con el fin de analizar las variaciones de la respuesta óptica de este tipo de materiales ante cambios en el entorno, se analizaron las modificaciones sufridas por los espectros de emisión y reflexión de estas estructuras ante cambios de la presión parcial de vapor de diferentes componentes. Para ello se introducen las multicapas en

una cámara cerrada en la cual la presión parcial de un líquido volátil varía de P/P_0 =0 hasta 1 (P_0 es la presión de saturación del líquido a temperatura ambiente). La cámara posee una ventana plana de cuarzo a través de la cual se toman los espectros de reflectancia y de luminiscencia *in situ*. En la Figura 22 se muestra una serie de espectros de reflectancia (líneas negras) y de luminiscencia (líneas rojas) obtenidos para diferentes presiones parciales P/P_0 de isopropanol en la cámara. Claramente se puede observar como la intensidad del pico de emisión a λ=708 nm disminuye a medida que la resonancia se aleja de esta posición debido al desplazamiento espectral que sufre. Esto es consecuencia de aumentar el índice de refracción promedio de la multicapa al adsorberse y condensarse el gas en las paredes de los poros. Entonces, se pueden obtener isotermas de adsorción representando la evolución de la luminiscencia frente a P/P_0. Dos series de datos, correspondientes a vapores de isopropanol (círculos sólidos negros) y tolueno (círculos abiertos rojos), están pintadas en la Figura 23.

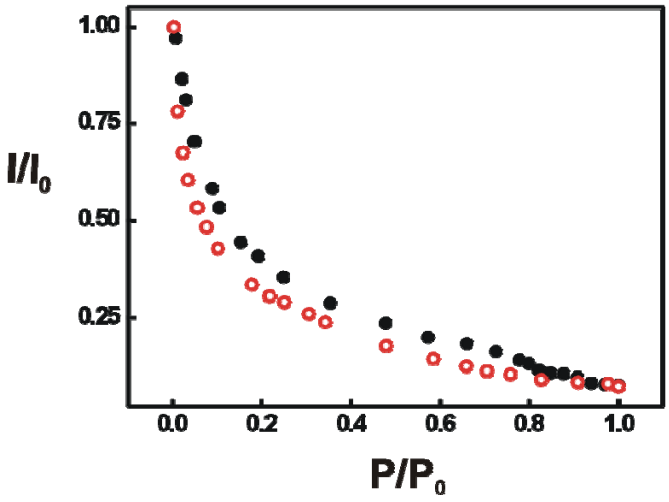

Figura 23. *Variación de la intensidad de luminiscencia de la línea de emisión localizada a λ=708 nm a medida que la presión parcial de isopropanol (círculos negros) y tolueno (círculos rojos) aumenta en la cámara.*

A continuación, se presenta un estudio acerca de la variación de la intensidad de las bandas de luminiscencia con el ángulo de colección, observándose una fuerte dependencia angular del aumento de las bandas del resonador respecto de la referencia. Estas propiedades angulares son también dependientes de los parámetros ópticos del resonador. Los datos obtenidos experimentalmente son analizados sobre

la base de un modelo teórico simple obtenido por H. Benisty et al.,[42] encontrándose un buen acuerdo para las propiedades direccionales de la intensidad de luminiscencia extraída. Estos resultados fueron obtenidos durante una estancia en el Laboratorio de Fotónica y Nanoestructuras (CNRS, Francia) bajo la supervisión de los Doctores Ariel Levenson y Alejandro Giacomotti y están publicados en la referencia 39.

En esta ocasión se utilizó de nuevo un láser verde (λ=532 nm) para realizar las medidas de luminiscencia, mientras que para obtener los espectros de transmitancia se usó un láser blanco supercontínuo que permite medir espectros ópticos en el rango comprendido entre 400 y 800 nm. El ángulo de extracción θ se midió colocando un iris delante del detector.

En la Figura 24 se muestran los espectros de transmitancia y luminiscencia de dos resonadores de 10 celdas con diferentes modos de la cavidad óptica: λ_c = 708 nm y λ_c = 742 nm (paneles de la izquierda y la derecha respectivamente). En las figuras 24(a) y 24(e) se muestran los espectros de transmitancia (líneas rojas) del resonador y de luminiscencia (líneas negras) de la muestra de referencia. En uno de los casos, la resonancia, a incidencia normal, coincide con la banda de emisión situada a λ_c= 708 nm (en resonancia), mientras que en la otra no coincide con ninguna línea de emisión, (fuera de resonancia). Los dos sets de Figuras 24(b-d) y 24(f-h) muestran la luminiscencia emitida en cada caso para diferentes ángulos de colección. Para ángulos pequeños, la banda situada a λ_B = 708 nm está fuertemente aumentada cuando está en resonancia, como se observa en la Figura 21(b) y casi totalmente atenuado cuando está fuera de resonancia, tal y como se muestra en la Figura 21(f). Para el primer caso, se observa que la intensidad de la banda situada a λ_B = 708 nm aumenta a medida que el iris se abre gradualmente, hasta alcanzar un valor constante. Para el caso del segundo resonador, la dispersión angular se estabiliza a ángulos mayores. La respuesta angular observada es el resultado de que la resonancia de la cavidad se desplaza a longitudes de onda menores a medida que el ángulo de colección de luz aumenta. Para cierto ángulo θ, la resonancia de la cavidad coincide espectralmente con la emisión de alguna de las bandas, cuya intensidad se ve aumentada.

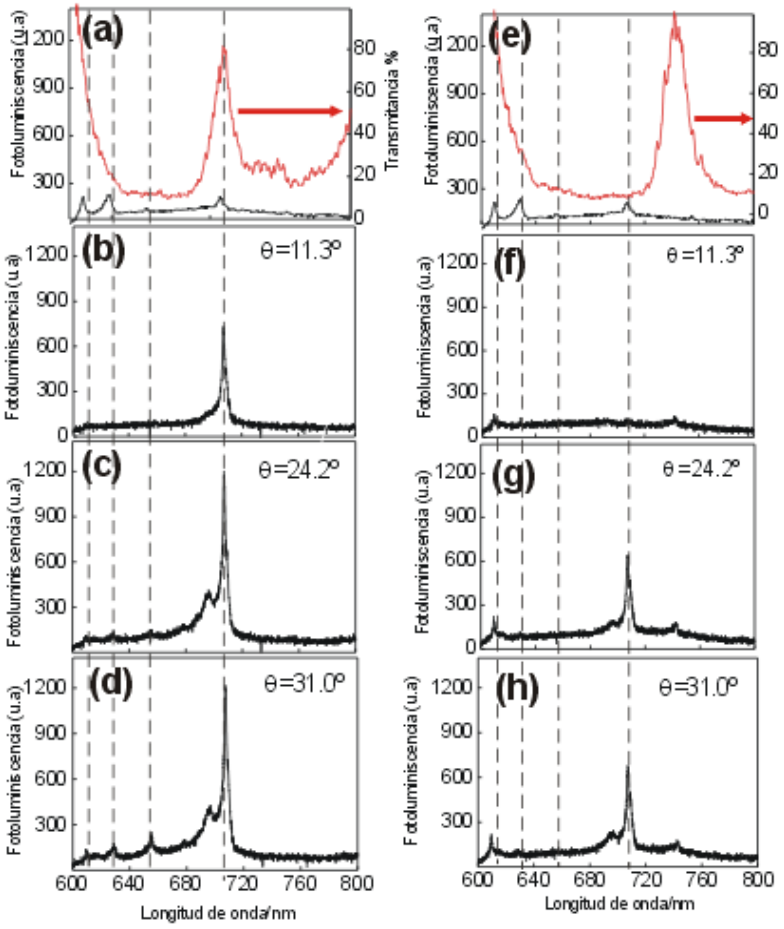

Figura 24. *Espectros de luminiscencia (líneas negras) de la muestra de referencia y espectros de transmitancia (líneas rojas) de resonadores ópticos cuyos modos de la cavidad están centrados a* λ_c = *708 nm, (a), y a* λ_c = *742 nm, (e). Sus correspondientes espectros de luminiscencia para diferentes ángulos de colección están representados en (b), (c), (d) y (f), (g) y (h), respectivamente. Las líneas verticales punteadas verticales indican la posición de las bandas de emisión de los nanofósforos.*

En la Figura 25 se presenta la evolución, observada experimentalmente, de la intensidad normalizada de las bandas de emisión afectadas por la cavidad frente al ángulo del cono de colección para los dos resonadores considerados y situados a λ_c = 708 nm (25(a)) y λ_c = 742 nm (25(b)). En el primer caso se representan las intensidades normalizadas correspondientes a las bandas situadas en λ_B = 655 nm

(círculos rojos) y λ_B = 708 nm (círculos negros), mientras que en el segundo caso sólo están dibujados los resultados obtenidos para la banda a λ_B = 708 nm, ya que esta es la única banda que coincide con la resonancia de la cavidad a cierto ángulo en el rango analizado. Para comparar, también están representadas las variaciones angulares de la intensidad de la luminiscencia correspondientes a la muestra de referencia (cruces negras y rojas para λ_B = 708 nm y λ_B = 655 nm, respectivamente).

Se ha realizado un análisis de los comportamientos angulares observados, comparando estos con los esperados para el caso de un resonador perfectamente uniforme consistente en un dipolo emisor situado en el centro de una cavidad rodeada por dos espejos. Este sistema fue analizado teóricamente por Benisty et al.[42] En este estudio se obtiene una expresión para la potencia extraída fuera del resonador, P_{out}, en una determinada dirección θ:

$$\mathbf{P_{out}}(\theta) \propto \frac{2\mathbf{T}_1}{\left|1-\mathbf{r}_1\mathbf{r}_2\mathbf{e}^{2i\phi}\right|^2}\frac{1+\mathbf{r}_2^2-2\mathbf{r}_2\cos(2\phi')}{2} \qquad [4]$$

Dónde L es el espesor de la cavidad, k el número de onda de la luz emitida dentro de la cavidad a λ_B ($k=2\pi n_c/\lambda_B$), r_1 y r_2 son los coeficientes de reflexión de los campos reflejados por los espejos anterior y posterior respectivamente, $T_1=1-r_1^2$ es la transmitancia del espejo delantero, $\phi = kL\cos\alpha$, $\phi' = kz\cos\alpha$, siendo z la distancia desde el emisor hasta el espejo trasero (z=L/2) y α es el ángulo de radiación interno relacionado con el externo θ mediante la ley de Snell.

Entonces, la potencia total extraída del resonador y recogida en un cono de anchura angular θ viene dada por:

$$P_{TOT}(\theta) \propto 2\pi\int_0^{\theta} P_{out}(\theta)\cdot\sin\theta\cdot d\theta \qquad [5]$$

Los parámetros de entrada son la posición espectral de la banda λ_B y la fineza de la resonancia F:

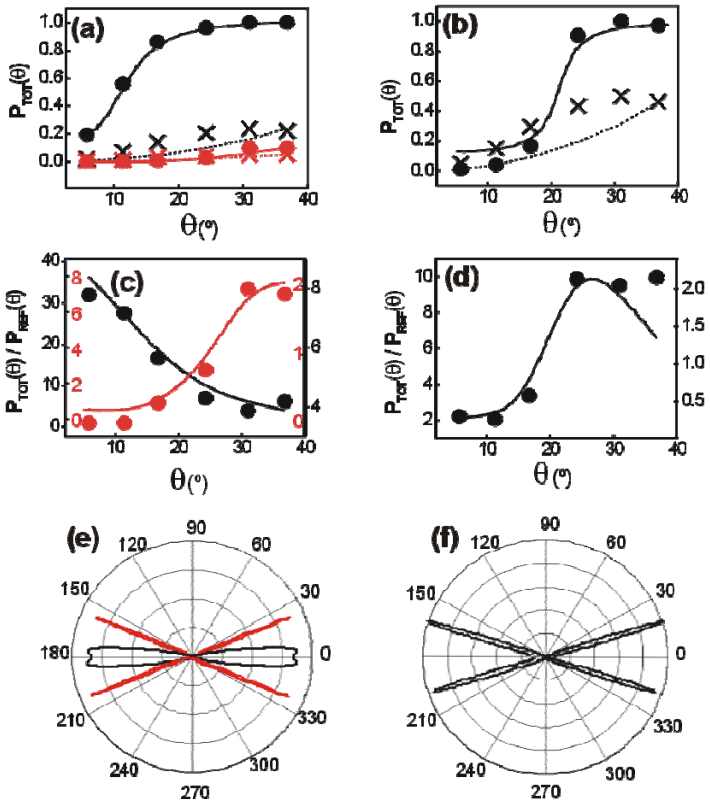

Figura 25. *(a) Potencia $P_{TOT}(\theta)$ extraída dentro de un cono de ángulo θ correspondiente a las bandas λ_B=708 nm y λ_B=655 nm medida para un resonador cuyo modo de la cavidad está situado en λ_C = 708 nm (puntos negros y rojos respectivamente) y para las muestras de referencia (cruces negras y rojas respectivamente). (b) Misma representación de $P_{TOT}(\theta)$ frente a θ para un resonador caracterizador por λ_C = 742 nm. (c) y (d) muestran los factores de aumento para estos dos resonadores, respectivamente, usando el mismo código de símbolos y de colores para identificar las bandas. Las curvas teóricas calculadas a partir de la ecuación 5 se muestran como líneas sólidas, mientras que los puntos son las experimentales. Finalmente, (e) y (f) muestran los correspondientes diagramas polares calculados para las bandas λ_B=708 nm (curvas negras) y λ_B= 655 nm (curvas rojas).*

$$F = \frac{\pi\sqrt{r_1 r_2}}{1 - r_1 r_2} \qquad [6]$$

En las Figuras 25(a) y 25(b), se muestran las curvas calculadas para $P_{TOT}(\theta)$ respecto del ángulo θ, obtenidas de la ecuación [5] para cada una de las bandas elegidas (líneas sólidas para el resonador y punteadas para la referencia). En todos los casos, se observa un buen acuerdo entre los datos obtenidos experimentalmente y los calculados teóricamente. Ha de tenerse en cuenta que el modelo no contempla las intensidades de las diferentes bandas de emisión de los nanofósforos en la referencia por lo tanto, sólo se podrá extraer información cualitativa de las curvas. Aunque las gráficas de 25(a) y 25(b) están representadas en unidades normalizadas, la relación entre todas las intensidades se preserva.

La dependencia angular de la intensidad de una banda de emisión a λ_B = 708 nm es función de la posición relativa entre λ_c y λ_B. En las Figuras 25(c) y 25(d) se muestran las dependencias angulares experimental y teórica del aumento de la emisión. Estas se estiman como el cociente entre la potencia luminiscente extraída del resonador para un cierto ángulo de colección y la colectada para referencia $(P_{TOT}(\theta)/P_{ref}(\theta))$. De nuevo, se observa que las tendencias teóricas (líneas sólidas negra y roja en las Figuras 22(c) y 22(d)) coinciden. Sin embargo, cuantitativamente los datos experimentales difieren de los teóricos en un factor comprendido entre 4 y 5. Estas diferencias se deben a las desviaciones que presenta la estructura experimental respecto de la simulada teóricamente. La principal diferencia entre ambas se debe a fluctuaciones en el espesor de la cavidad óptica debido estar hecha de nanopartículas de un tamaño promedio de 30 nm. Otra diferencia es que los emisores no están situados exactamente en el centro de la cavidad, tal y como se asume en el modelo teórico. A pesar de esto, este modelo reproduce bien el comportamiento observado. Por último, en las Figuras 25(e) y 25(f) se muestran diagramas polares teóricos de emisión. Se observa claramente las diferentes distribuciones angulares de la energía para las bandas emitidas a 708 (lóbulos negros) y 655 nm (lóbulos rojos) en función de la posición espectral del resonador en el cual han sido integrados los nanofósforos.

7. Conclusiones.

Se han presentado estudios sobre los dos diferentes métodos utilizados para fabricar todas las muestras analizadas en este trabajo de investigación: spin y dip coating. Para cada técnica, se han encontrado las condiciones experimentales óptimas

para construir cristales fotónicos unidimensionales de nanopartículas bajo estricto control de su respuesta óptica y de la calidad estructural de los mismos.

Se han construido espejos de Bragg porosos rígidos y flexibles, los cuales presentan reflectancia/transmitancia espectral plana a lo largo del rango infrarrojo cercano, visible y ultravioleta.

Se ha demostrado experimentalmente que se puede controlar la aparición de los órdenes secundarios del band gap fotónico.

Se han infiltrado multicapas de nanopartículas con arseniuro de galio obteniéndose una estructura fotónica que presenta picos de reflectancia de mayor anchura e intensidad en las regiones visible e infrarroja cercana del espectro electromagnético.

La absorción óptica característica de nanocoloides de oro recubiertos de sílice ha sido modificada al integrar dichas partículas en multicapas porosas.

Se han controlado las bandas de fotoluminiscencia típicas de nanofósforos dopados con Europio, aumentándolas o atenuándolas por integración de estas en cristales fotónicos unidimensionales hechos de nanopartículas. También se ha analizado la variación angular de dichas propiedades luminiscentes.

Las estructuras porosas estudiadas en esta tesis presentan una respuesta ante cambios en el entorno que puede ser de gran interés para la fabricación de dispositivos sensores.

8. Referencias.

[1] J.D. Joannopoulos, R.D. Meade, J.N. Winn, "Photonic Crystals: Molding the Flow of Light", Princeton University Press, Princeton, **1995**.

[2] S. Rabaste, J. Bellessa, A. Brioude, C. Bovier, J.C. Plenet, R. Brenier, O. Marty, J. Mugnier, J. Dumas, "Sol-gel fabrication of thick multilayer applied to Bragg reflectors and microcavities"*Thin Solid Films* **2002**, *416*, 242.

[3] R. M. Almeida, A. S. Rodrigues, "Photonic band gap and structures by sol-gel processing" *Journal of Non-Crystalline Solids* **2003**, *326*, 405.

[4] Y.C. Sung, M. Mamak, G. Freymann, N. Chopra, G. A. Ozin, "Mesopourus Bragg Stack color tunable sensors". *Nano Lett*, *11,* **2006**, 2456.

[5] M.C.Fuertes, F.J.López-Alcaraz, M.C.Marchi, H.E.Troiani, H.Míguez, G.J.A.A. Soler-Illia, "Photonic Crystals from ordered mesoporous thin-film functional building blocks", *Adv.Funct.Mater, 17* ,**2007**, 1247.

[6] S.Colodrero, M.Ocaña, A.R.González-Elipe, H.Míguez."Response of nanoparticle one dimensional photonic crystals to ambient vapour pressure" *Langmuir, 24*, **2008**, 9135.

[7] R.M. Crooks, M. Zhao, L. Sun, V. Chechik, L.K. Yeung, "Dendrimer-encapsulated metal nanoparticles: Synthesis, characterization, and applications to catalysis", *Acc. Chem. Res, 34,* **2001**, 181.

[8] D.J. Maxwell, J.R. Taylor, S. Nie. "Self-assembled nanoparticle probes for recognition and detection of biomolecules", *J. Am. Chem. Soc, 124,* **2002**, 9606.

[9] E. Hutter, J.H. Fendler. "Exploitation of localized surface plasmon resonance", *Adv. Mater, 16,* **2004**, 1685.

[10] K.L. Kelly, E. Coronado, L.L. Zhao, G.C. Schatz, "The optical properties of metal nanoparticles: The influence of size, shape, and dielectric environment " *J. Phys. Chem. B* **2003**, *107,* 668.

[11] K.A. Willets, R.P. Van Duyne. "Localized surface plasmon resonance spectroscopy and sensing "*Ann. Rev. Phys. Chem.* **2007**, *58*, 267.

[12] V.L. Colvin, M.C. Schlamp, A.P. Alivisatos. "Ligth Emitting-Diodes made from Cadmium Selenide Nanocrystals and a Semiconductor Polymer" *Nature, 370*, **1994**, 354.

[13] I.L. Medintz, H.T. Uyeda, E.R. Goldman, H. Mattoussi, "Quantum dot bioconjugates for imaging, labelling and sensing*", Nature Mat, 4*, **2005**, 435.

[14] J.K. Jaiswal, H. Mattoussi, J.M. Mauro, S.M. Simon "Long-term multiple color imaging of live cells using quantum dot bioconjugates", Nature Biotech. 21, 2003, 47.

[15] X. Peng, L. Manna, W. Yang, J. Wickham, E. Scher, A. Kadavanich, A. P. Alivisatos, "Shape control of CdSe nanocrystals", *Nature,404*, **2000**, 59.

[16] M.J. Bowers, J.R. McBride, S.J. Rosenthal, "White-light emission from magic-sized cadmium selenide nanocrystals"*J. Amer. Chem. Soc. 127*, **2005**, 15378.

[17] J.C. Boyer, L.A Cuccia,, J.A. Capobianco, "Synthesis of colloidal upconverting $NaYF_4$: Er^{3+}/Yb^{3+} and Tm^{3+}/Yb^{3+} monodisperse nanocrystals". *Nano Lett. 7*, **2007**, 847.

[18] F. García-Santamaría, V. Salgueirino-Maceira, C. López, L.M. Liz-Marzán, "Synthetic opals based on silica-coated gold nanoparticles" Langmuir 2002, 18, 4519.

[19] D.Y. Wang, V. Salgueiriño-Maceira, L.M. Liz-Marzán, F. Caruso. "Gold-silica inverse opals by colloidal crystal templating "*Adv. Mater.* **2002**, *14*, 908.

[20] E. Lidorikis, S. Egusa, and J.D. Joannopoulos. "Effective medium properties and photonic crystal superstructures of metallic nanoparticle arrays" *J. Appl. Phys, 101,* **2007**, 054304.

[21] P. Reithmaier, G. Sek1, A. Löffler, C. Hofmann, S. Kuhn, S. Reitzenstein, L.V. Keldysh, V.D. Kulakovskii, T.L. Reinecke, A. Forchel, "Strong coupling in a single quantum dot-semiconductor microcavity system". *Nature 432*, **2004**, 197.

[22] P.Lodahl, A.F. van Driel, I.S. Nikolaev, A.Irman, K. Overgaag, D. Vanmaekelbergh, W.L. Vos. "Controlling the dynamics of spontaneous emission from quantum dots by photonic crystals" *Nature, 430,* **2004**, 654.

[23] M. Aloshyna, S. Sivakumar, M. Venkataramanan, A. G. Brolo, F. C. J. M van Veggel,. "Significant suppression of spontaneous emission in SiO_2 photonic crystals made with Tb^{3+}-doped LaF_3 nanoparticles", *J. Phys. Chem. C, 111*, **2007**, 4047.

[24] Z. X. Li, L. L. Li, H. P. Zhou, Q. Yuan, C. Chen, L. D. Sun, C. H. Yan. "Colour modification action of an upconversion photonic crystal", *Chem. Commun*., *43*, **2009**, 6616.

[25] M. Calvo, O. Sánchez-Sobrado, S. Colodrero, H. Míguez "Control over the Structural and Optical Features of Nanoparticle based One-Dimensional Photonic Crystals" *Langmuir, 25***, 2008**, 2443.

[26] D. Meyerhofer, "Characteristics of resist films produced by spinning". *J. Appl. Phys. 49,* **1978**, 3993.

[27] D. P. Birnie, S. Hau, D.S. Kamber, D. M Kaz, "Effect of ramping-up rate on film thickness for spin-on processing*". J.Mater. Sci.-Mater. Electronics. 16*, **2005**, 715.

[28] O.Sánchez-Sobrado,M.Calvo, H. Míguez. "Versatility and multifunctionatility of high reflecting Bragg mirrors based on nanoparticlemultilayers", *J.Mater.Chem, 38*, **2010**, 8240.

[29] M. Calvo, O. Sánchez-Sobrado, G. Lozano, H. Míguez. "Molding with nanoparticle based One Dimensional Photonic Crystals: A Route to Flexible and Transferable Bragg Mirrors of High Dielectric Contrast." *J. Mater. Chem,19*, **2009**, 3144.

[30] S. Colodrero, M.Ocaña, H.Míguez. "Nanoparticle based one dimensional photonic crystals" *Langmuir.24*, **2008**, 4430.

[31] S. Colodrero, M. Ocaña, A. R. González-Elipe, H. Míguez."Response of nanoparticle one dimensional photonic crystals to ambient vapour pressure" *Langmuir, 24*, **2008**, 9135.

[32] O. Sánchez-Sobrado, K. Thomas, I. Povey, M. Pemble, H. Míguez, "Gallium arsenide infiltration of nanoporous multilayers: A route to high dielectric contrast one-dimensional photonic crystals", *Small, 6*, **2010**, 1283.

[33] A. Yariv, P. Yeh, "Optical Waves in Crystals", **2003** John Wiley and Sons Inc., ISBN 0-471-43081-1.

[34] S. Zollner. "Optical constants and critical-point parameters of GaAs from 0.73 to 6.60 eV" *J. Apply. Phys. 90*, **2001**,515.

[35] O. Sánchez-Sobrado, G. Lozano, M. E. Calvo, A. Sánchez-Iglesias, L. M. Liz-Marzán, H. Míguez. "Interplay of resonant cavity modes with localized surface plasmons: optical absorption properties of Bragg stacks integrating gold nanoparticles" *Adv. Mater* **2010**, 10.1002/adma.201004401.

[36] J. M. Bendickson, J. P. Dowling, M. Scalora. "Analytic expressions for the electromagnetic mode density in finite, one-dimensional, photonic band-gap structures"*Phys. Rev. E, 53,* **1996,** 4107.

[37] N. A. R. Bhat, J. E. Sipe. "Optical pulse propagation in nonlinear photonic crystals" *Phys. Rev. E, 64,* **2001**, 056604.

[38] T. Ung, L. M. Liz-Marzán, P. Mulvaney. "Optical properties of thin films of Au@SiO_2 particles" *J. Phys. Chem. B, 105,* **2001**, 3441.

[39] O. Sánchez-Sobrado, M.E Calvo, N. Núñez, M. Ocaña, G. Lozano, H. Míguez, "Environmentally Responsive Nanoparticle based Luminescent Optical Resonators" *Nanoscale, 2*, **2010**, 936.

[40] O. Sánchez-Sobrado, A. M. Yacomotti, M.E. Calvo, O. E. Martínez, M. Ocaña, N.Núñez, J. A. Levenson, H. Míguez. "Angular emission properties of a layer of rare-earth based nanophosphors embedded in one-dimensional photonic crystal coatings". *Appl.Phys.Lett*, **2011**, acepted.

[41] E.W. J. L. Oomen, A. M. A. van Dongen, "Europium (III) in Oxide Glasses-Dependence of the Emission-Spectrum upon Glass composition" *J. Non-Crys. Solids, 111*, **1989**, 205.

[42] H.Benisty, H. De Neve, C.Weisbuch. “Impact of planar microcavity effects on light extraction - Part I: Basic concepts and analytical trends”, *IEEE Journal of Quantum Electronics. 34*, **1998**, 9.

Abbreviations

1DPC	One Dimensional Photonic Crystal.
NIR	Near InfraRed.
UV	UltraViolet.
NIR-Vis-UV	Near InfraRed-Visible-UltraViolet.
MOCVD	Metal Organic Chemical Vapor Deposition.
PDMS	Poly DiMethyl Siloxane.
PC	PolyCarbonate.
SEM	Scanning Electron Microscopy.
FESEM	Field Emission Scanning Electron Microscopy.
TEM	Transmission Electron Microscopy.

Collaborations and short stays

Collaboration with Professor Luis Liz-Marzán and Ana M. Sánchez-Iglesias from *Departamento de Química Física and Unidad Asociada CSIC* (CSIC-Universidade de Vigo, Spain). Gold nanoparticles were synthesized by members of this group. The results obtained from this collaboration were reported in the publication 2 of the section "Publications and covers gallery".

September-November 2010. Short stay in the *Laboratoire de Photonique et de Nanostructures* (Centre Nationale Recherche Scientifique, France). Angular luminescent properties of nanoparticle 1DPCs embedding nanophosphors were analyzed in collaboration with Dr. Alejandro Giacomotti and Dr. Ariel Levenson. The results obtained were reported in the publication 1 of the section "Publications and covers gallery".

May-June 2009. Short stay in the *Tyndall Institute* (University College Cork, Ireland). Nanoparticles 1DPCs were infiltrated with GaAs by MOCVD. The research was carried out with Dr. Kevin Thomas under the supervision of Professor Martin Pemble. The results obtained were reported in the publication 4 of the section "Publications and covers gallery".

Publications and covers gallery

1. O. Sánchez-Sobrado, A. M. Yacomotti, M. E. Calvo, O. E. Martínez, M. Ocaña, N. Núñez, J. A. Levenson, H. Míguez.

"Angular emission properties of a layer of rare-earth based nanophosphors embedded in one dimensional photonic crystal coatings".

Appl.Phys.Lett, **2011**, (accepted).

2. O. Sánchez-Sobrado, G. Lozano, M. E. Calvo, A. Sánchez-Iglesias, L. M. Liz-Marzán, H. Míguez.

"Interplay of resonant cavity modes with localized surface plasmons: optical absorption properties of Bragg stacks integrating gold nanoparticles".

Adv. Mater, *23*, **2011**, 2108.

3. O. Sánchez-Sobrado, M. E. Calvo, H. Míguez.

"Versatility and multifunctionatility of high reflecting Bragg mirrors based on nanoparticle multilayers".

J.Mater.Chem, *20*, **2010**, 8240.

4. O. Sánchez-Sobrado, K. Thomas, I. Povey, M. Pemble, H. Míguez.

"Gallium arsenide infiltration of nanoporous multilayers: A route to high dielectric contrast one-dimensional photonic crystals".

Small, 6, **2010**, 1283.

5. O. Sánchez-Sobrado, M.E. Calvo, N. Núñez, M. Ocaña, G. Lozano, H. Míguez.

“Environmentally Responsive Nanoparticle based Luminescent Optical Resonators”.

Nanoscale, 2, **2010**, 936.

6. M. E. Calvo, **O. Sánchez-Sobrado**, G. Lozano, H. Míguez.

"Molding with nanoparticle based One Dimensional Photonic Crystals: A Route to Flexible and Transferable Bragg Mirrors of High Dielectric Contrast".

J. Mater. Chem, 19, **2009**, 3144.

7. M. E. Calvo, **O. Sánchez-Sobrado**, S. Colodrero, H. Míguez.

“Control over the Structural and Optical Features of Nanoparticle based One-Dimensional Photonic Crystals”.

Langmuir, 25, **2008**, 2443.

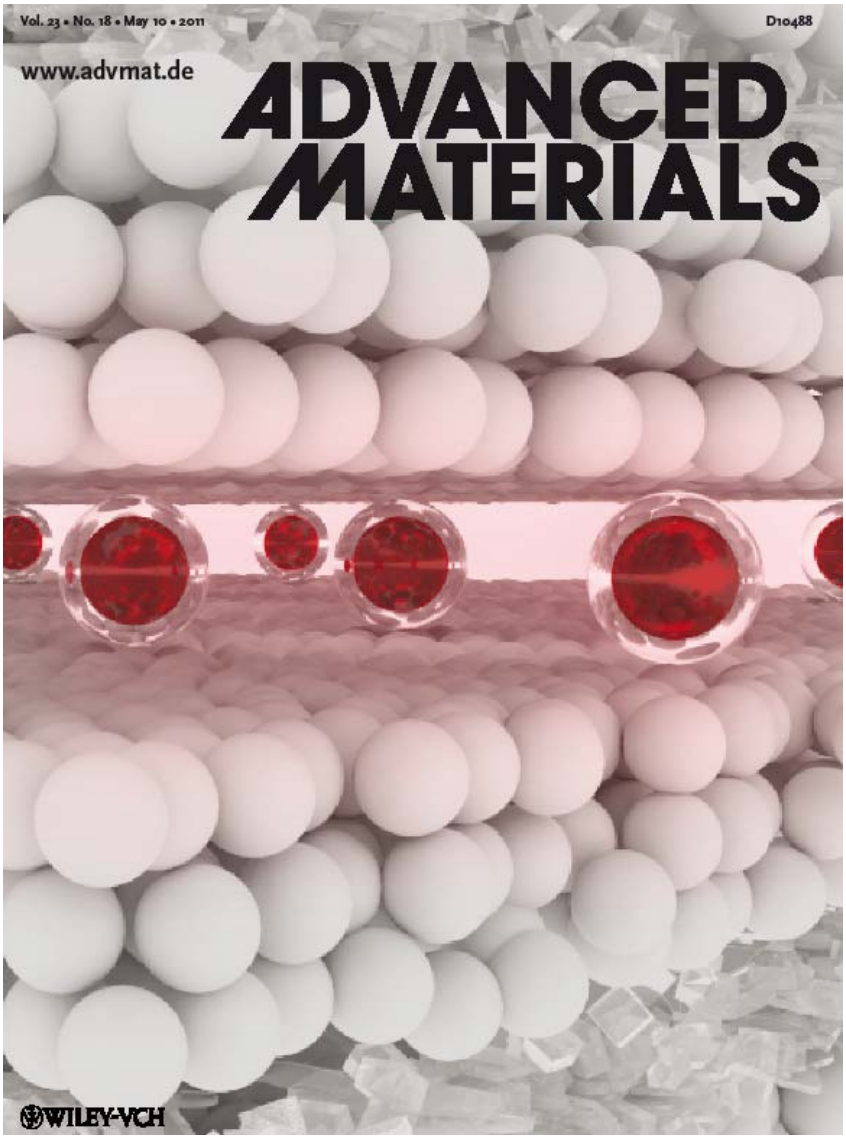

O. Sánchez-Sobrado, G. Lozano, M. E. Calvo, A. Sánchez-Iglesias, L. M. Liz-Marzán, H. Míguez.

"Interplay of resonant cavity modes with localized surface plasmons: optical absorption properties of Bragg stacks integrating gold nanoparticles".

Adv. Mater, *23*, **2011**, 2108.

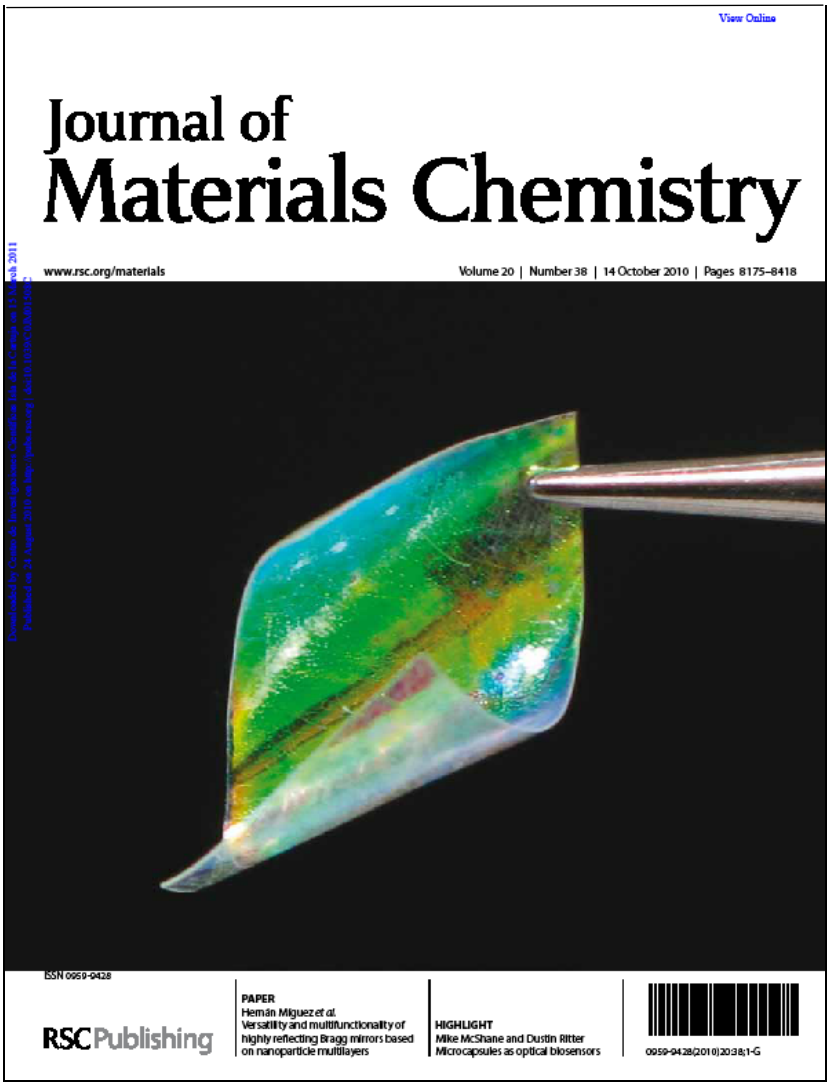

O. Sánchez-Sobrado, M. E. Calvo, H. Míguez.

"Versatility and multifunctionatility of high reflecting Bragg mirrors based on nanoparticle multilayers".

J.Mater.Chem, 20, **2010**, 8240.

O. Sánchez-Sobrado, M.E. Calvo, N. Núñez, M. Ocaña, G. Lozano, H. Míguez.

"Environmentally Responsive Nanoparticle based Luminescent Optical Resonators".

Nanoscale, 2, **2010**, 936.